

Dynamical Interaction between Atmosphere and Sea Ice in Antarctica

Alexander Haumann



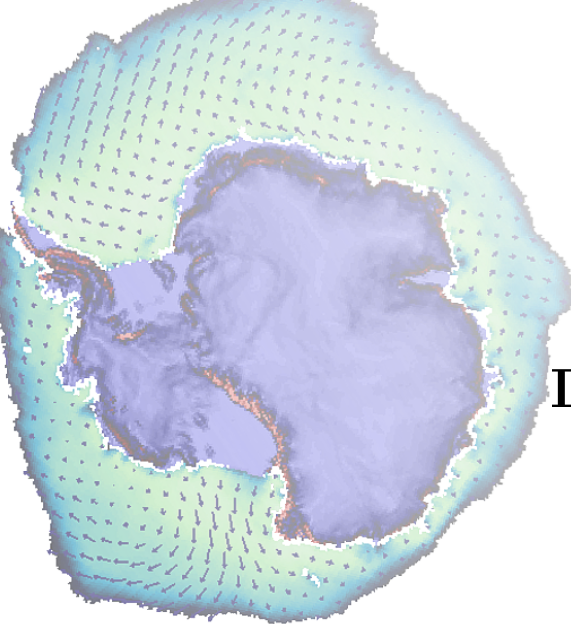
Universiteit Utrecht



Copyright © 2011, F. A. Haumann, Utrecht, The Netherlands
Author: F. Alexander Haumann
Printing: Utrecht University

Institute for Marine and Atmospheric research Utrecht (IMAU)
Department of Physics and Astronomy
Faculty of Science
Utrecht University

Cover: Strong and cold winds from the Ross Ice Shelf (lower right corner) push the sea ice away from the Antarctic coast and open up the large Ross Sea Polynya. Since the atmosphere is rather cold new sea ice forms continuously at the open water surface. The satellite image is recorded by Aqua/MODIS on November 16, 2011 at 04:10 UTC (Source: NASA/GSFC, by courtesy of Jeff Schmaltz, LANCE Rapid Response).



Dynamical Interaction between Atmosphere and Sea Ice in Antarctica

Master's Thesis

by

Alexander Haumann

Utrecht University

October 2011



Universiteit Utrecht



Institute for Marine and
Atmospheric research Utrecht

Supervisor: Prof. Dr. Michiel R. van den Broeke
E-mail: M.R.vandenBroeke@uu.nl

Co-Supervisors: Jan H. van Angelen
E-mail: J.H.vanAngelen@uu.nl

Jan T. M. Lenaerts
E-mail: J.Lenaerts@uu.nl

Abstract

Sea ice that covers large parts of the polar oceans throughout most of the year responds to changes in the atmosphere or the ocean within a short period of time. The rapid decrease of the Arctic sea ice cover in the past decades has led to a fundamental discussion of the role of sea ice in the climate system. Surprisingly, in contrast to the northern hemisphere, the sea ice in the Southern Ocean has been slightly increasing over the last decades. This is owing to essentially different processes that take place around Antarctica. There, the ice is not confined to a basin as in the Arctic Ocean but can move rather freely around the Antarctic continent which results in a strong response to changes in the wind field.

In this Master's thesis I examined the impact of the variations in the coastal Antarctic atmospheric boundary layer on the sea ice. By studying wind driven sea ice transport in the Southern Ocean and temporal and spatial variabilities in the period 1989 to 2006, I have revealed important characteristics of the sea ice cover and processes that determine its growth and decay. The near surface wind field over the coastal continent and ocean as well as its forcing mechanisms were described in detail by using output from a regional atmospheric climate model. This showed strong relations to key parameters that I have deduced from a satellite record of sea ice concentration and sea ice motion.

The regions of the largest sea ice extent, the Ross and Weddell Seas, are also those areas where most of the sea ice transport takes place and where its variability is the largest. Interannual variations and trends of transport are associated with varying sea ice concentration just north of these areas in the Ross and Weddell Seas. Comparing the wind field and the sea ice motion, I found out that spatial patterns of persistent southerly or south-easterly winds coincide with those of ice drift. The winds in these regions result from combined effects of the large-scale pressure distribution, cold air that accumulates over the ice shelves, and large topographic barriers that alter the flow. Adjacent to the large Ross and Ronne-Filchner Ice Shelves constant outflow of cold air takes place almost year-round. Here, sea ice is constantly exported from the coastal region, and large polynyas and leads form. As the cold winds not only lead to sea ice transport but also support refreezing of the open water, these areas are associated with strong sea ice formation. I have defined an index that captures the outflow of cold continental air from the ice shelves. The long-term variations in outflow correlate well with variations of the sea ice cover and meridional sea ice transport in the Ross and western Weddell Seas. Further, the results suggest that the positive trend of sea ice cover in western Ross Sea and the negative trend in the western Weddell Sea are related to a respective seasonal increase and decrease of cold air outflow. Overall, in my thesis, I showed that the dynamical interaction between the atmospheric boundary layer and the sea ice is a regional key element in the interannual variability and the long-term changes of the sea ice cover in the Southern Ocean.

Contents

Abstract	i
Boxes	iv
Figures	v
Tables	v
1 Introduction	1
2 Theoretical Background	7
2.1 The Antarctic Atmospheric Boundary Layer over Snow, Ice and Ocean	8
2.2 Forcing Mechanisms of the Antarctic Atmospheric Boundary Layer Dynamics	16
2.3 Forcing Mechanisms of Sea Ice Formation and Transport	21
3 Data & Model Description	27
3.1 The Regional Atmospheric Climate Model RACMO2.1/ANT	28
3.2 Sea Ice Concentrations from Passive Microwave Satellite Data	34
3.3 Sea Ice Drift Data from Satellites	40
3.4 Data Assimilation and Grid Adaptation	41
4 Simulated Atmospheric Boundary Layer Processes	45
4.1 Cold Air Pooling and Near-Surface Temperature	45
4.2 The Near-Surface Wind Field	56
4.3 The Forcing Terms of the Wind Field	62
4.4 Cold Air Pooling Along Topographic Barriers and Associated Flow	68
5 Observed Sea Ice Cover & Dynamics	74
5.1 Sea Ice Cover	74
5.2 Sea Ice Transport	86
5.3 Open Water Formation and Sea Ice Production	99
6 Regional Assessment of Cold Air Outflow over Sea Ice	106
6.1 Ross Sea and Ice Shelf Area	106
6.2 Weddell Sea and Ronne-Filchner Ice Shelves	112
7 Conclusions & Discussion	118
Bibliography	123
Acknowledgment	131

Boxes

4.1	Variance of Detrended Anomalies	51
4.2	Trend, Significance, and Uncertainty	53
4.3	Directional Constancy	59
5.1	Sea Ice Extent and Area, and Open Water Area	75
5.2	Sea Ice Area Flux	90
6.1	Cold Air Outflow	107

Figures

1.1	GISS polar surface temperature changes	2
1.2	Antarctic continent & surrounding seas	3
1.3	Antarctic topography & slope	5
2.1	Schematic surface radiation balance	9
2.2	Schematic ABL temperature profile	12
2.3	Schematic surface energy balance	13
2.4	Schematic ABL momentum terms	19
2.5	Schematic sea ice momentum terms	24
3.1	RACMO2.1/ANT horizontal grid	29
3.2	RACMO2.1/ANT vertical grid	30
3.3	RACMO2.1/ANT topography & orographic variance	31
3.4	Simulated average July roughness length	33
3.5	Difference between ERA-Interim & SSM/I Antarctic sea ice area anomalies	36
3.6	Difference between ERA-Interim & SSM/I Antarctic sea ice concentration	37
3.7	Average July sea ice concentration of ERA-Interim, SSM/I, and AMSR-E	39
3.8	Average July Polar Pathfinder sea ice motion	40
3.9	Comparison of grids of different data sets	42
3.10	Effects of the grid interpolation	43
4.1	Simulated net longwave radiation at the surface	46
4.2	Simulated atmospheric turbulent heat fluxes at the surface	47
4.3	Simulated atmospheric surface energy balance over the Southern Ocean	48
4.4	Simulated 2 m temperature	50
4.5	Simulated atmospheric surface layer potential temperature	51
4.6	Variance of detrended surface layer potential temperature anomalies	52
4.7	Decadal trend of simulated surface layer potential temperature	54
4.8	Simulated height of the temperature inversion	55
4.9	Simulated mean surface pressure below 120 m a.s.l.	57
4.10	Simulated atmospheric surface layer wind field & directional constancy	60
4.11	Variance of detrended surface pressure anomalies	61
4.12	Variance of detrended meridional & zonal wind speed anomalies	62
4.13	Decadal trend of surface pressure & surface layer wind field	63
4.14	Average July simulated surface layer potential temperature deficit & katabatic forcing . .	64
4.15	Average July simulated 500 hPa height & large-scale forcing	65
4.16	Average July simulated surface layer temperature deficit layer & thermal wind forcing . .	67
4.17	Average July simulated surface layer potential temperature deficit & temperature deficit layer with new extrapolation algorithm	69
4.18	Average July simulated large-scale & thermal wind forcing for model layer 30	70
4.19	Average July Ross & Ronne-Filchner Ice Shelves off-shore winds at model layer 32 . . .	71
4.20	Average July wind & potential temperature cross-sections along the Ross & Ronne-Filchner Ice Shelf edges	72
5.1	Southern Ocean sea ice extent & area anomalies	76

5.2	Power spectra of the sea ice extent anomaly residuals	77
5.3	Average of minimum & maximum sea ice concentration	78
5.4	Average annual cycle of the daily rate of change of sea ice area	79
5.5	Sea ice area & extent (seasonal cycle, anomalies, trends) for each sector	81
5.6	Variance of detrended sea ice concentration anomalies	82
5.7	Decadal trend of sea ice concentration anomalies	83
5.8	Hovmöller diagram for sea ice extent anomalies	85
5.9	Comparison of eastern Ross Sea & western Weddell Sea sea ice extent	85
5.10	Sea ice motion vectors & directional constancy	88
5.11	Sea ice drifting angle compared to wind direction	89
5.12	Meridional & zonal sea ice area fluxes (seasonal cycle, anomalies, trends) for each sector	92
5.13	Variance of detrended meridional & zonal sea ice area flux anomalies	94
5.14	Decadal trend of meridional & zonal sea ice area flux anomalies	97
5.15	Comparison of sea ice extent & mean area flux anomalies	98
5.16	Average annual cycle of the daily open water area	101
5.17	Average September polynyas & sea ice drift divergence	102
5.18	Sea ice area production	104
5.19	Yearly averaged sea ice area production anomalies & trends	105
6.1	Correlation between Ross Sea sea ice extent & meridional transport anomalies	108
6.2	Average July difference between years of low and high sea ice extent in the Ross Sea for surface pressure and meridional transport	108
6.3	Cold air outflow cross-section along the Ross Ice Shelf edge	109
6.4	Comparison of Ross Sea sea ice extent & Ross Ice Shelf cold air outflow anomalies	110
6.5	Correlation between Ross Ice Shelf cold air outflow anomalies & meridional transport & sea ice concentration anomalies	110
6.6	Total outflow from the Ross Ice Shelf for each season & trends	111
6.7	Correlation between Weddell Sea sea ice extent & meridional transport anomalies	112
6.8	Average July difference between years of low and high sea ice extent in the Weddell Sea for surface pressure and meridional transport	113
6.9	Cold air outflow cross-section along the Ronne-Filchner Shelf edges	114
6.10	Comparison of Weddell Sea sea ice extent & Ronne-Filchner Ice Shelves cold air outflow anomalies	115
6.11	Correlation between Ronne-Filchner Ice Shelves cold air outflow anomalies & meridional transport & sea ice concentration anomalies	115
6.12	Total outflow from the Ronne-Filchner Ice Shelves for each season & trends	116

Tables

3.1	RACMO2.1/ANT coordinates	30
5.1	Correlation between sea ice extent & transport	99
7.1	Correlation between sea ice, outflow, SAM & ENSO	121

1 Introduction

In recent years polar regions have gained more and more attention in the scientific community and in the public media because of their high sensitivity to variations in the climate system and because of dramatic changes that have taken place. In the last decades, the consequences of human induced climate change have been most noticeable in higher latitudes. These incorporate alterations of the circulation and heat content in the atmosphere and ocean, and changes of the cryosphere on land and ocean. Polar regions where large amounts of heat are emitted to space are a crucial part of the Earth's system. Thus, it is of major importance to understand the polar climates, their variability, and long-term changes.

The polar oceans are almost completely covered with a thin layer of ice in winter (only about one to a few meters thick) that decreases in thickness and extent during summer and almost vanishes in the southern hemisphere. Heat, momentum, and moisture are exchanged at the ice surface with the atmosphere and at its base with the ocean. As sea ice is only a very thin interface between the atmosphere and the ocean, it is very vulnerable to changes and adapts rather fast to anomalies. The feedback mechanisms involving sea ice are very strong which devotes sea ice a very important role in the climate system. This strong coupling of the processes is also owing to the unique properties of sea ice such as its high albedo. Whereas the open ocean surface absorbs almost all the incident solar radiation, sea ice reflects most of it. Consequently, this difference of the albedo gives rise to a positive feedback for the surface temperature because if more sea ice melts due to higher temperatures, more open water is present, more solar radiation is absorbed, and temperatures of the surface ocean and atmosphere rise even more. This process is commonly referred to as ice-albedo feedback.

Moreover, there are other processes that have a stabilizing effect on the sea ice cover and counteract the positive feedback. Because sea ice insulates the atmosphere and the ocean, less heat is lost to the cold atmosphere in winter over the sea ice covered ocean. In contrast, an open ocean surface cools much faster and sea ice forms more easily. The same is valid for thinner ice; as heat is better conducted through thin ice, it grows faster. As a consequence, if there is less sea ice in one summer, it regrows faster in the subsequent winter.

Additionally to the feedback mechanisms just described, sea ice can have an effect on the ocean circulation by producing cold and dense water masses during the sea ice formation process. These water masses sink to the ocean bottom where they are transported to lower latitudes and contribute to the meridional exchange of heat by the ocean. Further, sea ice affects the large-scale circulation in the atmosphere due to differential heating over the open ocean and the sea ice covered ocean which sets up pressure gradients over large spatial scales that change with changing sea ice cover. Long-term changes of the sea ice can also indirectly have an effect on the global sea level. Less sea ice cover in a coastal region leads to a local heating of the ocean and the atmosphere. This can destabilize the ice shelves or the surging outlet glaciers of ice sheets. If they disintegrate, the ice loss from the ice sheets is likely to increase and add to the global sea level rise. Moreover, sea ice can even be important for the global greenhouse gas concentrations in several ways such as the release of methane from the ocean to the atmosphere or the uptake of carbon dioxide by net primary production that is high in the polar oceans. The exchange of these gases depends on the temperature of the ocean and on the thickness of the ice cover that might act as a physical barrier. All these processes point out that sea ice is bestowed a key role in the climate system, especially in the polar regions but also in a global context and it is essential to understand the processes that are involved in detail.

Records of the Arctic sea ice have shown a dramatic decrease of its extent and thickness since the continuous satellite measurements have started in 1979 which has even accelerated during the last years (Comiso et al., 2008; Kwok et al., 2009; Parkinson and Cavalieri, 2008). Between 1979 and 1996 the sea ice extent decreased by about 2.2% per decade and in the years 1996 to 2007 by about 10.1% per decade (Comiso et al., 2008). In September 2007 the lowest sea ice cover since measurements have started was recorded, followed by the second lowest ice cover in September 2011 (cf. National Snow and Ice Data Center, <http://nsidc.org/arcticseaincnews>). Global climate models project that the September sea ice cover in the Arctic will vanish within this century and that the Arctic Ocean will be subject to a

seasonal ice cover only (Stroeve et al., 2007). These rapid changes of the northern hemisphere sea ice are associated with an amplified surface warming in the Arctic and large-scale circulation changes (cf. Deser et al., 2000; IPCC, 2007). Figure 1.1(a) shows that the Arctic region is subject to the strongest global surface temperature increase during the period 1979 to 2010 (Hansen et al., 2010).

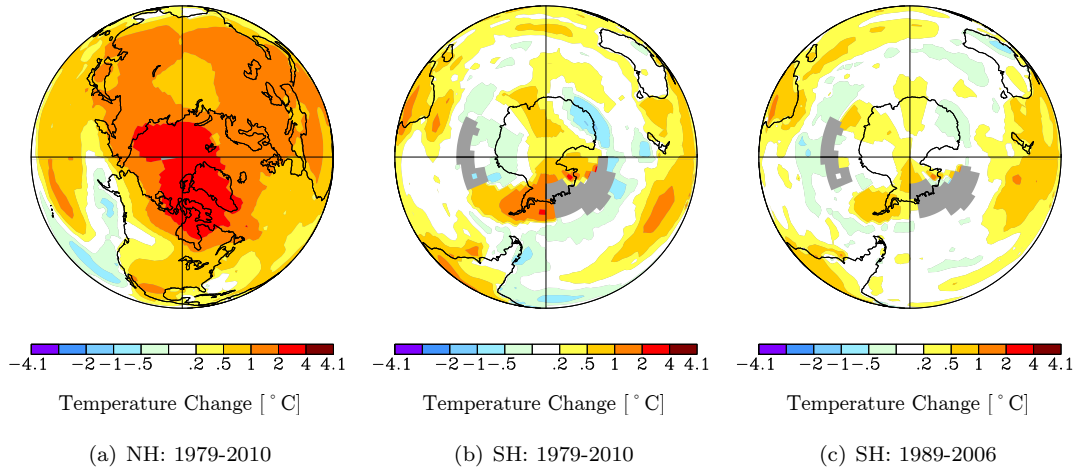


Figure 1.1: Goddard Institute for Space Studies (GISS) analysis of global surface temperature changes for the northern hemisphere in the period 1979 to 2010 (a) and for the southern hemisphere in the periods 1979 to 2010 (b) and 1989 to 2006 (c) (figures generated by <http://data.giss.nasa.gov/gistemp/maps> with data from Hansen et al., 2010). Gray areas indicate missing values.

While in the Arctic sea ice is confined to a basin that is surrounded by continents, in the Southern Ocean it forms around the Antarctic continent in winter. This different orographic set up and a different climate regime lead to essentially different processes that are causing variations and long-term changes of the Antarctic sea ice. The strong winds over the Southern Ocean, the meridional change from the dominant westerlies to easterlies near the coast, and the cyclones that move over the sea ice covered ocean around the continent imply that the freely moving sea ice is subject to a strong drift and that changes in the dynamics might be important. The difference between the two hemispheres is also reflected in amplitude and period of the variability of the sea ice extent (Cavalieri et al., 1997, 2003). Further, in contrast to the northern hemisphere sea ice, the total sea ice extent of the Southern Ocean has been increasing significantly by $1 \pm 0.4\%$ per decade in the period 1979 to 2006 (Cavalieri and Parkinson, 2008).

There has been a debate about the sign, magnitude, and accuracy of near-surface temperature trends over and around the Antarctic continent. This arises mainly from two problems to determine the trends: on the one hand, long-term and consistent measurements are scarce due to the extreme conditions, and, on the other hand, spatial and temporal temperature patterns are very complex as they depend strongly on the meridional heat transport and circulation changes. Whereas Doran et al. (2002) report an overall cooling trend over the continent between 1966 and 2000, Turner et al. (2002) state an overall slight but significant warming from 1958 to 2000. The regional inhomogeneity of the trends is pointed out by an analysis of station data by Turner et al. (2005) and by a study of Monaghan et al. (2008). Van den Broeke (2000a) highlights the connection between the circulation and the near-surface temperature trends as well as the role of sea ice for the temperature. When analyzing the effect of near-surface temperatures on sea ice, it should always be kept in mind that temperature is not an independent variable due to the feedback mechanisms with the sea ice described before. Figure 1.1(b) shows the Goddard Institute for Space Studies (GISS) analysis temperature changes over Antarctica and the surrounding ocean for the periods 1979 to 2010. It is apparent that there is no clear overall cooling trend that might explain the increasing sea ice cover of the Southern Ocean. A rather strong warming is present over West Antarctica and, especially, over the Antarctic Peninsula. A different period (1989 to 2006) of the same dataset is

shown in figure 1.1(c). I will use this period throughout this thesis which is the reason why it is included here. The changes in this period have a very similar spatial pattern but are generally much weaker.

Variations of the Antarctic sea ice are very regionally confined. Consequently, they are usually assessed for five different sectors of the Southern Ocean defined by Zwally et al. (1983). These sectors are shown in figure 1.2 in green (Weddell Sea, Indian Ocean, Western Pacific, Ross Sea, and Bellingshausen and Amundsen Seas). Cavalieri and Parkinson (2008) report a positive sea ice extent trend for all sectors except for the Bellingshausen and Amundsen Seas sector where a significant decrease of about $5.4 \pm 1.9\%$ per decade was determined in the period 1979 to 2006. The only sector with a significant increase of the other four is the Ross Sea. There, sea ice extent has a positive trend of about $4.4 \pm 1.7\%$ per decade. These regional trends also suggest that other factors than a large-scale near-surface temperature change (as it is the case in the Arctic) are responsible for the Antarctic sea ice changes.

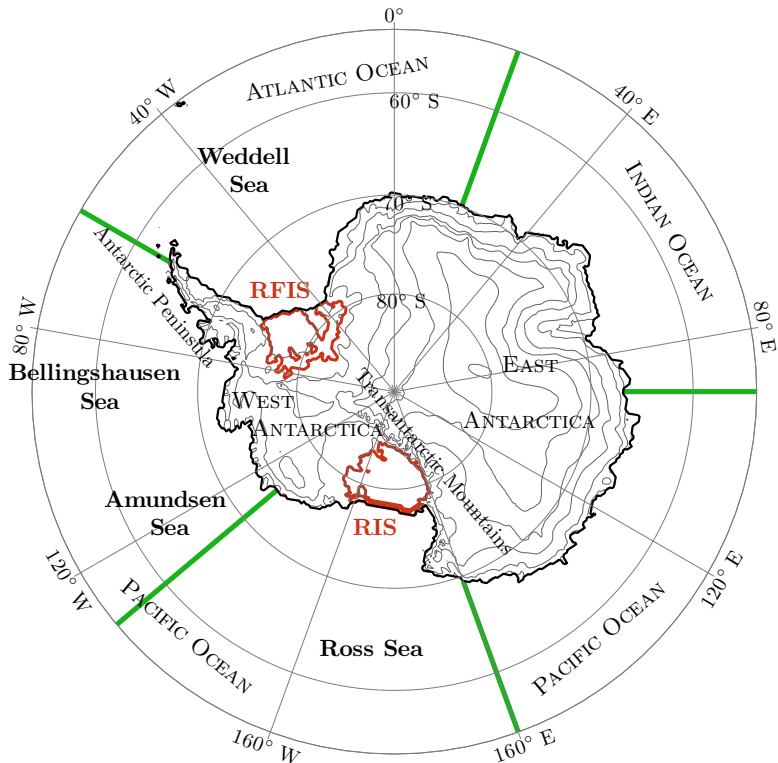


Figure 1.2: The Antarctic continent and the surrounding seas. The red contours indicate the large Ronne-Filchner (RFIS) and Ross (RIS) Ice Shelves. The green lines indicate the five sectors: Weddell Sea, Indian Ocean, Western Pacific, Ross Sea, and Bellingshausen and Amundsen Seas (as in Zwally et al., 1983).

Several authors have addressed the question why the Antarctic sea ice is increasing and what processes might cause its variations. Recently, Shu et al. (2011) claimed a regionally confined relation between the surface air temperature changes and those of the local sea ice concentration. Kwok and Comiso (2002b) showed that the temperature variations and trends, in turn, are strongly related to the Southern Annular Mode (SAM; also known as Antarctic Oscillation, AAO) and El Niño/Southern Oscillation (ENSO) which is most pronounced around the Antarctic Peninsula. Others directly relate the variability of the sea ice cover to the large-scale circulation and to SAM and ENSO signals. Teleconnections between the variability of SAM and ENSO have been related to regional variability of the sea ice cover (Carleton, 2003; Kwok and Comiso, 2002a; Yuan, 2004; Yuan and Martinson, 2000). Liu et al. (2004) state that this link is responsible for variabilities of the meridional heat flux in the Bellingshausen Sea which influences the sea ice cover. The overall sea ice variability shows stronger relations to the SAM signal than to ENSO

in most regions (Lefebvre et al., 2004; Stammerjohn et al., 2008) because SAM explains large parts of the interannual climate variability over the Southern Ocean and Antarctica (Thompson and Solomon, 2002). Still, large parts of the Antarctic sea ice variability and the processes relating it to the atmospheric circulation remain unexplained.

Neither SAM nor ENSO explain the long-term increasing sea ice cover. Turner et al. (2009) hypothesize that the positive trend in the Ross Sea in autumn is caused by a stronger cyclonic activity in the Amundsen Sea. According to their model study the increasing cyclonic activity is related to the stratospheric ozone depletion. They suggest that the wind stress curl in this region might have increased which accelerated the Ross Sea Gyre. However, there is no evidence for such changes. By analyzing climate model data Wang and Meredith (2008) even showed that the response of the strength of the Ross Gyre to the wind stress is weak and it is mostly determined by upper ocean layer density gradients. A model study by Sigmond and Fyfe (2010), in contrast to Turner et al. (2009), postulates that the ozone depletion would, actually, cause a decreasing Antarctic sea ice cover and that the observed increase should be related to other processes.

There have also been other suggestions to relate the changes to the ocean. Jacobs et al. (2002) report a freshening of the Ross Sea since the 1960s due to increased precipitation and melting from the West Antarctic Ice Sheet which led to a more stratified upper ocean. This would imply a decreasing ocean heat flux which favors sea ice formation (Zhang, 2007).

In sum, there have been many attempts to explain trends and variabilities of the sea ice cover in the Southern Ocean. It is well-known that the sea ice and the related processes need to be assessed on a very regional scale and that trend patterns are very complex in time and space. As in-situ observational data is really scarce, most of the analysis is based on strongly interpolated observations, satellite data, and model studies. All studies consistently suggest that the atmospheric circulation around the Antarctic continent is the responsible external forcing for most of the sea ice variability and might also be responsible for the long-term trends. Many of the driving mechanisms of the internal variability, though, remain unclear. The lack of understanding of the role that the atmospheric circulation plays for the sea ice cover is also reflected in the large disagreement between the observed sea ice cover of the Southern Ocean and the one simulated by climate models (cf. IPCC, 2007). This motivates a further study of the Antarctic sea ice from a process based perspective, meaning to investigate changes and variations of the direct forcing terms that are responsible for sea ice formation and decay.

So, what are the controlling factors of the Antarctic sea ice cover? We can, generally, distinguish three processes that determine sea ice formation. First of all, there is a pure thermodynamic forcing which is the most important process as it triggers initial ice formation and subsequent growth at the ice base. It is induced by the thermal gradient between the ocean and the atmosphere. By heat loss of the open ocean to the atmosphere or by heat conduction through the sea ice if it is already present, the ocean water cools and, eventually, freezes. Secondly, once a layer of ice is present, there are several effects imposed by sea ice dynamics. I have already mentioned that beside heat also momentum is transferred from the atmosphere and the ocean to the sea ice. Consequently, this wind and ocean current stresses imply a deformation of the sea ice that might break up and drift in the form of large or small ice floes. The drifting ice leads to a mechanical redistribution that is responsible for the formation of open water areas in regions where sea ice is exported and for a thickening due to so-called ridging of the ice in regions where it accumulates. Induced by the sea ice dynamics, a secondary effect plays an important role. The formation of open water in a region of sea ice export is followed by an almost immediate refreezing of the ocean surface as here temperatures are usually far below the freezing point. Subsequently, the newly formed ice gets exported again which makes open water areas in winter to regions of effective sea ice formation due to strong winds and currents. At last, the third important process is the accumulation of snow on top of sea ice. Beside the formation of snow-ice due to the densification of the snow-pack, it also alters the surface albedo and the heat conduction through the ice. I will discuss these forcing mechanisms of sea ice formation and decay in detail in chapter 2 of this thesis.

As the circulation over the Southern Ocean was found to be important for the sea ice, I will focus on the second described process of the sea ice formation related to the sea ice dynamics in this thesis. Further, I

will only consider the relation to the atmospheric forcing. In order to do so, it is important to study wind and temperature in the atmospheric boundary layer over the sea ice covered ocean and the processes that determine their evolution. The temporal and spatial variability of the boundary layer is caused by the differences in temperature and pressure in the atmosphere over the Antarctic continent, the sea ice, and the open ocean and by influences of the upper atmosphere. It is well known that temperatures over the Antarctic continent are extremely low and that near-surface winds, especially in coastal areas, can be very strong. In theory, dynamical processes in the Antarctic boundary layer are well known and have been studied for example by Ball (1960), Parish and Bromwich (1987), or van den Broeke and van Lipzig (2003a). I will provide an in-depth discussion of the theoretical processes in the Antarctic boundary layer in chapter 2.

The orographic set up of the Antarctic continent is very important for the distribution and characteristics of the wind and temperature regimes in the boundary layer. In figure 1.3 we can see the surface elevation of the ice sheets and mountains on the continent (a) and the corresponding slope of the terrain (b) (data from Bamber et al., 2009). The highest regions are the East and West Antarctic Ice Sheets and the two large mountain ranges, namely the Transantarctic Mountains and the Antarctic Peninsula that will be important to this thesis (see also figure 1.2). The mountains and the coastal regions clearly show the steepest slopes on the whole continent. These are also those regions where very strong winds are observed (e.g. Parish and Bromwich, 1987). Further, we can see the very flat ice shelves. The two largest ones that are very close to the mountain ranges mentioned before are the Ronne-Filchner and the Ross Ice Shelves that are also outlined in figure 1.2 in red. The continent that is subject to a very strong radiative heat loss in winter directly influences the boundary layer structure over the ice shelves and the coastal sea ice.

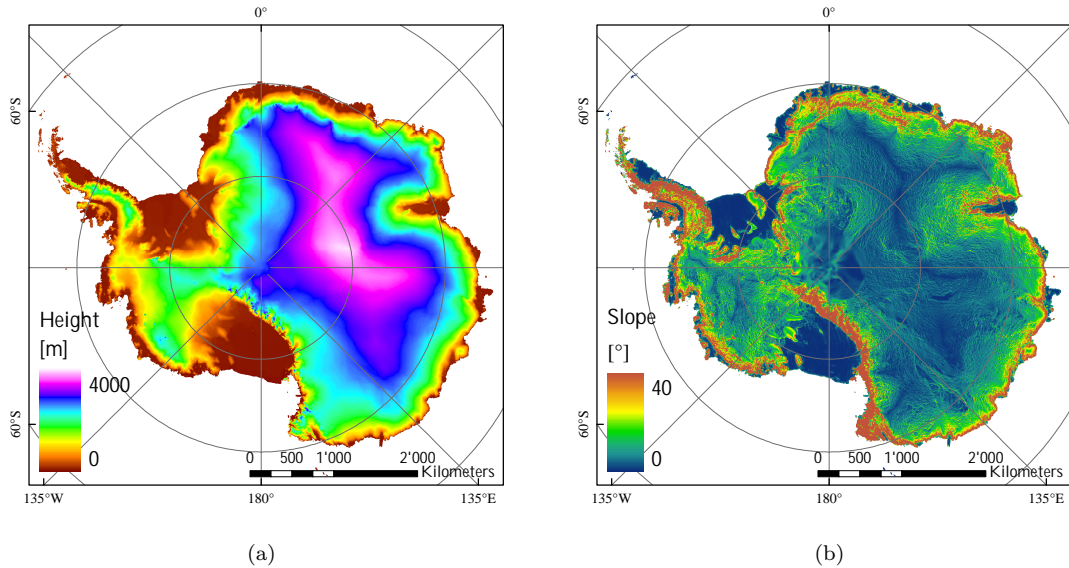


Figure 1.3: Antarctic topography (a) and corresponding slope (b) with a horizontal resolution of 1 km (own illustration with data from Bamber et al., 2009).

In the course of my thesis I aim to identify the regions in which the strong winds around the Antarctic continent influence the sea ice dynamics considerably and where the momentum transfer from the atmosphere to the sea ice is important to the evolution of the sea ice. Further, I will assess to what extent the sea ice dynamics can explain the observed trends and variability of the sea ice cover and I will analyze the physical mechanisms behind this relation. Thus, I will attempt to reveal patterns of variability that indicate which processes in the atmospheric boundary layer are causing the variations of the sea ice. Thereby, I will evaluate the role that the cold air that originates from the near-surface atmosphere of the

Antarctic continental interior plays for the coastal boundary layer and the sea ice. Further, I will try to capture and quantify the important atmospheric forcing terms and their variability. Finally, I intend to explain how the regional dynamical impact of the atmospheric boundary layer on the sea ice is related to the large-scale circulation and the findings of other authors that I have described before.

In order to fulfill these goals, I have studied satellite data of sea ice concentration and motion in the period 1989 to 2006. This is only possible for the two dimensional sea ice fields as sea ice thickness data is currently not available over a long period of time and with a large spatial coverage. Nevertheless, this has no major drawbacks for my analysis as I am mostly interested in the spatial distribution of the sea ice. I will relate the sea ice to the near-surface wind and temperature by using output data from a regional atmospheric climate model. In chapter 3 I will describe these datasets, explain why I have decided to use them for this analysis, and discuss their accuracy and the implications that the choice of the data has on the interpretation of the results.

After providing the theoretical background (chapter 2) and the necessary information about the data (chapter 3), I will proceed with the main analysis. This comprises an evaluation of the surface energy balance, and the surface layer temperature and wind fields of the model simulation in chapter 4. Moreover, in that chapter I will attempt to distinguish the different forcing terms of the flow in the near-coastal atmospheric boundary layer and point out the role that topographic barriers and the accumulation of cold air play. In a next step, I will then describe the variability and trends of the observed sea ice cover and the transport in chapter 5. At this point I will also relate the sea ice dynamics to the sea ice cover on the one hand, and to the surface layer wind field on the other. Additionally, I will expand on the importance of wind-driven sea ice export out of certain regions and the associated open water areas for the sea ice cover. In the last part of the analysis (in chapter 6) I will present a regional assessment of the impact that cold air from the Antarctic continent has on sea ice dynamics and coverage with a main focus on the Ross and Weddell Seas. Throughout the whole thesis I will perform most analyses on a regional scale which will also express the complexity of the variability of the Antarctic sea ice and emphasize the different processes that are dominating the variability. Finally, I will summarize my findings and bring them into the context of the general discussion on Antarctic sea ice in chapter 7.

2 Theoretical Background

In this chapter, I will discuss the fundamental physical processes and dynamics, as well as their mathematical manifestations, that are substantial in the course of my thesis. These basic concepts will be extended in the following chapters. Beside giving insights into the theoretical background, I provide an overview of several fundamental publications that have a relevance for this topic. They cover general aspects of geophysical fluid dynamics and thermodynamics of the lower atmosphere and the sea ice.

Generally speaking, the lowest part of the troposphere is strongly influenced by the presence of the earth's surface below it. This atmospheric boundary layer (ABL) is highly variable in time and space; Garratt (1994) explicitly defines it as “the layer of air directly above the Earth's surface in which the effects of the surface (friction, heating and cooling) are felt directly on timescales less than a day, and in which significant fluxes of momentum, heat and matter are carried by turbulent motions on a scale of the order of the depth of the boundary layer or less.” Over the ice and snow covered Antarctic continent and its adjacent sea ice covered ocean, the influence of the surface is maybe even more pronounced than in any other region in the world. This is due to the steep coastal slopes, the prevailing extreme conditions and the strong gradients between the surface and the atmosphere. According to Stull (1988) the depth of the ABL varies between “hundreds of meters to a few kilometers.” In the mid-latitudes the diurnal variations in the boundary layer are very pronounced. In the polar regions, however, this variability induced by the solar forcing extends to strong inter-seasonal variations, meaning that differences between winter and summer months are distinct. Throughout this report I will mainly focus on variations that take place on even longer timescales, but it is also crucial to understand the principal concepts of the annual cycle.

First of all, I deem it necessary to understand the surface characteristics and the availability of the energy at the surface. Thus, the first part of this chapter (2.1) is dedicated to the general structure of the Antarctic ABL, to the underlying surfaces, and to their influence on the atmosphere. The main emphasis will be on the coastal continent and the surrounding ocean. One could roughly classify four major surface types in the Antarctic coastal areas: the open ocean, the sea ice covered ocean, the flat ice shelves, and the ice sheet escarpment zone. Owing to their surface characteristics, such as albedo and roughness, they have different influences on the boundary layer. Consequently, as I will explain, the ABL might be cooled from below by the ice and snow surface but might also experience heating over the open ocean.

In a second step (section 2.2), in order to investigate the influence of the near surface winds in the Antarctic ABL on the sea ice, I pursue to theoretically discriminate the factors that determine the wind field. Here, the flow that results from the surface characteristics, that are discussed in the first part of this chapter, will be deduced. Further, I will outline some special features of the flow that will be of major importance in the proceeding chapters. The local momentum balance might be influenced by a varying slope of the surface, the structure of the ABL, strong thermal gradients, large barriers such as mountain ranges, or the large scale circulation. Furthermore, the roughness of the surface and even the rotation of the planet can alter the wind field considerably. The detailed spatial structure and the temporal evolution of the Antarctic ABL and its dynamics will be treated in chapter 4. Here, I will only explain some rather schematic concepts.

In the third part of this chapter, I attempt to relate the atmospheric processes to the underlying sea ice. Thermodynamically, sea ice, as a very thin boundary layer (only 1 or 2 m thick) between the atmosphere and the ocean, is subject to growth and decay depending on the forcing. Then, from a dynamical point of view, sea ice will be discussed as an approximated two-dimensional continuum. I will formulate the basic momentum equation and expand on the different terms. Furthermore, I will touch upon the basic principles of sea ice modeling. Even though both, atmospheric and oceanic forcing mechanisms, shall be considered, I intend to put a focus on the interaction with the atmosphere as this is the aim of this thesis.

2.1 The Antarctic Atmospheric Boundary Layer over Snow, Ice and Ocean

Before I elaborate on the near-surface flow, some knowledge about the structure of the Antarctic ABL is necessary. The surface of the Antarctic continent is covered with snow and ice year-round. The ocean surface, on the contrary, is dominated by a seasonal sea ice cover in most regions. Exceptions are, for example, the south-western Weddell Sea and some other small coastal regions that experience a persisting ice cover even by the end of the Austral summer (February and March). These surfaces have a very strong effect on the amount of radiation absorbed by and emitted from the surfaces. The balance of the total amount of radiation absorbed by the surface (R_{net}), with radiative fluxes towards the surface defined as positive, is given by (van den Broeke et al., 2004, 2011):

$$\begin{aligned} R_{net} &= SW_{net} + LW_{net} \\ &= SW_{\downarrow} + SW_{\uparrow} + LW_{\downarrow} + LW_{\uparrow} \\ &= SW_{\downarrow}(1 - \alpha) + \varepsilon_s \varepsilon_{eff} \sigma T_{eff}^4 - \varepsilon_s \sigma T_s^4, \end{aligned} \quad (2.1)$$

where SW and LW are the short- and longwave radiative fluxes respectively; the subscript *net* indicates the budget, and the subscript downward and upward directed arrows refer to the down- and upwelling fluxes respectively. The total shortwave flux can also be expressed as the downwelling shortwave radiation minus the amount that is reflected by the surface. This is given by the albedo of the surface α , where this albedo is defined as the fraction between the reflected and the downwelling flux ($\alpha = |SW_{\uparrow}/SW_{\downarrow}|$). Further, according to the Stefan-Boltzmann law, the absorbed longwave radiation by the surface is given by the product of the surface emissivity ε_s (which equals the absorptivity according to Kirchhoff's law), the effective emissivity ε_{eff} of the atmosphere, the Stefan-Boltzmann constant σ , and the fourth power of the effective atmospheric temperature (van den Broeke et al., 2011). Similarly, the emitted terrestrial radiative flux can be expressed using the surface temperature. I will discuss the single terms, that are schematically illustrated in figure 2.1, in the following.

As the shortwave radiation at very high latitudes is only available during a few months of the year, these terms are only of concern in summer. The amount of solar radiation that actually reaches the surface during these months is rather low due to the high solar zenith angle and, consequently, the long optical path through the atmosphere with a high extinction. Additionally, the incident radiation is absorbed and reflected by clouds, fog and water vapor. In general, there are more clouds over the surrounding ocean and the coastal ice shelves than over the slopes and the continent interior. Van den Broeke et al. (2004) describe the radiation balance from four automatic weather stations (AWS) along a transect from the coast to the plateau in Dronning Maud Land. Over the ice shelf in the coastal area they report a low total annual incoming solar radiation due to the thick overlying atmosphere and the high abundance of moisture and clouds which leads to a low transmissivity of the atmosphere. Cloud cover in these areas is also highly variable on short timescales. Further away from the coast, towards the interior of the continent, the overlying atmosphere gets thinner, and the absolute humidity and cloud cover decrease (van den Broeke et al., 2004). These effects lead to comparably less incident radiation reaching the surface over the ocean and the ice shelves than over the slopes and the continental interior (van den Broeke et al., 2004). In contrast, the latitudinal effect results in less downwelling shortwave radiation towards the continental interior.

At the surface, then, the amount of absorbed shortwave radiation depends on the surface broadband albedo (integrated over all wavelengths as albedo also depends on the wavelength). The albedo of the open ocean is about 0.06-0.07 (Brandt et al., 2005; Perovich, 1996), meaning that most of the incident radiation is absorbed by the water. In contrast, sea ice has a rather high albedo which varies depending on whether it is snow covered, bare ice or sea ice including melt ponds. Due to the crystal structure of snow and ice, the albedo of these surfaces is much higher whereas fresh snow might have an albedo of up to 0.9 (Kuipers Munneke, 2009; Wiscombe and Warren, 1980). As snow gets older, it changes its structure due to dry and wet metamorphism, and the albedo decreases (Kuipers Munneke et al., 2011). For old or melting snow the albedo might be as low as 0.7-0.75 (Kuipers Munneke, 2009). Clean and dry ice has an albedo between about 0.7 for white ice (Perovich, 1996) and 0.52-0.56 for blue ice (van den Broeke

and Bintanja, 1995; Perovich, 1996). Sea ice with melt ponds has an albedo between about 0.15 and 0.29 (Perovich, 1996). However, not only does the structure of the crystals itself change the surface albedo but also the solar zenith angle due to the strong forward scattering, any impurities in the snow or ice, and the cloud cover (Kuipers Munneke et al., 2011; Wiscombe and Warren, 1980). The latter leads to more diffuse radiation at the surface. These large ranges of the surface albedo, and the fact that only little amount of incident shortwave radiation is available, result in very strong effects on the amount of energy that is available at the surface.

Between the open ocean and the sea ice region there is a strong contrast of the albedo (cf. figure 2.1) which induces feedback mechanism that I will further discuss in section 2.3. Within the sea ice area, the amount of absorbed solar radiation is highly variable due to melt ponds, leads, and polynyas, but also differences in sea ice thickness and snow cover (King and Turner, 1997; Weller, 1980). Generally, the amount of absorbed solar radiation compared to the amount of incident radiation in the sea ice region strongly increases throughout the summer and reaches a maximum when almost all sea ice has melted. However, the amount of available radiation is already less toward the end of the summer which means that the maximum net absorbed radiation in this area will occur earlier in the season. The effect of the changing surface albedo also implies that the net shortwave radiation has a higher seasonality over the sea ice than over the open ocean (King and Turner, 1997; Weller, 1980).

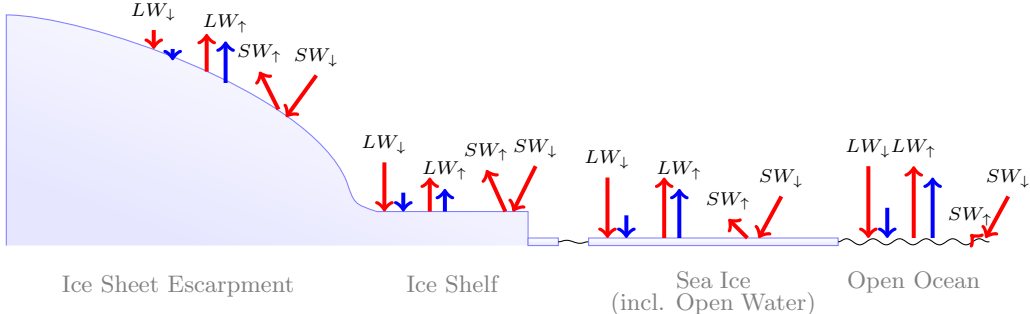


Figure 2.1: Schematic view of the surface radiation balance over the Antarctic continental slopes, ice shelves, sea ice, and open ocean for summer (red) and winter (blue).

In coastal areas, over the ice shelves, the cloud cover influences the albedo mainly in two ways: On one hand, they alter the incident solar zenith angle by increasing the diffuse fraction of the radiation, and, on the other hand, they lead to a shift in the spectrum towards the visible wavelengths (van den Broeke et al., 2004). The latter strongly increases the albedo in coastal areas and is not important in the higher regions towards the interior of the continent. Furthermore, snow metamorphism is faster in coastal areas where it is warmer. It might lead to a rapid decrease of the albedo in summer (van den Broeke et al., 2004). However, the precipitation rates are much higher along the coast as well. Additional fresh snow on the top of the snowpack strongly increases the albedo. Overall, these factors imply a, generally, decreasing albedo with an increasing distance from the coast towards the interior and decreasing albedo for all areas throughout the summer (van den Broeke et al., 2004). The variations in albedo are very pronounced along the coast because of varying weather conditions, whereas the higher areas are more influenced by variations of the solar zenith angle throughout the summer. Consequently, on average, not only is the available solar radiation higher in the upper regions of the ice sheet but also the absolute and relative absorbed shortwave radiation is higher. This makes the energy available at the surface of the ice shelves strongly dependent on the synoptic scale weather systems and sensitive to the shortwave radiation budget. The slopes and higher areas are more controlled by other factors that will be outlined in the following.

The downwelling longwave radiation depends mostly on the vertical temperature and moisture profiles but also on greenhouse-gas and aerosol concentrations. It varies strongly with cloud cover. A fully-cloud-covered sky with low clouds has an effective emissivity of up to 1.0, and for a clear sky it decreases to

about 0.5 (Stull and Ahrens, 2000), whereas clear sky emissivity varies considerably depending mostly on the atmospheric water vapor. As the atmosphere gets drier, colder, and thinner from the ocean to the continental interior, the clear sky emissivity decreases (van den Broeke et al., 2004). Additionally, the effective emissivity of the atmosphere over the ocean and the ice shelves is increased drastically by the presence of clouds. In general, the atmospheric effective emissivity increases with increasing temperature and moisture during summer. Hence, the highest values of downwelling longwave radiation are recorded in summer in coastal areas and the lowest values in winter over the continent (cf. figure 2.1; van den Broeke et al., 2004). It is of significance that the incoming longwave radiation over the ice shelves and the sea ice changes depending on whether the overlying air is cold and dry continental air or warm and moist maritime air.

The emissivity of a water surface is about one. This results in a very strong longwave emission of the ocean's surface as its temperature is comparably high (at or above the freezing temperature). Fresh dry snow, however, has an emissivity of about 0.98, very close to the one of water (van den Broeke et al., 2011; Wiscombe and Warren, 1980). A bare ice surface and old snow have an emissivity of about 0.96 and 0.82, respectively (Stull and Ahrens, 2000). Due to these relatively high values of the snow and ice covered surfaces, the longwave emission is a strong function of the surface temperature. Consequently, over sea ice that mostly has a surface temperature only slightly below freezing, depending on the thickness of the ice, longwave emission is still relatively high (Weller, 1980). Over the ice shelves, it, then, decreases dramatically due to the lower temperatures (cf. figure 2.1). Surprisingly, when going further up the slope of the continent, the longwave radiative loss even increase again. This is related to strong winds over the slopes that, persistently, mix warmer upper air towards the surface.

During summer, in coastal areas, the net longwave radiation is mostly close to zero or slightly negative as the emission is mainly compensated by a high downwelling longwave radiation due to the relatively high atmospheric temperature and moisture and the frequent cloud cover at lower altitudes. In early winter, however, when there are large areas of open water or only a thin sea ice cover, the atmospheric temperatures are comparably low (far below freezing), and there is less cloud cover and humidity. Subsequently, the strong longwave emission leads to very negative values of the longwave budget (Allison, 1989; Weller, 1980). These negative values of the net longwave radiation might persist throughout the winter and are largest in regions that include large areas of open water in the sea ice (Allison, 1989; King and Turner, 1997). The overall lowest values over the continent - even though not as low as over the ocean - occur along the slopes that are subject to strong longwave emission and experience only little downwelling longwave radiation (van den Broeke et al., 2004).

In sum, the net surface radiation budget is positive over the ocean during summer, slightly less positive over the sea ice, and even smaller, but still positive, over the coastal continent. In wintertime the differences get larger and horizontal gradients in the budget increase because it is solely determined by the longwave fluxes. It is very negative over the ocean surface when sea ice builds and gets slightly less negative throughout the winter as the sea ice thickens. On the ice shelves it is slightly negative in winter due to the low surface temperature and it is strongly negative on the slopes. The total annual radiation budget over the Antarctic continent and the surrounding sea ice covered ocean is negative as the wintertime heat loss exceeds the positive radiation balance in summer (van den Broeke et al., 2004). In order to conserve the energy of this region, this also implies that there must be compensating heat fluxes to the overall surface radiative loss from other regions through the atmosphere and the ocean.

The strong radiative cooling of the surface, further, results in a strong temperature gradient to the upper ABL with very low temperatures at the surface and comparably higher temperatures aloft. As the temperature is depending on air pressure which decreases with height, it is common practice to use potential temperature (θ) which is conserved for adiabatic motion to correctly analyze the vertical structure of the ABL (Stull, 1988). Potential temperature is, hence, defined as the temperature an air parcel would have at the surface reference pressure level ($p_0 = 1013.25 \text{ hPa}$; Stull, 1988):

$$\theta \equiv T(p) \cdot \left(\frac{p_0}{p} \right)^{\frac{R_d}{c_p}}, \quad (2.2)$$

where T is the temperature at a certain pressure level, p the pressure, R_d ($= 287.04 \text{ J}\cdot\text{K}^{-1}\cdot\text{kg}^{-1}$) the gas constant for dry air, and c_p ($= 1004.67 \text{ J}\cdot\text{K}^{-1}\cdot\text{kg}^{-1}$) the specific heat of dry air (Stull, 1988). The strongly positive lapse rate of the potential temperature implies a high static stability of the boundary layer which suppresses turbulence. However, if turbulent mixing towards the surface would not occur no heat could be transported vertically towards the surface and the surface temperatures would drop even more. This positive feedback on the atmospheric stability would result in a complete decoupling of the surface. Mahrt (1999) analyzed this case in detail and pointed out that the decoupling only occurs over short periods of time and in the absence of wind shear. In this case, there are very persistent winds over the cooling slopes that generate turbulence which compensates for the surface cooling. As I will examine in detail in the following section (2.2), the winds are strongly coupled to the cooling, and the induced turbulent mixing provides a negative feedback that compensates for the static stability. In terms of longwave emission, however, this mechanisms provides a positive feedback because heat is vertically mixed to the surface by turbulence which, in turn, leads to a higher longwave radiative emission.

The largest stability usually occurs just above the surface where the gradients are the largest (Stull, 1988). Figure 2.2 illustrates this. Gradients, then, decreases with height and at a certain point, the temperature inversion, the temperature lapse rate gets negative (but not the potential temperature lapse rate). The temperature inversion is often used as a measure of stability. However, there are other measures that might be more meaningful. If a constant potential temperature lapse rate (γ_θ) is assumed well above the ABL in the free troposphere, this profile can be extrapolated to the surface according to (van den Broeke et al., 2002):

$$\theta_0(z) = \theta_0(z_0) + \gamma_{\theta,z} \cdot z, \quad (2.3a)$$

where θ_0 is the background potential temperature profile with height z as vertical coordinate. Van Angelen et al. (2011a) outlined that for convenience the background potential temperature can also be depicted using pressure p as a vertical coordinate for the extrapolation:

$$\theta_0(p) = \theta_0(p_0) + \gamma_{\theta,p} \cdot p. \quad (2.3b)$$

The latter is used in this study. As θ_0 hereafter might also be needed in terms of height, its vertical coordinate could be converted. This can be performed using the hydrostatic equilibrium that assumes the absence of vertical motion and is valid for the mean state (Cushman-Roisin and Beckers, 2011):

$$\frac{\partial p}{\partial z} = -\rho \cdot g, \quad (2.4)$$

where ρ is the density of the air which one can calculate using the ideal gas law, and g ($= 9.80665 \text{ m s}^{-2}$) the acceleration due to gravity.

As the largest gradient occurs just above the surface, the strength of the ABL stability can be expressed in terms of the surface potential temperature deficit ($\Delta\theta_s$) which is defined as the difference between the actual potential temperature and the extrapolated background potential temperature at the surface (van den Broeke et al., 2002). Figure 2.2 shows an arbitrary surface deficit of about -18 K. The profile of the potential temperature perturbation, that might as well be positive for an unstable stratification, is given by (van den Broeke et al., 2002):

$$\Delta\theta(z) = \theta(z) - \theta_0(z). \quad (2.5)$$

If this temperature perturbation is integrated vertically, one obtains the total temperature deficit layer (TDL) which is expressed by (van Angelen et al., 2011a; van den Broeke et al., 2002):

$$\hat{\theta}(z) = \int_z^h \Delta\theta(z) dz, \quad (2.6)$$

where h is a rather arbitrary height that needs to be well above the TDL. In figure 2.2 the resulting

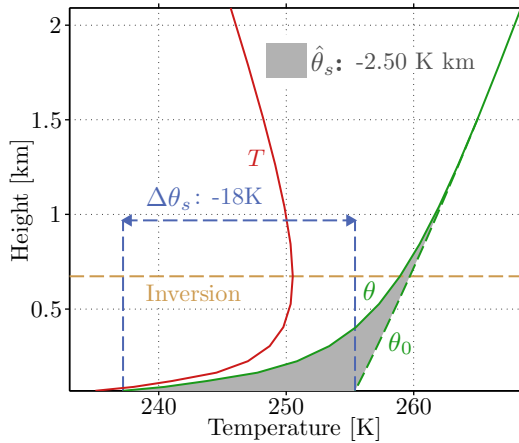


Figure 2.2: Schematic view of the stable ABL with temperature profile T , temperature inversion, potential temperature profile θ , background potential temperature profile θ_0 , surface potential temperature deficit $\Delta\theta_s$, and temperature deficit layer integrated from the surface $\hat{\theta}_s$.

TDL integrated from the surface $\hat{\theta}_s$ is about -2.50 K km . It can be also seen that the height of the TDL does not necessarily coincide with the height of the temperature inversion. So this formulation of the total temperature perturbation in the ABL has the advantage to take a varying height of the TDL into account but also bares some problems that will be encountered in chapter 4. Moreover, in that chapter, I will treat the atmospheric profiles in the stable ABL further.

In geophysical fluid dynamics a common measure for the atmospheric stability is the stratification or Brunt-Väisälä frequency N that is an expression for vertical oscillation (Cushman-Roisin and Beckers, 2011):

$$N^2 = -\frac{g}{\rho_0} \frac{d\rho}{dz}, \quad (2.7a)$$

where ρ_0 ($= 1.225 \text{ kg}\cdot\text{m}^{-3}$) is the standard density of air (Stull, 1988) and which is derived from Archimedes' buoyancy principle. If it is positive, the vertical density gradient is negative, meaning that a fluid of larger density is below a lighter fluid, and the stratification is statically stable (Cushman-Roisin and Beckers, 2011). With the assumption of incompressibility and by using the ideal gas law and the definition of the potential temperature (eq. 2.2), N can be expressed in terms of θ through (Cushman-Roisin and Beckers, 2011):

$$N^2 = +\frac{g}{\theta} \frac{d\theta}{dz}. \quad (2.7b)$$

After having defined some useful concepts to analyze the ABL stability that is induced by the radiative surface cooling, I would like to draw the attention back to the surface. The preceding explications on the radiation budget demonstrated that it is strongly coupled to the surface temperature and that the amount of energy that it provides depends strongly on the albedo and the emissivity of the surface. This coupling of the surface temperature is also owing to the dry and cold conditions and the large amounts of air included in the uppermost snowpack, so that heat conduction is suppressed (van den Broeke et al., 2004). Nevertheless, there are other factors that influence the surface temperature and the amount of energy available at the surface for freezing and melting. The surface energy balance (SEB) in polar regions, with energy fluxes towards the surface defined as positive, is given by the following equation (van den Broeke et al., 2011, 2005):

$$M = R_{net} + SHF + LHF + G, \quad (2.8)$$

where M denotes the amount of energy available for melting which is zero if the surface temperature is

below the freezing point over the continent. Over the ocean and the sea ice, however, M is the energy flux for the freezing of the ocean water (van den Broeke et al., 2011). It should also be noted that the melting or freezing point of the sea ice occurs, due to its inclusion of salt, at a lower temperature. I will explain this further in section 2.3. Moreover, SHF refers to the turbulent sensible heat flux and LHF to the turbulent latent heat flux. G stands for the subsurface conductive heat flux which is a ground heat flux over land and an ocean heat flux over water evaluated at the surface. The latter three terms and the total energy balance, resulting in melting or freezing, are briefly outlined afterwards. Figure 2.3 shows an approximated, schematic surface energy balance for the different regions. It is common practice to neglect the very small contribution of heat fluxes resulting from precipitation onto the surface (van den Broeke et al., 2011).

As the atmosphere at high latitudes is, compared to the ocean, rather cold throughout almost the whole year, the subsurface heat flux over the open ocean is positive and is a source of energy at the surface. It should be noted that the transport of heat from the ocean to the surface does not only take place through molecular diffusion, but rather through mixing (turbulent and buoyant; McPhee, 2008, 1992). Not much is known about the temporal and spatial variations of the ocean heat fluxes as measurements are scarce. For the purpose of the thesis, I deem it sufficient to consider the ocean as a source of energy. Over sea ice the subsurface heat flux decreases considerably with increasing ice thickness. Allison (1989) states that the subsurface heat flux over sea ice decreases drastically once the ice has grown beyond approximately 500 mm thickness. Heat is transported through the ice by conduction from the ocean to the surface. This term is positive everywhere on the sea ice throughout most the year (cf. figure 2.3). In later winter, when the sea ice is thick, it still has a large contribution to the SEB because of the large and persistent open water areas in the ice pack. An exception might occur during the melting season in areas with strong surface melting where it might, locally, turn negative due to a positive surface radiation budget. However, surface melting of the Southern Ocean sea ice is a rather minor factor (Andreas and Ackley, 1982). Vancoppenolle et al. (2009) estimated it to be only 5% of the total sea ice melt, whereas the rest occurs on the base. This would, in turn, mean that even in the melting season the subsurface heat flux over the sea ice is mostly positive. Overall, this positive subsurface heat flux over sea ice compensates for most of the radiative loss at the surface.

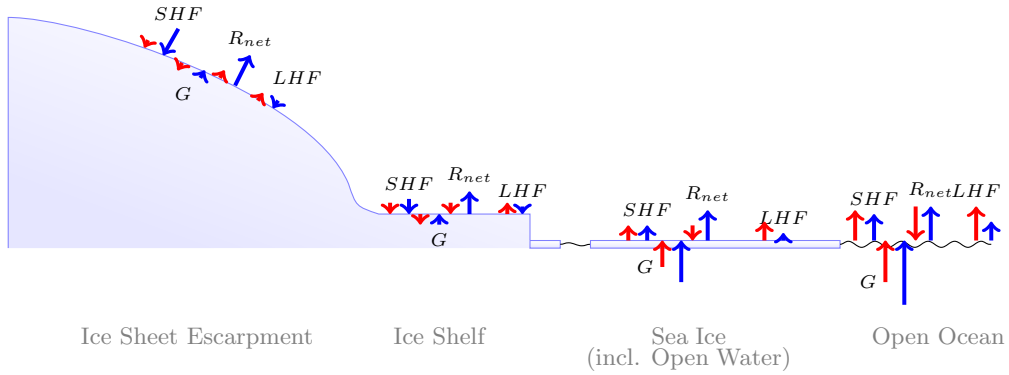


Figure 2.3: Schematic view of the surface energy balance over the Antarctic continental slopes, ice shelves, sea ice, and open ocean for summer (red) and winter (blue).

The ground flux over the continent, in contrast, is rather small. This is owing to the large air content of the snow that dampens heat conduction (van den Broeke et al., 2011). Heat conduction in snow and ice is a function of the temperature gradient between the subsurface layers and the surface. As shown in figure 2.3, it is slightly negative in summer when the surface warms due to a positive radiation balance and positive in winter when surface cools due to the longwave radiative heat loss. The only time that it might get large and important in the SEB is over short timescales when the surface over the slopes is cooling and it is not compensated by turbulent heat transport (van den Broeke et al., 2011), which I will discuss in the following.

Heat between the lowest part of the atmosphere and the surface is exchanged vertically. This exchange occurs due to a temperature and/or moisture gradient above the surface that is usually the largest very close to the surface. In order to compensate for the gradient, either latent or sensible heat is transported in two ways. These are molecular diffusion in a very thin layer just above the surface and (mechanical) mixing over a larger scale above the surface (Stull, 1988). As the latter is the, by far, larger term, both, molecular diffusion and turbulent mixing of heat, are commonly combined into the turbulent sensible and latent heat fluxes (hereafter SHF and LHF; van den Broeke et al., 2011). Mixing can be produced either by buoyancy in a statically unstable atmosphere due to a warmer surface or by turbulent motion in a dynamically unstable atmosphere due to wind shear (Stull, 1988).

Throughout the year over the open ocean, both, SHF and LHF, are negative and might be rather large (Weller, 1980). These fluxes compensate for the strong ocean heat flux and lead to a large production of turbulence. This also implies a heating of the ABL from below and, thus, a statically unstable atmosphere. It should be emphasized that the only places where an unstable atmosphere can be found during winter in this region is over the open ocean. Open water areas within the sea ice play a major role during winter. Weller (1980) argues that about 40% of the total heat loss from the surface in the sea ice region is due to the open water areas within the ice.

Open water areas are either polynyas (large and persistent open water areas in the ice) or leads (narrow, elongated and temporal open water in the ice; Barber and Massom, 2007; Wolfe et al., 2011). Leads form due to divergence of ice and refreeze shortly after their opening because of the strong heat loss of the surface. Those leads that form close to the coast and that come into existence through an opening of the sea ice forced by prolonged strong winds are called flaw leads (Barber and Massom, 2007). Flaw leads deviate from coastal polynyas as they occur irregularly in space and time. Polynyas, however, persist throughout most of the winter and might open and close several times in one season, but always return. They are classified either according to their location into shelf-water and deep-water polynyas or in terms of their characteristic energy exchange into latent heat and sensible heat polynyas (Barber and Massom, 2007).

Sensible heat polynyas occur mainly off-shore due to a large supply of heat from the lower ocean by vertical mixing (Barber and Massom, 2007). In these areas, usually, no sea ice is formed; it rather melts because of the heat supply from below that ensures the open water surface (Barber and Massom, 2007). Latent heat polynyas result from persistent winds or ocean currents and are mostly located in coastal areas (Barber and Massom, 2007). The wind driven polynyas are sometimes also referred to as flaw polynyas (Williams et al., 2007). Here, sea ice is continuously formed due to radiative and turbulent heat loss at the surface and is, subsequently, pushed out of this area again by the wind or the ocean current. This means that I will focus on the - according to this definition - latent heat polynyas that are responsible for sea ice formation. This definition can be somewhat misleading as over both types strong negative SHF and LHF occur due to the large gradients in temperature and moisture (Minnett and Key, 2007). Vertical mixing of heat over open water occurs due to both reasons, wind shear generated turbulence and buoyancy. Compared to the continent SHF and LHF over leads and polynyas are much larger throughout the whole winter and have a strong cooling effect on the surface (Minnett and Key, 2007). In coastal open water areas, where high wind speeds occur, largest negative SHFs are found. Open water areas do not only provide a heat flux to the atmosphere but also a moisture flux that enhances cloud formation (Barber and Massom, 2007).

Over the sea ice covered ocean the turbulent exchange might look very different. If the ice cover is still thin as in early winter, SHF and LHF are negative (Allison, 1989). However, in winter over thicker sea ice LHF becomes zero and SHF turns positive and provides a net source of heat for the surface (Allison, 1989). This can be explained by the fact that the surface cools to low temperatures due to the radiative loss and a decreased subsurface conductive heat flux due to the thick ice layer. In spring, the LHF is negative due to snow and ice sublimation (Allison, 1989). If the heat fluxes are averaged over a larger sea ice region in winter that includes open water areas, the overall turbulent heat flux is still very negative (Weller, 1980) depending on the amount of open water within the ice pack (cf. figure 2.3).

I have already stressed before that in the SEB over the Antarctic continent the positive turbulent heat

flux, especially in winter, in form of sensible heat, is of great importance. The SHF generated by wind shear over the slopes of the continent is the most important compensation for the radiative energy loss (van den Broeke et al., 2005). It is strongest in winter and decreases towards the summer when the longwave cooling decreases as well, and the vertical gradients in temperature decrease (van den Broeke et al., 2004). In coastal areas, this effect is usually not as pronounced due to lower wind speeds and less persistent winds. Why there is such a strong coupling between the radiative heat loss and the SHF will become clear in the following section (2.2). During summer, SHF might also become negative due to a positive radiation balance and lead to convection and a statically unstable ABL. The LHF over the continent is only of minor importance to the SEB. In summer, it becomes slightly negative in most places due to sublimation of snow. Even though this term is not that important in the SEB, it is a crucial factor in terms of the surface mass balance of the ice sheet (Lenaerts and van den Broeke, 2011; Lenaerts et al., 2011). LHF is, then, approximately zero in winter everywhere on the continent or is extremely small and positive due to moisture deposition at the surface (van den Broeke et al., 2011, 2005).

Next to the sublimation, the surface mass balance of the Antarctic continent is influenced by surface melt in summer in the coastal regions. In the SEB, it is only a small heat loss at the surface that is triggered by the positive radiation balance (van den Broeke et al., 2005). If the melt flux temporarily becomes a net gain of heat for the surface (SEB is negative), it is due to a refreezing of meltwater.

When discussing the ocean heat flux, I have already outlined that the surface energy flux due to melt is rather small over the Antarctic sea ice as most of the melt occurs at the base. Over open ocean areas, the net SEB is strongly negative during winter (Weller, 1980) which leads to freezing of the ocean surface. The model study of Vancoppenolle et al. (2009) suggests that the freezing in open water areas is as important as the freezing at the sea ice base in the sea ice mass budget and accounts for about 38% of the total mass budget. If we reconsider that this heat loss is solely due to radiative cooling and a negative SHF, this points to the importance of the atmosphere and the SEB in the sea ice budget which I will reseize in section 2.3.

I have stressed that the immense surface cooling over the continent and the ocean or sea ice is compensated by vertical downward mixing of heat in the ABL and by vertical upward mixing of heat over the ocean. So, where does this heat come from? Van de Berg et al. (2007, 2008) used a regional atmospheric climate model to estimate the heat budget of the lower troposphere and concluded that the heat loss at the surface is compensated by large-scale horizontal and vertical advection of heat in winter which is reduced in summer. Further, above the ABL over the continent large-scale subsidence occurs. This subsidence which appears due to the surface cooling is enhanced by a divergent wind field over the continent (van de Berg et al., 2008) which will be further explained in the following section (2.2). In the sea ice areas the heat budget is to a large extent compensated from the deeper ocean which provides heat from lower latitudes by large-scale ocean circulation.

To sum up, in the whole region, the surface albedo and emissivity were depicted to be the controlling surface properties in the radiation budget. However, cloud cover and atmospheric humidity variations lead to important differences between coastal areas and the inner continent. Over the continent the longwave radiative cooling in winter and the compensating positive SHF are the key parameters in the SEB. In the sea ice region both longwave cooling and the turbulent heat fluxes provide a net sink of energy for the surface, where the open water within the sea ice is the important factor. This strong heat loss in winter is compensated by the ocean heat flux and freezing of water at the surface.

I have described the radiation and SEB as forcing mechanisms for the stable ABL over the continent and the sea ice, and outlined a few crucial parameters to analyze the vertical profile and the stability. Further, it was mentioned that a statically unstable atmosphere can occur over large open water areas during winter. The spatial distribution of the surface characteristics and related forcing mechanisms in the ABL provide the source of the motion in the ABL that I will describe in the following sub-chapter.

2.2 Forcing Mechanisms of the Antarctic Atmospheric Boundary Layer Dynamics

In the introduction to this thesis I have indicated that over the Antarctic continent and along its coastal areas we find the strongest winds on Earth. A mean wind speed of 19 m s^{-1} from 1912-1914 at Cape Dension is highest ever measured (Parish, 1981). If one wants to understand these wind systems, one needs to examine the force balance close to the surface that accelerates the particles in the air. Forces in the ABL result from the strong gradients that I have explained in the previous section (2.1). These gradients exist very locally, for example, in a rather thin layer just above the surface, over larger distances such as from one side of the ice shelf to the other, or over largest distances for instance between the continent and the open ocean. The acceleration of a particle, according to Newton's second law, results from the sum of all active and passive forces in the three dimensional space acting on the particles. The former terms are induced by horizontal and vertical pressure gradients and the latter by friction and the Earth's rotation. If rotational effects were not included, one would speak of the general Navier-Stokes equations for momentum (Cushman-Roisin and Beckers, 2011). However, all large-scale processes taking place on Earth are influenced by its rotation and, hence, it needs to be included. Further, it is common practice to multiply the acceleration with the density instead of mass. The resulting momentum balance, however, is too complex to solve it for the variations in the flow. Some further simplifying assumptions are necessary that do not necessarily change the outcome very much.

One of the simplifications is the commonly used Boussinesq approximation. It assumes that the density of the fluid fluctuates around a mean state and that these fluctuations in the horizontal momentum balance are small compared to the value of the mean state (Cushman-Roisin and Beckers, 2011). It can be shown that it is a good approximation to neglect these fluctuations. In the vertical, however, one needs to account for the decreasing pressure with height that results from the negligence of vertical motion in the already formulated hydrostatic balance (cf. equation 2.4). The so-called Reynolds-averaging further simplifies the horizontal force balance by dividing the flow speed, again, into a mean state and a fluctuation, where the average fluctuation is zero by definition (Cushman-Roisin and Beckers, 2011). The fluctuations represent turbulence and might be merged with frictional terms (Cushman-Roisin and Beckers, 2011). One can also simplify the frictional terms by assuming horizontal homogeneity for the horizontal turbulence, which means that there is no horizontal divergence of momentum due to the turbulent fluxes (Stull, 1988). If some additional scaling analysis is performed, the following horizontal momentum equations in a Cartesian coordinate system result (van den Broeke, 2009a):

$$x\text{-momentum : } \frac{du}{dt} = \underbrace{-\frac{1}{\rho} \frac{\partial p}{\partial x}}_{\text{PGF}} + \underbrace{fv}_{\text{COR}} - \underbrace{\frac{\partial \overline{(u'w')}}{\partial z}}_{\text{FDIV}}, \quad (2.9a)$$

$$y\text{-momentum : } \frac{dv}{dt} = \underbrace{-\frac{1}{\rho} \frac{\partial p}{\partial y}}_{\text{PGF}} - \underbrace{fu}_{\text{COR}} - \underbrace{\frac{\partial \overline{(v'w')}}{\partial z}}_{\text{FDIV}}, \quad (2.9b)$$

where u and v denote the mean flow and the prime indicates the fluctuations around the mean. Further, f is the Coriolis parameter that is defined as $f = 2\Omega \sin(\varphi)$ which includes the Earth's angular rotation speed $\Omega (= 7.2921 \cdot 10^{-5} \text{ s}^{-1})$ and the latitude φ (Cushman-Roisin and Beckers, 2011). On the right-hand side the equations 2.9 consist of the already mentioned active forces which are the pressure gradient forces (PGF), and the passive forces that only act if motion is present which are the Coriolis force (COR) and the vertical divergence of momentum due to friction (FDIV). The derivative d/dt , on the left-hand side, is the total or material time derivative which is defined as (Cushman-Roisin and Beckers, 2011):

$$\frac{d}{dt} = \underbrace{\frac{\partial}{\partial t}}_{\text{ADVH}} + \underbrace{u \frac{\partial}{\partial x}}_{\text{ADVV}} + \underbrace{v \frac{\partial}{\partial y}}_{\text{ADVV}} + \underbrace{w \frac{\partial}{\partial z}}, \quad (2.10)$$

where $\partial/\partial t$ is the local time derivative and the latter three terms represent horizontal and vertical advection (hereafter ADVH and ADVV respectively) of the considered variable. Usually, compared to all other terms, vertical and horizontal advection of momentum in the Antarctic ABL are small (van den Broeke and van Lipzig, 2003a; van den Broeke et al., 2002).

The two horizontal momentum equations together with the vertical momentum equation, the continuity equation that conserves mass, and the energy equation (the latter three are not presented here) form a complete set of five equations for five variables (u, v, w, p, ρ) that could be solved if FDIV was neglected (Cushman-Roisin and Beckers, 2011). The fact that the inclusion of the frictional terms in equations 2.9 lead to a so-called “closure problem” (u' , v' , and w' are not defined) is one of the major challenges in ABL dynamics (Stull, 1988). I will further discuss this problem later in this section.

First, I would like to draw the attention to the active forces, the PGF terms, in the equations 2.9. As I have mentioned already, a horizontal pressure gradient in the ABL might result from different sources. If we are able to formulate the individual pressure gradients resulting from the main sources, we can discriminate the flow that arises from these gradients. The sum of all the PGFs from these sources should, then, result in the total PGF that we can detect. It is, however, rather likely that there will be small discrepancies between the sum of the individual forcing mechanisms and the total PGF due to either a wrong estimate of one forcing or to a completely different forcing that was not considered. These differences are also very useful as they allow us to evaluate the method and our knowledge of the Antarctic ABL. In the following, I will describe the main PGFs in the Antarctic ABL.

One main force, that is clearly important and seems to be a good start, is the influence of the background PGF on the flow in the ABL. It is associated with the large-scale circulation that is present above the ABL and would be dominant if the influences of the surface that alter the flow in the ABL were not present. Such a large-scale PGF in the ABL over Antarctica is, for example, given by the circumpolar vortex that is present due to the planetary temperature gradient induced by the solar radiation. Its influence on the surface layer is analyzed in detail by van den Broeke and van Lipzig (2002). In order to express the force balance of this flow, all forces in the momentum budget 2.9, except for the Earth’s rotation that definitely has an influence on the flow on such large scales, and the large-scale PGF, can be neglected. This results in a very simple balance between two terms which is commonly referred to as the geostrophic balance (Holton, 2004):

$$x\text{-direction : } \frac{1}{\rho} \frac{\partial P_{LSC}}{\partial x} \approx f V_{LSC}, \quad (2.11a)$$

$$y\text{-direction : } \frac{1}{\rho} \frac{\partial P_{LSC}}{\partial y} \approx -f U_{LSC}, \quad (2.11b)$$

where the subscript LSC indicates the large-scale contributions to the flow and pressure field in the ABL.

According to the geostrophic balance, the large-scale flow velocity is needed to determine the resulting PGF. In order to do that the so-called thermal wind relation can be applied which states that “[t]he geostrophic wind must have vertical shear in the presence of a horizontal temperature gradient” (Holton, 2004). The horizontal temperature gradient in the ABL that would be present without the influence of the surface was already approximated through the extrapolation of the background temperature profile to the surface by equation 2.3b. First, we assume that the large-scale flow is approximately in hydrostatic balance. Together with the ideal gas law (Stull, 1988) the hydrostatic balance (equation 2.4) can be rewritten as (Holton, 2004):

$$dz \approx -\frac{1}{\rho g} \cdot dp = -\frac{R_d T}{g} \frac{1}{p} \cdot dp = -\frac{R_d T}{g} \cdot d \ln p, \quad (2.12)$$

which expresses the thickness of the layer between two isobaric surfaces with respect to the temperature of the corresponding layer. If we now differentiate the geostrophic balance with respect to pressure and use the hydrostatic balance, we get the thermal wind relation for the large-scale circulation (Holton,

2004). Together with the equation 2.12 and the definition of the potential temperature (equation 2.2) this results in (van den Broeke et al., 2002):

$$x\text{-direction : } \frac{\partial U_{LSC}}{\partial \ln p} = + \frac{R_d}{f} \left(\frac{p}{p_0} \right)^{\frac{R_d}{c_p}} \frac{\partial \theta_0}{\partial y}, \quad (2.13a)$$

$$y\text{-direction : } \frac{\partial V_{LSC}}{\partial \ln p} = - \frac{R_d}{f} \left(\frac{p}{p_0} \right)^{\frac{R_d}{c_p}} \frac{\partial \theta_0}{\partial x}. \quad (2.13b)$$

If the flow well above the ABL is in geostrophic balance, these relations can be used to find the contributions of U_{LSC} and V_{LSC} to the total flow in the ABL by discretized step-wise downward extrapolation of the wind profile.

Next, I will analyze the flow generated inside the ABL. Gravity might accelerate the flow over a sloping surface due to a vertical buoyancy forcing which is referred to as gravity flow (Mahrt, 1982) or katabatic flow (Ball, 1956). This type of flow is very characteristic over the slopes of the Antarctic ice sheet. The strong radiative cooling over the slopes, as I have described in section 2.1, induces negative buoyancy which leads to a drainage of the cold air in a downslope direction. Moreover, the persistence of the longwave cooling over the slopes makes the katabatic forcing a very persistent term in the momentum balance. One of the first set of momentum equations that describe katabatic winds was developed by Prandtl (1942). He included the radiative cooling of the surface and vertical turbulent mixing of heat. Later, the equations were further developed to analyze the flow over the slopes of the Antarctic continent in all three dimensions with varying slopes, such as by Ball (1956, 1957, 1960) and Mahrt (1982). Parish (1984) and Parish and Waight (1987) performed numerical simulations to study the near surface flow over the continent. In the latest stage of advancement the momentum equations have been evaluated numerically with more realistic forcing terms from climate model data to estimate the contribution of katabatic winds in the ABL (van den Broeke and van Lipzig, 2003a; van den Broeke et al., 2002; Parish and Cassano, 2001, 2003).

In order to derive the PGF resulting from the negatively buoyant air, I, again, assume that the ABL is in approximate hydrostatic equilibrium and that the air is incompressible. Figure 2.4 schematically illustrates the case of a temperature perturbation over a slope with a constant thickness of the TDL (in blue). As the TDL is statically stable the lower layer has a higher density (ρ_2) than the layer above (ρ_1). The horizontal pressure gradient (P_{KAT}) can be expressed in terms of density using the hydrostatic balance (equation 2.4). As shown in figure 2.4, in a discretized manner, this results in the following pressure difference between the indicated points in the TDL:

$$P_2 - P_1 = -g \cdot \Delta z^* \cdot (\rho_2 - \rho_1). \quad (2.14)$$

Here, I use the vertical coordinate z^* that is defined perpendicular to the surface and arises if one uses so-called sigma-coordinates that are terrain following (cf. section 3.1). Finally, the assumption of incompressibility together with the ideal gas law allow to express the density variations in terms of potential temperature variations in all three dimensions (van den Broeke, 2009b):

$$x\text{-direction : } \frac{1}{\rho_0} \frac{\partial P_{KAT}}{\partial x} \approx -g \frac{\Delta \rho}{\rho_0} \frac{\Delta z^*}{\Delta x} \approx +g \frac{\Delta \theta}{\theta_0} \sin \alpha_x, \quad (2.15a)$$

$$y\text{-direction : } \frac{1}{\rho_0} \frac{\partial P_{KAT}}{\partial y} \approx -g \frac{\Delta \rho}{\rho_0} \frac{\Delta z^*}{\Delta y} \approx +g \frac{\Delta \theta}{\theta_0} \sin \alpha_y, \quad (2.15b)$$

where ρ_0 , in this case, is the density profile of the background and α_x and α_y are the angles of the slope in the respective direction.

The dependence of the katabatic flow on the sloping terrain that is expressed in equations 2.15 leads

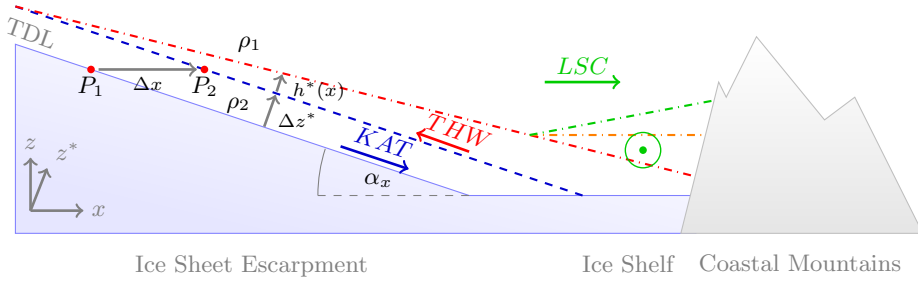


Figure 2.4: Schematic two-dimensional view of the generation of katabatic flow in a TDL with constant height (blue) and thermal wind due to a varying TDL height (red). Also shown is the effect of a barrier on TDL for example by coastal mountain range (orange). The TDL with an additionally large-scale flow towards the barrier is shown in green (own illustration; after van den Broeke, 2009b).

to a spatially inhomogeneous pattern of the cold air drainage. Parish and Bromwich (1987) simulated the katabatic flow over Antarctica and derived confluence zones in which the topographic setting favors the cold air flow. Ball (1960) outlined that the katabatic flow strengthens “to the east of a headland and in the western part of a bay” and visualized the effect with converging and diverging streamlines. He illustrates that this effect gets even stronger if there is a combination of consecutive headlands and embayments, and even a katabatic jet might form if the isohyps are distorted. Further, he investigates how a low pressure system off the coast affects the katabatic flow over a spatially homogeneous slope. He concludes that the flow will be stronger at the coast on the western side of the pressure trough and weaker to the east (Ball, 1960).

Further, an additional PGF might arise due to a varying height of the TDL which is illustrated in figure 2.4 in red. The acceleration of the flow that is induced by horizontal thermal gradients is, for instance, due to differential surface heating or a varying slope. If the pressure at point P_2 in the figure is considered and there is an additional layer of denser air with density ρ_2 above, the pressure in P_2 increases and the difference between P_2 and P_1 decreases. This difference can be taken into account by reformulating the relation 2.14 to:

$$(P_2 - P_1) - P_3 = -g \cdot \Delta z^* \cdot (\rho_2 - \rho_1) + g \cdot h^* \cdot (\rho_2 - \rho_1). \quad (2.16)$$

The first term on the right hand side of this equation is the katabatic PGF that was already analyzed. Nevertheless, the second term is the PGF that reduces this gradient and is induced by the horizontal variation of the TDL. Even though both terms are related to horizontal temperature variations, the second term that is due to a change in the TDL will be referred to as PGF that induces thermal wind (THW). Hence, P_3 is now P_{THW} and we can write the resulting PGF as it was performed in equations 2.15 for both horizontal directions (van den Broeke et al., 2002; Mahrt, 1982):

$$x\text{-direction : } \frac{1}{\rho_0} \frac{\partial P_{THW}}{\partial x} \approx + \frac{g}{\rho_0} \frac{\Delta \rho h^*}{\Delta x} \approx - \frac{g}{\theta_0} \frac{\partial \Delta \theta h^*}{\partial x} \approx - \frac{g}{\theta_0} \frac{\partial \hat{\theta}}{\partial x}, \quad (2.17a)$$

$$y\text{-direction : } \frac{1}{\rho_0} \frac{\partial P_{THW}}{\partial y} \approx + \frac{g}{\rho_0} \frac{\Delta \rho h^*}{\Delta y} \approx - \frac{g}{\theta_0} \frac{\partial \Delta \theta h^*}{\partial y} \approx - \frac{g}{\theta_0} \frac{\partial \hat{\theta}}{\partial y}. \quad (2.17b)$$

It should be noted that the temperature perturbation changes in the horizontal direction which is the reason to differentiate it with respect to x or y . In the last step of these equations the vertically integrated temperature perturbation is used (cf. equation 2.6) as by Mahrt (1982). O’Connor et al. (1994) uses the height of the ABL in combination with the average ABL potential temperature and the potential temperature above the ABL to derive the PGF due to thermal gradients. From this procedure no vertical evolution of the thermal wind can be obtained and problems arise when defining the height of the ABL. This supports the choice of the integrated TDL to derive the thermal wind. Further, the THW has an opposing effect on KAT which means that the thickening of the TDL towards the coast decelerates the

flow.

An interesting case that might occur and influence the TDL is a coastal barrier, such as a mountain range, as it is illustrated in figure 2.4. However, the flow might also be blocked by a large-scale flow towards the ice shelf, for example by a low pressure system that moves in front of the ice shelf (not shown in the figure). If the cold air is drained from the slopes by katabatic winds, it can lead to cold air pooling on the ice shelf in front of the barrier (in orange in figure 2.4). This is the case if no additional gradient is present that exports the air from the ice shelf. As a result, depending on the thickness of the cold pool, the katabatic flow on the slope might be already decelerated further up-slope due to the TDL thickening and less cold air is drained. This effect implies a dynamical negative feedback. It is often observed that winds in Antarctica close to the coast suddenly cease (Ball, 1956). Usually such an event is associated with a jump in pressure that is related to a sudden change of the thickness of the TDL. The pressure jump can move up and down the slope depending on the pool of cold air. This case and the implications on the dynamic stability of the flow are analyzed in detail by Ball (1956, 1957). The TDL can also vanish if thick low clouds occur and strongly increase the downwelling longwave radiation.

Another important effect is the piling-up of cold air towards a barrier which leads to tilted isentropes and is induced by a large-scale flow perpendicular to the barrier. This case is illustrated in figure 2.4 in green. Because of the high stable stratification of the air, it can, usually, not cross the barrier (Schwerdtfeger, 1984). A measure of whether the air is able to cross the mountain or not is given by the Froude number (Cushman-Roisin and Beckers, 2011; O'Connor et al., 1994):

$$Fr = U \left(gH \frac{\Delta\theta}{\theta} \right)^{-1/2} \approx \frac{U}{NH}, \quad (2.18)$$

where H is the scale of the height of the barrier and U the scale of the synoptic flow speed perpendicular to the barrier (O'Connor et al., 1994). The Froude number is usually used as an expression of the importance of the stratification on the flow. If it is below unity the kinetic energy of the air is not sufficient to cross the barrier (King and Turner, 1997). A height of the barrier of 2000 m, an average potential temperature of 260 K, and a deficit of 10 K, together with a flow speed of 10 m s^{-1} would already result in a Froude number of 0.36 (O'Connor et al., 1994).

The scale on which the barrier affects the flow can be given by the internal Rossby radius of deformation as distance perpendicular to the barrier (King and Turner, 1997; Overland, 1984):

$$R_d = \frac{1}{|f|} \left(gH \frac{\Delta\theta}{\theta} \right)^{1/2} \approx \frac{NH}{f}. \quad (2.19)$$

By using the above example the flow will be influenced by the barrier over about 200 km distance from the barrier. It should be noted that here H is rather the scale of the height of the TDL than of the barrier. This also implies that H is variable. The distance over which the flow is influenced by the barrier, hence, depends on the height of the TDL and the temperature deficit compared to the background.

The flow that is induced by such a barrier is referred to as barrier wind (Schwerdtfeger, 1984). It is a combination of a large-scale PGF and a thermal wind effect. As the air dams up on the windward side of the mountains, the pressure increases towards the mountains which induces a geostrophic flow parallel to the barrier with the barrier to its left (southern hemisphere; cf. figure 2.4). The sloping isentropes in the lower layers of the stable atmosphere are responsible for a low-level jet (Stull, 1988) that forms close to the barrier with a peak velocity a few hundred meters above the ground.

In association with such a barrier wind Schwerdtfeger (1984) explains a Föhn effect that occurs on the lee side of the mountain. The cold stable air is not able to flow over the barrier. However, the overlying warmer air is pushed over the colder layer and the barrier by the large-scale flow and descends on the lee side. Here, strong and rather warm winds can occur due to this Föhn effect at the same time as barrier winds occur on the windward side of the barrier (Schwerdtfeger, 1984).

Having discussed the PGFs in the momentum balance (equations 2.9), I will now assess the importance of the passive force which are the Earth's rotational effects (COR) and the frictional effects (FDIV). I already assumed that the large-scale flow is in geostrophic balance. Nevertheless, also the flow in the ABL is influenced by the Coriolis force which can be shown using the Rossby number of the flow (Cushman-Roisin and Beckers, 2011; Mahrt, 1982):

$$R_0 = \frac{U}{|f|L}, \quad (2.20)$$

where L is the horizontal length-scale of the flow. If the Rossby number is smaller than unity, the flow is considerably influenced by the Coriolis force. The winds that are generated over the continental slope are a phenomenon stretching over hundreds of kilometers. Assuming a wind speed of about 15 m/s and a length-scale of 100 km, the Rossby number is about unity. It implies that gusts with high wind speeds over short distances are not influenced and the persistent ABL winds over a larger distance are influenced by the Coriolis force.

In the previous section of this chapter (2.1), I have stressed the importance of the SHF to compensate the longwave radiative loss on the slopes of the ice sheet. Therefore, turbulent mixing of heat and momentum in the stable ABL that is induced by wind shear and surface friction is crucial if one wants to understand the ABL flow over Antarctica. The already mentioned closure problem induced by the FDIV term in the equations 2.9 can be approached in several ways using closure techniques based on parameterizations. At the surface in the stable ABL it is common to apply the Monin-Obukhov similarity theory (Garratt, 1994). The turbulent fluxes between the surface and the atmosphere are then parameterized using bulk transfer relations that relate the turbulent flux to the mean flow (Garratt, 1994). Assuming a logarithmic wind profile above the surface, the wind speed becomes zero at a certain height that is referred to as the aerodynamic roughness length (Stull, 1988). This surface characteristic can, then, be used to define a neutral drag coefficient that solely accounts for surface friction. Further, the flow stability is considered as well by implementing a stability parameter that depends on the aerodynamic roughness length and on the so-called bulk Richardson number (Garratt, 1994). In conclusion, the turbulent exchange in the surface layer depends on the dynamic stability and the roughness length. Above the surface layer, usually, first order closure procedures are applied that use the gradient of the quantity and an exchange coefficient that again depends on the stability of the flow.

The surface roughness influences the turbulent exchange in a way that, if the surface roughness is small, turbulent exchange is small. In terms of the turbulent heat flux this means that the static stability of the atmosphere is larger (Reijmer et al., 2004). In this case, the turbulent flux of momentum is also reduced which leads to higher wind speeds and a smaller dynamic stability. Vertical diffusion of momentum (FDIV), thus, increases if the dynamic stability of the atmosphere decreases.

All the discussed PGFs together with the Coriolis and frictional terms can now be used to explain the wind field over the Antarctic continent and the surrounding ocean. In chapter 4, I will proceed to analyze these terms in a quantitative fashion. I have pointed out how important the topography is in terms of the generation of the flow but also in consideration of spatial variations of the strength of the flow in the horizontal and vertical directions due to topographic patterns. In the following, I will now explain how the momentum and energy balance (section 2.1) influence the growth, decay and transport of sea ice around Antarctica.

2.3 Forcing Mechanisms of Sea Ice Formation and Transport

Around the Antarctic continent a rather thin layer of sea ice forms throughout the winter at the interface between the cold atmosphere and the relatively warmer ocean. Atmosphere and ocean exchange momentum, heat, and moisture through this interface and its evolution is coupled to the strength of these fluxes. Here, I will discuss in detail how the exchange between atmosphere and sea ice takes place and how the sea ice responds.

Since the ocean in the polar regions has a salinity of about 35 psu, the freezing temperature of the water is about -1.86°C (Eicken, 2003). Once the water surface has cooled to this temperature, so-called frazil ice is formed. This consists of small, needle-like ice crystals that float at the surface (Wolfe et al., 2011). When water freezes, salt that was embedded in the molecular structures is released into the ocean. This, however, implies a negative feedback on the freezing process as the release of salt increases the salinity of the water just below the ice and, therefore, lowers the freezing temperature. After the formation of frazil ice the consecutive ice growth can evolve in two ways depending on whether the ocean surface is rough or calm. In the first case, the ice accumulates into circular disks because of the frequent collisions between the ice patches. This type is referred to as pancake ice which is, then, depending on wind and waves, colliding further. Rafting and ridging might occur that thickens the ice and forms a closed ice surface (Wolfe et al., 2011). In case of calm waters, the frazil forms a thin film called grease. If the growth continues and an ice surface is formed, this type of ice is called nilas (Wolfe et al., 2011). At last, a closed ice sheet, congelation ice, that is the result of this type of growth is characterized by a rather smooth surface and bottom (Wolfe et al., 2011).

The growth of sea ice during a season when sunlight is still available is enhanced by a positive feedback mechanism owing to changing surface properties. In section 2.1, I have already mentioned the large difference between the albedo of sea ice and the one of open water. If sea ice forms, the surface albedo is increased considerably which means that the surface is cooling much faster than before and the ice formation is enhanced. This positive feedback is referred to as the ice-albedo feedback (Curry et al., 1995; Eicken, 2003). Not only does the feedback enhance ice growth but it also accelerates ice melt in spring when the albedo of the surface is lowered due to the open water surfaces within the ice. Curry et al. (1995) and Notz (2009) also discuss the influence of the ice-albedo feedback on the sea ice cover under long-term changing climatic conditions.

Returning back to the sea ice formation, the salt that is extracted from the water when it freezes is rejected into the water below as so-called brine. However, the exclusion of the salt from the crystals should be regarded as a continuous process that depends on the temperature. Brine is also enclosed in sea ice and forms brine pockets. Hence, sea ice consists of two phases and components: A solid fraction that is pure freshwater ice and a liquid fraction, the brine. For this reason sea ice is also referred to as a mushy layer (Feltham et al., 2006).

There are five major processes how brine is released from the sea ice (Notz and Worster, 2009). One of them, that was already mentioned, is the direct segregation into the water below the sea ice which accounts for most of the total desalination. Further, after the sea ice has formed the enclosed brine can be rejected by diffusion, expulsion, gravity drainage or flushing of the brine (Notz and Worster, 2009). The first process is rather slow and almost negligible. The second occurs due to a cooling of the ice and a continuous increase of the solid fraction that pushes the brine aside. This, however, leads more to a redistribution of the brine within the ice than a rejection out of the ice pack. Gravity drainage occurs due to density gradients and subsequent convection within the ice and was found to be an important process of desalination (Notz and Worster, 2009). At last, flushing by percolating melt water might be important in case that melt water is present at all (Notz and Worster, 2009).

From all these considerations, it can be concluded that growth and melt of sea ice do not only depend on the temperature but are also related to the salinity. Further, the temperature at which sea ice freezes and melts changes due to the salinity in time and space. Small variations in temperature, usually, lead to a change between the solid and the liquid fraction within the ice but do not disintegrate the ice. Internal processes in sea ice are related to the profile of salinity and temperature. Thermodynamically, they alter the heat capacity and, accordingly, the heat content of the ice and are crucial for its growth and decay (Hunke et al., 2011; Notz and Worster, 2006). I will not further discuss these issues as only a basic understanding of the thermodynamics of sea ice is necessary in this thesis.

Nevertheless, in terms of sea ice formation it is important to consider the evolution of the ice thickness that depends on the sea ice thermodynamics. Once sea ice is formed its thickness changes continuously. Heat, that is provided by the ocean heat flux, is conducted through the ice and released to the atmosphere at the surface. This transfer depends on the properties of the ice, the thickness of the ice, and the

temperature gradient between the surface and the base of the ice. If the surface temperature decreases, for example, due to radiative cooling, the temperature gradient and, consequently, the heat conduction through the ice increase. Given the case that this heat flux is not balanced by the ocean heat flux at the base, the ocean water starts to freeze. This phase change, then, releases additional energy. Consequently, the growth and melt of the sea ice depends to a large extent on the surface energy balance that I discussed in section 2.1.

Simplified, the rate of change of the sea ice thickness can be expressed using Stefan's law (Notz and Worster, 2006):

$$\frac{\partial h}{\partial t} = \frac{Q_i}{\rho_i L_i}, \quad (2.21)$$

where h denotes the ice thickness, ρ_i is the mean ice density, L_i (≈ 300 kJ kg $^{-1}$) is the latent heat of fusion for sea ice, and Q_i is the heat flux in the ice (Notz and Worster, 2006). The heat flux in the ice can be related to the temperature gradient and the ice thickness by (Eicken, 2003):

$$Q_i = -k \frac{T_{top} - T_{bottom}}{h}, \quad (2.22)$$

where k is the heat conductivity of the ice, and T_{top} and T_{bottom} are the temperatures at the surface and the base respectively. The former can be obtained from the surface energy balance (Eicken, 2003). This set of equations is a zero-layer sea ice model that was developed by Semtner (1976) and is a very simplistic approach that neglects many important processes of sea ice thermodynamics. Still, it is used in many current climate models and leads to large inaccuracies (Semtner, 1984). More complete, but also more complex, formulations are given by the one-dimensional model of Maykut and Untersteiner (1971) and the three-layer model suggested by Semtner (1976).

If only the thermodynamic growth of sea ice would be considered, the sea ice around Antarctica would only grow to a maximum thickness of about 0.7 m (Haas, 2003). However, the sea ice thickness can vary considerably and it can be far larger than the previously mentioned value. Another important process that needs to be considered is the accumulation of snow on the sea ice. Vancoppenolle et al. (2009) suggest that it makes up to 25% of the total wintertime sea ice mass budget in the Southern Ocean.

Moreover, if we consider sea ice to be a fluid, momentum can be transferred from the atmosphere and the ocean to the sea ice and mechanically redistribute it. Sea ice can break up into single pieces, ice floes that eventually collide and, by rafting and ridging, form pressure ridges (Haas, 2003). This process is schematically illustrated in figure 2.5. Thorndike et al. (1975) formulated an ice thickness distribution theory in which they define an ice thickness distribution function G that changes in space and time. The ice thickness distribution is determined by ice advection, thermodynamic growth and decay, and mechanical processes. These factors result in the following equation (Thorndike et al., 1975):

$$\frac{\partial G}{\partial t} = -\nabla \cdot (\vec{u}G) - \frac{\partial(\Phi G)}{\partial h} + \psi, \quad (2.23)$$

where \vec{u} is the ice motion in both horizontal directions, Φ is the thermodynamic growth rate, and ψ is the mechanical redistribution function. The latter must conserve the total ice area and the volume per unit area (Thorndike et al., 1975). It is related to internal ice stresses and represents ridging processes. The nabla operator (∇) denotes $\partial/\partial x + \partial/\partial y$ of the product which translates to the advection and divergence of a certain thickness distribution.

Nevertheless, I will not further elaborate on the ice thickness distribution in the course of my thesis but it is important to notice that sea ice dynamics play an important role for the local sea ice thickness. Mechanical redistribution of sea ice does not only affect the thickness distribution but it also is important to create open water areas in which new frazil ice can be formed and continuously exported. Such regions can be very important in terms of sea ice production throughout the winter as sea ice is formed quickly and efficiently over the cooling ocean surface. In sum, sea ice dynamics are important to assess where regions of diverging and converging sea ice occur (cf. figure 2.5). Divergence can be associated with open

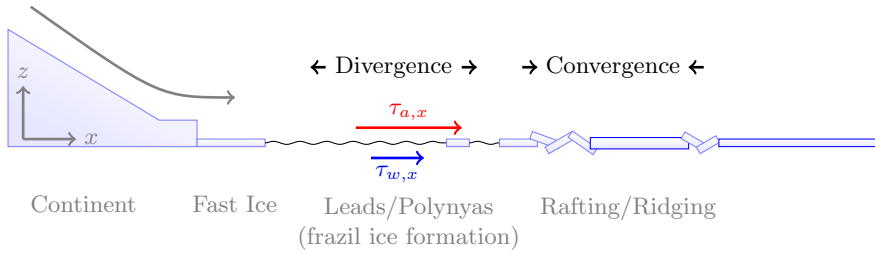


Figure 2.5: Schematic illustration of sea ice dynamical processes and the mechanical redistribution of ice. Shown are the effects of convergence and divergence of the ice and the resulting open water areas, and rafting and ridging of the ice. Further, wind τ_a and ocean current stress τ_w components on the sea ice are indicated (after Haas, 2003).

water formation and frazil ice production, and convergence indicates areas where the sea ice is dense and becomes thicker due to rafting and ridging.

Even though sea ice consists of single ice floes, leads, and polynyas in reality, the simplifying assumption that it is a two dimensional continuum on a large scale is a useful approximation to analyze the sea ice dynamics (Coon et al., 1974). The momentum balance of sea ice is given by (Coon et al., 1974; Hibler III, 1979):

$$x\text{-momentum : } \frac{du}{dt} = -g \frac{\partial \eta}{\partial x} + fv + \frac{1}{m} \left(\tau_{a,x} + \tau_{w,x} + \frac{\partial \sigma}{\partial x} \right), \quad (2.24a)$$

$$y\text{-momentum : } \frac{dv}{dt} = -g \frac{\partial \eta}{\partial y} - fu + \frac{1}{m} \left(\tau_{a,y} + \tau_{w,y} + \frac{\partial \sigma}{\partial y} \right), \quad (2.24b)$$

where η is the sea surface height, f is the Coriolis parameter, m is the mass of snow and ice per unit area, $\vec{\tau}_a$ and $\vec{\tau}_w$ are the wind and ocean current stresses (cf. figure 2.5), and σ is the internal stress tensor. The advective terms contained in the total time derivative on the left-hand side of the equations are usually much smaller than the other terms and, therefore, are negligible (Oberhuber, 1993). Generally, as in equations 2.9 in section 2.2, we can distinguish between active and passive forcing terms. The passive terms are the internal stress and the Coriolis force. The active terms could be further classified into external forcing mechanisms by the atmosphere and the ocean. However, it should be noted that the terms of surface tilt and ocean current stress are not solely ocean forcing terms but are, in turn, influenced by the atmosphere. The surface tilt, for example, is related to the atmospheric pressure distribution. The only pure atmospheric forcing term is the wind stress τ_a . I will treat these forcing terms in the following.

The term that is of major interest in this project is the wind stress. It represents the interaction between the ABL dynamics and the sea ice momentum balance. There has been a strong debate about the importance of the single terms in the momentum balance (Hunke and Dukowicz, 1997; Parkinson and Washington, 1979). Coon (1980) states that wind stress is the dominating external force in the balance. Thorndike and Colony (1982) confirm that this is valid on shorter timescales from days to months as they found out that in the central Arctic Ocean about 70% of the total variance of the ice drift is explained by the geostrophic wind. However, they also concluded that on longer timescales winds and ocean currents are about equally important. According to a scale analysis by Rothrock (1975b), the forcing by wind and ocean currents is by far the largest. If we consider that there are large regional and hemispheric differences in the wind field and the ocean currents, the different opinions on the importance of the external forcing terms are not surprising. The importance of the wind stress in several regions of the Southern Ocean will be further discussed in chapters 4 and 6.

The momentum transfer from the atmosphere to the sea ice can be expressed in a vector notation using

the quadratic drag law (Coon, 1980; Parkinson and Washington, 1979; Thorndike and Colony, 1982):

$$\vec{\tau}_a = \rho_a C_d |\vec{U}| \mathbf{B}_{\mathbf{a}} \vec{U}, \quad (2.25)$$

with the rotation matrix

$$\mathbf{B}_{\mathbf{a}} = \begin{bmatrix} \cos \alpha & -\sin \alpha \\ \sin \alpha & \cos \alpha \end{bmatrix}, \quad (2.26)$$

where ρ_a is the density of air, C_d is the atmospheric surface drag coefficient, α is the rotation angle, and \vec{U} is the wind velocity in both horizontal directions. Whereas Coon (1980), Hunke and Dukowicz (1997) and Parkinson and Washington (1979) use the geostrophic wind velocity, Thorndike and Colony (1982) take the difference between the geostrophic wind velocity and the ice velocity. Hibler III (1979) explains that it is a good approximation to just use the geostrophic wind because it is several orders of magnitude larger than the ice velocity. Parkinson and Washington (1979) apply a constant drag coefficient of 0.0024, whereas Overland and Davidson (1992) point out that it is rather a function of sea ice roughness length and surface layer stability, and that sea ice drift is very sensitive to this parameter.

According to the Ekman theory the surface drift current in the southern hemisphere is directed 45° to the left of the wind (Ekman, 1905). However, Hunkins (1966) reports that this relation does not hold for sea ice where the turning angle is much smaller. The absolute value of the rotation angle depends on the structure of the ice pack and the internal and lateral stresses. Parkinson and Washington (1979) use a mean value of 20° ; Thorndike and Colony (1982) find an average rotation angle of 8° from buoy drift in the Arctic Ocean and report a strong variation depending on the season; and Kottmeier et al. (1992) find a good agreement with measurements from buoys in the Weddell Sea for an angle of 20° in winter and 40° in summer. Overland and Davidson (1992) conclude that the turning angle also depends on the atmospheric stability and might vary, therefore, by up to 15° . In conclusion, the total wind stress term is very much dependent on local properties of the ice and the structure of the atmospheric surface layer, and can vary considerably from one region to the other according to the surface drag and the rotation angle. This supports the hypothesis that the dynamical influence of the atmosphere on sea ice is dominating the variability in some regions but is less important in others.

If the stress exerted by the ocean currents was assessed, a similar approach to the relation 2.25 could be used. However, in this case it is important to use the difference between the geostrophic current velocity and the sea ice because their order of magnitude is similar (Hibler III, 1979). I will not further expand on this topic here as it is not part of the analysis. A detailed discussion of the momentum transfer between ice and ocean is performed by McPhee (2008, 1975). It should be kept in mind that the variability of the ocean current stress acts on much longer timescales than the variability of the atmospheric wind stress.

The remaining active term in the momentum balance, that has not been discussed yet, is the acceleration of the sea ice due to a tilted ocean surface. This forcing term is usually much smaller than the wind and ocean current stresses (Hunke and Dukowicz, 1997). The dynamic topography of the ocean influences the sea ice momentum on rather large spatial and temporal scales. However, Heil et al. (2008) report a strong response of the sea ice motion to tidal influences on a sub-daily timescale.

Next, I will briefly describe the passive force exerted by internal sea ice stress. If the ice consists of single separated floes, as it might occur in summer, most of the sea ice motion can be explained by just the wind and ocean current stresses because the ice floes can move freely (Coon, 1980). In a dense ice pack, however, internal stress divergences cannot be neglected and the sea ice rheology plays a crucial role in the momentum balance (Coon, 1980). In order to understand the formation of open water areas in the ice pack, it is crucial to know when the ice is deformed sufficiently so that it breaks. Therefore, sea ice can be considered as an elastic-plastic material (Coon et al., 1974; Rothrock, 1975a). It elastically stretches under the influence of a certain stress and returns to the previous state when the stress is released. If the deformation exceeds a certain value, the sea ice deforms irreversibly (Feltham, 2008). In the case that the stress exerted gets really large, the sea ice might break. A detailed description of sea ice rheology is given by Coon et al. (1974) and Feltham (2008).

In order to provide a simple approach to model the internal stresses and deformation of sea ice, Hibler III

(1979) suggests a nonlinear viscous-plastic rheology. By replacing the elastic yield behavior with a viscous formulation, he achieved to make sea ice models computationally more efficient. This approximation is valid with respect to average deformation rates over a large area and long timescales (Feltham, 2008). The viscous-plastic method is implemented in most current coupled climate models that include sea ice dynamics (Hunke and Dukowicz, 1997). It simulates the mean sea ice drift reasonably well but also implies several drawbacks as it is not able to accurately simulate convergence and divergence. In several regions, and especially in the Southern Ocean, this might result in an underestimation of open water areas that are crucial for sea ice formation. An even more computationally efficient method that is able to resolve convergence and divergence of the ice is given by Hunke and Dukowicz (1997). They formulated an elastic-viscous-plastic model that is based on the original formulation by Hibler III (1979), but includes terms that introduce some elastic behavior. Recent progresses in sea ice modeling support the choice of an elastic-viscous-plastic model (cf. Bouillon et al., 2009; Vancoppenolle et al., 2009).

In sum, the atmospheric wind stress is a dominant term in the sea ice momentum balance that induces sea ice drift and can lead to strong redistribution of sea ice. The internal stress, a passive force in the momentum balance that is only active when acceleration is present, results in deformation of sea ice. This is an important characteristic as divergence causes the ice to break up and form open water areas under sufficiently large internal stress.

Moreover, I have outlined that the surface energy balance at the atmosphere-ocean interface triggers sea ice growth in the open water areas. Consequently, a strong wind stress over the sea ice that breaks it up and forms open water areas together with a heat loss of the surface, present a combined effect of sea ice dynamics and thermodynamics that results in a very efficient sea ice production process. I have not mentioned yet that this processes is very self-sustainable in two ways. Firstly, in terms of thermodynamics, it is more efficient to form sea ice in open water or under a thin ice cover than at the base of an existing thick ice pack because, as the heat conductivity depends on the ice thickness, the ocean water loses its heat faster. Secondly, from a dynamical point of view, thin ice breaks up again more easily than a thicker ice pack because the internal deformation and the critical stress depend on the ice thickness. These mechanisms, however, do only apply if a persistent wind forcing and supply of cold air or radiative cooling is present.

In section 2.1 I have already mentioned the importance of open water areas and the formation of frazil ice in these areas in the total sea ice mass balance of the Southern Ocean. In addition to the estimate that was given by the model study of Vancoppenolle et al. (2009), ice core analysis in the Ross and Amundsen Seas by Jeffries et al. (1997) and Worby et al. (1998) confirm that about 45% of the sea ice originates from frazil ice formation in open water. Accordingly, one would expect a strong dynamic and thermodynamic atmospheric influence on the sea ice variability in these regions.

I showed in section 2.2 that strong katabatic winds can occur in coastal areas that provide a substantial and persistent wind stress on the sea ice. However, due to the opposing THW forcing they usually cease within a short distance from the coast. There are other wind systems such as the described barrier winds that can be characteristic for certain areas and have a much larger scale influence in an off-shore direction than the katabatic winds and might have an important impact on the sea ice.

Consequently, after discussing the underlying datasets for this analysis in chapter 3, I will proceed to analyze these winds in chapter 4, describe the variability of sea ice formation and dynamics in chapter 5, and finally focus on the interaction in chapter 6. In this chapter I have intended to focus solely on the physical processes that form the background understanding of the variabilities and interactions that I analyze in this thesis. I will give statistical methods and further definitions that are necessary for the analysis at a later stage.

3 Data & Model Description

Before I proceed with the analysis, a detailed description of the data sets that I included in this study and a motivation why I used them in this case is necessary. Generally, in order to investigate the impact of the atmospheric boundary layer dynamics on sea ice, one needs two different kinds of data: atmospheric fields such as wind, temperature, and pressure on one hand, and sea ice cover and motion on the other hand. There are several options that all have advantages and disadvantages which should be evaluated depending on the application. Therefore, it is necessary to note under what circumstances and assumptions a certain dataset can be used and how the retrieval of the data set might influence the results and their interpretation.

The formerly mentioned atmospheric data set already bears a rather large challenge because observational data over the Antarctic continent and the Southern Ocean are, due to the harsh conditions and the lack of population, scarce. Moreover, I would prefer highly resolved data in space and time in all three spatial dimensions in order to analyze the boundary layer processes in detail. Such an observational data set, however, is impossible to obtain. Many studies that have been performed so far use reanalysis data which has the advantage of a consistent time series with a large spatial coverage. Nevertheless, some of the major disadvantages, in terms of this project, are the rather coarse horizontal resolution of the reanalysis data which is, depending on the dataset, between 1.125° and 2.5° , and their large uncertainties in the polar regions which is, among other reasons, again due to a lack of observational in-situ and satellite data. A further option for the analysis is to use data that is provided by simulations with a regional climate model (RCM). These kinds of models have several advantages that are preferable for this study such as a high resolution, three dimensional fields of all needed meteorological variables and consistency in space and time. As polar regions have gained higher attention in the past decade due to rapid climate changes, the understanding of physical processes in these regions have increased rapidly and, therewith, the level of complexity of these processes in the RCMs. However, these data also implicate several drawbacks and major differences to observational data that one should consider and which will be mentioned in section 3.1. At that point I will give a detailed description of the model itself and its output data.

In terms of sea ice, the options of databases to consider are less. In-situ measurements of sea ice are used mainly for local studies or model and satellite validation purposes. Complex sea ice models that resolve and include all the processes that I require for my analysis are still in a premature state and not yet coupled to regional ocean and atmospheric models. Sea ice cover in reanalysis data is usually the same data as the originating satellite data but on a coarser grid which implies several problems due to the grid interpolation in coastal regions. There, important structures of the sea ice such as the alteration of open water and closed sea ice cover are not resolved. Because of these reasons, most studies rely on satellite data that are available at a rather high resolution since the early 1970s and with major improvements in quality since the late 1970s. Preprocessed data of sea ice concentration that was derived from the passive microwave brightness temperature is provided by several institutions and I will discuss it in section 3.2.

For the targeted investigation of the dynamical implication of the lower atmosphere on sea ice, it is, further, necessary to have information about sea ice motion. One of the first records of sea ice motion resulted from the famous drift of Fridtjof Nansen and the ship *Fram* that drifted across the Arctic basin, while frozen into the ice, between 1893 and 1896 (Comiso, 2009). Similar to the ship one can deploy buoys into the ice and record their tracks to get an indication of the sea ice motion. This kind of data, again, is scarce in the Southern Ocean and not beneficial for this project. Instead, I use a data set derived from satellite recordings that provide high spatial and temporal coverage. This, again, preprocessed and provided motion vectors will be treated in the third part of this chapter.

The last part (3.4) is dedicated to a synchronization of the different datasets in space and time. This includes data assimilation and grid interpolation as well as some of the consequences that one should consider for the analysis and the interpretation.

3.1 The Regional Atmospheric Climate Model RACMO2.1/ANT

In the introduction to this chapter I explained my motivations for drawing on output data from a regional climate model in this project. Furthermore, it should be mentioned that this is a purely atmospheric RCM, called RACMO2.1 (Regional Atmospheric Climate MOdel, version 2.1). This model version was originally developed at the Royal Netherlands Meteorological Institute (KNMI) by van Meijgaard et al. (2008) and later adapted at the Institute for Marine and Atmospheric research Utrecht (IMAU) for the application to polar regions. This includes, for example, the implementation of a multi-layer snow scheme (Ettema et al., 2010, 2009). The simulation of the present day climate, that I rely on here, was performed over the Antarctic continent and the surrounding Southern Ocean with RACMO2.1/ANT (hereafter the abbreviation RACMO refers to this version of the model) by Lenaerts et al. (2011).

Generally, when using data produced by a climate model, one should be aware of the essential difference to observational data and that, in this case, reality is approximated by applying knowledge of physical processes and local surface properties that change the state of the current conditions in time and space. If the climate system and its investigated variability is described by model data, it is assumed that the simulation is reflecting the reality accurately enough to resolve the investigated processes. A model calculates from an initially deployed state at a certain location and time a new state of the system at the next timestep, for instance, six hours later, by solving a set of partial differential equations numerically. These equations are based on principal physical laws of conservation of mass, heat and momentum. A so called prognostic variable, such as temperature, changes from one state to another depending on other variables and external forcing mechanisms, such as solar radiation. Other variables that are not a function of time but only depend on the current state are called diagnostic variables.

The set of equations in RACMO consists of two major parts; those formulations dealing with physical processes and those that treat the model atmospheric dynamics. The former is based on the description by the European Center for Medium-Range Weather Forecast (ECMWF, cycle 23r4 and partly updated to cycle 28r1; cf. van Meijgaard et al., 2008). A detailed description of the physical processes involved is given by White (2003). Nevertheless, the dynamical core is provided by the formulation of the High Resolution Limited Area Model (HIRLAM, version 6.3.7; cf. van Meijgaard et al., 2008). At this point, I do not deem it necessary to provide any further details on these formulations.

Any numerical climate model solves partial differential equations based on a discretization in space and time. Therefore, it is necessary to choose a certain spatial resolution and size of the timestep, where one depends on the other in order to guarantee numerical stability. However, there are three major reasons that formulations of physical processes need to be replaced by empirical functions that simplify the reality. This is either the case if a process is too complex and too computationally expensive to be fully calculated, if a process takes place on a smaller scale than resolved by the model, or if the exact physical formulation is unknown. Certainly, these so called parameterizations incorporate the risk that - since they are based on measurements at a certain place and time - they might not be valid with the same parameters in another climatic regime. As this version of RACMO relies on parameterizations that were adjusted to employ on Antarctica and under current climate conditions, its output data within this period and spatial domain should represent reality very closely.

One further artifact that comes along with a model, and which I should mention at this point, is uncertainty induced by model tuning. This is a widely applied technique to adjust for model biases. Certain parameters are changed in such a way that the final simulations better match with the observations, even though the parameters do not correspond to the empirically retrieved values any longer. Usually, tuning is performed to account for underrepresented physical processes and should be handled carefully and should be considered in the interpretation. Again, it might be questionable whether a strongly tuned model is able to represent reality at a different time and location.

In the horizontal plane, as displayed in figure 3.1, the model consists of 262 and 240 grid points in the models x- and y-direction respectively, whereas it is centered at the South Pole (90° S; Lenaerts et al., 2011). As one can observe in figure 3.1 the x-y-plane of the model is rotated by 10° to the east with respect to the central meridian (0° longitude). Positive x- and y- directions are defined to the right and

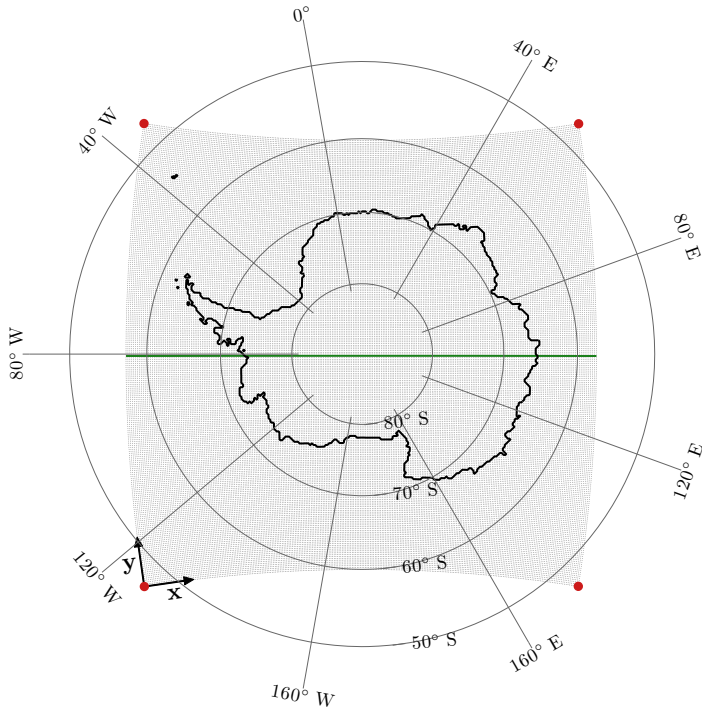


Figure 3.1: RACMO2.1/ANT horizontal grid and coastline on a polar stereographic projection with domain corner points in red (coordinates listed in table 3.1) and a transect along the y-direction center line in green of which figure 3.2 shows the vertical profile.

upward respectively as shown in the figure. The lower left corner in the figure represents the first point in the model matrix. Table 3.1 gives an overview of the geographical coordinates of the total extent of the domain. The grid is quasi-rectangular (Lenaerts et al., 2011), meaning that due to the bent Earth surface the grid cells are deformed towards the boundaries of the domain. On the other hand, towards the middle they get rectangular which is the aim of the application of such a grid in this case. As longitudinal bands converge towards the pole, the grid was constructed for practical reasons over the equator (grid center) where the longitudinal spacing is more regular. The grid at this location then has a horizontal resolution of 0.25° in both directions. Hereafter, the grid is moved over the pole. That also implies that the spacing in the y-direction (former meridional) is actually constant, with a value of about 27.8 km, and the one in the x-direction varies between a maximum of about 27.8 km at the central row to corresponding minimum values of about 24.1 km at the lower and upper most rows.

In order to gain numerical stability in models dealing with advective processes, it is necessary to consider the dimensionless Courant-Friedrichs-Lowy (CFL) criterion which is calculated according to the ratio of timestep (Δt) times the propagation speed (U) of the process to the horizontal grid size (Δx ; Cushman-Roisin and Beckers, 2011):

$$CFL = \frac{U\Delta t}{\Delta x}. \quad (3.1)$$

If the CFL criterion exceeds one, the solutions get unstable (Cushman-Roisin and Beckers, 2011). This means that always both, horizontal and temporal resolution, have to be increased or decreased simultaneously. The timestep for which the RACMO solutions were found to be stable and which has been used is 600 seconds (J. Lenaerts, personal communication). For the maximum CFL criterion of one this would result in a resolution of flow speeds with a maximum of just above 40 m/s. If very strong wind speeds occur due to storms, for example, and the model gets unstable, it recalculates the current month of the simulation using a lower timestep of 450 seconds (J. Lenaerts, personal communication). The model

output timestep is, then, every three hours.

A staggered grid has been used for the simulation, meaning that scalar data values (e.g. temperature, pressure, etc.) are evaluated in the grid cell center, whereas vector quantities, such as wind, are computed on the grid cell interfaces. In order to map the data throughout this thesis, I interpolated all data to the grid cell center and plotted them on a polar stereographic projection (cf. figure 3.1).

Table 3.1: Geographical coordinates of the four corner grid points in the quasi-rectangular RACMO2.1/ANT domain.

Corner point	Longitude	Latitude
lower left	126.8630° W	46.7492° S
lower right	147.0578° E	46.9198° S
upper left	33.4259° W	46.9022° S
upper right	53.2309° E	47.0738° S

Figure 3.2 shows a vertical profile of the model domain along a central transect indicated in figure 3.1 (in green). It includes the average vertical model grid, the topography, and the average isobars. The model has a total of 40 vertical atmospheric levels, but here, for illustration purposes, I only displayed the lowest 30 layers. The highest layer (level 1) is at an average altitude of about 29 km above sea level and the lowest layer (level 40) is, on average, about 8.6 m above the surface. As the levels are irregularly spaced and the lowest kilometer of the atmosphere alone consists of 12 levels, it is possible to study boundary layer processes in detail. This type of a vertical coordinate system is referred to as hybrid sigma-pressure levels (Lenaerts et al., 2011). In the lower layers, as one can see in figure 3.2, the isobars intersect with the topography which would be an undesired effect of a coordinate system that has pressure as a vertical coordinate. Instead, sigma coordinates with a constant reference surface pressure ($p_{ref} = 1013.25$ hPa), that are defined as $\sigma = p/p_{ref}$, are used for the lowest model layers (Holton, 2004). This has the advantage that the lower layers follow the surface terrain closely. Higher up in the atmosphere the levels gradually adjust to the isobaric surfaces which makes the combined system to a hybrid sigma-pressure system (Lenaerts et al., 2011). One should keep in mind the structure of the vertical grid when analyzing and interpreting the model output.

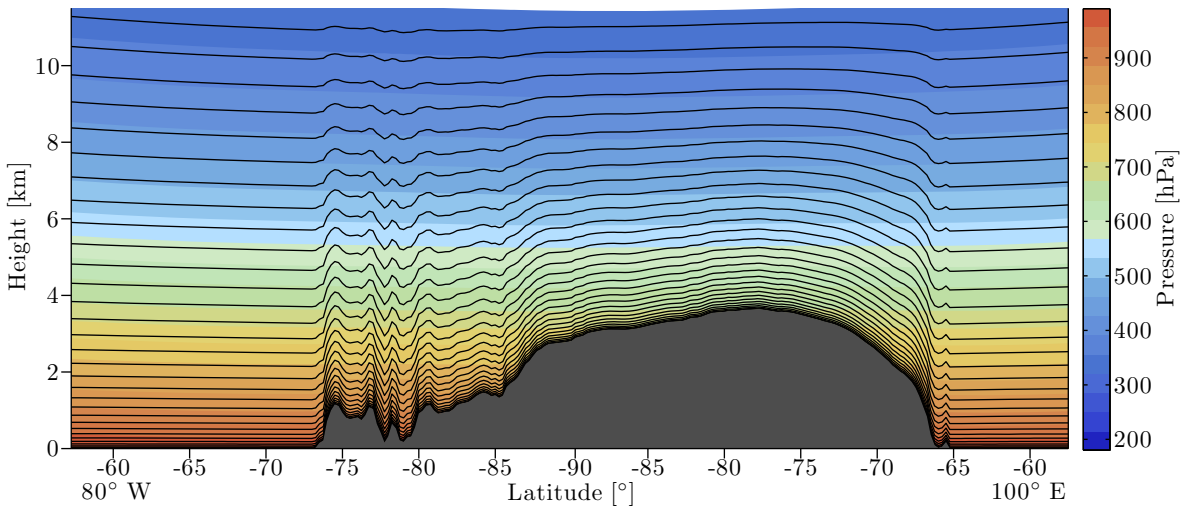


Figure 3.2: RACMO2.1/ANT vertical hybrid sigma-pressure grid (lowest 30 layers) with model topography (gray) and pressure (in color) along the transect outlined in figure 3.1 in green.

In figure 3.2 the model topography along the transect already showed that the topography of the

Antarctic ice dome is well represented in the model. Besides, in chapter 2.2 I emphasized how important the topography for the near surface wind field is over the continent. Figure 3.3(a) exhibits the topographic set up in the model which is adapted from a digital elevation model (DEM) that is provided by Liu et al. (2001) and has an original horizontal resolution of 5 km (J. Lenaerts, personal communication). As the model only resolves orographic variations on a scale of about 27 km, subgrid-scale variations are considered by assigning a orographic variance to each grid point that is derived from the higher resolution DEM and is presented in figure 3.3(b). Orographic variance is mainly important for gravity wave drag. At this point it should be noticed that the DEM in RACMO is not the newest available and should, probably, be replaced for future simulations by the updated version of Bamber et al. (2009) which has a horizontal resolution of 1 km (cf. figure 1.3). Lenaerts et al. (2011) evaluated that there are major local differences in the surface topography between these two DEMs that in turn might affect the accuracy of the wind field.

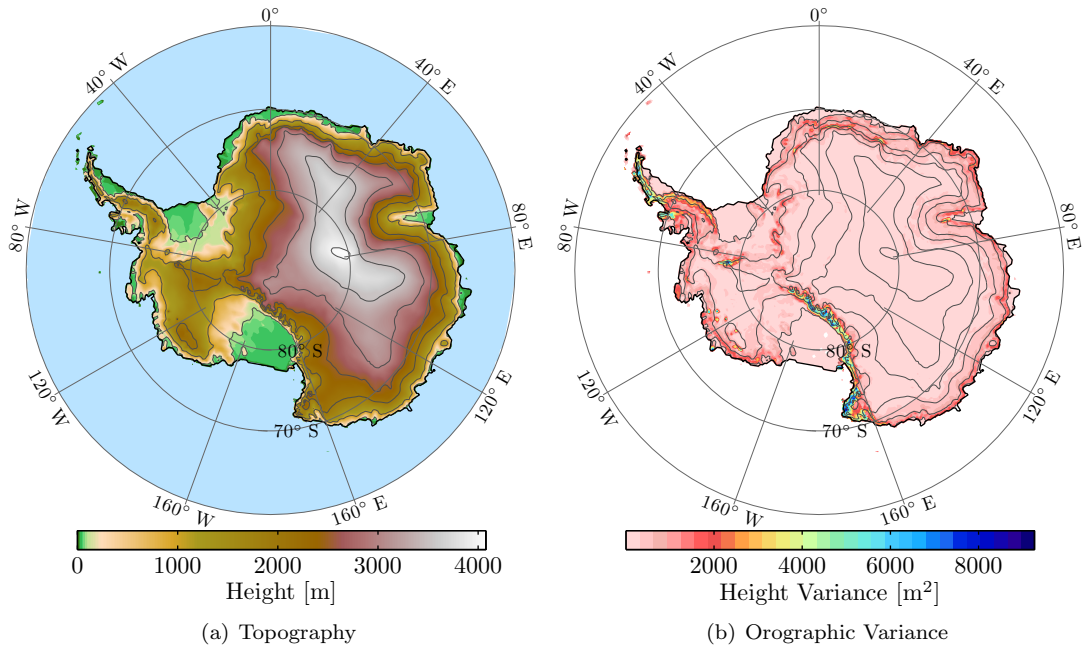


Figure 3.3: RACMO2.1/ANT topography (a) and subgrid-scale orographic variance (b) derived from Liu et al. (2001).

At the lateral boundaries the model was forced with ECMWF reanalysis data (ERA-Interim) every six hours with a horizontal resolution of 1.5° from the year 1989 to 2009 (Lenaerts et al., 2011; Simmons et al., 2007). The simulation was initialized by using fields from preceding test simulations (J. Lenaerts, personal communication). Sea surface temperature and sea ice cover at the ocean surface as well as implications of the chemical composition in the atmosphere on the radiation are prescribed by ERA-Interim forcing over the whole period. The atmospheric interior and the snow model on the land surface evolve freely within the domain. Over the Antarctic continent the ERA-Interim data shows several important advantages in comparison to its preceding, but still widely used, version ERA-40. Among these are a higher horizontal resolution, reduced errors in the stratosphere and in the hydrological cycle over Antarctica, several updated atmospheric and surface processes, as well as a new treatment of the bias corrections (Lenaerts et al., 2011; Simmons et al., 2007). Consequently, by inducing the model forcing at the boundaries and simulating the interior domain with a high resolution, this dataset provides the desired information about the climate over Antarctica from 1989 to 2009.

RACMO, in a former version, has already been deployed for many studies over Antarctica; for instance

by van de Berg et al. (2006, 2007) and van den Broeke and van Lipzig (2002, 2003b), just to name a few. The overall goal of the adaptation of the model to polar regions is to get estimates of the ice sheets surface mass balance (SMB; e.g. by van de Berg et al., 2005; Lenaerts et al., 2010; van Lipzig et al., 2002). The atmospheric boundary layer momentum budget over Antarctica, for which I mainly aim to use the model data here, has been studied with an older version of the model already extensively by van den Broeke et al. (2002) and van den Broeke and van Lipzig (2003a). Recently, several parameterizations have been updated or newly developed in order to increase the complexity and physical realism of the model. Some major changes and adaptations are an updated description of the roughness length for momentum and heat (Reijmer et al., 2005, 2004), a new formulation of the albedo parameterization (Kuipers Munneke et al., 2011), an updated snow model (Ettema et al., 2010), and an implementation of a snowdrift scheme (Lenaerts and van den Broeke, 2011; Lenaerts et al., 2011, 2010). Further, a time-dependent firn densification is included in the model in the upper five to ten meters (Lenaerts et al., 2011). Some of these changes that might affect an alteration of the boundary layer momentum budget will serve as discussion points in the following.

In chapter 2.2 I pointed out the importance of the roughness lengths of momentum (z_{0m}), heat (z_{0h}), and moisture (z_{0q}) in terms of the boundary layer dynamics. The modeling of the roughness length requires attention in particular when considering that the here analyzed coastal regions are the areas of highest orographic variations. In this case, the newest version of the model includes some major changes. It was stressed by van den Broeke et al. (2002) that the old formulation of the roughness length led to a strong underestimation of wind speeds in areas with a rough topography and an overestimation of the turbulent fluxes. In that former version the aerodynamic roughness length was set to a constant value of 1 mm over snow surface and on top of that subgrid-scale orographic variations were added. This implied that, in a region of high orographic variations, values of z_{0m} were unrealistically high which is mainly due to the fact that, in reality, it is more influenced by smaller scale obstacles than by mountains (Reijmer et al., 2004). Moreover, z_{0h} and z_{0q} were set equal z_{0m} which explains the overestimated turbulent exchange in these regions. Consequently, this unrealistic data points had to be excluded from the analysis.

This overestimation of the aerodynamic roughness length and the according underestimation of the wind speed due to a higher friction in RCMs over Antarctica in general are investigated in detail by Jourdain and Gallée (2011). They used a formulation of z_{0m} that, similar to RACMO, had a base value for snow covered surfaces and a superimposed subgrid-scale orographic roughness. Subsequently, they performed two experiments in the area of the Transantarctic Mountains, one with a rather rough and another with a rather smooth subgrid-scale orography, and compared the resulting wind speed, pressure, and temperature to observational data. The case where a rather rough terrain was imposed resulted in a strong underestimation of the wind speed, especially in the glacial valleys. In the latter simulation with a smoother terrain, and a total value of z_{0m} that is very close to the base value of snow, the winds in the glacial valleys were slightly overestimated but comparably much closer to the observations (Jourdain and Gallée, 2011).

In the new formulation z_{0m} is again set to a constant value of 1 mm over snow surfaces. The orographic correction, however, has been restricted and does not apply in this high resolution simulation. This can be seen in figure 3.4(a) which shows the average simulated July z_{0m} (1989-2009) and where it is 1 mm almost everywhere over the continent. According to the analysis by Jourdain and Gallée (2011) this should produce more realistic results but it should be kept in mind that wind speeds in the really rough terrains, such as the Transantarctic Mountain valleys and in some areas of the Antarctic Peninsula might be overestimated. A more complex formulation of z_{0m} might be desired if one would like to study the glacial katabatic winds in the Transantarctic Mountains, for example. Here, however, I perform a larger scale analysis and a slight overestimation might be even in favor of compensating for underestimated wind speeds due to unresolved slopes (Reijmer et al., 2004). Over areas that are not covered by snow, the original formulation as described by van Meijgaard et al. (2008) is applied. This is the case over the open ocean (low values) and the sea ice covered region (low to intermediate values) that is partly covered by snow and also includes open water areas (cf. figure 3.4(a)).

Additionally, z_{0h} is then an empirical function of z_{0m} and the wind speed and is about one order of

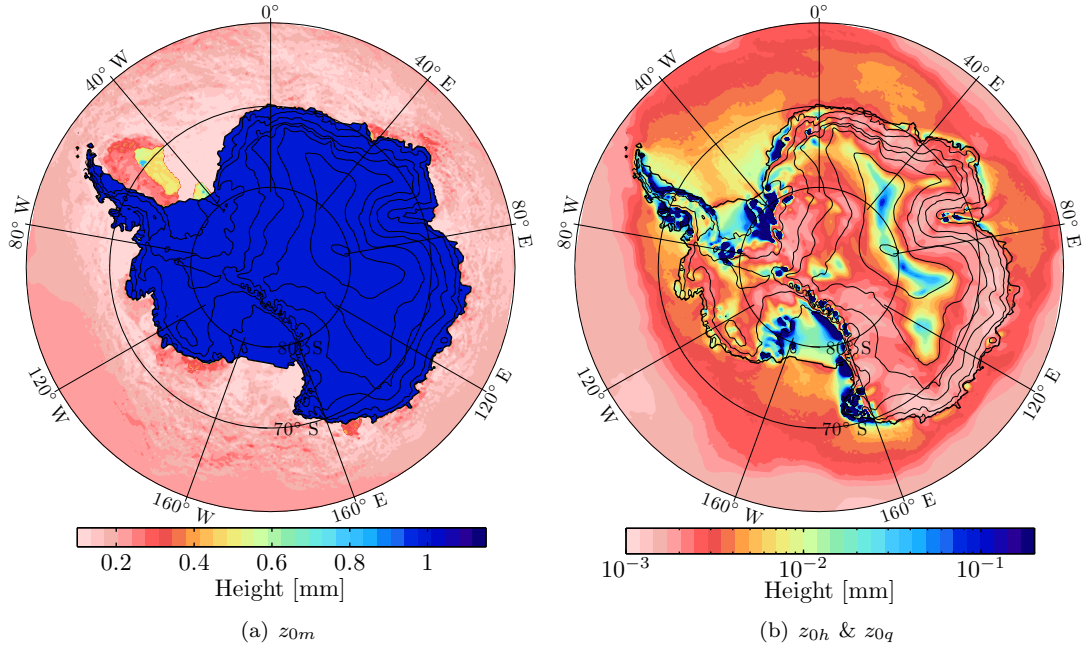


Figure 3.4: Simulated average July roughness length for momentum (a), heat and moisture (b) over the period 1989 to 2009.

magnitude smaller than z_{0m} , and z_{0q} is set equal to z_{0h} (Reijmer et al., 2005). Andreas (1987) originally formulated this surface renewal model to estimate the roughness length over sea ice. However, it was shown that it also works reasonably well over the Antarctic continent (Andreas, 2002; Reijmer et al., 2004). Figure 3.4(b) illustrates the strong dependence of z_{0h} and z_{0q} on the wind speed. The highest values are found along the Transantarctic Mountains, the western Ross Ice Shelf, Victoria Land, western Marie Byrd Land, the Antarctic Peninsula and the Filchner Ice Shelf. Over the rather gradual slopes of the escarpment zone in East Antarctica values are rather low. The sea ice covered ocean shows intermediate and the open ocean low values. The detailed structure and the generally lower values of z_{0h} and z_{0q} compared to older formulations in the model are large improvements and more realistic. Reijmer et al. (2004) showed that this gives a much better correspondence of the turbulent fluxes with observed estimates. Overall, the changes in z_{0h} influence the wind speed only slightly due to the high stability of the atmosphere (Reijmer et al., 2004).

Another progress that influences the here considered processes is the implementation of a new albedo parameterization by Kuipers Munneke et al. (2011). Whereas the preceding parameterization was based on the snow density, the new version relates the albedo to the size of the snow grains. Therefore, a so called effective snow grain size has been implemented as a prognostic variable. As the scattering of the incident radiation on the snow grains depends on their size and shape, this parameterization induces a higher degree of physical realism. Further, a correction for cloud optical thickness and solar zenith angle have been added to the retrieved base values. Model validation at the Neumayer station showed that the old formulation overestimated the shortwave radiation considerably which is not the case in the new version (Kuipers Munneke et al., 2011). This has, in the first instance, strong impacts on the surface temperature but also on the atmospheric stability and the wind field over the continent. If the surface temperature is lower in the new formulation, the atmospheric stability increases. This might, in turn, lead to a stronger gravitational forcing of the surface wind field (cf. chapter 2.2). However, slightly enhanced wind speeds would, then, increase the production of turbulence in form of an increased downward sensible heat flux which results in a decrease of the stability. Accordingly, the adjustment of the surface albedo triggers a negative feedback mechanism on the atmospheric stability and effects on the wind speed are

expected to be minor. The largest changes due to this progress probably occur in coastal regions where the strongest variations in snow pack take place.

The newly incorporated snowdrift routine by Lenaerts et al. (2011) includes transport and sublimation processes due to drifting snow and are important parameters when estimating the SMB of the ice sheet. Especially, sublimation influences the atmospheric surface layer, in particular, in coastal regions. Major changes occur in the humidity profile and in the latent heat flux. Furthermore, also the surface temperature slightly increases locally and weakens the atmospheric stability when snowdrift is included in the simulation. However, the effects on the wind speed in turn seem to be minor (Lenaerts and van den Broeke, 2011).

In order to check the assumption that the model simulates all investigated processes to a satisfactory degree and performs reasonably one can compare the results to observations. Reijmer et al. (2005) concluded from a comparison with several automatic weather stations (AWS) and balloon soundings that the model performs reasonable in terms of wind speed when the new formulation of the roughness length is applied, and shows major improvements compared to reanalysis data. The simulated near-surface wind field, that I investigate here, was evaluated by Lenaerts et al. (2011) using 115 stations in mainly coastal and a few continental locations. After omitting several stations in the Transantarctic Mountains, at Cape Dension, and close to Law Dome that showed strong deviations due to a complex topography, a good agreement with the modeled wind speed was found (Lenaerts et al., 2011). It was further deduced that the model underestimates very high wind speeds. Recent investigations showed that this can, to a large extent, be explained by effects induced by the horizontal resolution of the topography and locally underestimated slopes (personal communication J. Lenaerts). A direct comparison of modeled and observed wind speeds, however, is rather incompatible as wind has a strong local influence and might show large variations over short spatial and temporal scales.

The boundary layer momentum budget has successfully been derived and explained with the current version of RACMO over Greenland with a horizontal resolution of 11 km by van Angelen et al. (2011a). This indicates that it is an adequate tool to analyze the boundary layer over Antarctica as well. Further, van Angelen et al. (2011b) related variations in the momentum budget to the Fram Strait sea ice export and showed that RACMO is applicable to study the atmospheric forcing of sea ice transport mechanisms in detail. This, again, provides confidence to use RACMO output data in this study.

For this thesis I made use of the three dimensional modeled fields of temperature, pressure and wind, primarily, and further processed them as I will describe in chapter 4. In several cases also other variables such as radiation or turbulent fluxes have been considered. All these output data are stored by the model in a ASIMOF-GRIB format (van Meijgaard et al., 2008). This special format originates from the HIRLAM consortium. Several FORTRAN 90 routines are available to convert the data into a text format or to read and write variables from and into these files for further processing. The variables are stored for each timestep according to ECMWF convention with a unique identity number, the type of the vertical grid, and the vertical level number.

Finally, it should be mentioned that even though the ERA-Interim sea ice concentration fields, that are given in the simulation as a boundary condition, are available, I do not utilize them in this study. The reasons for this will be discussed in the following section.

3.2 Sea Ice Concentrations from Passive Microwave Satellite Data

Sea ice concentration is not directly measured from space by remote sensing. Instead, the most common technique is to retrieve the emitted electromagnetic radiation from the earth's surface at a microwave wavelength, ranging from about 1 mm to several meters, through polar orbiting satellites. This approach benefits from the dielectric properties of the sea ice. Because of the crystal structure of the ice, it emits at a different wavelength than the unfrozen ocean which makes them differential (Comiso, 2009; Wolfe et al., 2011). The final composite of these multichannel passive-microwave sensors is referred to as radiometric brightness temperature (Cavalieri et al., 1999; Comiso, 2009). The advantage over other techniques is

that clouds or the availability of sunlight do not play a large role and data can be retrieved year-round. In contrast, the amount of energy emitted at such long wavelength is rather low which means that photons have to be collected over a large area and uncertainties are larger (Comiso, 2009; Wolfe et al., 2011).

The dielectrical properties of fresh and ocean water are rather well known and spatially very homogeneous (Comiso, 2009). Sea ice characteristics in the uppermost layer that is sensed by the satellite, however, are affected by the different crystal structures of either pure ice or snow covered ice and by the inclusion of brine and air pockets in the ice (Comiso, 2009; Comiso and Nishio, 2008). This makes sea ice a very inhomogeneous surface in space and time. An area that is dominated by a seasonal ice cover for instance has very different properties than one that is mainly covered by multi-year ice. Accordingly, there are even inter-hemispheric differences that need to be considered when analyzing the satellite data (Comiso and Nishio, 2008).

Further, the measured brightness temperature is also influenced by other factors such as a blurry contrast between land, ocean and sea ice due to the coarse resolution which is referred to as land-to-ocean spillover (Cavalieri et al., 1999). It might be that accidentally the, mostly ice covered, land influences the sea ice signal and leads to errors along the coasts. Also weather effects as cloud water, water vapor, wind speed and atmospheric temperature have a considerable influence on the brightness temperature and need to be taken into account (Cavalieri et al., 1999).

Finally, all these issues are considered in computer algorithms to retrieve sea ice concentration (the fraction of the image that is covered by sea ice) from the brightness temperature (Comiso, 2009; Comiso and Nishio, 2008). Currently, there are many different algorithms available that process the brightness temperature to sea ice concentration. Among the most widely used are the datasets obtained from the NASA Team algorithm and the Bootstrap algorithm that were both programmed at the NASA Goddard Space Flight Center (GSFC; Comiso, 2009). There are major differences between the algorithms, especially in the way that thin ice areas and coastal regions are treated and they all have their advantages and disadvantages that are not further discussed here (Parkinson and Comiso, 2008; Screen, 2011).

Nevertheless, there are other methods to retrieve sea ice cover from space, even though they include major drawbacks. One drawback is to measure the electromagnetic radiation emitted in the infrared wavelength passively. The cold surface of the sea ice covered ocean can be well distinguished from the warmer ocean surface. This method, though, is restrained by the cloud cover which also emits at these wavelength and the melting conditions in spring and summer when the melt water on top of the ice has about the same temperature as the ocean (Comiso, 2009; Wolfe et al., 2011). Moreover, it is possible to study sea ice in the visible wavelength where, again, the strong contrast between the weakly reflecting ocean surface and the sea ice with a high albedo is the essential property. Alongside with the same disadvantages as for the infrared wavelength, this approach is also limited to the time of the day and the year when sunlight is available which makes it rather impractical to use in polar regions (Comiso, 2009; Wolfe et al., 2011). Thus, all these additional methods are not useful to construct a long-term time series of sea ice but are essential for validation, short-term, or smaller scale studies and are complementary to passive systems.

An approach that increasingly gained attention in recent years is the active remote sensing method to retrieve, for instance, sea ice thickness. So called synthetic aperture radars (SAR) enable someone to distinguish thick and thin ice. The most recent satellite system, CryoSat-2, is used to retrieve ice thickness by calculating the freeboard (ice and snow above the sea level) with dual frequency Doppler radar altimetry (Comiso, 2009). Further, laser altimeters such as ICESat are used to detect the freeboard by measuring the return signal of the laser pulse (Comiso, 2009; Wolfe et al., 2011). As I mentioned earlier sea ice thickness is not included in this project, because existing data records are insufficient in terms of temporal coverage and reliability.

As I indicated in the previous section (3.1) the ERA-Interim data for sea ice, as it is incorporated in RACMO, seems not suitable for this project. This is because of two major reasons; one being issues introduced by the comparably low resolution of the original ERA-Interim data and the other being the restricted domain covered by RACMO (cf. figure 3.1).

Figure 3.5 compares the ERA-Interim data on the model grid (in red) to two other estimates of monthly total Antarctic sea ice area anomalies (cf. box 5.1). One of them (in blue) shows the climatology that was derived from passive microwave satellite data by Stroeve and Meier (1999, updated 2011) at the NASA GSFC and is provided by the National Snow and Ice Data Center (NSIDC). It is based on brightness temperature measured by the Special Sensor Microwave/Imager (SSM/I). In this case I take this dataset as a reference climatology and it will be further needed in chapter 5.1. Moreover, the sea ice covered area calculated from the same underlying satellite data, but interpolated onto the RACMO grid, can be seen in the figure in green. A description of this dataset, its retrieval, and the instrument will follow subsequently. All anomalies are defined with respect to the average annual cycle of the period 1989 to 2007 of the SSM/I dataset on the RACMO grid. The ERA-Interim data has been adjusted with the average annual cycle of the difference between ERA-Interim and the SSM/I data.

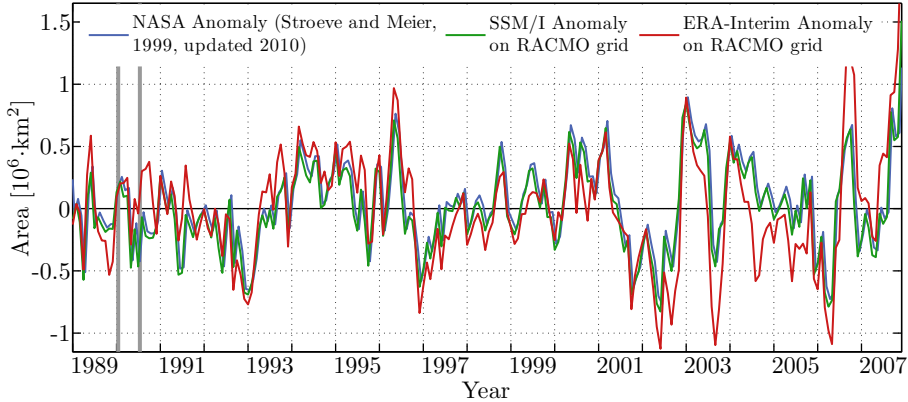


Figure 3.5: Comparison of three different databases of monthly total Antarctic sea ice area anomalies (with respect to the period 1989 to 2007 of the SSM/I data on the RACMO grid). The two gray bars indicate values in January and July 1990 respectively and are displayed spatially in figure 3.6. The ERA-Interim data is corrected by the average annual cycle of the offset to the SSM/I data on the RACMO grid.

Even though the ERA-Interim data shows similar long-term variations, there are rather larger discrepancies to the reference climatology. On average they deviate by $0.51 \cdot 10^6 \text{ km}^2$, whereas ERA-Interim gives the overall much higher values. This cannot be depicted in figure 3.5 as it has been corrected. After the correction the average absolute difference with about $0.21 \cdot 10^6 \text{ km}^2$ is still rather high. However, now the ERA-Interim anomaly is overall lower (as shown in the figure). It should be noted that anomalies in some years can even be of opposite sign, which is a critical aspect in terms of this thesis. Differences between the reference climatology and the SSM/I data on the RACMO grid are minor (average absolute difference: $0.04 \cdot 10^6 \text{ km}^2$). As methods to retrieve the sea ice area anomalies were identical, these differences probably originate from a slightly different horizontal resolution, from the grid interpolation, as well as from a different definition of the coastline in RACMO and the original satellite data. The offsets between ERA-Interim and the satellite data are also observed when considering the total sea ice extent anomalies (not shown) which indicate that differences occur not only in the open water area within the ice pack but also at the ice edge.

This gives rise to a further analysis of the spatial disagreements. Therefore, figure 3.6 illustrates the differences between the ERA-Interim and the satellite sea ice concentration for two months that are indicated by gray bars in figure 3.5 (January (a) and July (b) 1990). In January 1990 the total sea ice area anomaly in ERA-Interim is higher ($0.32 \cdot 10^6 \text{ km}^2$) than the one retrieved from the SSM/I data. In figure 3.6(a) it can be observed that there are also large spatial differences that occur mainly at the retreating sea ice edge and in coastal areas. The concentration in ERA-Interim is mainly underestimated along the East Antarctic coast and in some parts of the remaining central pack. An overestimation can be found along the ice edge of the Bellingshausen Sea, the Weddell Sea, and off the coast of Queen Maud Land. In the wintertime example of July 1990 the total sea ice area anomaly was much higher in ERA-

Interim ($1.18 \cdot 10^6 \text{ km}^2$). Figure 3.6(b) exemplifies that this is mainly explained by an overestimation of the concentration in the main sea ice pack by about 0.1. Additionally, the ice edge of the Bellingshausen and the Weddell Seas are not well represented. There are disagreements in the sea ice cover in several coastal regions. These differences for summer and winter show similar but less extreme patterns in the long-term climatologies (not displayed). Noticeable is that differences due to a deviating coastline and domain are already accounted for and cannot be the reasons for the deviations shown in figure 3.6(b).

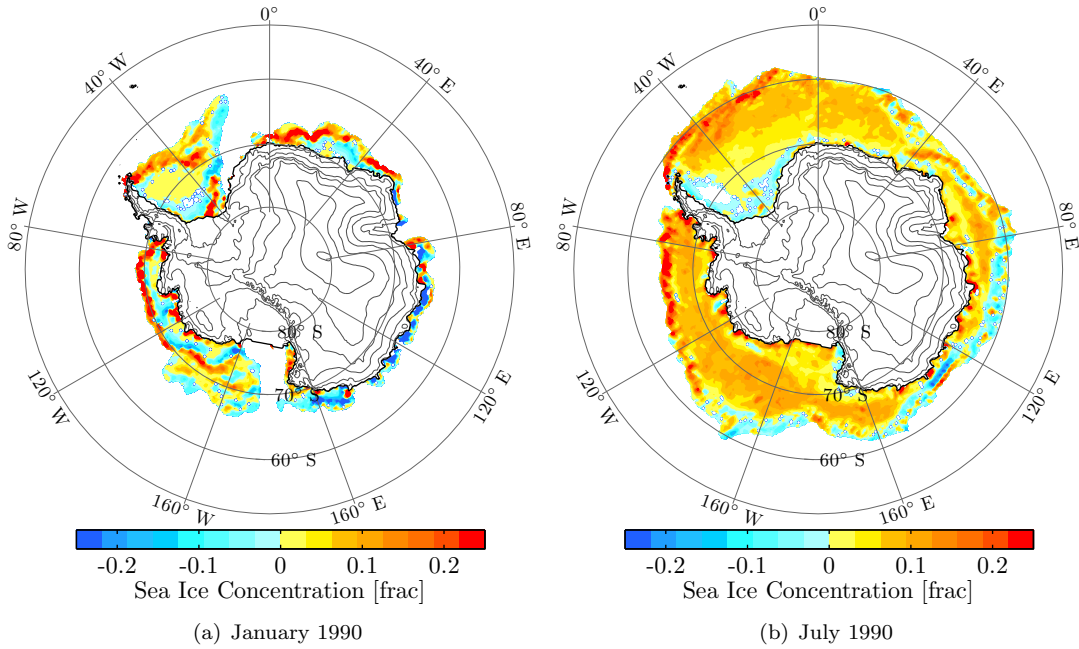


Figure 3.6: Differences between the sea ice concentration in ERA-Interim and in the SSM/I data (ERA-Interim - SSM/I) on the RACMO grid for January (a) and July (b) 1990.

The differences are in a way remarkable as the sea ice that is present in ERA-Interim and RACMO is based on the National Centers for Environmental Prediction (NCEP) data (Dee et al., 2011) which, in turn, uses satellite data from the SSM/I until April 2009 and from the Advanced Microwave Scanning Radiometer - Earth Observing System (AMSR-E) from May 2009 onwards (cf. NCEP MMAB Sea Ice Analysis, <http://polar.ncep.noaa.gov/seacie/Analyses.html>). In other words the data origin of the two databases is the same. This suggests that the occurring differences are related to the data processing method. The difference of the concentration in the central ice pack is probably related to the fact that the SSM/I sea ice concentration used here has been derived with a revised NASA Team algorithm (1996, Cavalieri et al., updated 2008), whereas the NCEP data, and also the ERA-Interim data, is probably based on the even later NASA Team 2 algorithm (cf. NCEP MMAB Sea Ice Analysis Page) that generally gives a slightly higher concentration (Screen, 2011). Moreover, the original satellite data is available on a horizontal resolution of about 25 km and was, hence, decreased to a coarser resolution of about 1.5° in the ERA-Interim fields. Hereafter, it was interpolated on to the RACMO grid with a finer resolution. Presumably, these different steps led to a strong bias in the fields. Nevertheless, in order to track the different errors induced by each processing step, further investigation would be necessary. It is likely that variations between open water and sea ice covered ocean in coastal and sea ice edge regions are not well represented anymore in the ERA-Interim data.

The second issue that has not been addressed yet and leads to a discrepancy between the ERA-Interim data in RACMO and the satellite data is the fact that the RACMO domain does not cover the full wintertime sea ice extent over the Southern Ocean (cf. figures 3.7(a) and (b)). This is the case for the

north-eastern part of the Weddell Sea. Consequently, offsets in sea ice extent and sea ice area in the wintertime are larger.

To conclude, ERA-Interim in RACMO does not provide the desired resolution to resolve smaller scale variations in coastal regions that should be captured by the database to analyze the atmosphere-sea ice interaction. Presumably, this also causes the large difference in the long-term variabilities of sea ice area and extent. Additionally, the cutoff of parts of the sea ice covered ocean enhances the disagreement in winter. Here, the main purpose is to investigate how the atmospheric changes affect the sea ice variations and not the other way around, therefore sea ice should be as realistic as possible. Consequently, I used the SSM/I and AMSR-E satellite data in this project as I will describe below.

This implies for the analysis that the variabilities observed in the atmospheric fields and in the sea ice cover are completely independent in terms of the underlying dataset. Even though one might argue that also the simulation will not be accurate if the implemented forcing of the sea ice on the atmosphere is actually deviating considerably from the conditions that I am using for comparison, this can also implicate a meaningful advantage. If physical relations between the two datasets were found and variations coincided, then one could conclude that the model's atmospheric variability represents reality to a satisfactory degree and could analyze the physical interaction between sea ice and atmosphere in detail.

Over the total time period of the 20 years (1989 to 2009) that were simulated, there is no record of sea ice retrieved by only one single instrument. Hence, it is necessary to consider several databases that should be as coherent as possible. As I mentioned already, the NCEP database and, consequently, ERA-Interim are mostly built on data from SSM/I and in recent years on AMSR-E. Both are available on a preferred spatial (25 km) and temporal (daily) resolution and accessible electronically at the NSIDC sea ice databases (http://nsidc.org/data/seaice/data_summaries.html) and have been derived with the NASA Team algorithm (Cavalieri et al., updated 2008,u).

The SSM/I average July sea ice concentration (1989-2006) that I will use in this project is shown in figure 3.7(b). It is noticeable that the overall sea ice concentration in the central pack is lower than the one of the ERA-Interim data which has been mentioned before and is quite likely related to the algorithm that was applied. During the considered period the SSM/I instrument was launched on series of Defense Meteorological Satellite Program (DMSP) satellites (F8, F11, F13; Cavalieri et al., updated 2008). The database of Cavalieri et al. (updated 2008) is even longer and starts in 1978 with the scanning multichannel microwave radiometer (SMMR) on the Nimbus 7 satellite, merges into the SSM/I data in 1987 and is currently available until 2007.

There would be a complementary dataset of the Special Sensor Microwave Imager/Sounder (SSMI/S) since 2007. On the other hand, the AMSR-E instrument on the NASA Earth Observing System (EOS) Aqua satellite should provide a higher accuracy thanks to a wider spectral range and swath width, and to a higher horizontal resolution (Comiso and Nishio, 2008; Screen, 2011). The average July sea ice concentration (2003-2010) retrieved by the AMSR-E instrument and evaluated with the NASA Team 2 algorithm is illustrated in figure 3.7(c) (2004, Cavalieri et al., updated daily). However, recently Screen (2011) and Parkinson and Comiso (2008) discussed major discrepancies between the recording instruments and also between the algorithms applied in detail. Obviously, the central ice pack has much less open water than the one of the SSM/I data. Screen's figure 4 (2011) illustrates the differences between the high sea ice concentration areas of the different sensors and algorithm. He pointed out that the convergence of the two different records by SSM/I and AMSR-E led to an artificial trend enhancement in the climatologies, namely the Hadley Centre Ice and Sea Surface Temperature (HadISST) and NCEP products.

Interestingly, these discontinuities in the NCEP data seem to propagate also into the ERA-Interim sea ice concentration. The figures 3.7(d) and (e) compare the sea ice concentration for the month July in 2009. This is the first winter in which the sea ice concentration retrieved with AMSR-E is present in the NCEP data and, accordingly, in the ERA-Interim data. Evidently, the central ice pack is characterized by a higher concentration than in the period 1989-2006 (cf. figure 3.7(a)) which is probably caused by a change in the sensor and not by one in the climate system. How this affects the simulation is, however, not

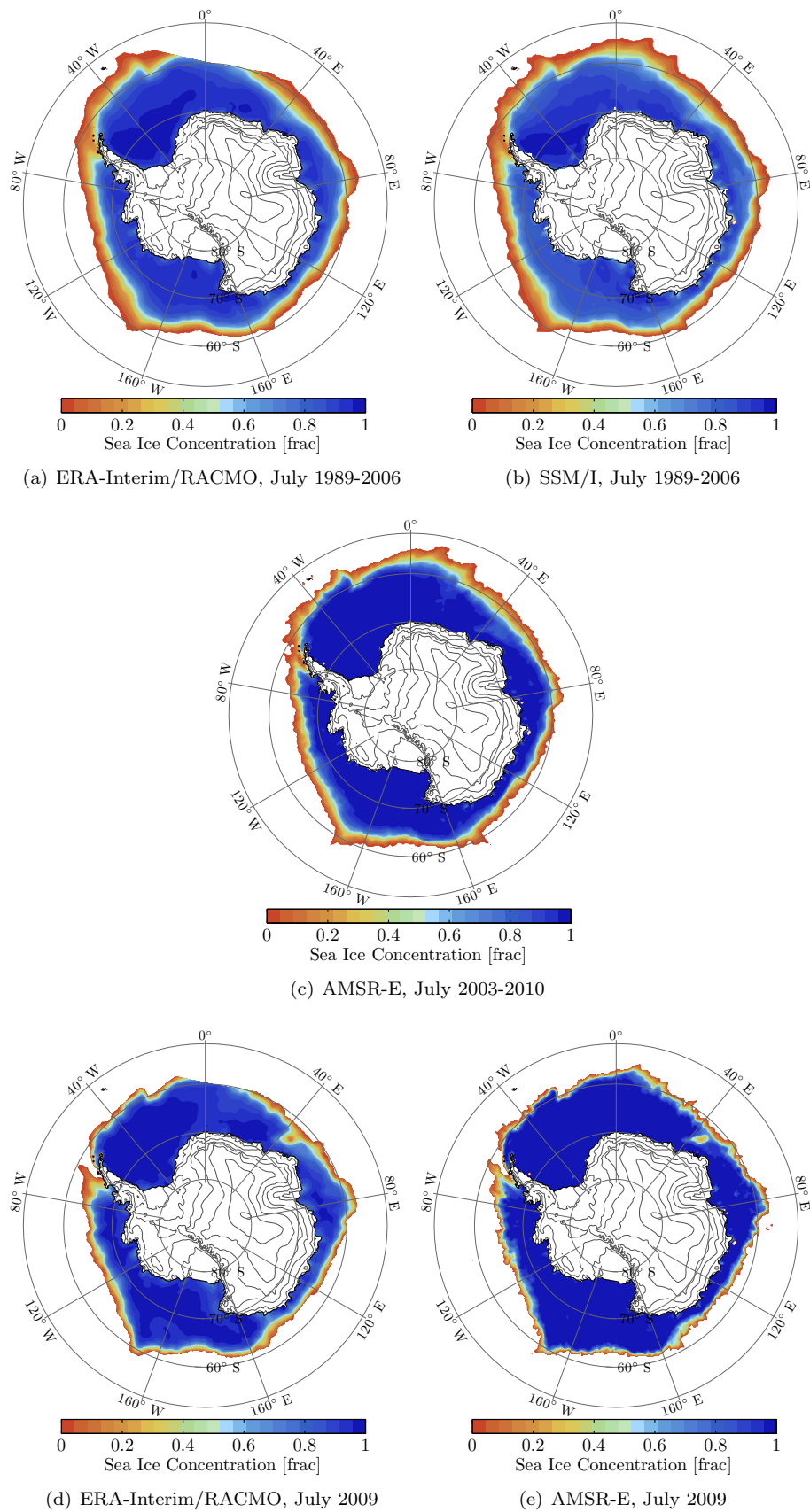


Figure 3.7: Comparison of different July sea ice concentrations between ERA-Interim on the RACMO grid, SSM/I and AMSR-E over different periods.

subject to analysis in this thesis. Finally, this argument supports the recommendation to preferably use a satellite dataset directly in order to perform simulations with RACMO in the future. It also underlines the decision to rely on the datasets that I described before in this project in order to avoid resolution issues and inconsistencies between different data origins.

3.3 Sea Ice Drift Data from Satellites

At last, sea ice motion serves as essential information for investigating the impact of the dynamics on the variability. It can be estimated from different types of sensors as long as the satellite passes over the regarded area within a time frame of about one day and resolves surface characteristics accurately enough to detect single features in the measured wavelength. These features can than be tracked and their spatial displacement from one passage to the other results in the motion vector (Fowler, updated 2008; Maslanik et al., 1997).

Here, I rely on a database of daily Polar Pathfinder sea ice motion vectors constructed by Fowler (2003, updated 2008) with a horizontal resolution of 25 km over a period from 1989 to 2006. An example vector field of the average July sea ice motion (1989-2006) is given in figure 3.8, where for illustration purposes only every fifth vector is plotted. These fields resulted from a combination of Advanced Very High Resolution Radiometer (AVHRR) and SSM/I data. They have been computed initially for the Polar Pathfinder project of NOAA/NASA which had the goal to provide different consistent, and satellite derived, long-term time series of cryospheric parameters (Fowler, updated 2008; Maslanik et al., 1997).

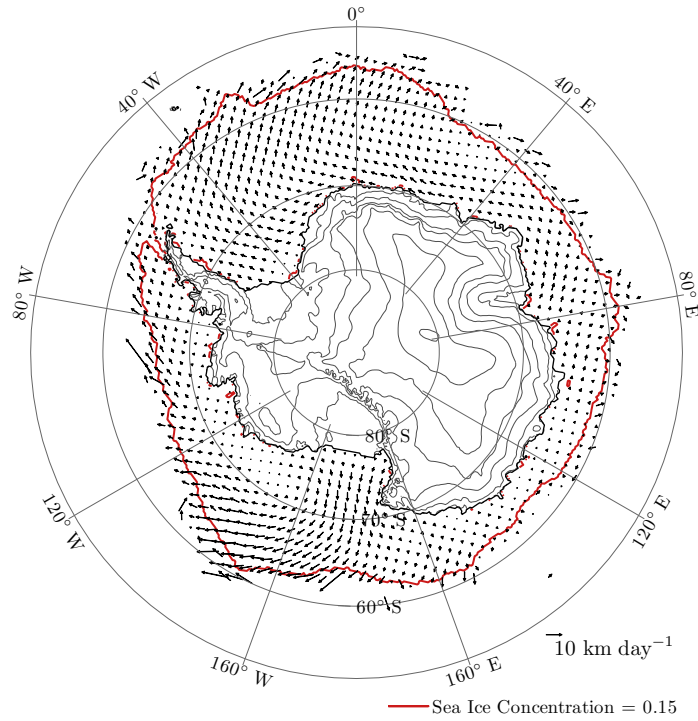


Figure 3.8: Polar Pathfinder sea ice motion for the average month of July in the period between 1989 and 2006 (only every fifth grid point is plotted). Also shown is the 15% sea ice concentration contour that serves as a threshold to exclude unrealistic motion vectors and coincides with the approximate sea ice edge.

From the AVHRR sensor, the visible and infrared bands (channel 2 and 4), available four times daily (every six hours) on a 5 km resolution, have been analyzed (Fowler, updated 2008). Measurements in these wavelengths are accompanied by the problems which I already mentioned in section 3.2. The infrared wavelengths are not useful during the melting season and the visible band is not available during

polar night and overcast conditions. The displacement of ice is evaluated from one day to the other for each pair of the respective hour of the day. This resulted in a maximum number of eight vectors from the two channels and four passages per day, and all the available vectors have been averaged afterwards (Fowler, updated 2008).

According to Fowler (updated 2008) the 37-GHz and 85-GHz channels of the SSM/I brightness temperature have been assessed on a 25 and 12.5 km resolution respectively. As the latter (85-GHz) has the higher accuracy, the vectors retrieved from this frequency have been used if available. However, this high-frequency channel is sometimes strongly influenced by the atmosphere. Compared to the AVHRR these recordings are available year-round. For each frequency images in both, horizontal and vertical, polarizations are included. Similar to the AVHRR data two to four overpasses, depending on the area, are averaged to daily vectors (Fowler, updated 2008).

The advantage when it comes to the retrieval of ice drift vectors is that the exact value of sea ice concentration is not relevant. The only concern is to get a clear feature detection. To achieve this, Fowler (updated 2008) applied several corrections to the images. Hereafter, a complex algorithm that computes the maximum cross correlation between two consecutive images of 10 times 10 pixels according to Emery et al. (1995) is applied to both satellite records (Fowler, updated 2008).

Errors resulting from clouds, for example, have been removed by several filtering techniques that check the coherence between neighboring vectors. The final accuracy according to the grid resolution given by Fowler (updated 2008) is about 1.7 km/day for the AVHRR vectors. He argues that the here described approach is only valid within a closed ice pack and over a relatively short distance away from the ice edge. If conditions are rather unstable in time, meaning that the features in the ice change fast due to a strong deformation or if the ice rotates over short distances, this method does not apply anymore (Emery et al., 1995). This has to be considered as exclusion of the unrealistic values at the ice edge is not performed beforehand. Hence, it is necessary to adjust the dataset with respect to the application.

Together with the motion vectors Fowler (updated 2008) provides error estimates based on comparison to buoy data which, however, was retrieved in the Arctic region. As ice motion around Antarctica has very different characteristics, I decided to use another approach for the exclusion of unrealistic vectors close to the ice edge. In figure 3.8 the 15% sea ice concentration contour line is outlined. I considered vectors located outside this line to be too far away from the ice edge and excluded them from the analysis. This method is based on the definition of the ice edge to derive the sea ice extent by Gloersen et al. (1992) (cf. box 5.1). I here assume that this approximation is valid for long-term variations in sea ice motion. Sea ice motion along the ice edge would be a valuable information to analyze ice dynamics in general but is obviously hard to obtain.

3.4 Data Assimilation and Grid Adaptation

Having a basis of three different datasets with different spatial references and different temporal resolutions, I am left with the task to combine them into one coherent database. At this point it is necessary to make a choice of what spatial grid is most suitable. For this reason figure 3.9 summarizes the different grids and shows their spatial extent together with the maximal possible daily sea ice concentration per grid cell that had more than 1% sea ice concentration (1989–2007) from the SSM/I data. Clearly, this maximum extent exceeds the RACMO grid in the north-eastern Weddell Sea and coincides with the edge of the grid in the Indian Ocean. Further, satellite data of the SSM/I and the AMSR-E data are both on a planar polar stereographic grid with a projection plane tangent at 70° S which leads to a maximum distortion of 22% at the grid boundary and about 3% at the pole (Cavalieri et al., updated 2008,u). The Polar Pathfinder motion vectors, in contrast, are constructed on a Equal-Area Scalable Earth Grid (EASE-Grid) which is centered at the South Pole (Fowler, updated 2008).

It can be observed in figure 3.9 that in the satellite data grids large portions of the Southern Ocean are not covered with any information on sea ice as well as no information about the atmospheric fields from RACMO which means that these fields use large amounts of memory on the computer that is not

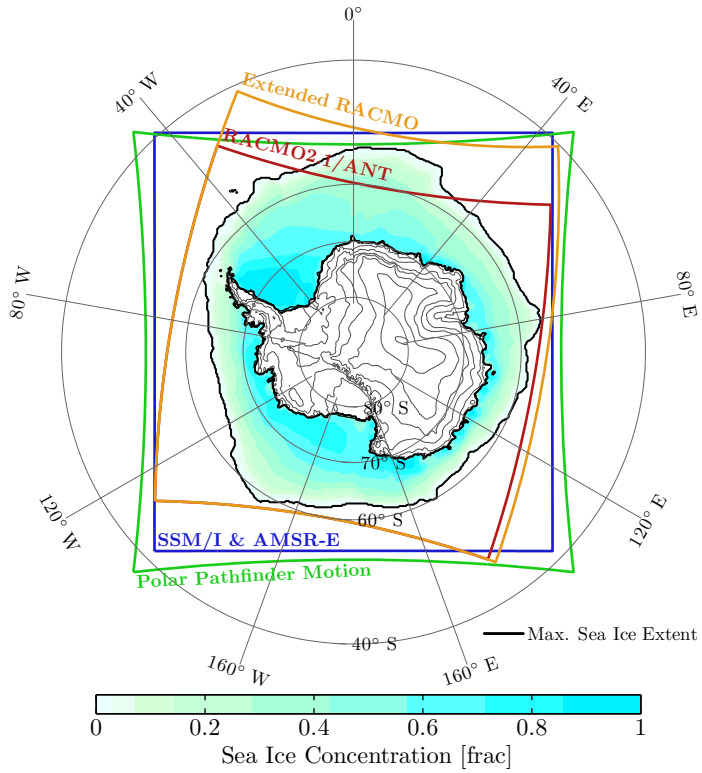


Figure 3.9: The two different original grids from the sea ice satellite data (blue and green) and the grid of the RACMO2.1/ANT atmospheric fields (red) as well as the maximum possible daily sea ice concentration for each grid cell that had more than 1% sea ice concentration in the period 1989-2007. Shown in orange is the new extended RACMO grid on which all data is interpolated.

needed. Further, there are much more fields that are already on the RACMO grid (three dimensional atmospheric fields) than on the other grids. These two arguments would make it computationally more efficient to use the RACMO grid that already exists as a reference grid and interpolate the satellite data onto it. However, by doing so, as described before, I would loose valuable information about the sea ice cover at the addressed boundaries where the RACMO grid does not cover the full sea ice extent. For these reasons I have constructed a new, extended RACMO grid in the same way as I described in section 3.1. The difference between the two grids is an extension by 36 rows on the upper side and 6 columns on the right side as it can be seen in figure 3.9. This ensures that the whole sea ice extent is covered at all times by the grid. An additional advantage of using the RACMO grid in general is to adapt the coastline of the simulation in the satellite data which differs in some regions considerably. Moreover, I do not need to interpolate the atmospheric data onto the extended RACMO grid as their coordinates in the overlapping part coincide and the outer upper and right boundaries are treated as missing data points because no information is available whatsoever.

Subsequently, all daily data values of sea ice concentration from SSM/I and AMSR-E as well as the Polar Pathfinder data have to be projected onto the new extended RACMO grid. No matter what kind of an algorithm is applied, an interpolation of the data would always result in a slight deviation of the values from those on the original grid. However, it is desirable to keep the data as close to the real grid as possible. In order to do so, I applied a zero order nearest neighbor interpolation. I deem this simplistic method valid because the resolutions of all grids have about the same value, between 25 and about 28 km. This means that every new grid point gets most likely assigned with one unique value of the old grid which is very close (within half of a grid cell at most). It further ensures that values do not exceed the range of realistic values which is, for instance, in the case of the sea ice concentration values between zero

and one. A higher order function such as a linear or spline interpolation would be more useful if there were spatial gaps in the data or the resolution of the satellite data was much coarser than the new grid.

The interpolation was performed using a MATLAB® (2009) function for data gridding and surface fitting. In a first step, I converted all geographical to Cartesian coordinates. Hereafter, the function uses a two dimensional Delaunay triangulation algorithm developed by Qhull (<http://www.qhull.org>) (as in Barber et al., 1996) to build triangles between all grid points, so that each grid point is connected with its natural neighbors (MATLAB®, 2009). At last the function finds the point in the old grid which is closest to the new grid point by using the triangular vertexes, and assigns the values of the old grid point to the new one. This procedure follows the suggestions of Watson (1992). It has been applied to the sea ice concentration and the two directional components of the motion vectors.

Figure 3.10 compares the wintertime sea ice concentration of an example day (8th August, 1990) in the Ross and Amundsen Sea before and after the interpolation. The overall structure and the absolute values do not change, only the spatial locations might shift slightly during the change of the reference grid. It can further be observed that the coastline for example along the Ross Ice Shelf was over land (by RACMO definition) in the satellite grid. This artifact has been removed by deleting all data points that were situated over land. The opposite, as it can be observed in the south-eastern Amundsen Sea where there was land in the satellite and ocean in RACMO, is treated as missing data and will be excluded from the analysis. While talking about the exclusion of data, I would also like to stress once again at this point that the unrealistic motion vectors away from the sea ice edge were removed as I described in section 3.3.

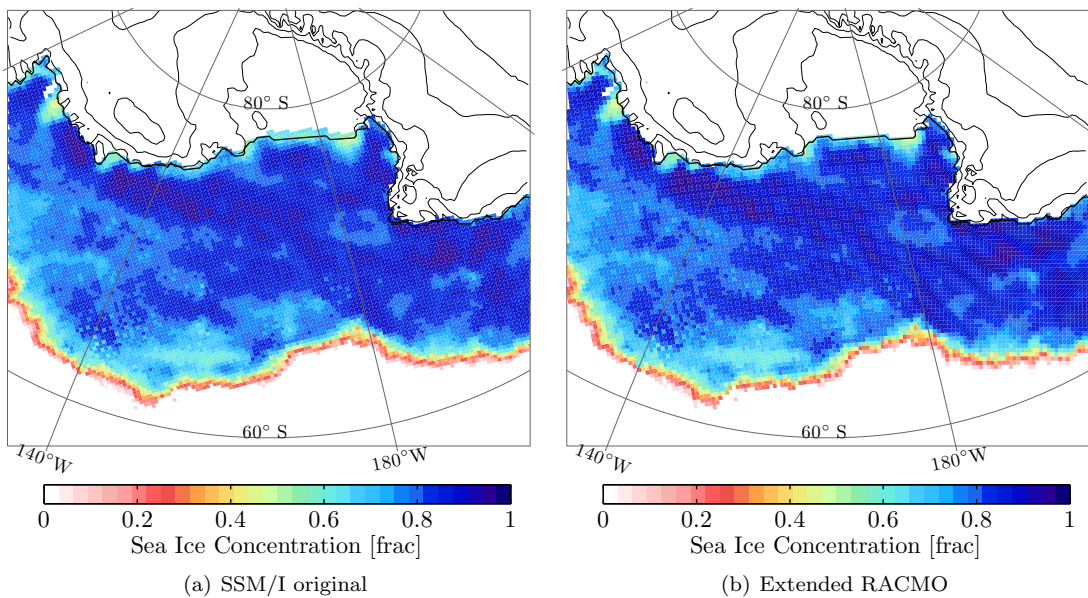


Figure 3.10: Example of the sea ice cover in the Ross and Amundsen Sea on 8th August, 1990: Before the interpolation on the original SSM/I grid (a) and after the interpolation on the extended RACMO grid (b).

The satellite data also had a few temporal gaps. In the SSM/I sea ice concentration these gaps had been removed already beforehand by Cavalieri et al. (updated 2008) using a linear interpolation. The AMSR-E data, on the other hand, had a few gaps as it was provided. In total thirteen days in the period 2003 to 2010 were missing with the longest period of six days in the year 2003. The Polar Pathfinder sea ice drift had seventeen missing days in the period 1989 to 2006 with a maximum of three consecutive days. I filled all these gaps with a linear, first order interpolation by using the first day before and the first day after the data gap.

The three-hourly RACMO output data was, hereafter, averaged to daily values so that all data could be analyzed on a daily timescale. However, for some analysis and long-term variability it is more efficient to consider averages over longer timescales. Consequently, I calculated monthly, seasonal, and yearly averages as well as long-term climatological means for each day, month, and season of the year. If not explicitly defined, the analysis that I perform in the following three chapters is based on the time period 1989 to 2006 in which all three datasets are available. To sum up, the datasets described in this chapter provide the basis for all further post-processing, analysis and interpretation.

4 Simulated Atmospheric Boundary Layer Processes

In chapter 2 I have schematically described the processes that take place in the Antarctic atmospheric boundary layer over the sea ice covered ocean and the coastal continent. I have further discussed the different forcing mechanisms of the boundary layer dynamics in detail. I will now explain the spatial structure and temporal evolution of these processes and also consider their long-term changes that might affect the sea ice. For this purpose, I will use the data from the RACMO simulation.

Moreover, I have related the atmospheric processes to the sea ice growth and decay in chapter 2.3. From these considerations, we can identify two major variables that are useful for studying the impact of the atmosphere on the sea ice. These are the temperature field, or more precisely, the temperature gradient between the ice or ocean surface and the atmosphere above, and the wind field. The near-surface temperature field determines the thermodynamic sea ice formation which is the freezing of the ocean water due to a transfer of heat from the ocean to the colder atmosphere and which takes place at the base of the sea ice. The wind field, principally, is responsible for the dynamical redistribution of sea ice but also influences the thermodynamics through production of turbulence and advection of heat. The temperature distribution, in turn, also influences the wind field due to horizontal anisotropy and, hence, indirectly, also affects the dynamics. In this chapter, I will study both of these variables and describe the origin of their variability. The focus, however, will be on the atmospheric dynamics.

At first, in section 4.1, I will provide explanations of the structure of the dominant terms in the surface energy balance and outline the regional characteristics of the temperature field and the stable boundary layer. This reveals insights into the accumulation of cold air in several regions. Further, I will consider long-term trends of the temperature field and its interannual variability. In the second sub-chapter (4.2), I will generally describe the surface pressure distribution over the sea ice covered ocean and the coastal ice shelves, followed by a description of the resulting surface layer wind field. The long-term changes and variations are also included for each season. In section 4.3, I will then attempt to retrieve the single terms of the forcing of the wind according to the study by van den Broeke et al. (2002) and van den Broeke and van Lipzig (2003a). This should reveal insights into the importance of the different forcing mechanisms of the wind field over the sea ice and the ice shelves. At last, in section 4.4, I will relate the regional accumulation of cold air to the surface layer wind field and point out the importance of the topography for the coastal atmospheric boundary layer structure.

4.1 Cold Air Pooling and Near-Surface Temperature

The surface energy balance and the related vertical and horizontal temperature distribution are important for this thesis for two major reasons: On the one hand, they are driving forces of the boundary layer wind field and, on the other hand, they determine sea ice growth and melt. In this section, I will illustrate the spatial, seasonal, and interannual variations as well as the long-term trends by interpreting maps of the simulated fields.

The controlling factors of the surface energy balance during winter, as I have discussed in chapter 2.1, are the longwave radiative and turbulent heat fluxes. In summer, however the absorption of shortwave radiation depending on the surface albedo plays an important role as well. Long-term monthly averages of the simulated longwave radiative and turbulent heat fluxes, and the total atmospheric surface energy balance (without the ocean heat flux) are illustrated in figures 4.1 to 4.3, respectively. Six different months have been selected to illustrate the fluxes throughout the year. Negative values imply a net heat loss of the surface and positive values imply a net heat gain.

Over most of the Southern Ocean the net longwave radiative flux is slightly negative throughout the year, even though the ocean is relatively warm (cf. figure 4.1). This is owing to a strong downward directed longwave radiative flux induced by the relatively high atmospheric humidity. Towards the edge of the domain the longwave heat loss seems to increase which is probably related to the transition from the boundary conditions. Along the coast in February and March the net longwave emission is high as sea ice is not yet present or only very thin and the air is cold and dry. Throughout the winter the

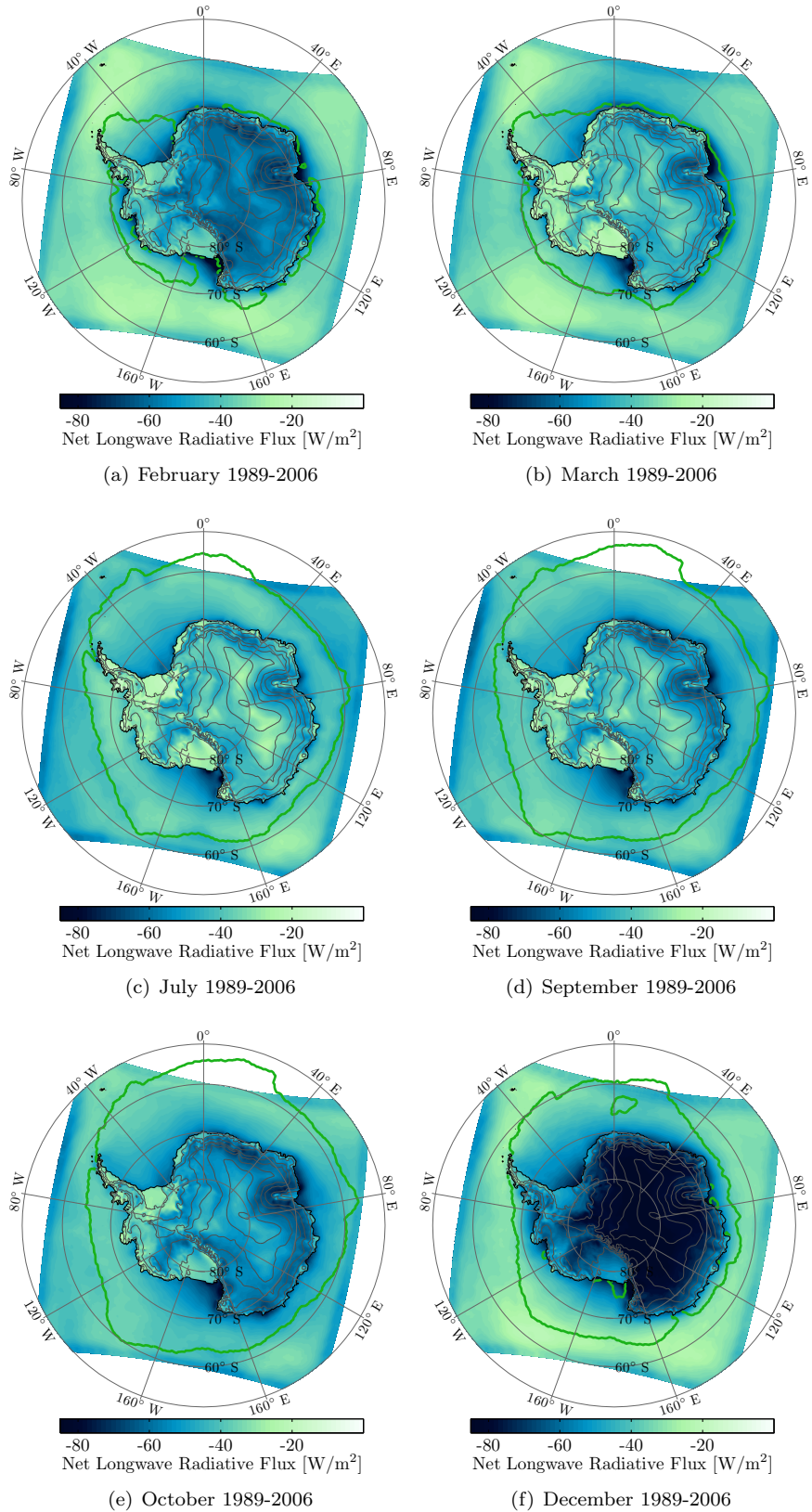


Figure 4.1: Simulated net longwave radiation at the surface. The green contour line denotes the average observed sea ice edge.

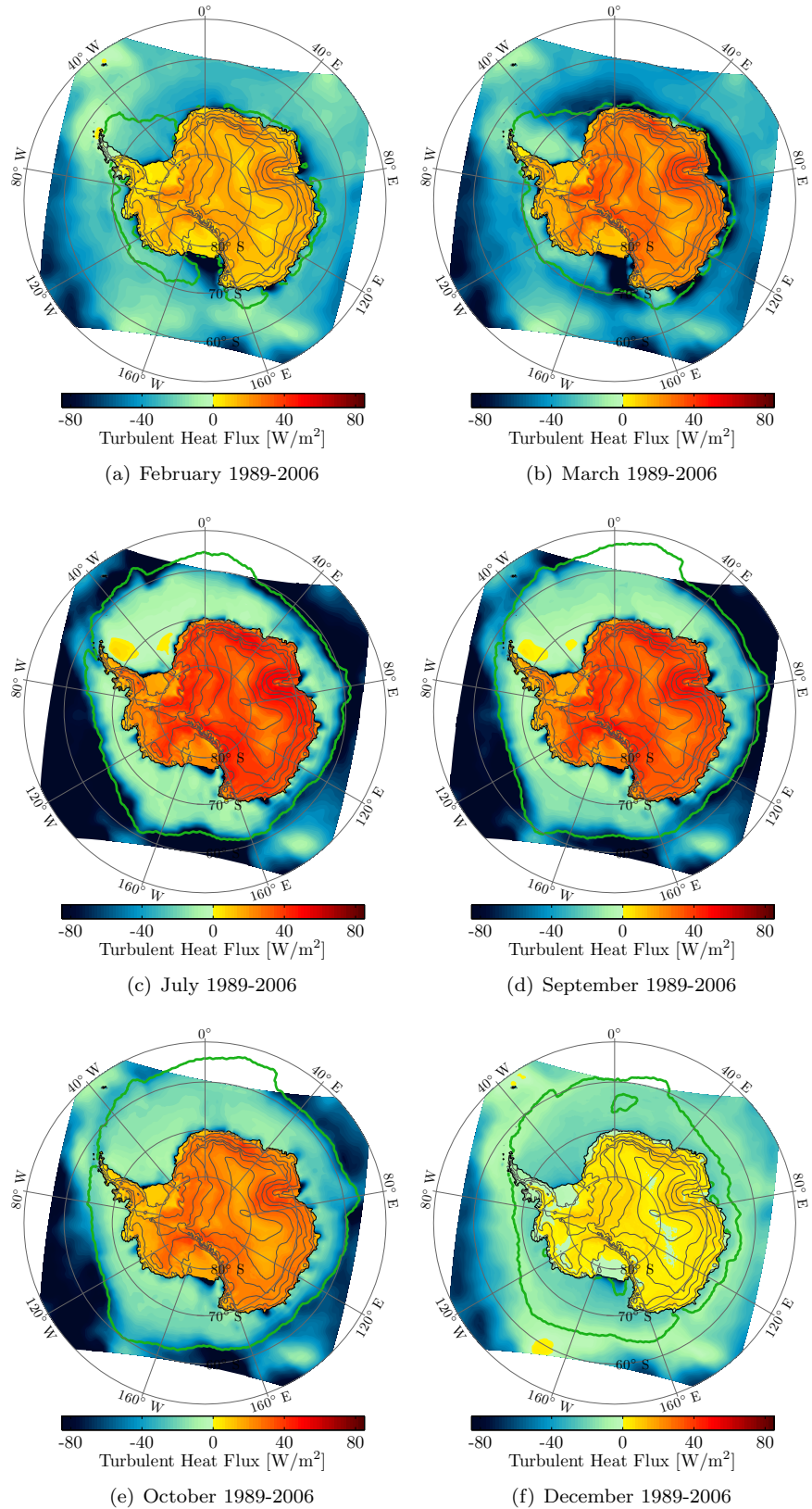


Figure 4.2: Simulated atmospheric turbulent heat fluxes at the surface. The green contour line denotes the average observed sea ice edge.

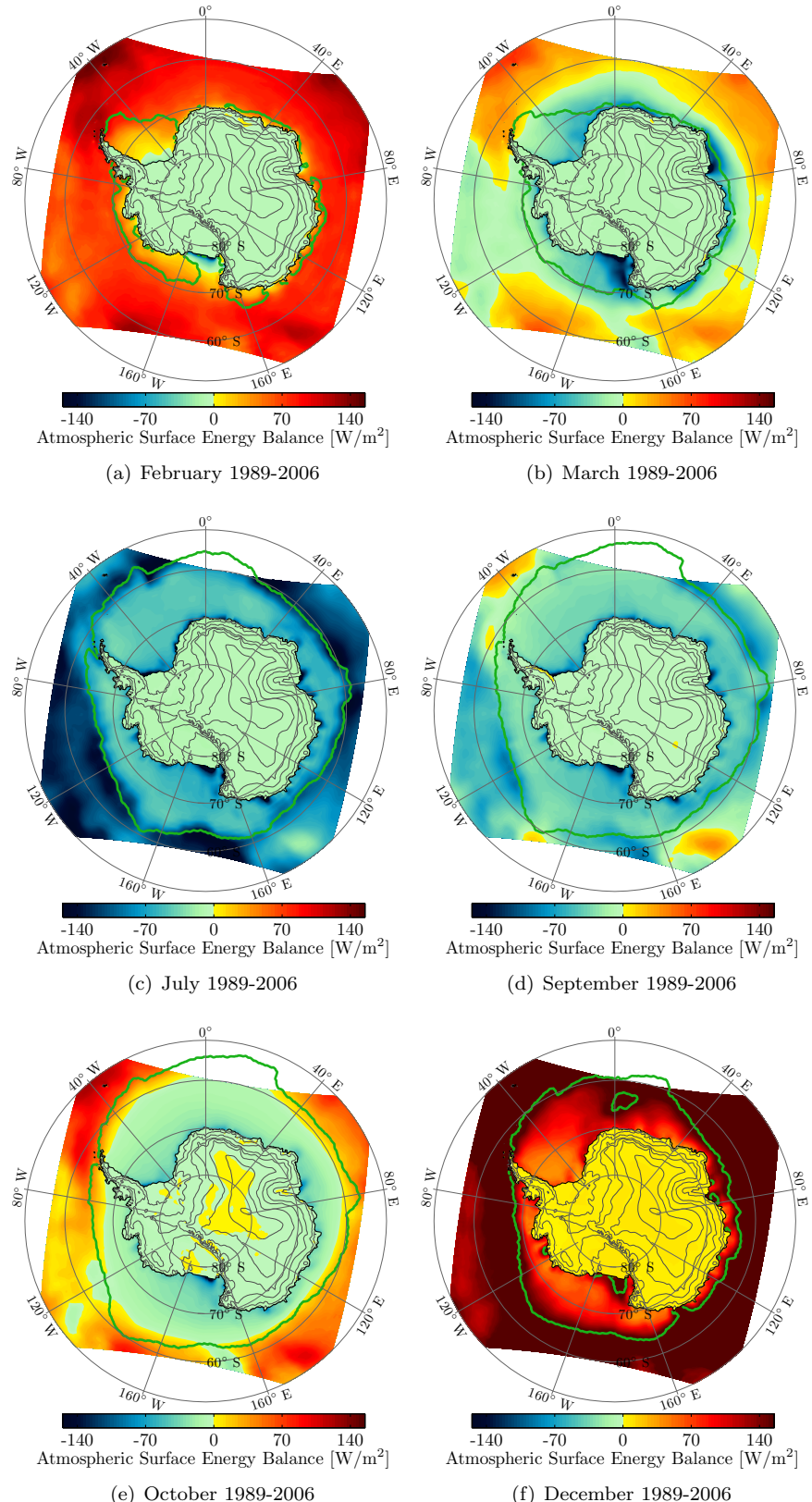


Figure 4.3: Simulated atmospheric surface energy balance over the Southern Ocean. Ocean heat flux is not included in the balance. Negative values imply a cooling of the ocean surface from the atmosphere and positive values a heating from the atmosphere or the solar radiation. The green contour line denotes the average observed sea ice edge.

emission decreases with a thickening ice cover. However, relatively, the overall emission is always stronger in coastal areas where large open water areas are present as I will further illustrate in chapter 5.3. This effect is most pronounced in the Ross Sea.

The strong heat loss of the ocean to the atmosphere in the Ross Sea is even more clearly visible when considering the turbulent heat flux (sum of sensible and latent heat) in figure 4.2. It is very high in March when the atmosphere strongly cools the ocean surface and decreases to almost zero or even becomes positive regionally in July over the thicker sea ice that suppresses the heat conduction. This results in a very sharp gradient between the open ocean where turbulent heat loss is very strong and the sea ice covered ocean in winter. Again, the coastal open water areas are clearly visible in July, September, and October where the ocean is cooled by the atmosphere.

If we now consider the sum of the net longwave radiative and the turbulent heat fluxes together with the net shortwave radiative flux, we obtain the net heat loss or gain of the ocean surface which is mainly balanced by the ocean heat flux and to some extent by the latent heat of freezing and melting (cf. figure 4.3). Apparently, along the edges of the Ross and Ronne-Filchner Ice Shelves the cooling of the ocean surface starts first in February, whereas the rest of the ocean still gains heat from the solar shortwave radiation. In March, the cooling extends northward and becomes stronger. During the polar night, then, the net heat loss is almost solely determined by the sum of net longwave radiative flux and turbulent heat flux. In September, when the sea ice extent reaches its maximum, the surface still experiences a net cooling by the atmosphere. Afterwards (in October) when the sea ice begins to melt, the atmospheric surface energy balance starts to get positive along the ice edge and is positive everywhere by December.

The continent has a much colder surface than ocean or sea ice. Consequently, the outgoing longwave radiative flux is much lower. We can observe this over the ice shelves in figure 4.1. Nevertheless, towards the interior the net longwave radiation gets more negative, especially, over the slopes of the ice sheet as the atmosphere gets colder and drier and the incoming longwave radiative flux drastically decreases. Over the slopes the values are most negative which is owing to the constant supply of turbulent heat to the surface as it can be seen in figure 4.2. The highest values of the turbulent heat flux over the slopes are present in mid-winter when wind speeds are highest and the strongest mixing occurs. I will discuss the wind field in chapters 4.2 and 4.3 in detail. However, at this point it is important to notice that over the slopes cold air is persistently formed by the strong longwave cooling and then transported downslope. As this cooling is mainly balanced by the turbulent heat flux, the net surface energy balance in figure 4.3 is almost zero throughout the year. The gain of heat in summer (December) by solar shortwave radiation over the continent is balanced by a negative longwave radiation and the turbulent heat flux decreases to almost zero.

The energy transfer between the surface and the atmosphere is directly coupled to the temperature: The surface temperature determines the longwave emission at the surface, the atmospheric temperature determines the incoming longwave radiation at the surface, and the near-surface temperature gradient determines the turbulent heat exchange. Consequently, the considerations of the surface energy balance are helpful to analyze the near-surface temperature fields.

Often the long-term variability and changes of sea ice are related to the atmospheric near-surface temperature without considering that temperature is not an independent variable. Higher temperatures above the melting point imply that sea ice melts faster. However, less sea ice at a certain location also means that heat conduction from the ocean is enhanced and if open water is present more shortwave radiation is absorbed at the surface. Hence, temperatures rise even more. Moreover, it should be noticed that a change of the surface temperature does not necessarily imply a change of the sea ice cover. If the temperature is far below the freezing point anyway, a change of the temperature does not alter the area that is covered by the ice. However, the sea ice thickness might change due to an alteration of the vertical temperature gradient and a resulting change of the growth rate at the sea ice base.

Figure 4.4 shows the mean January and July 2 m temperature over Antarctica and the surrounding ocean. Despite the generally expected temperature deviation between winter and summer, we can observe that the spatial distribution of the lower temperatures is very different. In January cold air is restricted

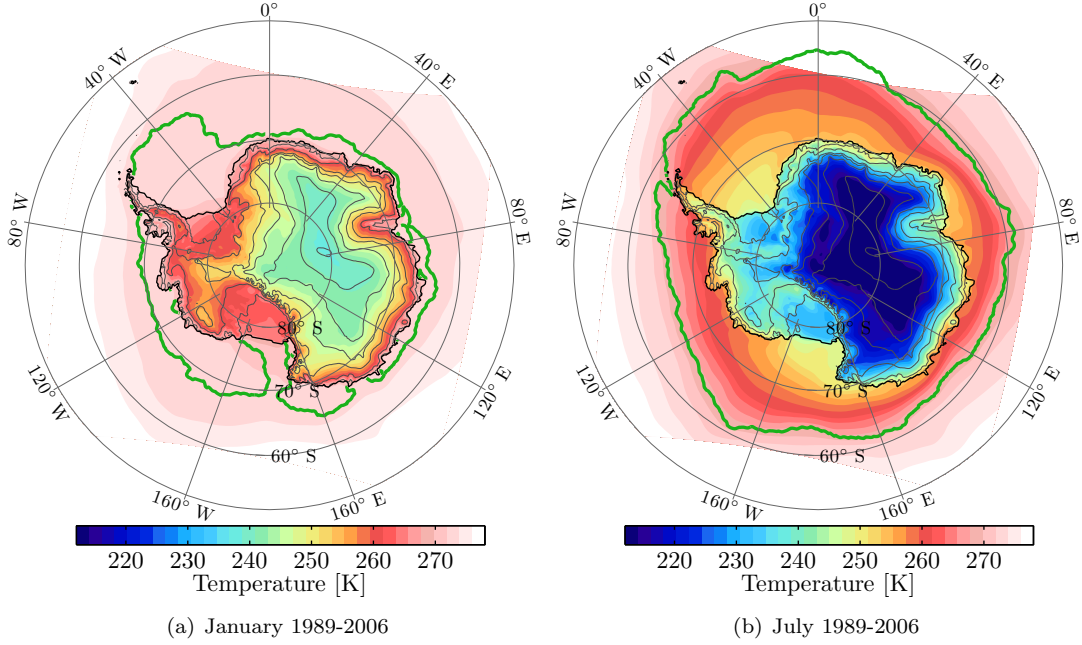


Figure 4.4: Simulated 2 m temperature. The green contour line denotes the average observed sea ice edge.

to the continent with the lowest temperatures of about -35° C over the East Antarctic Plateau and temperatures just below the freezing point over the ice shelves and the coastal regions. Over the ocean and the remainder of the sea ice (sea ice edge in green), temperatures are just above the melting temperature. In winter, however, the isotherms follow the shape of the sea ice edge. Here, the cold air is isolated from the warmer ocean due to the sea ice. As the sea ice thins towards the edge, the atmosphere gets warmer. The keen observer can even notice that the surface in summer is slightly cooler where the sea ice was present in winter. Consequently, the wintertime sea ice affects the summer ocean and atmosphere temperatures which leads to a memory effect of anomalies in the system that will be further described in chapter 5.1. We can also see that in the wintertime cold air is situated over the large Ross and Ronne-Filchner Ice Shelves. The steep slopes are slightly warmer and the East Antarctic Plateau is, by far, the coldest with a minimum temperature of -68.9° C. Here, we find the lowest temperatures on Earth.

In order to adjust for the affect of the decreasing pressure with height on the temperature, figure 4.5 shows the average surface layer (about 8 m above the surface) potential temperature (cf. equation 2.2) for the same months as in figure 4.4. For both months, clearly, the two large ice shelves (Ross and Ronne-Filchner Ice Shelves) stand out in the figures as regions with the potentially coldest air in the whole domain. The cold air that is drained down the slopes of the ice sheet escarpment by the katabatic winds, as I have described in chapter 2.2, accumulates on the flat ice shelves. Here, the gravitational forcing vanishes (cf. section 4.3) and a deep layer of cold and stable air builds up. This process is referred to as cold air pooling and will be of major importance in this thesis. Over the slopes of the ice sheet the potential temperature is slightly higher. Here, warmer air from above is mixed to the surface by turbulent heat as we have observed before. The same is valid for the mountains of the Antarctic Peninsula and the Transantarctic Mountains.

In sum, cold air that is formed over the slopes of the ice sheet by radiative cooling at the surface and persistent downward mixing of upper atmospheric air, drains onto the large flat ice shelves where it accumulates. The cold air extends over the sea ice in winter when the lower atmosphere is isolated from the warmer ocean below.

Next, I will study the spatial patterns of the interannual variations of the spatial patterns of the near-

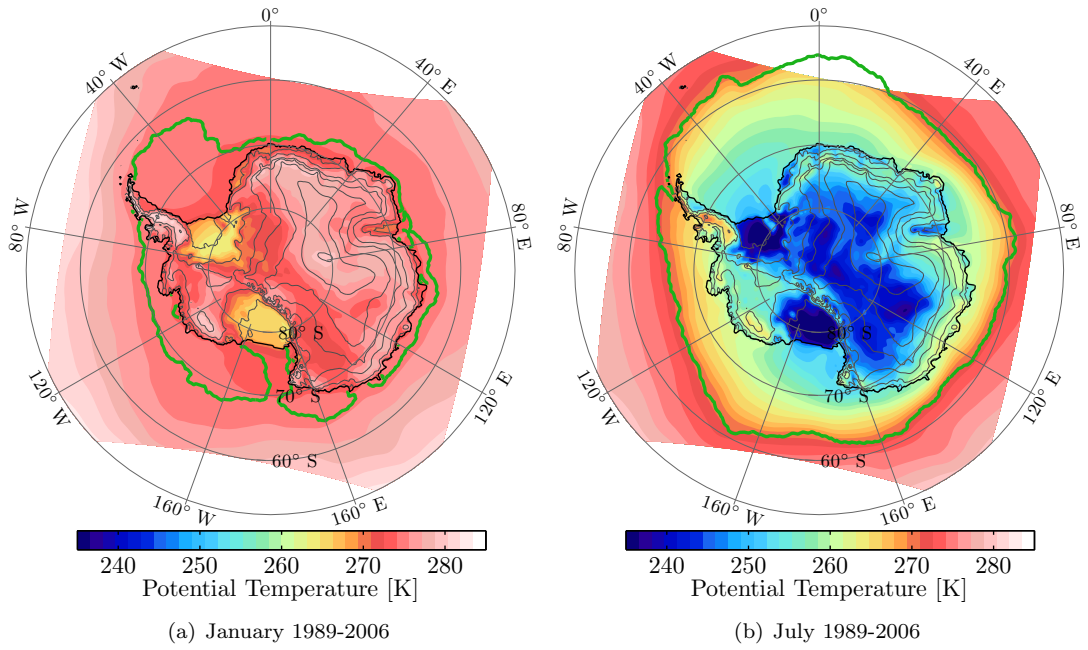


Figure 4.5: Simulated atmospheric surface layer potential temperature. The green contour line denotes the average observed sea ice edge.

surface potential temperature and the long-term trends. I will use the variance of detrended anomalies to identify regions where potential temperature changes most from one year to the other. This concept is explained in box 4.1 and I will apply it throughout this thesis. Furthermore, the retrieval of the long-term trends and their significance is explained in detail in box 4.2. Both parameters might have very different values throughout the year. Consequently, I will consider the overall trends and variance but also the changes for parts of the year. Because the time series from 1989 to 2006 is rather short for assessing long-term trends, I will use seasonal trends rather than monthly values that I have used to describe the mean state.

Box 4.1: Variance of Detrended Anomalies

Important information on changes of a climatological variable from one year to another can be obtained by studying its interannual variance. It is calculated by using the monthly anomalies with respect to the long-term mean of each corresponding month, and subtracting the long-term trend from the anomalies.

The variance of the detrended anomalies needs to be interpreted relatively. This means that a region of comparably low variance of a certain variable is not very vulnerable to changes in the system and values of the variable are rather persistent from one year to the other. In a region where the variance is high, largest changes occur. This concept is also helpful to identify relations between different climatological variables. So that causes of interannual variations of one variable could be found by the spatial distribution of the variance of another variable.

Figure 4.6 shows the variance of the detrended surface layer potential temperature anomalies for the whole time series in panel (a) and the each season in panels (b) to (e). Largest interannual variations of the potential temperature anomalies occur over the two large ice shelves and over the adjacent sea ice covered ocean. This implies that the cold air pooling on the ice shelves might be high in one year and very low in the other year. By considering the single seasons, we can observe that these interannual differences

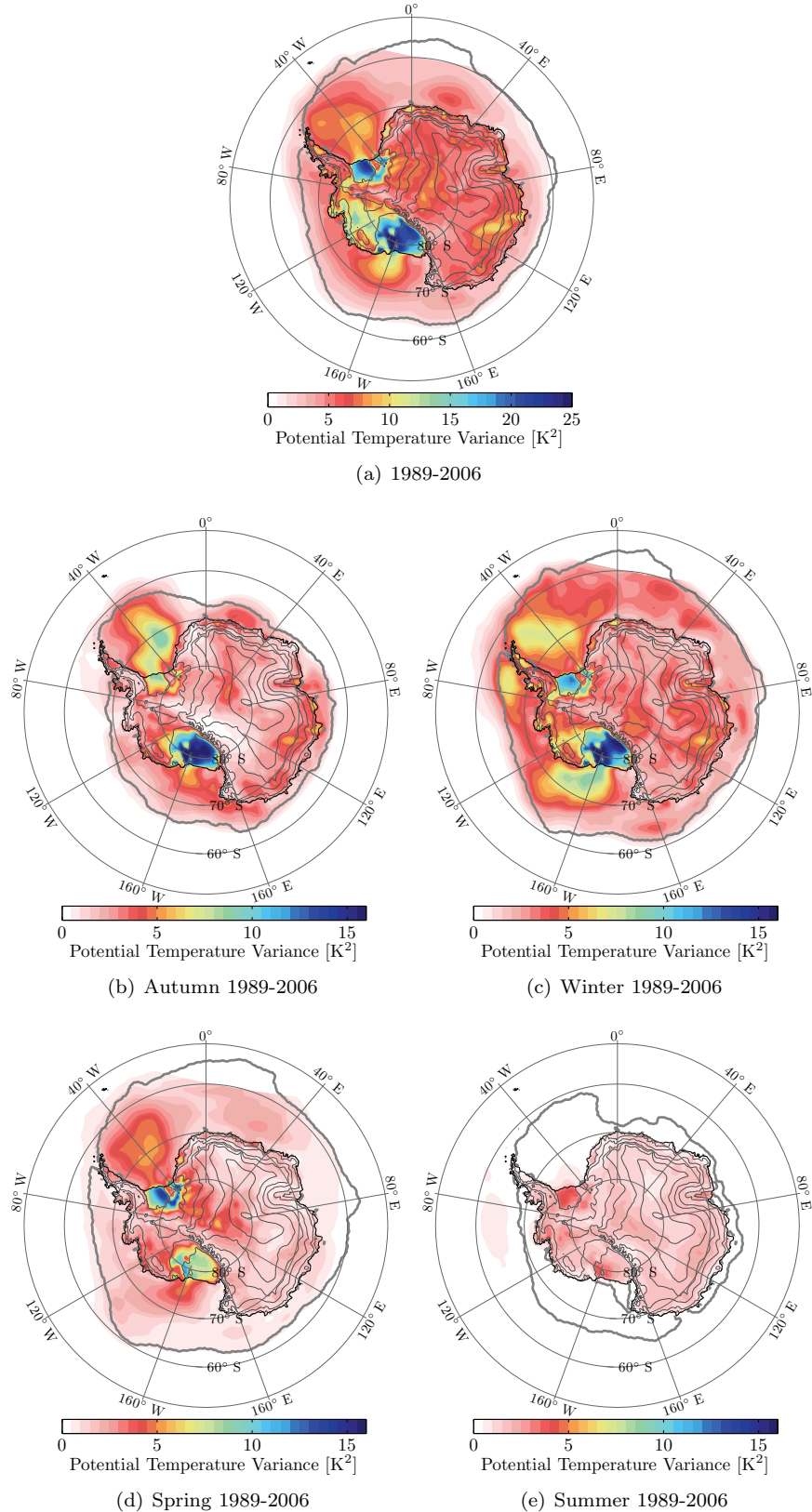


Figure 4.6: Variance of detrended surface layer potential temperature anomalies. The gray contour line denotes the average observed sea ice edge.

over the Ross Ice Shelf are most pronounced in autumn and winter. Over the southern Ross Sea variations are usually highest in winter. In contrast, over the Ronne and Filchner Ice Shelves most variability occurs in winter and spring and over the Weddell Sea in all three seasons. The overall summertime variations are small. If we compare the two regions, we can notice that interannual variations over the Ross Sea and Ice Shelf are generally stronger than those over the Weddell Sea and the adjacent ice shelves.

Box 4.2: Trend, Significance, and Uncertainty

A trend can be estimated using a first order polynomial fit ($\hat{y}(t) = a + bt$) obtained with a least square fitting method (Wilks, 1995). As long as no extreme outliers are present this procedure gives a good estimate (Santer et al., 2000). In order to test whether a trend is statistically significant or not, I use a procedure that is documented by Santer et al. (2000). It assumes that most processes in nature are, statistically, dependent in time which means that they are autocorrelated. First, the ratio of between the estimated trend b and its standard error s_b is computed:

$$t_b = \frac{b}{s_b}. \quad (4.1)$$

Here, the standard error of the slope is given by (Santer et al., 2000):

$$s_b^2 = \frac{\frac{1}{n_e - 2} \cdot \sum_{t=1}^{n_t} (y(t) - \hat{y}(t))^2}{\sum_{t=1}^{n_t} (t - \bar{t})^2}, \quad (4.2)$$

where n_t is the sample size and n_e is the effective sample size, taking into account the lag-1 autocorrelation coefficient r_1 :

$$n_e \approx n_t \cdot \frac{1 - (r_1 \cdot 0.5)}{1 + (r_1 \cdot 0.5)}. \quad (4.3)$$

In this thesis I will use half of the lag-1 autocorrelation to account for the time dependence. The obtained ratio t_b is compared to the critical t -value of the Student's t distribution that is obtained by using the chosen significance level α and $n_e - 2$ degrees of freedom (Santer et al., 2000). If t_b is larger than the critical value a trend is significantly different from zero at the given confidence level. In many cases the interpretation of the significance of a trend depends strongly on the procedure that was applied and mostly only gives an indication rather than an absolute statement. An estimate of the statistical uncertainty of the trend can be given using the 95% confidence interval which is ± 1.96 times the standard error of the slope under the assumption that the trend obeys a Gaussian distribution. It should be noted that this estimate of the uncertainty does not account for uncertainties in the data retrieval.

So now I will proceed with a discussion of the long-term trends of the atmospheric near-surface temperature. The trend patterns that are reported by other studies I have already briefly described in the introduction. Figure 4.7(a) shows the overall trends of the surface layer potential temperature as simulated by RACMO. There are two major regions of significant warming (green and black contours denote the 90% and 99% confidence level respectively): One region extends from the Bellingshausen and Amundsen Seas to the eastern Ross Sea and the other one can be found along the coast from eastern Dronning Maud Land to Enderby Land. In the southern Weddell Sea, adjacent to the ice shelf, we can observe a slight significant cooling trend. These patterns, to some extent, agree with patterns observed in figure 1.1(c) even though the magnitude and location deviates. However, the strong warming around the Antarctic Peninsula is not present in the model. Over the ocean that surrounds the sea ice weak but significant cooling trends are visible in figure 4.7(a). These are confirmed by figure 1.1(c) but, again, not of the same magnitude and location. Further, the trends towards the edges of the domain might be unreliable due the transition from the boundary conditions.

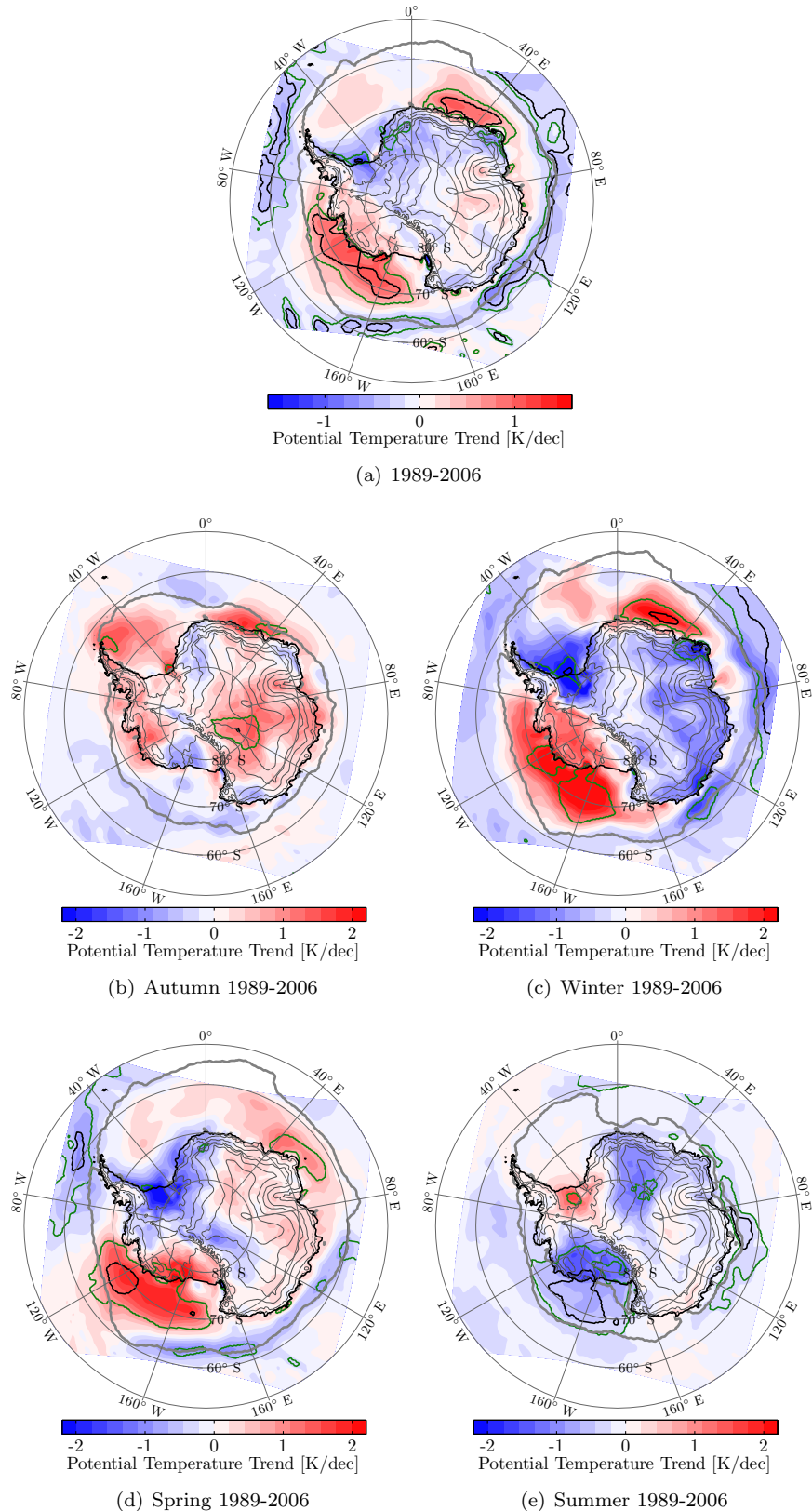


Figure 4.7: Decadal trend of simulated surface layer potential temperature. The gray contour line denotes the average observed sea ice edge and the green and black contour lines indicate the 90% and 99% confidence level, respectively.

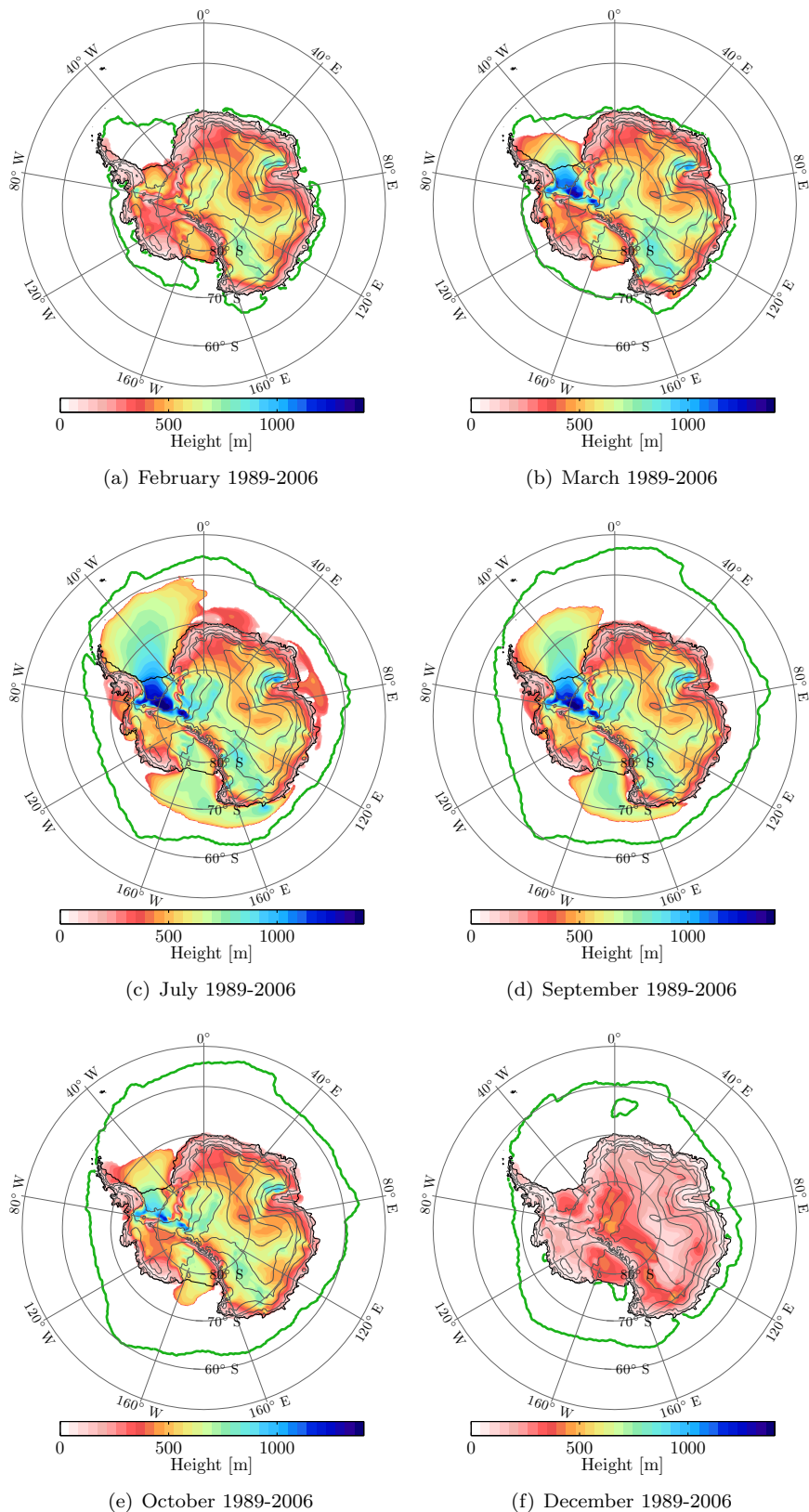


Figure 4.8: Height of the temperature inversion retrieved with an algorithm that detects the lowest temperature maximum in the modeled temperature profile. The green contour line denotes the observed sea ice edge.

In consideration of figures 4.7(b) to (e), we can notice that the trends are seasonally dependent. The warming in the Bellingshausen, Amundsen, and eastern Ross Seas only occurs in winter and spring. In summer, however, we can find in this region a slight but significant negative trend. The trends in the southern Weddell Sea and over the Ronne and Filchner Ice Shelves seem to be opposite to those just described. Whereas a cooling persists in winter and spring, a positive trend is present in summer. Northeast of the Antarctic Peninsula one can observe a significant warming in autumn. The warming along the coast of eastern Dronning Maud Land and Enderby Land apparently results from a warming that is present from autumn through spring and is strongest in winter.

It should be noticed that most of the trends are strongly influenced by extreme events in some years which is reflected by the fact that only a few regions show a significant trend. This is mainly due to the relatively short time period. The causes of these temperature trends might be of different origin. They can be related to changes of the sea ice cover or thickness (albedo effect or heat conduction), to changes of the ocean heat flux, to changes of vertical stability and mixing, or to changes of the large-scale circulation and air advection. I will briefly discuss the latter reason in the following section 4.2. In chapter 5.1, I will explain how the changes of the near-surface temperature field affect the sea ice cover.

Before turning the discussion to the wind field, I deem it necessary not only to consider the surface temperature fields but also to include the depths of the cold stable layer above the surface. I have introduced the concept of the cold stable atmospheric boundary layer that is induced by the longwave cooling of the surface schematically in chapter 2.1. I also discussed several ways to qualitatively and quantitatively capture the cold stable layer. One of the most commonly used methods is to determine the height of the temperature inversion that is indicated in figure 2.2. One should notice that the height of the temperature inversion does not give any information of the strength of the temperature deficit and also deviates from the height of the temperature deficit layer (TDL) which is usually slightly higher. Nonetheless, the temperature inversion height gives valuable information about the depth of the stable layer and its horizontal distribution.

An algorithm to detect the lowest temperature inversion in the model output has been applied. The long-term monthly average height of the temperature inversion for the same months as in figure 4.3 is shown in figure 4.8. During summer (December and February) the stable boundary layer is restricted to the continent as the ocean heats the atmosphere from below and leads to an unstable stratification. The inversion is rather low in coastal or steep regions. An exception are the two large ice shelves where on average a relatively deep stable layer persists in summer. Towards winter the cold stable layer of air also extends north over the sea ice covered ocean together with the northward extent of the sea ice. Especially in the Ross and Weddell Seas, the cold air seems to flood from the ice shelves over the sea ice and accumulates to a rather thick layer. Deepest inversions are again present over the ice shelves, especially over the Ronne Ice Shelf where the inversion reaches an average height of more than 1500 m in July. The shallowest inversion layer is still situated over steep or coastal regions.

The cold air pooling on the ice shelves and the extension of the cold air layer over the sea ice are, apparently, strongly related. The driving force, however, that leads to such a large scale advection of cold air over the sea ice must be found in the wind field which I will discuss in the following sub-chapter.

4.2 The Near-Surface Wind Field

As I have outlined in the previous section and in chapter 2.3, the near-surface wind is, on one hand, a driving mechanism of the sea ice drift and redistribution, and, on the other hand, important for large-scale advection of cold or warm air masses. In this sub-chapter, I will discuss the general distribution of the surface pressure field and the associated wind field. Further, I will describe variability and long-term changes of these variables. The forcing components of the wind that I introduced in chapter 2.2 are, then, of interest in the following section (4.3).

Figure 4.9 shows the mean surface pressure distribution around the Antarctic continent where the surface elevation is below 120 m for four selected months. In all of these months a belt of low pressure

surrounding the Antarctic continent at about 60° to 70° S is clearly visible: the circumpolar pressure trough. The existence of this low pressure around the continent can be explained by general considerations of the planetary circulation that can be found in any climatological text book. In a meridional direction, it develops between the subtropical descending branch of the Hadley cell with the associated high pressure areas over the three oceans and the thermally induced high pressure over the Antarctic continent due to surface cooling and related large-scale subsidence.

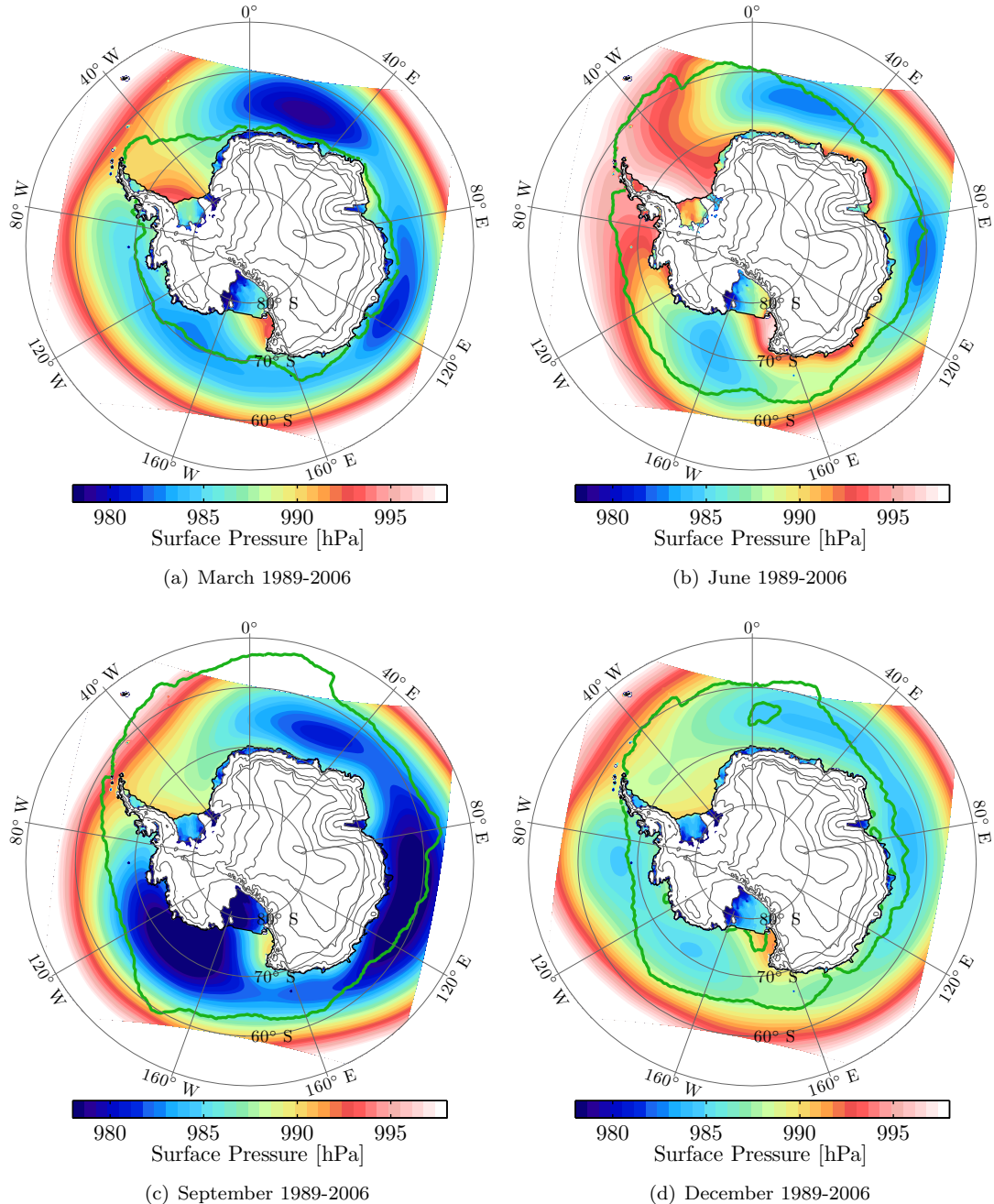


Figure 4.9: Simulated mean surface pressure below 120 m a.s.l.. The green line denotes the average observed sea ice edge.

It should be noted that the low pressure belt rather consists of moving depressions than static low pressure areas. The figure shows that, depending on the month, there are three to five pronounced pressure minima. These are areas where cyclones that, generally, move southeastward preferentially have their destination. Why these are the preferred trajectories of the cyclones is still not fully understood. One influence are the subtropical high pressure areas over the oceans and their annual and interannual variability. Another factor that is important for the position and strength of the climatological low pressure areas is the orography of the Antarctic continent. Lachlan-Cope et al. (2001) showed with a numerical experiment, in which they compared a simulation with a real orography to one with a axis-symmetric orography, that the position and variability of the Amundsen Sea Low can only be reproduced with the real asymmetric orography. They report that the formation pattern of the planetary Rossby waves is triggered by a displaced center of mass from the pole. A detailed understanding of the variability of these three climatological low pressure areas is crucial to explain the variability of the climate in coastal Antarctica.

In figure 4.9 we can notice a strong annual variability of the pressure distribution. The pressure trough strengthens and shifts twice a year. There are pressure minima during the equinoxes in March and September rather close to the coast, and two maxima during the solstices in June and December further away from the coast. This phenomenon is referred to as semi-annual oscillation (SAO) (van Loon et al., 1972). It is triggered by differences in the surface energy balance between the Antarctic continent and the Southern Ocean and an associated change of the baroclinicity that determines the movement of the depressions. Moreover, in March the deepening of the pressure trough is stronger in the eastern Weddell Sea than in the Amundsen and eastern Ross Seas. During the strengthening in September, however, this distribution is the other way around and the Amundsen Low is the strongest.

Despite the meridional gradient of the pressure, in figure 4.9, we can identify regions of strong zonal gradients. These are caused by the preferred trajectories of the depressions and the higher pressure close to the meridional barriers imposed by the Transantarctic Mountains and the Antarctic Peninsula. The zonal gradient is also visible over the large ice shelves and might be as high as 10 hPa. The gradients are large when the pressure trough is closest to the coast (March and September), but also in June when the subsidence that is induced by the cooling over the continent is strongest. In the Weddell Sea the zonal pressure gradient is strongest in March and June. In contrast, in the Ross Sea it is strong from March through September and only decreases in summer.

The average surface layer wind field that is related to the pressure distribution is illustrated in figure 4.10 for the same months as in figure 4.9. Together with the wind vectors the wind directional constancy is shown in color. The definition of this useful climatological quantity is given in box 4.3. We can see that the movement of the depressions in the circumpolar pressure trough leads to a very frequently varying wind direction and a very low directional constancy. North of the pressure trough the strong and directionally constant westerlies prevail. Over the slopes of the ice sheet the directional constancy and the wind speed are very high. I will analyze the contribution of the katabatic forcing to these winds in the next section 4.3. The winds follow the topography rather closely with a slight easterly component induced by the Coriolis force. Along the coast where the surface friction vanishes these winds turn easterly. They are strongest and extend furthest north in June when the pressure trough is further away from the coast and the cooling over the continent is strongest.

An exception to the coastal easterlies can be found in the southern Ross and Weddell Seas. Here, the zonal pressure gradient induces geostrophic southerly winds that are, especially in the Ross Sea, of high directional constancy close to the ice shelf edge. In the Weddell Sea the effect is not as strong and is most visible in March and June. Further, we can observe that the cold air on the continental slopes is drained onto the ice shelves by the terrain-following katabatic winds. This air is, then, exported over the sea ice by the southerly winds in these regions. These mechanisms explain the extension of the cold air layer over the sea ice that I have described in the previous section (4.1) and that is present in the Ross and Weddell Seas. The export of cold air over the sea ice is much stronger in the Ross Sea because here we find the higher and more persistent wind speeds. In the Weddell Sea where the southerly winds are not as strong more cold air accumulates on the Ronne-Filchner Ice Shelves which is the reason why we

find here the much thicker cold air layer than over the Ross Ice Shelf.

Box 4.3: Directional Constancy

When vector data is analyzed climatologically, the directional constancy is an interesting parameter and is defined as (van den Broeke et al., 2002):

$$DC = \frac{\sqrt{\bar{u}^2 + \bar{v}^2}}{\sqrt{\bar{u}^2 + \bar{v}^2}}. \quad (4.4)$$

An average vector in a certain direction might be large even though the actual direction of the quantity is variable over time and the resulting vector is owing to some extreme values in one direction. The directional constancy, however, indicates whether the vector is mostly directed in the same direction (high DC) or varying in direction (low DC).

In order to relate the long-term changes and the variability of the sea ice to the atmospheric circulation in the following two main chapters (5 and 6), I will now proceed to analyze the interannual variability and the trends of the surface pressure and near surface wind field. Similar as for the potential temperature in the previous section. Figure 4.11 shows the overall and seasonal variance of the detrended surface pressure anomalies and figure 4.12 shows the overall variance of the detrended meridional and zonal wind speed anomalies over the continent and the sea ice covered ocean. The interannual surface pressure variability shows that most of the variation takes place in the Amundsen and Bellingshausen Seas and that the high variance extends as far as the western Weddell Sea and the eastern Ross Sea. This clear maximum of the variance is referred to as the Southern Annular Mode (SAM/AAO). Figures 4.11(b) to (e) show that the variability is strongest in winter and weakest in summer. A high variability of pressure in this region implies that the zonal pressure gradient in the Ross and Weddell Seas changes accordingly. This should be associated with a high variability of the wind field.

Figure 4.12(a) confirms that there is a rather high variance of the detrended surface layer meridional wind speed anomalies in the western Weddell Sea, in the Bellingshausen and Amundsen Seas, and in the Ross Sea. The highest overall variance occurs in the western Ross Sea very close to the Transantarctic Mountains. Just east of this region, the variance is rather low. In consideration of the mean flow, this means that the strength of the southerly winds over the Ross Sea is rather persistent from one year to the other at a certain distance from the mountain range and very variable closer to the mountains. Interestingly, the variance of the detrended surface layer potential temperature anomalies in figure 4.6(a) showed the exact opposite distribution with a high variance further away from the mountain range and lower variance closer to the mountains. How the variability of these two variables is connected in this region will be explained in the following two sections (4.3 and 4.4). Over the continent the interannual variability of the meridional wind field is only high in some coastal regions of West Antarctica and otherwise extremely low. Furthermore, the variability of the zonal wind as shown in figure 4.12(b) is very high in the south-eastern and north-western Ross Sea. Over the continent and in the embayments sheltered by the two large topographic barriers (Antarctic Peninsula and Transantarctic Mountains) the interannual variability of the zonal flow is very low.

Figure 4.13 shows the long-term trends of the surface pressure and the associated changes of the wind field. The overall trends are very small and mostly insignificant. Only the the region north of the Antarctic Peninsula shows a small and significant increase of the surface pressure (at a 90% confidence level). This results in a small northeasterly wind speed trend (decreasing strength of the westerlies) in the northern Bellingshausen and Amundsen Seas and a southwesterly trend in the Weddell Sea. On the one hand, the low significance of the trends is related to high interannual variations of the surface pressure and a rather short time series. On the other hand, by considering figures 4.13(b) to (e), it becomes clear that the trends are very much seasonally dependent and might even be of opposite sign in a different season. This lowers the overall strength and significance of the trends. Nevertheless, the trends are also not significant on a seasonal timescale.

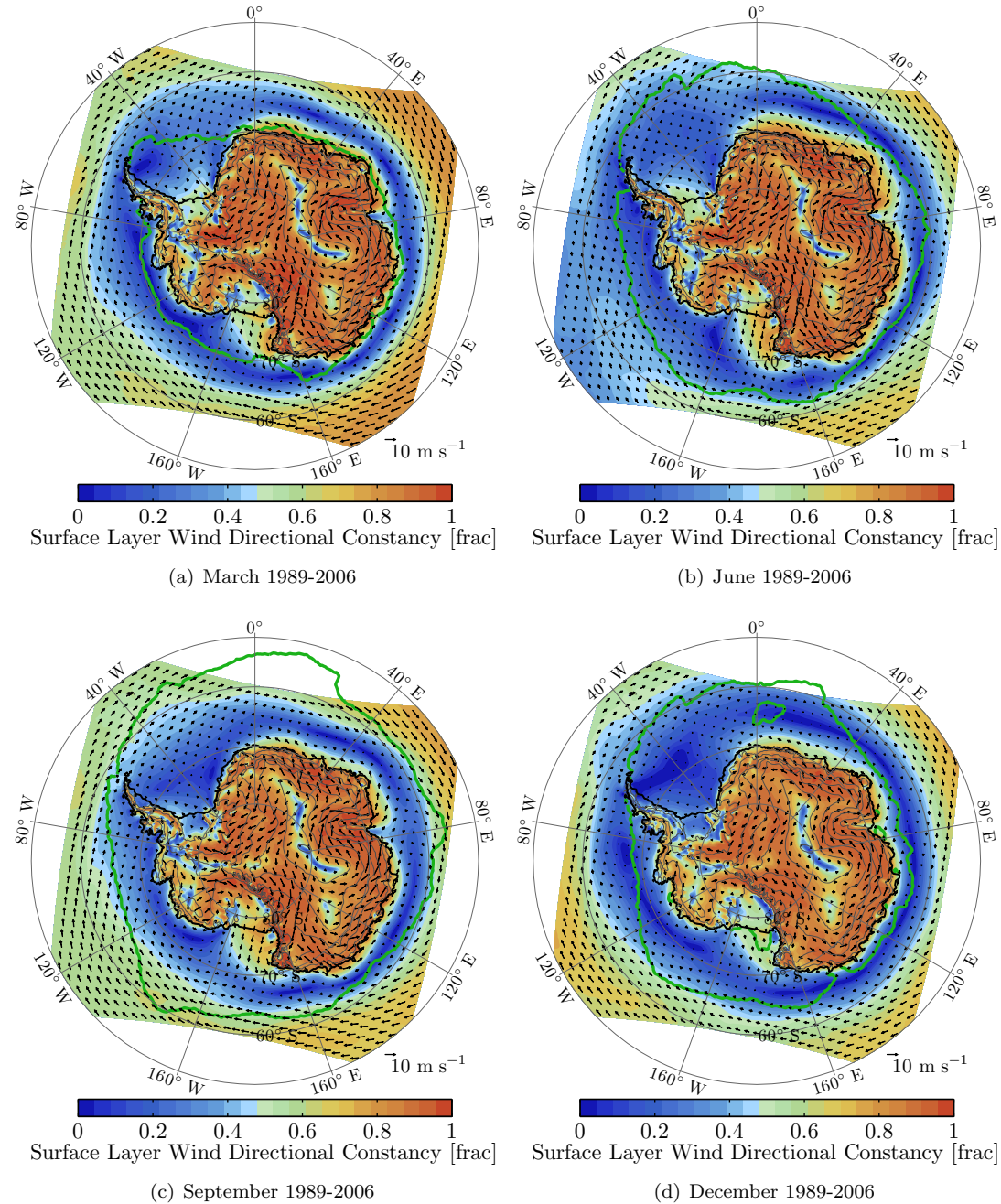


Figure 4.10: Simulated atmospheric surface layer wind field (only every seventh vector is plotted) and corresponding directional constancy. The green contour line denotes the average observed sea ice edge.

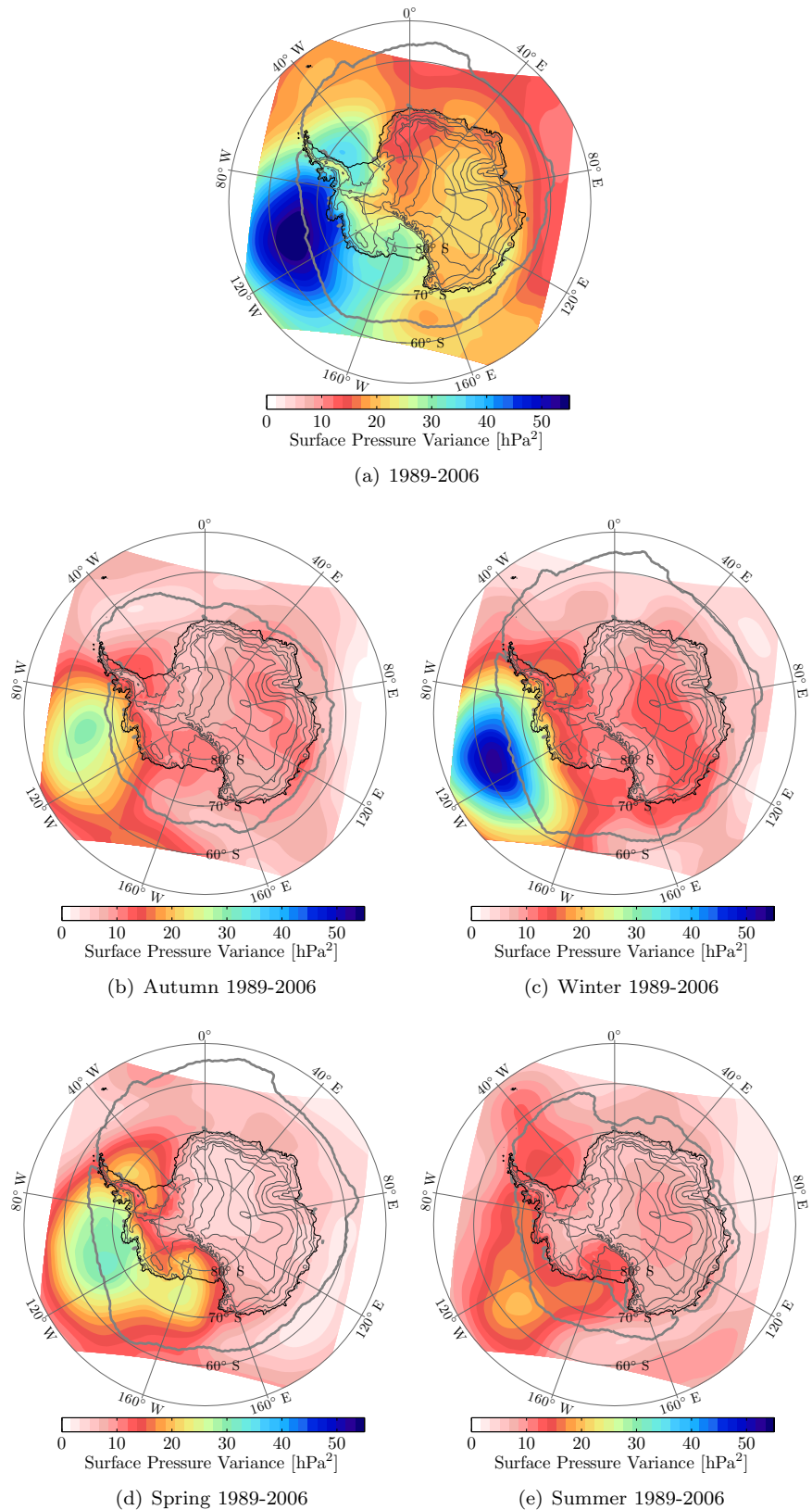


Figure 4.11: Variance of detrended surface pressure anomalies. The gray line denotes the average observed sea ice edge.

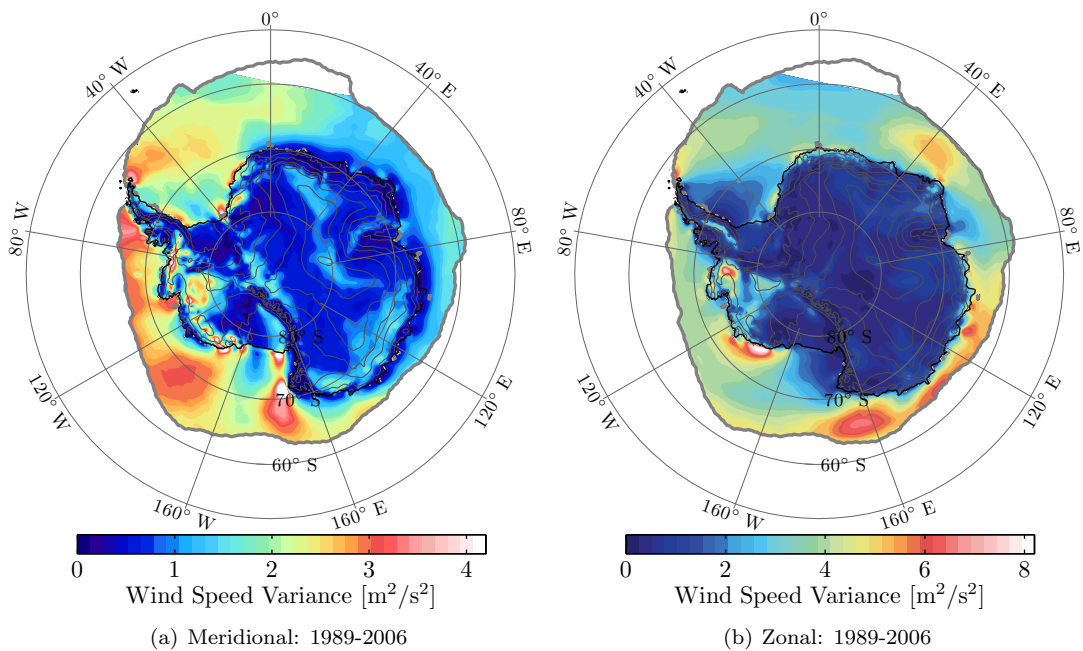


Figure 4.12: Variance of detrended meridional (a) and zonal (b) wind speed anomalies over the continent and the sea ice covered ocean. The gray contour line denotes the average observed sea ice edge.

The increasing pressure north of West Antarctica occurs in winter and spring. This also explains the increasing temperature in winter and spring noted in the previous section in figure 4.7 in the Bellingshausen and Amundsen Seas and in the Ross Sea. Here, an advection of warmer airmasses from lower latitudes takes place. Similarly, the cooling trend in the Weddell Sea might be related to an increased advection of colder air from the south. Also, the increasing temperatures along the coast of eastern Dronning Maud Land and Enderby Land can be explained with an increasing warm air advection from lower latitudes. Interesting to note is also a decreasing pressure in the central Ross Sea in winter that leads to stronger southerly winds along the coast of Victoria Land.

Even though, all these trends are insignificant, they give an indication of how the temperature field is related to the large-scale circulation which is useful for the latter analysis in this thesis. This link of the pressure field surrounding the Antarctic continent and the coastal temperatures is also reflected in the SAO pattern that is present in the temperature variations as well (cf. van den Broeke, 1998). The pressure changes suggest a weakening of the SAO in the Bellingshausen and Amundsen Seas in the considered time period. Results from a study by van den Broeke (2000b) indicate that such a weakening of the SAO in this region causes a negative trend of the sea ice cover.

How trends and variability of the wind field and temperature are related to the sea ice cover will be further explained in chapter 5. Next, I will describe the single forcing terms of the wind field which are important in order to understand the processes that take place in the Antarctic boundary layer in the coastal areas, over the ice shelves, and the sea ice covered ocean.

4.3 The Forcing Terms of the Wind Field

I have already described the single forcing terms of the Antarctic boundary layer momentum and how their magnitude can be estimated in theory in chapter 2.2. In this section, I will show the horizontal distribution of these terms as they were derived from the model simulation. Ideally, these terms would explain the near-surface wind field in the coastal regions of Antarctica and over the sea ice covered ocean,

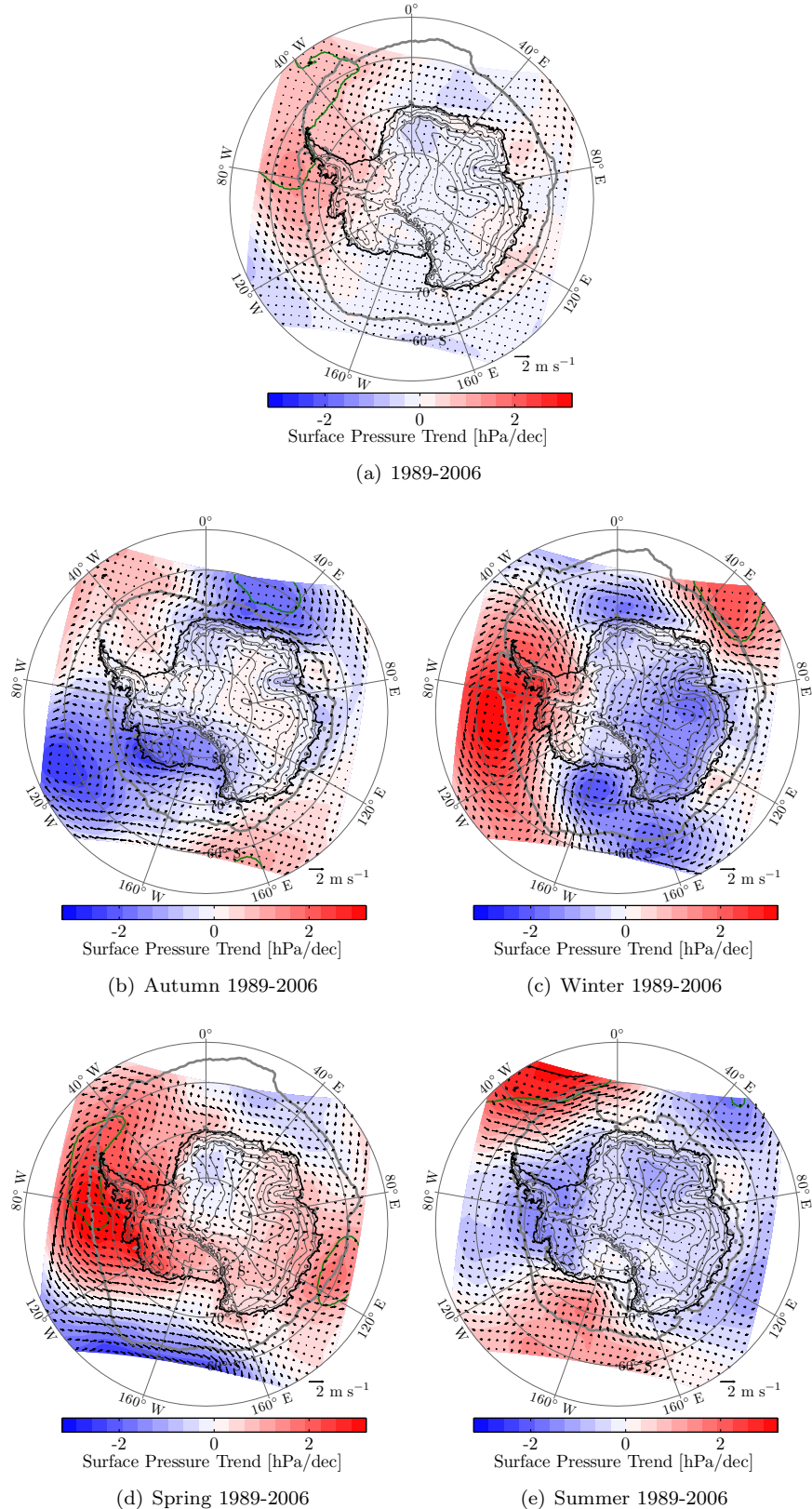


Figure 4.13: Decadal trend of surface pressure and associated trend of surface layer wind field per decade. The gray contour line denotes the average observed sea ice edge and the green and black contour lines indicate the 90% and 99% confidence level, respectively.

and its long-term changes and variability. However, to anticipate the outcome, an analysis of the changes and the variability is not possible in this thesis. The methodology to deduce these terms, that I have described in chapter 2.2, has several drawbacks for this study which I will also outline in this section. I will briefly describe and interpret the mean state of these forcing terms similar to the study performed by van den Broeke and van Lipzig (2003a) with a previous version of RACMO and a horizontal resolution of about 55 km for the period 1980 to 1993 and compare the results. Despite the problems with the methodology, the analysis of the forcing terms gives valuable insights for my thesis. Furthermore, I will restrict the analysis to the average fields of the winter month July as I am mostly interested in a general understanding of the momentum budget during a month with high sea ice cover.

The strong and persistent longwave radiative cooling over the slopes produces large amounts of cold air that are drained down the slopes by the katabatic winds. In chapter 2.2 I formulated the relation between the negative buoyancy induced by the surface temperature deficit to the katabatic flow (cf. equation 2.15). The surface layer potential temperature deficit for the average month of July is illustrated in figure 4.14(a). As already illustrated by the temperature inversion in figure 4.8, a surface deficit is present over the sea ice covered ocean and the continent. Over the open ocean we mostly find an unstable boundary layer caused by the heating from the ocean. In some coastal areas the surface deficit decreases to almost zero or it even gets positive in the south-western Ross Sea. I have already mentioned the open water areas in this region that heat lowest atmosphere. As expected, the surface deficit is large over the ice shelf, comparably small over the slopes, and very large in the interior.

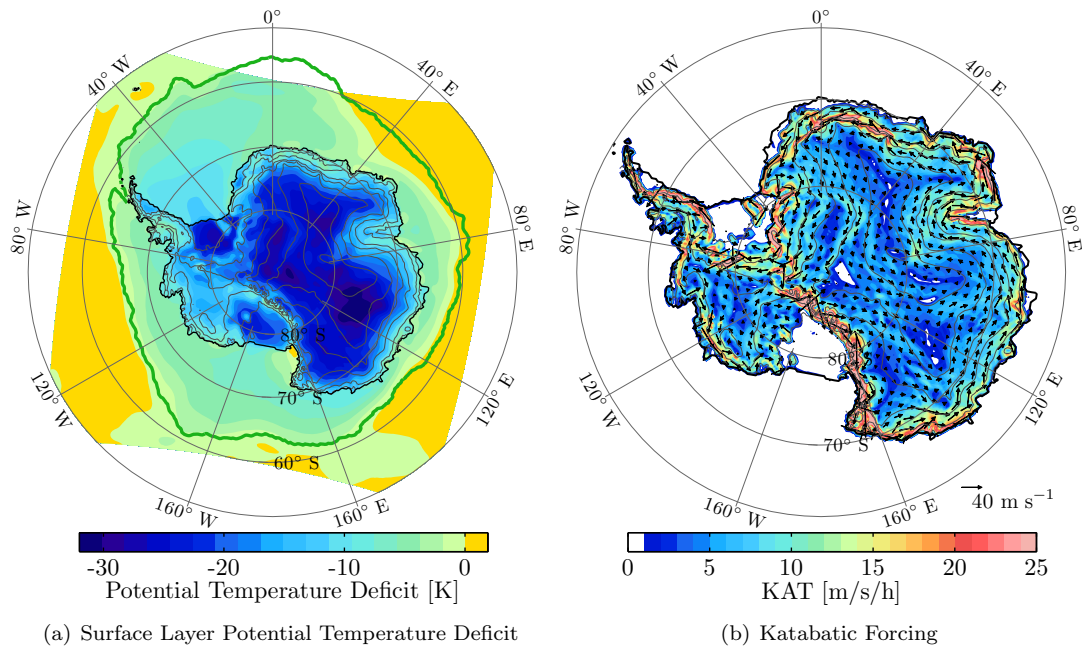


Figure 4.14: Average July (1989 to 2006) simulated surface layer potential temperature deficit (a) and resulting katabatic wind forcing with associated wind vectors that are balanced with the Coriolis force (only every fifth vector is plotted) (b). The green contour line denotes the sea ice edge.

The described pattern of the surface deficit together with the steepness of the slopes (cf. figure 1.3(b)) determine the katabatic pressure gradient force shown in figure 4.14(b). Also shown are the associated wind vectors that were retrieved by balancing the katabatic forcing with the Coriolis force. This leads to the effect that the downslope forcing results in an easterly along-slope flow. If we would also consider the effect of surface friction that acts in the opposite direction, the flow would have a downslope component again which is more realistic in consideration of the total wind field in figure 4.10. Consequently, surface friction imposed by the roughness length in the model is important to capture the downslope component

of the cold air drainage from the ice sheet into coastal areas.

We can see that the katabatic forcing increases towards the slopes even though the surface layer deficit decreases. Along the coast where the topography can be really steep and along the Transantarctic Mountains the forcing gets really strong. The average calculated wind speeds may exceed 60 m s^{-1} . In consideration of the total wind speed, this is rather high. Consequently, there must be a force next to the surface friction that leads to a forcing in the opposite direction. Further, the wind vectors in these steep regions show a varying direction due to the local variation of the aspect of the topography. In general, patterns agree very well with the findings by van den Broeke and van Lipzig (2003a) for the period 1980 to 1993. The higher resolution of the simulation used in this thesis has two effects: firstly, the magnitude of the forcing and the wind speed is slightly higher in some regions due to increasing surface slopes, and, secondly, the spatial patterns are more detailed, especially along the Transantarctic Mountains.

The forcing by the large-scale circulation can be subdivided into two driving mechanisms: one is the influence of the flow above the TDL on the near-surface winds, and the other is the horizontal gradient of the extrapolated background profile with an associated thermal wind effect (van den Broeke and van Lipzig, 2003a). The height of the 500 hPa level (above the TDL) is illustrated in figure 4.15(a). It shows that the large-scale westerlies of the polar vortex are induced by a strong gradient of the pressure towards the pole. Around the pole we can find a strong asymmetry of the pressure distribution. This results from the asymmetry of the orography of the Antarctic continent with the high East Antarctic Ice Sheet that almost reaches up to these levels. It cools the upper atmosphere and increases the pressure. Furthermore, regions with lower surface elevation that are closer to the pole, such as the Ross Ice Shelf, show a very low elevation of the 500 hPa level (van den Broeke and van Lipzig, 2003a).

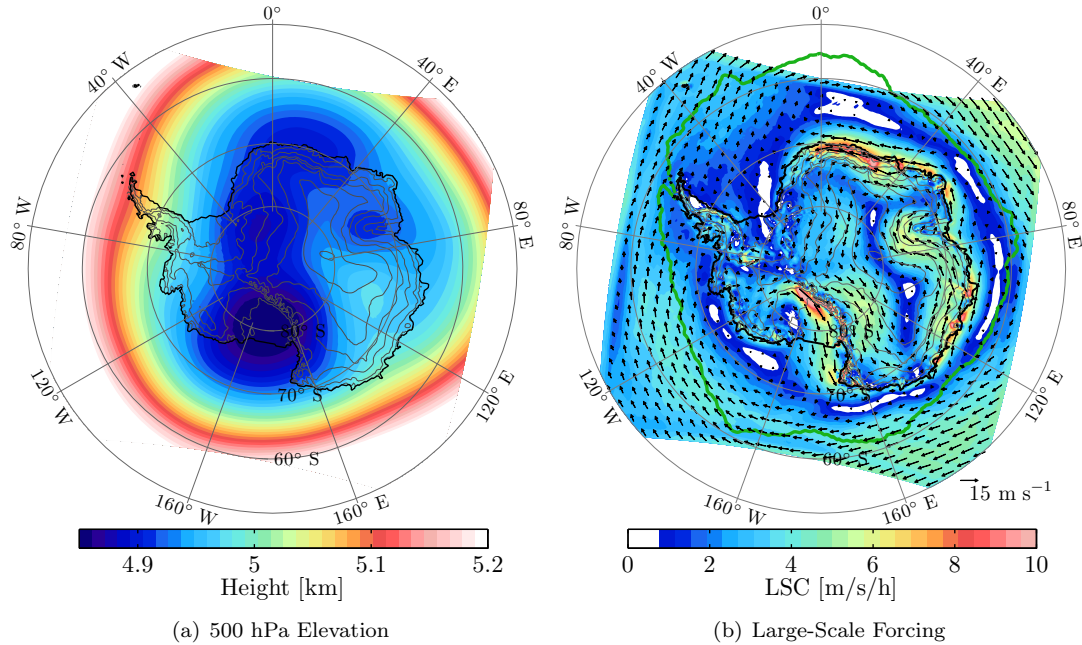


Figure 4.15: Average July (1989 to 2006) simulated 500 hPa height (a) and extrapolated surface layer large-scale wind forcing with associated wind vectors that are balanced with the Coriolis force (only every eighth vector is plotted) (b). The green contour line denotes the sea ice edge.

Figure 4.15(b) shows the average July surface layer large-scale forcing and wind field that was calculated with the extrapolation of the temperature and wind profile to the surface as I have described in chapter 2.2. In this case the model layers 23 (about 3.1 km high) to 20 (about 4.4 km high) have been used for the linear fit of the background potential temperature profile. In the resulting forcing field, the westerlies

are clearly dominant over the northern parts of the Southern Ocean. Further south, one can identify the circumpolar pressure trough where the forcing and the wind speed are low. Over the continent and in coastal areas in particular the flow is mostly easterly. This anticyclonic circulation is mainly related to a large-scale background temperature gradient between the East Antarctic continent and the surrounding ocean. Van den Broeke and van Lipzig (2003a) isolated the effect of the horizontal gradient of the background temperature profile (cf. their figure 6). Interestingly, this large-scale circulation enhances the easterly winds along the slopes of the ice sheet that are present due to the katabatic forcing (cf. figure 4.15(b)). Moreover, it increases the export of colder continental air into a narrow band along the coast over the sea ice.

Spatial patterns of the large-scale forcing in the study by van den Broeke and van Lipzig (2003a) (cf. their figure 7) are somewhat different to those retrieved here. The strength of the westerlies with a forcing of about 4 to $5 \text{ m s}^{-1} \text{ h}^{-1}$ is similar (note the different scale). However, across the Antarctic Peninsula the forcing is lower in figure 4.15(b). Regions of strongest large-scale forcing in figure 4.15(b) are the coastal band from Wilkes Land to the Amery Ice Shelf, eastern Dronning Maud Land, parts of the East Antarctic ice sheet just west of the Transantarctic Mountains, and the Ross Ice Shelf and south-western Ross Sea. In the latter region, the forcing exceeds $6 \text{ m s}^{-1} \text{ h}^{-1}$ and might be as high as $10 \text{ m s}^{-1} \text{ h}^{-1}$. In the southern part of the Ross Ice Shelf the forcing is the strongest and decreases towards the north but stays strong also over the south-western Ross Sea. Winds are mostly southerly to south-easterly and seem to follow the range of the Transantarctic Mountains. The effect is the strongest within a distance of about 200 to 300 km from the mountains and decreases further away.

The elevation of the 500 hPa level shows a strong gradient west to the Transantarctic Mountains which means that the stronger forcing on the eastern East Antarctic ice sheet is caused by the large-scale circulation in the upper atmosphere. East of the Transantarctic Mountains, on the Ross Ice Shelf and adjacent sea ice, however, no strong gradient of the 500 hPa level is visible that might cause the southerly flow. Figure 6 of the study by van den Broeke and van Lipzig (2003a), that shows the horizontal gradient of the background temperature profile, suggests that the winds are forced by a thermal gradient with lower upper atmospheric temperatures closer to the Transantarctic Mountains. The cyclonic motion over the Ross Ice Shelf induces a flow that is rather directed towards the mountain range than away from it. This set up of temperature gradient and large-scale wind field correspond to a phenomenon that is referred to as barrier wind effect that I introduced in chapter 2.2. Along the other large barrier, the Antarctic Peninsula, we can only notice a very small increase of the forcing over the western Ronne Ice Shelf and the adjacent ocean. This is very likely related to the same effect. I will analyze these wind systems further in the next section (4.4).

Before studying the wind field associated with the horizontal and vertical thermal gradients over the ice shelves in more detail, one needs to consider the thermal gradients that are present within the TDL. This can be studied by deriving the thermal wind forcing as I have described in chapter 2.2 and which should not be confused with the large-scale forcing induced by the gradient of the background temperature profile. Figure 4.16(a) shows the average July TDL and figure 4.16(b) shows the thermal wind forcing that is associated with the gradients of the TDL as well as the related geostrophic wind vectors. The overall thickest TDL is situated over the Ronne-Filchner Ice Shelves and the adjacent sea ice. It is slightly thicker towards the peninsula. This cold air pooling induces an anticyclonic thermal circulation around the ice shelves with a stronger forcing on the western side. On the slopes around the ice shelves the thickening of the TDL causes a force that counteracts the katabatic forcing and, hence, decelerates the flow. In the south-eastern Weddell Sea, along the coast, the thermal gradient leads to a south-westerly wind forcing. This is probably the reason why the overall coastal anticyclonic wind field around the continent that we have seen in figure 4.10 is interrupted in this region. In the most western part of the Weddell Sea the thermal gradient is associated with a slight easterly forcing towards the Antarctic Peninsula.

Further, one can identify a local thickening of the TDL off the Amery Ice Shelf, and in coastal George V and Adélie Lands. In the latter region figure 4.16(b) shows a strong easterly wind forcing that amplifies the overall easterly winds in this region. The local thickening of the TDL over the sea ice coincides with

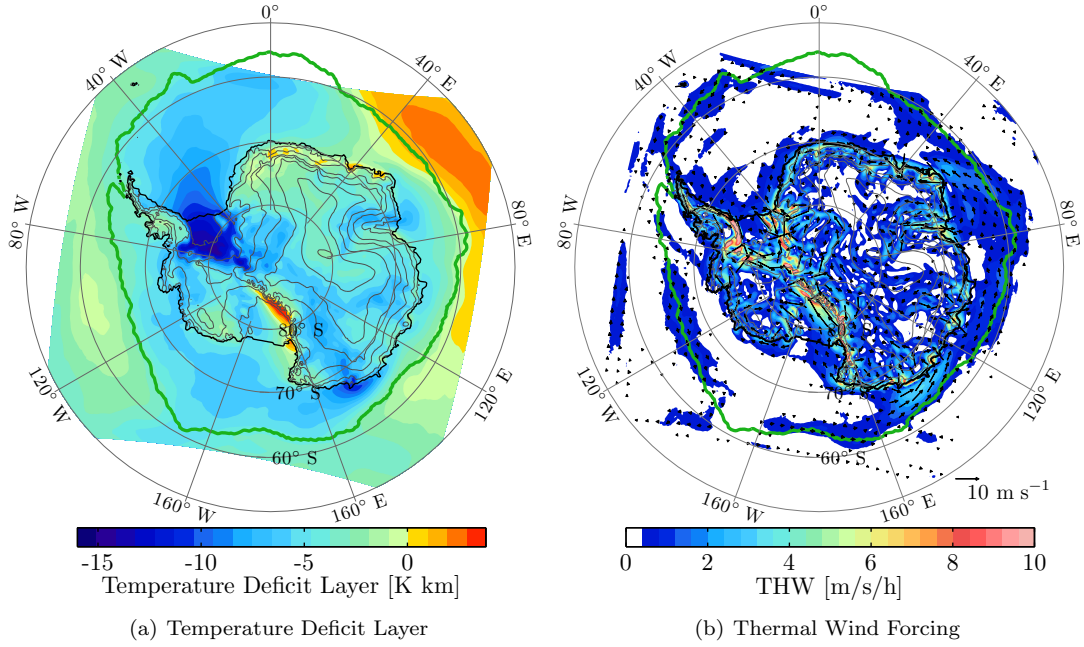


Figure 4.16: Average July (1989 to 2006) simulated surface layer temperature deficit layer (a) and resulting thermal wind forcing with associated wind vectors that are balanced with the Coriolis force (only every seventh vector is plotted) (b). The green contour line denotes the sea ice edge.

the confluence zones of the katabatic winds in coastal areas (cf. Parish and Bromwich, 1987). In general, the TDL is thicker over the sea ice than over the surrounding ocean. This implies an easterly geostrophic wind forcing along the sea ice edge. In regions where the sea ice extends as far as the westerly winds, the thermal gradient of the TDL dampens the westerlies. In those regions where the ice edge is closer to the coast it amplifies the easterlies. Overland et al. (1983) study the marginal ice zone wind and temperature fields in detail and point out that also the surface roughness of the sea ice is important because it can lead to off-ice winds along the margin when the roughness is large which would imply a sea ice divergence.

Over the Ross Ice Shelf and the south-western Ross Sea there is a strong gradient of the TDL with a shallower or even positive TDL towards the Transantarctic Mountains. This gradient induces a rather strong north-westerly wind forcing with geostrophic wind speeds exceeding 15 m s^{-1} . In consideration of the total southerly to south-easterly winds in this region this seems to be a rather high value as it would compensate for almost the total large-scale forcing depicted in figure 4.15(b). It is rather intriguing that the TDL has such large positive values along the mountain range. A positive TDL in absence of radiative heating is only possible due to a very strong vertical advection which seems rather unrealistic to reach such high values. This hints at the failure of the extrapolation procedure. Even though the extrapolation might not give a good estimate, the temperature gradient within the TDL with a decreasing strength towards the mountains is of opposite direction to the large-scale temperature gradient which induces the southerly flow. Apparently, the temperature gradient across the ice shelf leads to a change of the forcing with height.

Beside the positive TDL over the Ross Ice Shelf there are also regions with positive values along coastal Dronning Maud and Enderby Lands. The TDL strength is very sensitive to the amount and height of model layers that are used to fit the background profile. By having studied several cases (not shown here), I conclude that it is not possible to find a fixed set of layers that seem to provide reasonable results over the whole domain. Choosing a higher set of layers gives better results over the ice shelves. However, then, the procedure fails over the sea ice covered ocean and the overall strength decreases considerably. This means that processes induced by the surface cannot be captured any longer.

Another indication that the retrieval of the momentum budget in this study only provides a qualitative understanding rather than giving accurate quantitative estimates is given by a comparison of the sum of all major forcing terms with the total wind speed given by the model. Van den Broeke and van Lipzig (2003a) report a correlation coefficient of 0.94 for the average month of July (1980 to 1993) between the vector mean wind speed and the sum of the katabatic, large-scale, thermal wind, and horizontal and vertical advection forcing terms which are the active forcing terms. Further, they state that advective terms are really small. Here, I did not explicitly solve the advective terms and the correlation coefficient between the vector mean wind speed and the sum of the katabatic, large-scale, and thermal wind forcing terms is only 0.48. The reason why the procedure fails in this case is probably due to the increased resolution. A higher resolution implies that advection plays a more important role and that the structure of the boundary layer gets more detailed in the horizontal and vertical which probably results in the failure of the extrapolation procedure.

Within the course of research for this thesis, I have attempted to develop a new algorithm for the extrapolation procedure. This algorithm first determines the height of the lowest temperature inversion for each grid box. Next, it fits a linear potential temperature profile through the four layers just above the height of the inversion and determines the goodness of the fit. It, then, moves upward the four fitting layers until the error minimizes. This leads to an optimized set of fitting layers for each grid box.

The resulting surface layer potential temperature deficit and deficit layer for the average month of July are shown in figure 4.17. Comparing figures 4.17(a) and 4.14(a), it shows that the surface layer temperature deficit does not change much and is, consequently, not very sensitive to the set of layers used for the extrapolation. The TDL, however, changes considerably (cf. figures 4.17(b) and 4.16(a)). First of all, the positive values over the continent turn into very small negative values (which seems more realistic). This also means that the derived thermal wind forcing in figure 4.16(b) is probably overestimated over the Ross Ice Shelf. Secondly, the TDL over the steeper coastal continent where the inversion height was found to be very low gets rather shallow which also seems reasonable. Nevertheless, new problems arise. There are obvious jumps in the TDL where the set of layers that are used for the fitting change. These induce very strong artificial horizontal gradients that affect the retrieval of the large-scale and thermal wind forcing and make a derivation of the momentum budget impossible. In order to find a solution to this problem further research is necessary. One suggestion might be to find a mathematical function that changes the height that is used for the extrapolation more gradually in the horizontal.

I will now turn the discussion to the dynamics related to the cold air pooling on the ice shelves. In figure 4.17 we can notice that the strength of the surface layer deficit over the Ronne-Filchner Ice Shelves decreases towards the Antarctic Peninsula and the TDL strength increases in the same direction. This means that the structure of the vertical temperature profile changes across the ice shelves. The depth of the cold air pooling is shallow on the eastern side and the deficit is rather strong. In the west it is much higher but the deficit decreases. Over the Ross Ice Shelf this seems to be different; the surface layer deficit is also stronger in the east, away from the topographic barrier but, here, the TDL also decreases towards the mountains. In order to gain insights into these structures we will need to consider the vertical profiles.

4.4 Cold Air Pooling Along Topographic Barriers and Associated Flow

In chapter 2.2 I have shown that so-called barrier winds can develop along the Antarctic Peninsula and the Transantarctic Mountains. I will now analyze the effect of the mountain ranges on the cold air pooling and the related wind field. The reason to focus on these processes is that in these regions we find rather strong and persistent southerly winds that export cold continental air over the sea ice and might have a profound effect on the sea ice dynamics and formation. I will try to use the theoretical concept to explain the model output. We could already see in the previous section (4.3) that the winds are much stronger and more persistent over the Ross Ice Shelf and Ross Sea than along the east coast of the Antarctic Peninsula. Consequently, I will focus more on the effect of the Transantarctic Mountains.

The surface layer temperature deficit in figure 4.17(a) was found to be higher on the eastern side of the

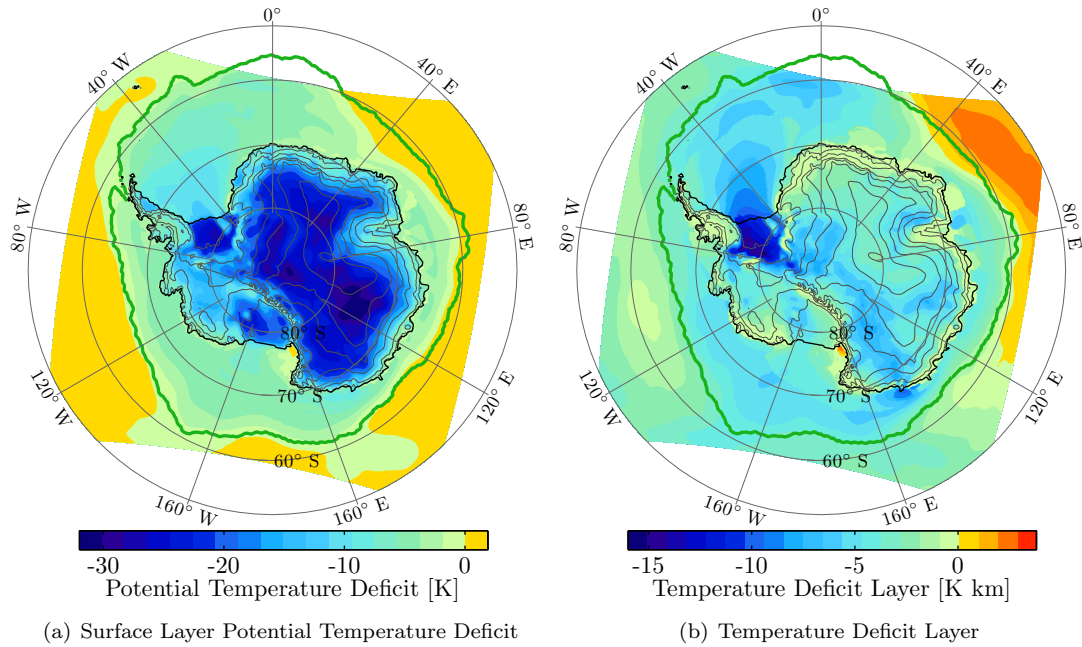


Figure 4.17: Average July (1989 to 2006) simulated surface layer potential temperature deficit (a) and temperature deficit layer (b) retrieved with an algorithm that detects the most suitable set of layers for the extrapolation of the background layer for each grid point. The green contour line denotes the sea ice edge.

Ronne and Ross Ice Shelves. This is caused by higher surface layer southerly wind speeds in winter on the western side (cf. figure 4.10(b)) that are responsible for stronger cold air export from the ice shelves. Whereas over the Ronne Ice Shelf the TDL is slightly thicker towards the west, it is thinner towards the barrier over the Ross Ice Shelf. This gradient seems to be counterintuitive as we would expect a thickening cold air layer towards the mountain range by a tendential westward transport of cold air due to the large-scale anticyclonic motion over the ice sheet. It should be kept in mind that the TDL is mostly determined by the lowest layers where the temperature deficit is the strongest and that the contribution of the higher atmosphere is rather small. The temperature gradients that are related to gradients in the higher atmosphere are reflected in the large-scale forcing that shows a clear amplification of the wind speed towards the barriers induced by a horizontal gradient of the background temperature profile with lower temperatures towards the barrier. Consequently, the accumulation of cold and stable air in front of the barrier is present only over very large horizontal and vertical scales.

Close to the surface on the Ross Ice Shelf the east-west gradient of the temperature deficit counteracts the southerly flow. One would expect this effect to vanish higher up in the atmosphere and the large-scale temperature gradient to dominate. Figures 4.18(a) and (b), consequently, show the large-scale and thermal wind forcing respectively as in figures 4.15(b) and 4.16(b) but for the model layer 30 which is about 1 km above the surface (note that the scale is the same). They illustrate that the large-scale forcing close to the two mountain ranges at this height is still almost as strong as at the surface and that the thermal wind forcing induced by the TDL has almost vanished. Further, we can notice that over the Weddell Sea the large-scale forcing turns more and more westerly whereas a southerly flow prevails over the Ross Sea. This shows that the barrier effect on the eastern side of the Antarctic Peninsula is not as strong as the one over the Ross Sea and Ice Shelf. The reason is that the Antarctic Peninsula with a height of about 1500 to 2000 m a.s.l. is not as high as the Transantarctic Mountains which exceed 2000 m a.s.l. and where the East Antarctic ice sheet to the west provides additional shielding from other influences.

The vanishing of the horizontal TDL gradient with height means that the wind speed must be increasing

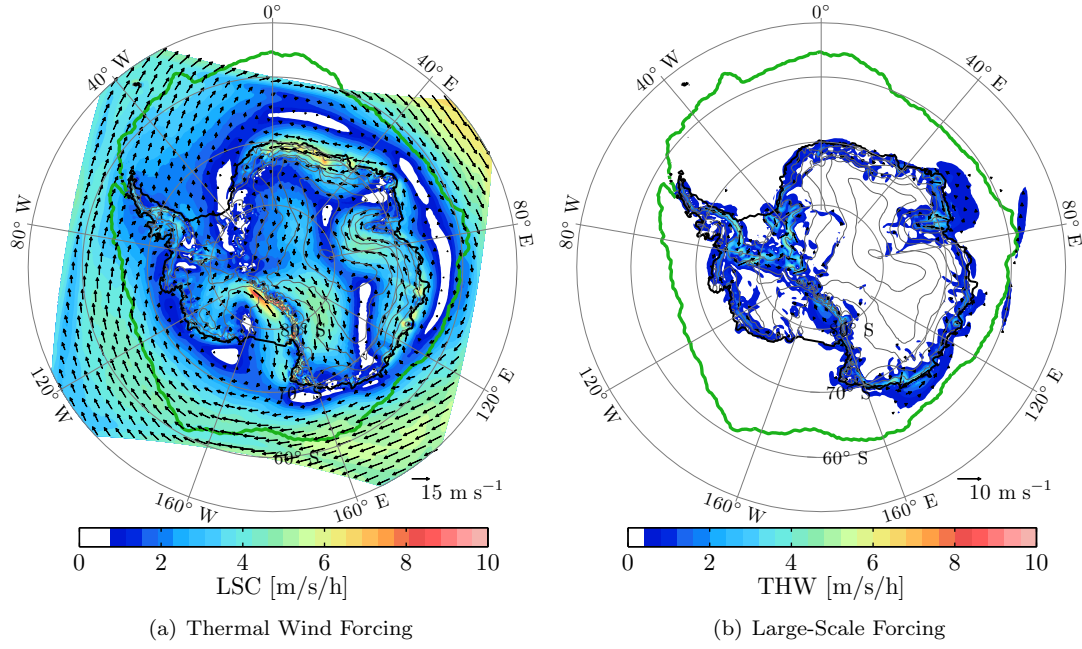


Figure 4.18: Average July (1989 to 2006) simulated large-scale wind forcing with associated geostrophic wind vectors (only every eighth vector is plotted) (a) and thermal wind forcing with associated geostrophic wind vectors (only every seventh vector is plotted) (b) for the model layer 30 at about 1 km above the surface. The green contour line denotes the sea ice edge.

up to a certain height above the surface. However, also the large-scale background temperature gradient decreases with height and the southerly forcing vanishes at about 3000 m a.s.l. in the south-western Ross Sea (not shown). Consequently, there must be a boundary layer jet close to the Transantarctic Mountains that forms due to changing horizontal temperature gradients. Figure 4.19(a) shows the mean July wind speed component that is perpendicular to the Ross Ice Shelf edge and is defined as positive from the ice shelf towards the ocean. The wind reaches a speed of up to 10 m s^{-1} . At the surface the wind speed only reaches a value of about 5 m s^{-1} . Moreover, we can identify three wind speed maxima. The most northern two are probably associated with the topographic indentations and the most southern one might be related to the narrowing of the ice shelf and an increasing gradient or to an inertia of the katabatic confluence zone. As soon as the western barrier is not present anymore in the north, the southerly wind speed decreases over the central Ross Sea. Also noticeable is that the wind speed maximum occurs at a distance of about 100 to 300 km from the mountain range.

Similar as over the Ross Ice Shelf and Sea highest barrier parallel wind speeds are visible close to the mountain range in figure 4.19(b) over the Ronne Ice Shelf and the adjacent sea ice. The Antarctic Peninsula clearly alters the flow pattern and amplifies the off-shore winds. Again, at the topographic indentation, where the air is forced around the mountains, we can observe the highest wind speeds. Another maximum occurs at the southern edge of the ice shelf where probably again the katabatic inertia is the reason.

The vertical profile for the average July fields of potential temperature, ice shelf edge perpendicular wind speed, and pressure along the Ross Ice Shelf edge (indicated in figure 4.19(a) by the red and gray lines) is shown in figure 4.20(a). The potential temperature, in color, shows the cold air pooling on the ice shelf. The coldest air with a large temperature deficit can be found just above the surface. Further, one can observe that the isentropes are tilted. Close to the surface they decrease towards the Transantarctic Mountains and higher up in the atmosphere they increase towards the mountains until a rather short distance (about 10 to 50 km) away from the mountains. Then, they decrease again. This lowering of the

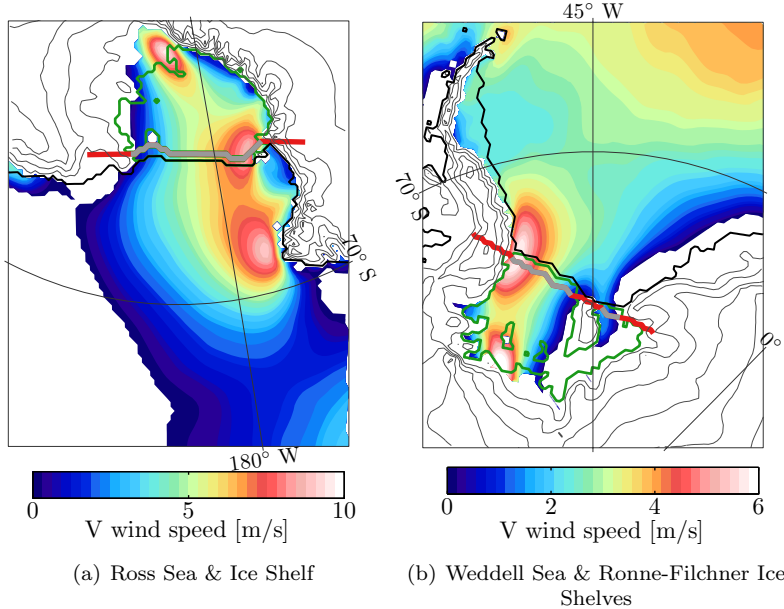


Figure 4.19: Wind speed component perpendicular to the edges of the Ross Ice Shelf (a) and the Ronne-Filchner Ice Shelves (b) at model layer 32 at about 600 m above the surface for the average month of July (1989 to 2006) which is defined as positive directed from the ice shelf towards the sea. For illustration purposes all data with a surface elevation above 250 m a.s.l. has been removed. The green contour lines indicate the ice shelves. The red and gray lines denote the transects that are used for the profiles shown in figure 4.20. The gray lines are the parts of the transects situated on the ice shelves.

isentropes very close to the mountains is likely related to downward mixing of upper atmospheric air due to subsidence. The subsidence is probably induced by the gravitational forcing along the steep slopes of the mountains.

The white contours in figure 4.20(a) that show the isobars are also slightly tilted and are increasing towards the mountains. This illustrates the large-scale pressure gradient across the ice shelf that I have already mentioned in section 4.2. The resulting wind field is shown by the gray contours where positive values have the same definition as in figure 4.19(a). Despite the general southerly wind direction we can identify a clear jet with maximum at about 400 to 600 m above the surface. The maximum coincides with the region where the isentropes diverge and the sign of the horizontal temperature gradient changes. Apparently, the lowering of the isentropes towards the mountains close to the surface is related to the higher wind speeds in this region that are the cause for a stronger export of cold air from the ice shelf. The tilting of the upper atmospheric isentropes is caused by an easterly large-scale forcing component (higher pressure over the continent and lower pressure over the ocean) that pushes the cold and stable air on the ice shelf towards the mountains. Due to its high stability it is not able to cross the mountain range and, instead, accumulates on the western side of the ice shelf.

The strong southerly barrier winds over the Ross Ice Shelf that persist on average over the whole winter have been studied already by many authors and the phenomenon is also commonly referred to as Ross Ice Shelf Air Stream (RAS) (O'Connor et al., 1994; Parish et al., 2006; Schwerdtfeger, 1984; Seefeldt and Cassano, 2008; Seefeldt et al., 2007; Steinhoff et al., 2009). When considering a smaller timescale than monthly means, it becomes clear that this system is very variable and might vanish completely. All the studies that I have mentioned before relate the development of the system to synoptic scale cyclones that pass in front of the ice shelf and end at the climatological Amundsen low. Consequently, the frequency of the occurrence of the barrier wind system depends on the cyclonic activity in the Ross Sea but also on the amount of cold air that is situated on the ice shelf and is responsible for the formation of the jet.

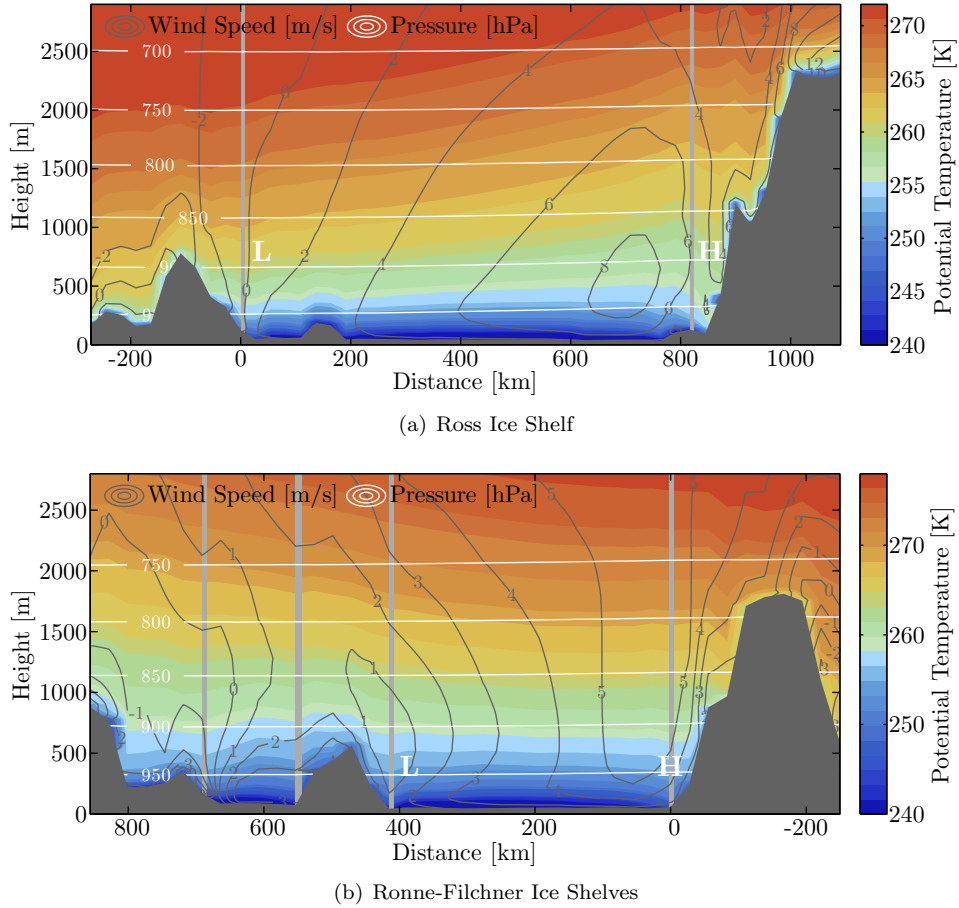


Figure 4.20: Average July (1989 to 2006) cross-sections along transects across the Ross Ice Shelf edge (a) and the Ronne-Filchner Ice Shelf edges that are outlined in figure 4.19 with the Transantarctic Mountains and the Antarctic Peninsula to the west (right in the figures), respectively. The viewing angle is from the ocean onto the ice shelf. The light gray vertical lines indicate the ice shelves. Potential temperature is shown in color, wind speed by dark gray contour lines, and pressure by white contour lines. The surface pressure is lower on the eastern side (L) than on the western side at the foot of the mountains (H) in both cross-sections.

Even though the system in the south-western Weddell Sea is much weaker, it shows similar patterns. However, the large-scale forcing in this region, first of all, is not as strong as in the Ross Sea and, secondly, the mean flow has hardly any easterly component towards the barrier (cf. figures 4.9 and 4.10). Consequently, there is no pronounced driving force that leads to a piling up of cold air on the western side of the ice shelf. Figure 4.20(b) shows a cross-section along the Ronne (on the right) and Filchner (on the left) Ice Shelves. Cold air that is pushed towards the Antarctic Peninsula as it was the case on the Ross Ice Shelf, is not visible in the figure. To the east (left), the ice sheet rises high up and we can clearly see the cooling effect of the ice sheet on the lower atmosphere. Nevertheless, the Antarctic Peninsula causes an accumulation of a thick layer of cold air over the ice shelf. The large-scale forcing leads to a stronger export of cold air near the surface on the western side which is very similar to the Ross Ice Shelf. As a consequence, the isentropes close to the surface are lowering towards the mountains which counteracts the large-scale forcing and decelerates the flow. No clear barrier wind system could be identified in figure 4.20(b) but still it occurs on shorter timescales and it has been studied and described by Parish (1983) and by Schwerdtfeger (1975, 1979, 1984).

I will proceed with an analysis of the impact of the cold air pooling on the large ice shelves and the

associated southerly winds on the sea ice covered ocean of the adjacent seas in chapter 6. In this chapter I have first studied the pooling of cold air that is drained from the ice sheet slopes onto the large ice shelves and the sea ice. Subsequently, I have described the wind field in coastal regions and over the sea ice that is an important driver of sea ice dynamics and large-scale air advection. The southerly winds in the Ross and Weddell Seas are responsible for accumulation of cold continental air over the sea ice. I have identified the temperature distribution in these areas that is induced by the large mountain barriers as a cause for the southerly winds and their amplification close to the mountain range. Now, I will continue with an analysis of the sea ice cover and transport in the Southern Ocean.

5 Observed Sea Ice Cover & Dynamics

This chapter aims at providing a detailed analysis and understanding of the temporal and spatial variability, and the long term changes of sea ice properties and related processes. In the introduction to this thesis (chapter 1), I have already listed several studies that deal with the variability and trends of the sea ice cover in the Southern Ocean. I have mentioned that the spatial and temporal patterns have been already described in detail and it is well known where largest changes of the sea ice occur. Nevertheless, as my goal is to analyze the dynamical interaction, I will reveal the relation between the sea ice cover and the sea ice dynamics. Moreover, I will compare patterns of the mean state, the variability, and the trend to findings of chapter 4.

In order to account for regional differences, I will compare the overall sea ice covered Southern Ocean to the regional averages of sectors that are illustrated in figure 1.2 in chapter 1. For reasons of consistency with results of other authors (Cavalieri and Parkinson, 2008; Zwally et al., 2002), I adapted the five regions defined by Zwally et al. (1983). These are the Weddell Sea, the Indian Ocean, the western Pacific Ocean, the Ross Sea, and the Bellingshausen and Amundsen Seas. Furthermore, maps of trends and variance will provide insight into local patterns. I attempt to focus on interannual variabilities by using 12-month-running mean data. However, I will also consider the seasonal cycle and climatological values of single months.

The first sub-chapter (5.1) deals with the sea ice cover. Here, I will describe variabilities and trends of the sea ice concentration, extent, and area similar to the studies performed by Cavalieri and Parkinson (2008), Comiso and Nishio (2008), and Zwally et al. (2002). This will not show many new results as the data is of similar origin but rather aims at exploring the satellite datasets that I discussed in chapter 3.2 and in order to understand the variations.

Further, in section 5.2, I intend to describe the patterns of sea ice motion and to outline regions where the drift is strong and persistent. Then, I will proceed to investigate the redistribution of sea ice by transport. As no ice thickness data is available, the transport will be expressed in terms of sea ice area instead of mass or volume. Eventually, I will relate the characteristics of the transport variations to the sea ice extent to obtain an indication of the role that the dynamics play for the total sea ice cover.

In the last section of this chapter (5.3), I will analyze the open water area within the ice pack and implications of sea ice divergence and convergence. In chapter 2.3, I have already outlined the importance of open water areas for the formation of sea ice and I have stressed the essential role of the dynamics in this process. I will try to relate the sea ice formation to the dynamics by defining and exploring a parameter that I will refer to as 'sea ice area production'.

5.1 Sea Ice Cover

The sea ice cover is commonly explored by studying sea ice extent and sea ice area. A definition of these two parameters is given in box 5.1. The difference between these two values is that the former also includes the open water in the pack ice and the latter changes with the changing amount of open water. This means that if the sea ice area is much lower than the sea ice extent, the ice pack includes frequent open water areas. It also implies that the sea ice area can, actually, not be larger than the sea ice extent. This might, however, still occur if the ice pack has a high concentration and the concentration thins gradually towards the edge. In this case the ice extent threshold might cut off a substantial part of very sparse sea ice cover around the edge that is still included in the total sea ice area.

Figure 5.1 shows sea ice extent and area anomalies of three different datasets in the period 1979 to 2010. All anomalies are defined with respect to the average seasonal cycle of the reference period 1989 to 2006 of the SSM/I data on the RACMO grid (in green) between the gray bars. The reference SSM/I dataset, that was already used in chapter 3.2, is also shown in blue in order to extend the time series further back in time and compare it with the here derived sea ice extent and area. Additionally, the AMSR-E sea ice anomalies are shown in brown. The differences between the SSM/I and the AMSR-E data, that I

discussed in 3.2, have here been partly taken into account by applying a correction. The AMSR-E data generally has a much higher sea ice concentration. I corrected it by defining the anomalies with respect to the average seasonal cycle between 1989 and 2006 of the SSM/I data in a first step. Secondly, the average seasonal cycle of the difference between the two datasets in the overlapping period 2003 to 2007 (here SSM/I data is only shown until 2006) has been subtracted from the total AMSR-E dataset. This procedure works well for the period 2003 to 2006 as can be seen in figure 5.1. However, no statement can be made for the later years. A detailed description of the problems that arise due to discontinuity is given by Screen (2011). If the reference dataset (blue) and the corrected AMSR-E data are merged in the year 2006 an overall time series from 1979 to 2010 results. The smoothed variability and the corresponding long-term trend of this time series are displayed in red.

Box 5.1: Sea Ice Extent and Area, and Open Water Area

There are two key parameters that are used to express the sea ice cover. In a gridded field of sea ice concentration, which is the fraction of sea ice cover per grid box, the sea ice area (*SIA*) of a region is the sum of the products between sea ice concentration (*c*) and grid cell area (*A*) of all grid cells (Cavalieri et al., 1999):

$$SIA = \sum_{i=1}^n A_i \cdot c_i. \quad (5.1)$$

The sea ice extent (*SIE*) is defined as the sum of all grid cell areas that have a sea ice concentration of at least 15% (Gloersen et al., 1992):

$$SIE = \sum_{i=1}^n A_{i,c \geq 0.15}, \quad (5.2)$$

The threshold fraction is rather arbitrary. Parkinson et al. (1999), Cavalieri et al. (2003) and Zwally et al. (2002) all show that the variability and trend of the sea ice extent are not sensitive to the exact definition of the sea ice edge as long as it is defined between 15 and 30% sea ice concentration. Furthermore, it is important to derive monthly sea ice extent from daily averages and not from monthly averaged sea ice concentration and grid box area because the result would be different due to the threshold (Gloersen et al., 1992). The difference between the sea ice area and extent can, then, be interpreted as the total open water area within the ice pack.

Moreover, a comparison of figures 5.1(a) and (b) shows that there are no large deviations between the interannual variability and the trend of the sea ice extent and the sea ice area. This is also reflected by a high correlation coefficient of 0.93 between the monthly anomalies of the two overall time series and a value of 0.97 for the smoothed data. Additionally, both parameters show a similar increasing trend which I will analyze in the following.

Trends are derived following the procedure that I have described in box 4.2. The overall time series (red in figure 5.1(a)) shows a significant increase of the total Antarctic monthly sea ice extent anomalies by $0.164 \pm 0.046 \cdot 10^6 \text{ km}^2/\text{dec}$ at a 99% confidence level (about 1.4% of the total Antarctic sea ice extent per decade). If seasonal variations of the anomalies are removed with a 12-month-running mean filter, the trend and the uncertainty reduce to $0.152 \pm 0.022 \cdot 10^6 \text{ km}^2/\text{dec}$ (about 1.3% of the total Antarctic sea ice extent per decade). The monthly sea ice area anomalies have a similar overall positive trend of $0.153 \pm 0.042 \cdot 10^6 \text{ km}^2/\text{dec}$ (about 1.8% of the total Antarctic sea ice area per decade). We can further observe that the sea ice extent anomalies strongly increase in the last five years which only becomes obvious when considering the corrected AMSR-E dataset (in brown) which has an overall increase of $0.518 \pm 0.442 \cdot 10^6 \text{ km}^2/\text{dec}$ at a 90% confidence level (about 4.5% of the total Antarctic sea ice extent per decade). As this trend is retrieved over a relatively short period of time, its large value also results from

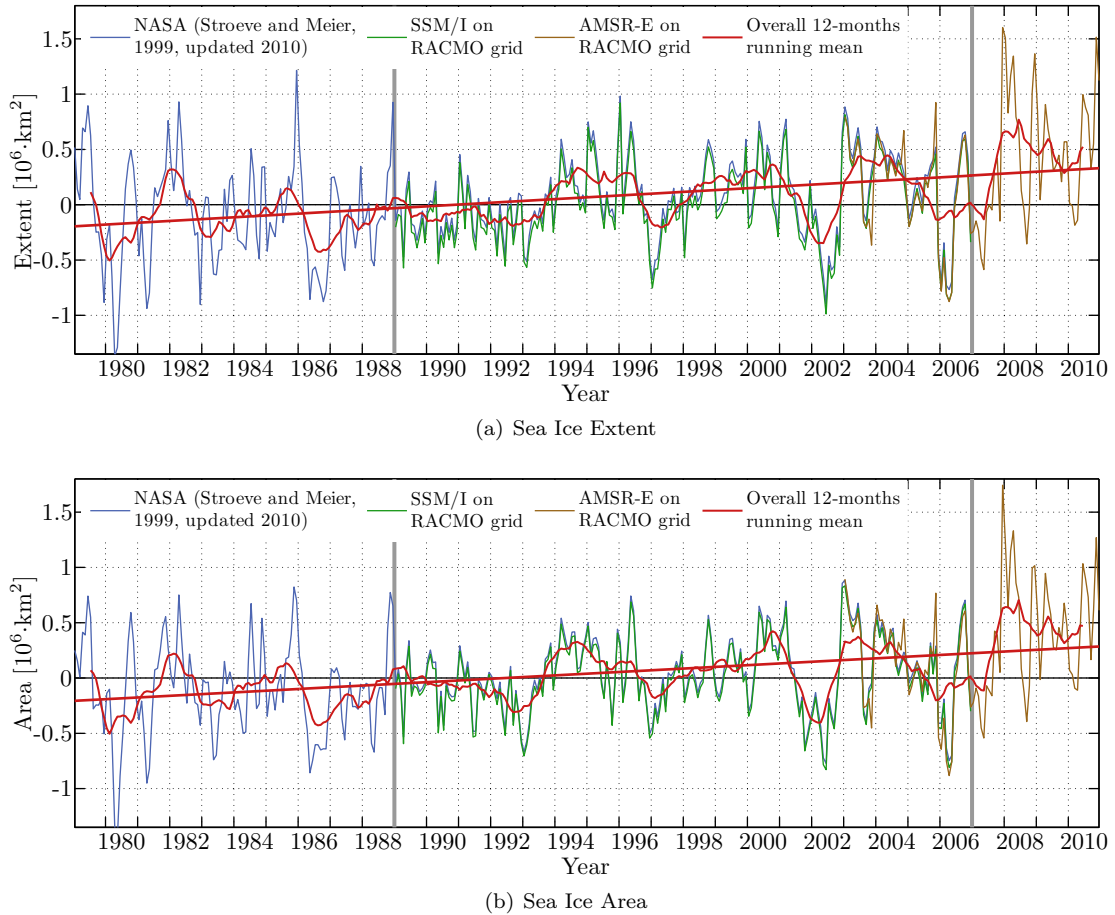


Figure 5.1: Time series of monthly sea ice extent (a) and area (b) anomalies for the total Southern Ocean for different data sets for the period 1979 to 2010 with respect to the average seasonal cycle of the period 1989 to 2006 of the SSM/I data on the RACMO grid (in green). The reference SSM/I dataset (1979-2006) is shown in blue. Anomalies derived from the AMSR-E dataset are given in brown and had been adjust for an offset (see text). The overall smoothed interannual variability is shown in red by a 12-month-running mean and the corresponding estimated trend. The change between the SSM/I data and the AMSR-E data occurs by the end of the year 2006.

a minimum of the interannual variability in 2006 which is reflected in the large statistical uncertainty. The reference dataset gives a rather robust increasing signature with $0.114 \pm 0.052 \cdot 10^6 \text{ km}^2/\text{dec}$ at a 99% confidence level for the period 1979 to 2006 (about 1.0% of the total Antarctic sea ice extent per decade). This is in line with results reported by Cavalieri and Parkinson (2008). As I have discussed in 3.2, I will mostly use the SSM/I data on the RACMO grid for the period 1989 to 2006 that is shown in green in this thesis. Even though the correction of the discrepancies between the AMSR-E and the SSM/I datasets seem to be reliable in this time series, it will not be possible to achieve the same accuracy on a smaller spatial scale where less data points are available (consider also Screen, 2011). Finally, the monthly SSM/I sea ice extent anomalies on the RACMO grid (in green) show a positive trend of $0.143 \pm 0.090 \cdot 10^6 \text{ km}^2/\text{dec}$ at a 95% confidence level (about 1.3% of the total Antarctic sea ice extent per decade).

In spite of large uncertainties about the absolute values of the trends over the last three decades, it is clear that the overall Antarctic sea ice cover has been increasing. Due to a lack of measurements, it is not really possible to make reliable statements on how long this increase has been present. By using earlier satellite data that are less reliable and exist since the early 1970s Cavalieri et al. (2003) conclude that

the current positive trend should be seen in perspective to a very strong decline of the sea ice extent in the early 1970s. A model study by Goosse et al. (2009) even suggests that the decline might have been persisting throughout most of the last century. Several authors list a decline of the Antarctic sea ice over the past hundred years by comparing current values to observations by ships. A summary of these findings is given by Mayewski et al. (2009).

Next to the long-term increase in the last decades, the sea ice cover is subject to a large interannual variability which becomes apparent by examining the 12-month-running mean (in red in figure 5.1). It can be studied by considering the residuals after subtracting the trend from the anomalies. In figure 5.1, it can be seen that the amplitude of the variations in the 1980s was somewhat larger than in the early 1990s. It increased again in the late 1990s, and became even larger in the period of the AMSR-E dataset. It is unclear whether the latter increase can be associated with the change of the instrument. The standard deviation of the period between 1979 to 2006 is with about $0.39 \cdot 10^6 \text{ km}^2$ slightly higher than the one in the period 1989 to 2008 with about $0.35 \cdot 10^6 \text{ km}^2$ which is induced by the rather low variability in the early 1990s and higher variations in the 1980s.

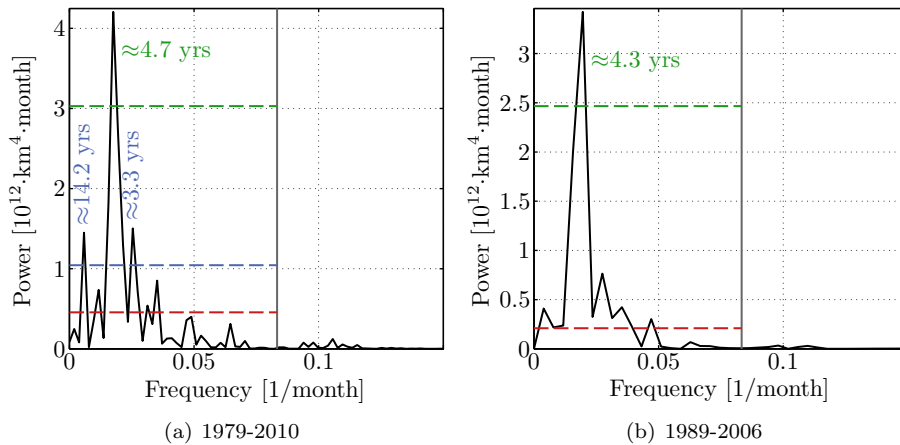


Figure 5.2: Power spectra of the sea ice extent anomaly residuals for the time series 1979 to 2010 (a) and 1989 to 2006 (b). Obtained by computing the Fourier transform function from the 12-month-running mean data. The gray bar indicates the frequency limit imposed by the running mean filter ($1/12 \text{ month}^{-1}$). The red dashed line is the average power until the limit. In the left figure (a), there is a peak at a period of about 4.7 years with a corresponding lower 99% confidence bound in green. Further, there are two significant peaks at 14.2 and 3.3 years (in blue). For the shorter time period (b) there is only one significant peak at 4.3 years at a 99% confidence level.

The interannual variabilities of the residuals of sea ice extent anomalies in the periods 1979 to 2010, and 1989 to 2006 are presented in figure 5.2 in form of power spectra which I have derived with a Fourier transform function (Trauth and Sillmann, 2010). The significance of the peaks is estimated by comparing the 99% confidence interval to the mean power of the resolved frequencies using a χ^2 -test (Warner, 1998). In the longer time series, there are three significant peaks at a period of about 14.2, 4.7, and 3.3 years, where the 4.7 years period is dominant. In contrast, the shorter time series only resolves the latter peak that has a period of about 4.3 years. Consequently, this is the only interannual variability that can be studied with this dataset. This is reflected in figure 5.1(a) by either positive or negative anomalies that typically last for 2 to 3 years. Between 1989 and 2006 there have been three strong positive anomalies (1994 to spring 1996, 1998 to spring 2001, 2003 to spring 2005) and four weaker negative anomalies (early 1990s, spring 1996 to 1997, spring 2001 to 2002, spring 2005 to 2006).

The Antarctic sea ice cover has a very strong seasonal cycle with a minimum extent in February and a maximum extent in September (cf. figure 5.3(a) and (b)). During summer the sea ice almost completely melts except for some ice cover along the East Antarctic coast and in the Bellingshausen and Amundsen Sea sectors as well as a substantial ice pack that persists in the south-western Weddell Sea. In September,

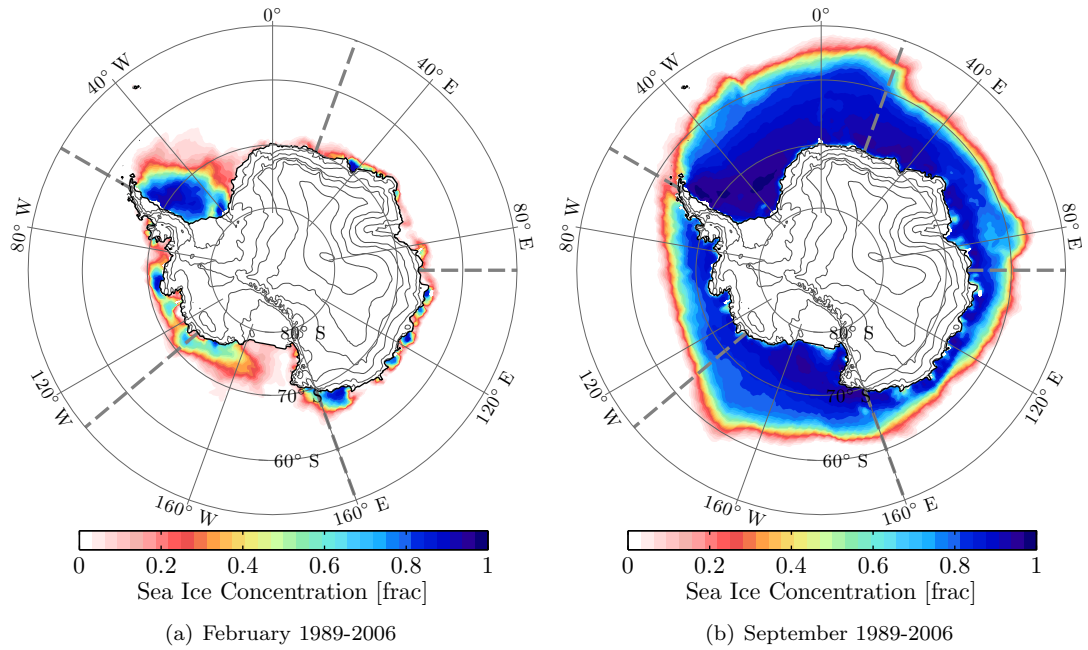


Figure 5.3: Sea ice concentration for the month of minimum (a) and maximum (b) ice extent in the mean seasonal cycle 1989 to 2006. Dashed lines indicate the five sectors.

largest extents of the ice pack are situated in the Weddell and Ross Seas. The overall highest sea ice concentration occurs in the south-western Weddell Sea where thick multiyear ice can be found. The coastal regions of the wintertime ice pack are frequently interrupted by low sea ice concentrations that are coastal polynyas.

The growth and decay of the Antarctic ice pack is shown in figure 5.4. It has been derived by, first, calculating the change of sea ice area per grid cell from one day to the other, then, summing up all grid cells, and, at last, calculating the average for each day of the year throughout the total time period. The seasonal cycle is mainly determined by the surface energy balance as I have discussed in chapter 4.1. Figure 5.4(a) illustrates that the overall growth of the ice pack starts by the end of February when the ocean surface regionally becomes subject to strong cooling (cf. figure 4.3(a)). It peaks in late April and early May when most of the open ocean is covered with ice again. Hereafter, the growth rate continuously decelerates. In late September the ice slowly starts to melt from the ice edge. The melt rate accelerates quickly during this period which is owing to the ice-albedo feedback (cf. chapter 2.3). It peaks in early December and, then, decreases again as the total ice area strongly reduces and the ice pack disintegrates.

By comparing figures 5.4(b) to (d), that show the 20-days running mean rates of area change for the Ross, Bellingshausen and Amundsen, and Weddell Seas respectively, one cannot only observe a different amplitude of the growth rate but also a different phasing. The strongest autumn increase of the growth rate occurs in the Ross Sea and peaks already in late March and early April which is much sooner than in the other regions. In the southern Ross Sea, adjacent to the Ross Ice Shelf, the large open water region that was formed in summer (cf. figure 5.3(a)) freezes first which is owing to the very negative atmospheric surface energy balance (cf. figures 4.3(a) and (b)). This also implies that the ice pack is formed much sooner in the Ross Sea. The overall largest growth rate, however, occurs in the Weddell Sea in May which is caused by the large total sea ice area of this sector. We can further observe that there is a dip in the growth rate in August for the Ross and Weddell Seas and even a loss of ice in the Ross Sea sector. As the surface still experiences cooling by the atmosphere at this time of the year, this is owing

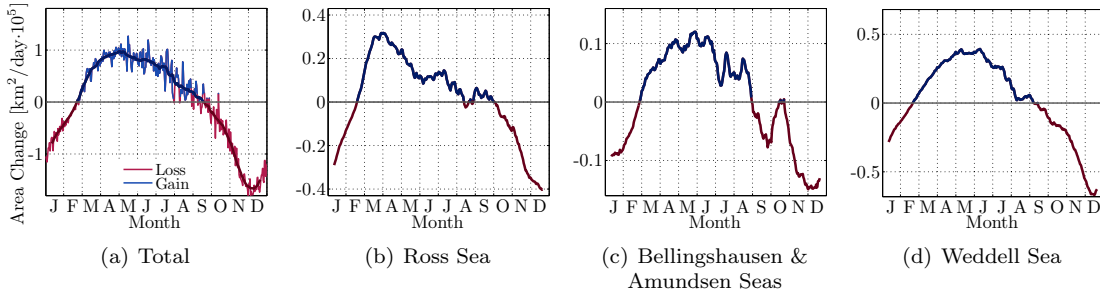


Figure 5.4: Average annual cycle of the daily rate of change of sea ice area (growth and decay rate) over the period 1989 to 2006 for the total Southern Ocean (a) and three sectors (b to d). Blue indicates the growth (or gain) and red the decay (or loss). The brighter colors for the total (a) are daily values and the darker colors are smoothed daily values with a 20-days running mean filter.

to other factors that I will discuss in the next section (5.2). Moreover, the earliest onset of the ice decay occurs in the Bellingshausen and Amundsen Seas sector in late August and the latest decay occurs in the Ross Sea. This points out that processes that trigger sea ice growth and decay are essentially different in these regions even on a seasonal basis.

The different growth and decay rates in the different regions of the Southern Ocean lead to an inhomogeneous pattern of sea ice cover in space and time. Consequently, in the following, I will discuss the interannual variabilities and trends for the different regions separately and I will also consider the differences in the long-term changes at different times of the year. Therefore, figure 5.5 shows the mean seasonal cycle of the sea ice cover (left), the monthly sea ice extent anomalies with respect to the mean seasonal cycle and the according 12-month-running mean and trend (middle), and the monthly trends of the sea ice extent and area (right) for each region. The spatial distribution of the variability is illustrated in the maps 5.6(a) to (e) for the whole year and each season respectively. They show the variance of the residuals of the sea ice concentration anomalies which can be used to detect regions of highest interannual variations (cf. box 4.1). The third set of figures that I am going to use here are the maps 5.7(a) to (e) that show the overall and seasonal trends of the sea ice concentration per gridbox.

I have already elaborated on the total Antarctic sea ice cover in the beginning of this section. However, for the sake of completeness, it is shown again in figure 5.5(a). In the right panel one can observe that the increasing sea ice extent and area mainly results from a strong increase in the second half of the year, in the months June through November. During summer and spring only a slight but insignificant positive trend is depicted.

The Ross Sea sector has the second largest wintertime sea ice extent and area, and the longest sea ice covered season of the Southern Ocean as it becomes apparent in the left panel of figure 5.5(b). This long season is related to the early onset of growth and late onset of decay as it was discussed before. Further, the time series indicates that the Ross Sea ice cover is subject to very large interannual variability. The sea ice concentration variance of the Ross Sea in figure 5.6 shows that this interannual variability occurs mostly in the south-eastern part of the sector, where the ice edge varies strongly in winter and spring. Here, the sea ice forms a bulge that might extend as far as 60° S. Not much variability takes place in the rest of the sector except for a slightly higher variance in summer along the coastline in the east.

The sea ice extent of the Ross Sea shows an overall increase of about $6.59 \pm 6.53 \cdot 10^4 \text{ km}^2/\text{dec}$ at a 90% confidence level (about 2.3% of the Ross Sea sea ice extent per decade) which is the strongest and only significant increase of all sectors. In the right panel of figure 5.5(b) one can observe that the increase is strongest in the season of the ice pack growth, even though it is not significant on a monthly basis. In consideration of figure 5.7(a), one can identify two major areas of significant increase in the western Ross Sea. The ice edge seems to advance further northward in the north-west. This signal is present throughout all seasons, except for summer, and seems to penetrate eastward in spring. Another region of

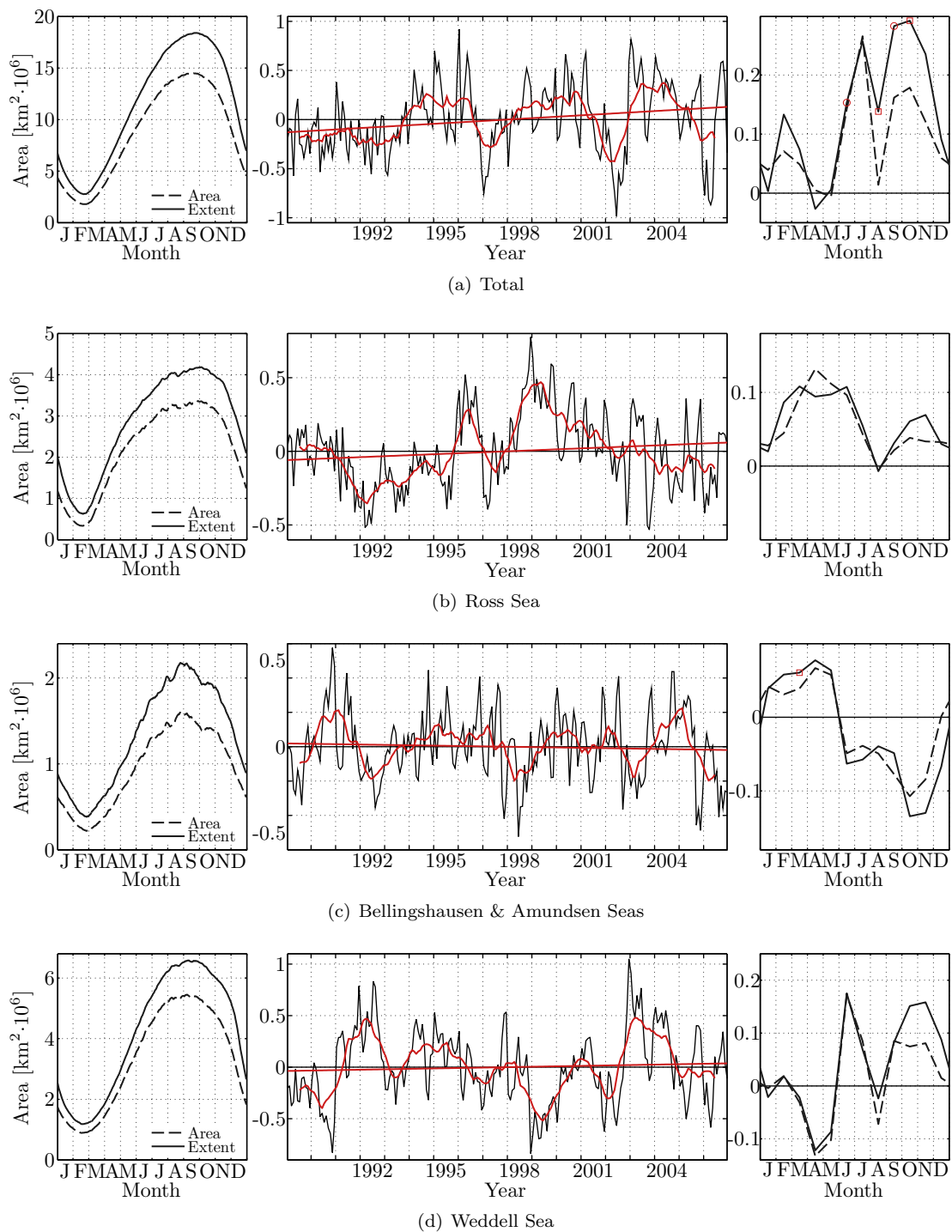


Figure 5.5: (continued on page 81)

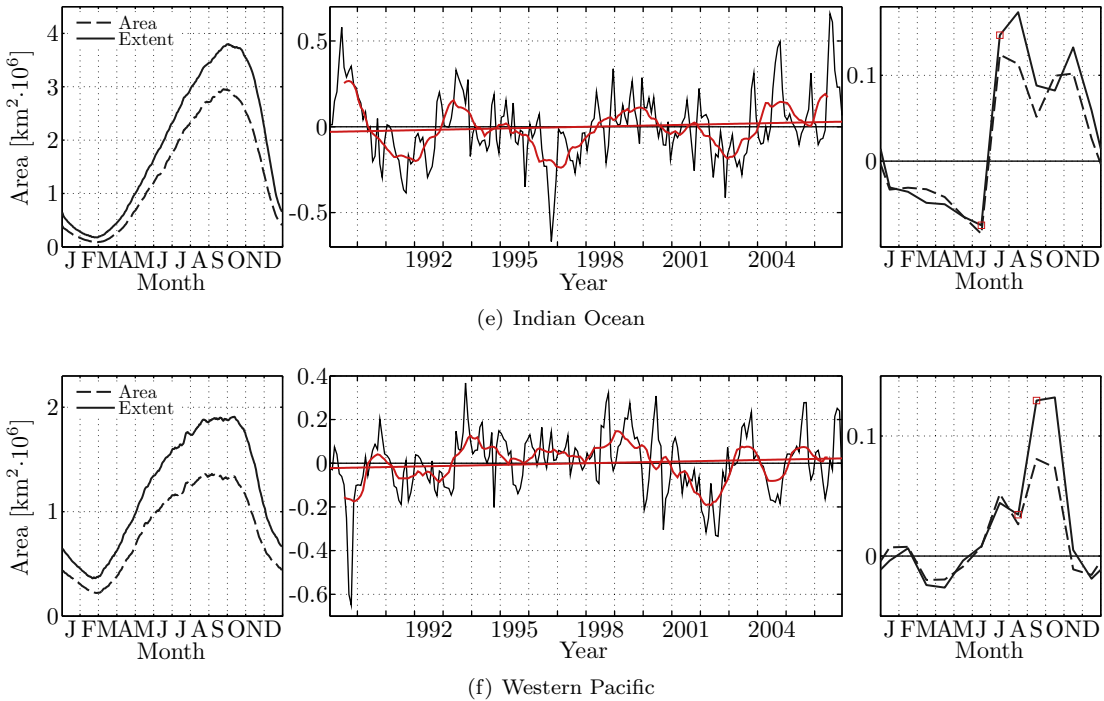


Figure 5.5: (continued) Left: Average seasonal cycle of sea ice area (dashed line) and extent (solid line). Middle: Interannual variations of sea ice extent anomalies and the corresponding 12-month-running mean and trend (red). Right: Monthly trends of sea ice area (dashed line) and sea ice extent (solid line) in $10^6 \cdot \text{km}^2/\text{dec}$. For the monthly trends of sea ice extent circles indicate a 95% and squares a 90% confidence level.

increase can be found close to the Ross Ice Shelf which is mainly due to a higher sea ice concentration in summer and autumn. This is probably related to a summertime cooling trend in the lower atmosphere in this region which we can observe in figure 4.7(e). In contrast, in the eastern Ross Sea, a rather strong negative trend occurs in spring and summer which is mostly insignificant due to the high interannual variability that is present in this region.

The overall trend in the Bellingshausen and Amundsen Seas is slightly negative which is, however, insignificant (cf. figure 5.5(c)). Cavalieri and Parkinson (2008) report a strongly negative trend for this sector which is mainly related to a significant decrease in the period 1979 to 1989 which is not considered here. Interestingly, the trend depends on the season, as one can detect in the right panel of figure 5.5(c), with an increase of the autumn sea ice cover and a decrease in winter and spring. This pattern also occurs in figures 5.7(b) to (e). Along the west coast of the Antarctic Peninsula sea ice cover increases year-round. In contrast, in the Amundsen Sea the spring decrease is significant. It is quite likely that this trend is coupled to increasing temperatures in the atmospheric surface layer that are visible in the simulated temperature trend in figure 4.7(e). A modeled increased advection of warmer air masses from lower latitudes in winter and spring (cf. figures 4.13(c) and (e)) result in higher temperatures. The effect on the sea ice in winter, however, is not as strong as in spring because the temperatures are mostly well below freezing and a negative ice concentration trend occurs only at the ice edge in the Amundsen Sea and eastern Ross Sea. In spring, the higher temperatures enhance the melting of the sea ice and trends get more negative. Increasing temperatures imply a thinner ice cover which increases the heat conduction from the ocean through the ice and warms the atmosphere even further. Consequently, once the ice starts to melt or just less sea ice freezes a positive feedback is induced. By studying the interannual variability in figure 5.6, a rather high variation of the ice edge becomes apparent in winter and spring. However, we cannot observe such a pattern in the variance of the potential temperature (cf. figure 4.6). Accordingly, other processes must be responsible for these variations.

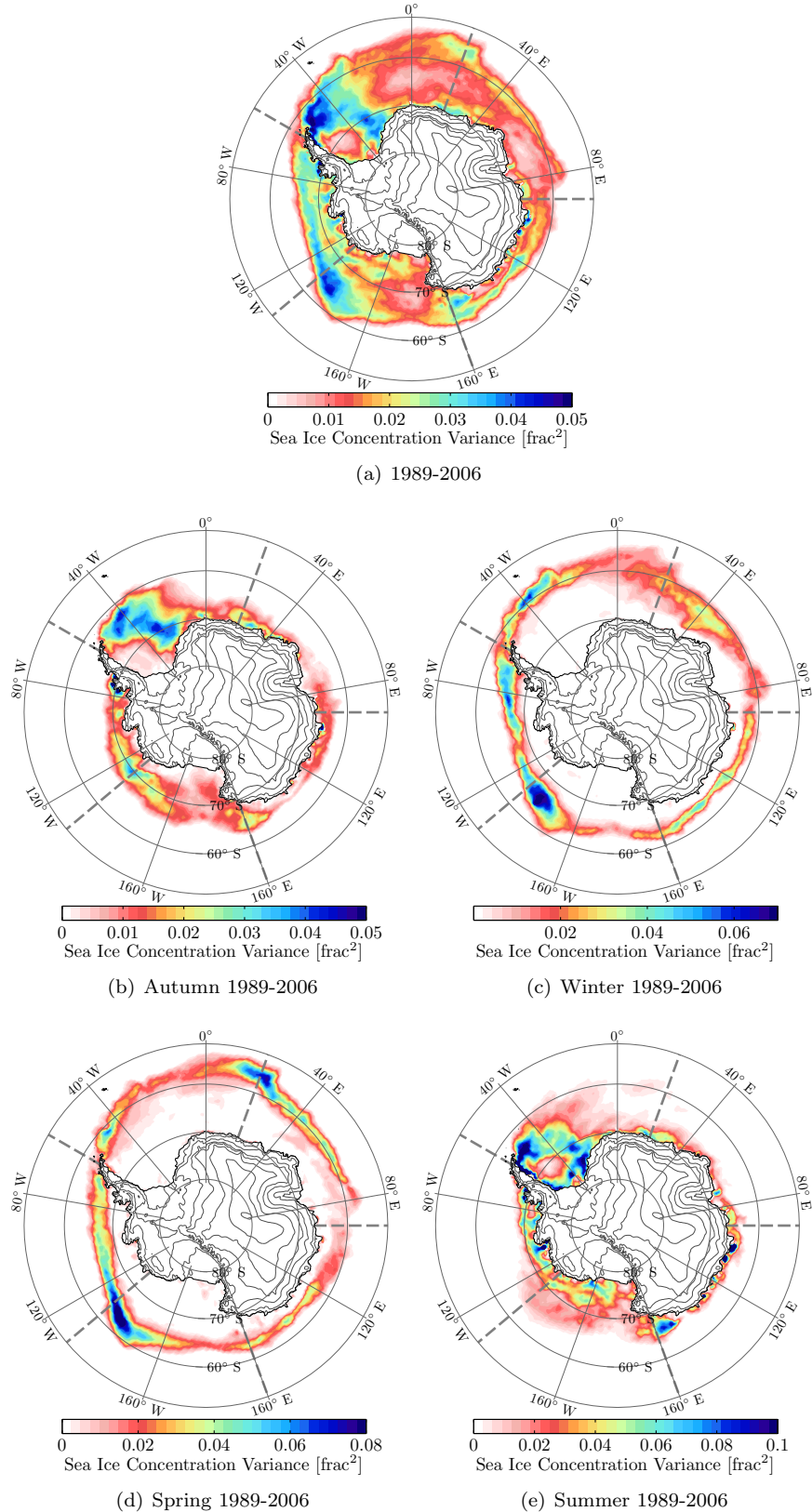


Figure 5.6: Variance of detrended sea ice concentration anomalies. Dashed gray lines denote the five sectors.

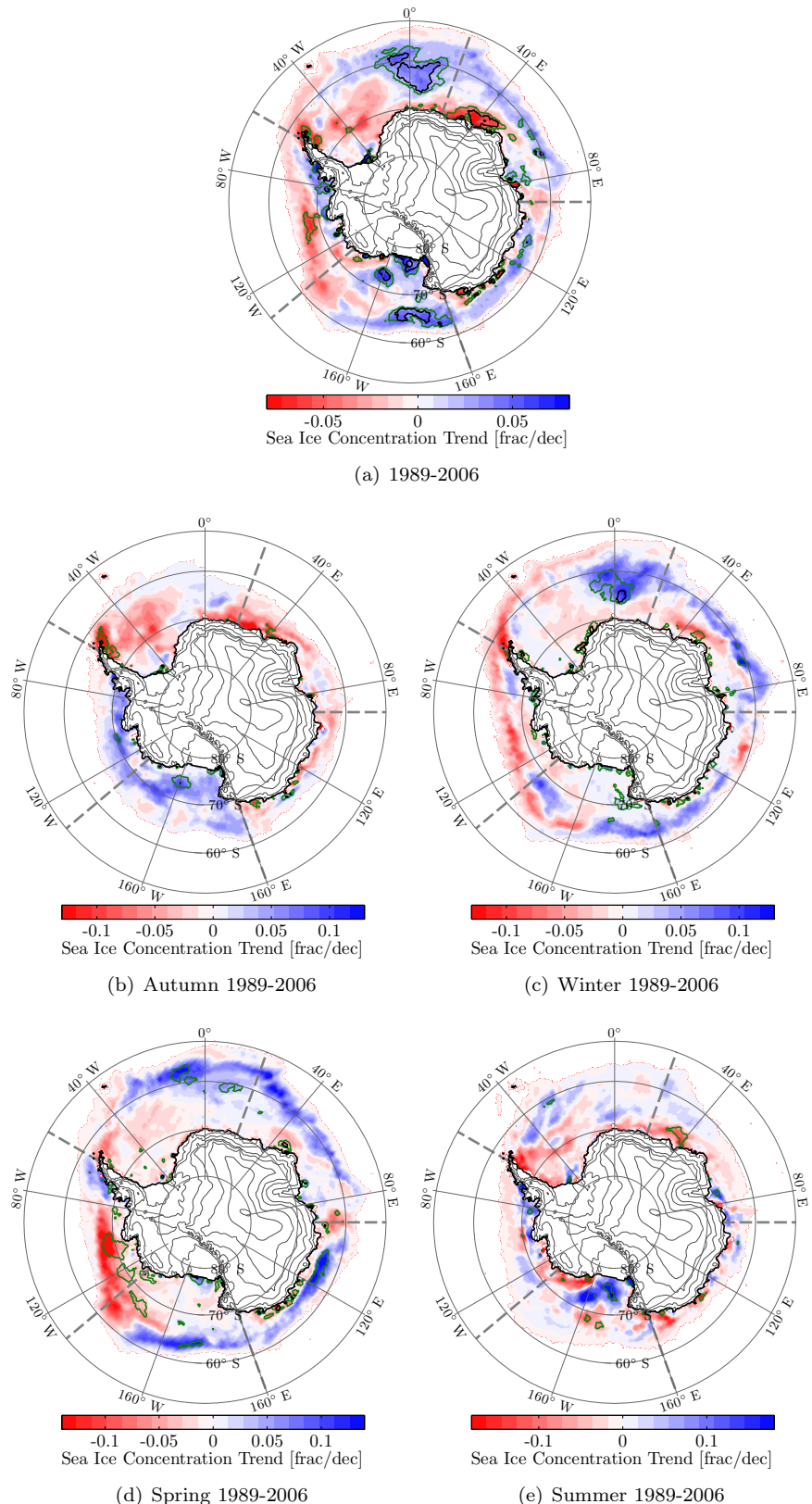


Figure 5.7: Decadal trend of sea ice concentration anomalies. Dashed gray lines denote the five sectors, and the green and black contour lines indicate the 90% and 99% confidence level respectively.

In the Weddell Sea the wintertime sea ice extent is the largest and subject to large interannual variability. Figure 5.6(a) shows that these variations mainly take place in the western Weddell Sea at the ice edge just north-east of the Antarctic Peninsula and off the coast of Coats Land. Most of the variability takes place in summer and autumn. At the ice edge, however, there are also substantial variations in winter. In springtime one might notice that the variance at the ice edge in the north-east of the Weddell Sea is rather large where a bulge occurs which we can also observe in the Ross Sea. Just south-west of this bulge a further region of significant sea ice concentration increase is situated which is mainly owing to an increase in winter and spring as illustrated in figure 5.7, in contrast to a decreasing ice cover in the western Weddell Sea. There, the strongest decrease occurs in autumn with significant values along the north-east coast of the Antarctic Peninsula. Further, one can observe that the ice pack in the south-west, which is the largest ice pack in summer, has a small and insignificant negative trend. This could be related to an increasing temperature over the Ronne and Filchner Ice Shelves and the adjacent sea as displayed in figure 4.7(e).

As I have already mentioned, there is an area of high variance in the north-eastern Weddell Sea at the ice edge where the sea ice extents further north. This bulge seems to propagate eastward from winter to spring into the Indian Ocean sector. Here, the highest variability in this sector is present together with a slightly increased variance along the ice edge in most of the sector during winter and spring (cf. figures 5.6(c) and (d)). The left panel in figure 5.5(e) shows that the seasonal cycle of the sea ice extent in the Indian Ocean sector peaks rather late in late September and early October. This is probably related to the propagation of the bulge from the Weddell Sea sector into the Indian Ocean sector and will be further discussed in the next section (5.2). The middle panel reveals a small and insignificant increase of the sea ice extent in this sector. However, on a monthly basis (right panel) a seasonally varying trend becomes apparent with a decreasing ice extent from January to June and an even stronger increasing ice extent from July to November. This pattern is confirmed by figure 5.7 that shows that the decrease is significant along the coast of western Enderby Land which mainly occurs in summer, autumn, and winter. Figure 4.7 shows a strong increase of the surface layer potential temperature in this region which is most pronounced in winter. The reasoning, here, is very similar to that of the warming in the Amundsen Sea as figure 4.13 shows an stronger advection of warmer air from lower latitudes. The winter and spring increase of the regional average can be attributed to a positive trend along the ice edge.

At last, the Western Pacific sector shows the overall lowest ice extent and area (cf. left panel of figure 5.5(f)). The time series and the monthly trends suggest a slightly increasing sea ice extent in late winter and spring. Figure 5.7 shows that this increase is significant along the ice edge mainly off the coast of western Wilkes Land. This coincides with a slight winter and spring cooling trend in figure 4.7. It should also be noted that there is an almost year-round significant decrease of sea ice concentration along the coast of George V and Adélie Lands. These trends are strongly regionally confined but are all significantly negative. In summer all along the coast of the Western Pacific sector a high interannual variance becomes apparent in figure 5.6. Medium values of variance are present in winter along the ice edge.

Before concluding this section, I am briefly going to discuss the dominant 4-to-5-year period of the interannual variability that was determined in figure 5.2 and that is most pronounced in the eastern Ross Sea and western Weddell Sea. Figure 5.8 shows a Hovmöller diagram for the 12-month-running mean of the sea ice extent anomalies. Anomalies are calculated for each 5° longitude bin. The dashed gray line is the time where the AMSR-E dataset starts. For this period the absolute amplitude of the anomalies might not be comparable to the period of the SSM/I data as the anomalies are calculated with respect to the mean seasonal cycle of the AMSR-E data. However, the pattern should be comparable. The blue bars (160° W and 110° W) indicate the eastern Ross Sea and the green bars (60° W and 10° W) the western Weddell Sea.

White (2003) reported the same dominant 4-to-5-year period of the variability in the years 1979 through 1991 and examined the evolution of the anomalies in a longitudinal direction by filtering all higher and lower frequencies. They showed that the anomalies are also present in the sea surface temperature, the meridional wind stress, and the sea level pressure and suggest that they propagate eastward with the circumpolar current which is referred to as Antarctic Circumpolar Wave. However, their conclusion is

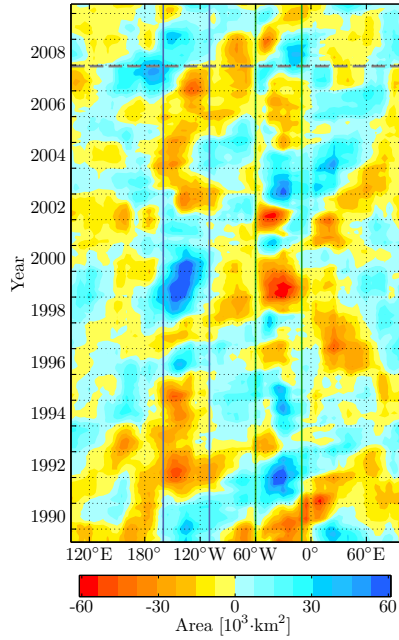


Figure 5.8: Hovmöller diagram for sea ice extent anomalies (12-month-running mean) per 5° longitude. The period 1989-2007 shows the SSM/I data and the period 2007-2010 shows the AMSR-E data (divided by the gray dashed line). The blue and green lines indicate the regions compared in figure 5.9.

mainly based on one event where the eastward propagation seems apparent. It should also be noticed that sea surface temperature anomalies are not independent from the sea ice extent anomalies and it is not clear whether they are caused by the sea ice anomaly or trigger the sea ice anomaly. An interesting thought experiment is to imagine a positive sea ice extent anomaly at a certain place in the Southern Ocean in late winter. The anomaly in lower latitudes might, then, propagate eastward with the circumpolar current and the westerlies, leading to a negative sea surface temperature slightly east of the sea ice anomaly as the ice melts in spring and summer. This colder ocean water freezes more quickly in autumn and trigger a positive sea ice extent anomaly further east. In figure 5.8 such a propagation of the anomaly might be detected by following lines from the lower left corner to the upper right corner. With some imagination one could identify a few such lines. However, this would need a more thorough investigation.

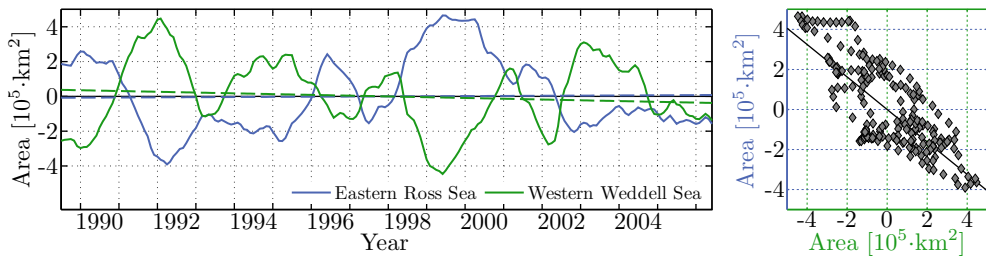


Figure 5.9: Time series (left) and scatter plot (right) of the 12-month-running mean of sea ice extent anomalies in the eastern Ross Sea (110° W to 160° W) and the western Weddell Sea (10° W to 60° W).

Another pattern that stands out in figure 5.8 is a dipole of the anomalies in the two regions of highest variance. Several strong events, such as in the years 1992 or 1999, show that the anomalies can be found in both regions at approximately the same time with an opposite sign. Yuan and Martinson (2001) analyze this pattern in detail and call it the Antarctic Dipole. A detailed statistical study revealed that

a relation between El Niño Southern Oscillation events and the temperature and sea ice extent anomalies is present in this dipole pattern (Yuan and Martinson, 2001). In figure 5.9 the sea ice extent anomalies of the two regions of highest variability indicated by the bars in figure 5.8 are compared. This reveals a very strong negative correlation between the interannual variability in the eastern Ross Sea and western Weddell Sea with a zero-lag correlation coefficient of -0.77 which is significant at a 99% confidence level. This suggests that the interannual variations in these regions are, indeed, linked to large-scale circulation processes in the atmosphere and the ocean.

In sum, the findings of this section showed increasing sea ice extent and area in the Southern Ocean which is mainly attributed to an increase in the western Ross Sea and eastern Weddell Sea. Nevertheless, there are also regions of significant decreasing sea ice cover in the western Weddell Sea, the eastern Ross Sea, the Bellingshausen and Amundsen Seas, and coastal areas in East Antarctica. Interestingly, there is either a meridional (Ross and Weddell Sea sectors) or a zonal (other three sectors) dipole pattern in the trends (cf. figure 5.7). This suggests a strong link to weakened or enhanced circulations on which I will elaborate in the following section. Moreover, trends also show a strong seasonal dependence and might even be of opposite sign at a different time of year. Patterns of interannual variance reveal that strongest variations occur in the western Weddell Sea and eastern Ross Sea. Generally, the highest variability occurs along the ice edge. In winter and spring it is most pronounced in the south-eastern Ross Sea and in summer and autumn it is strongest in the western Weddell Sea. Variabilities in these two regions are strongly negatively correlated which also suggests a link to large-scale circulation patterns.

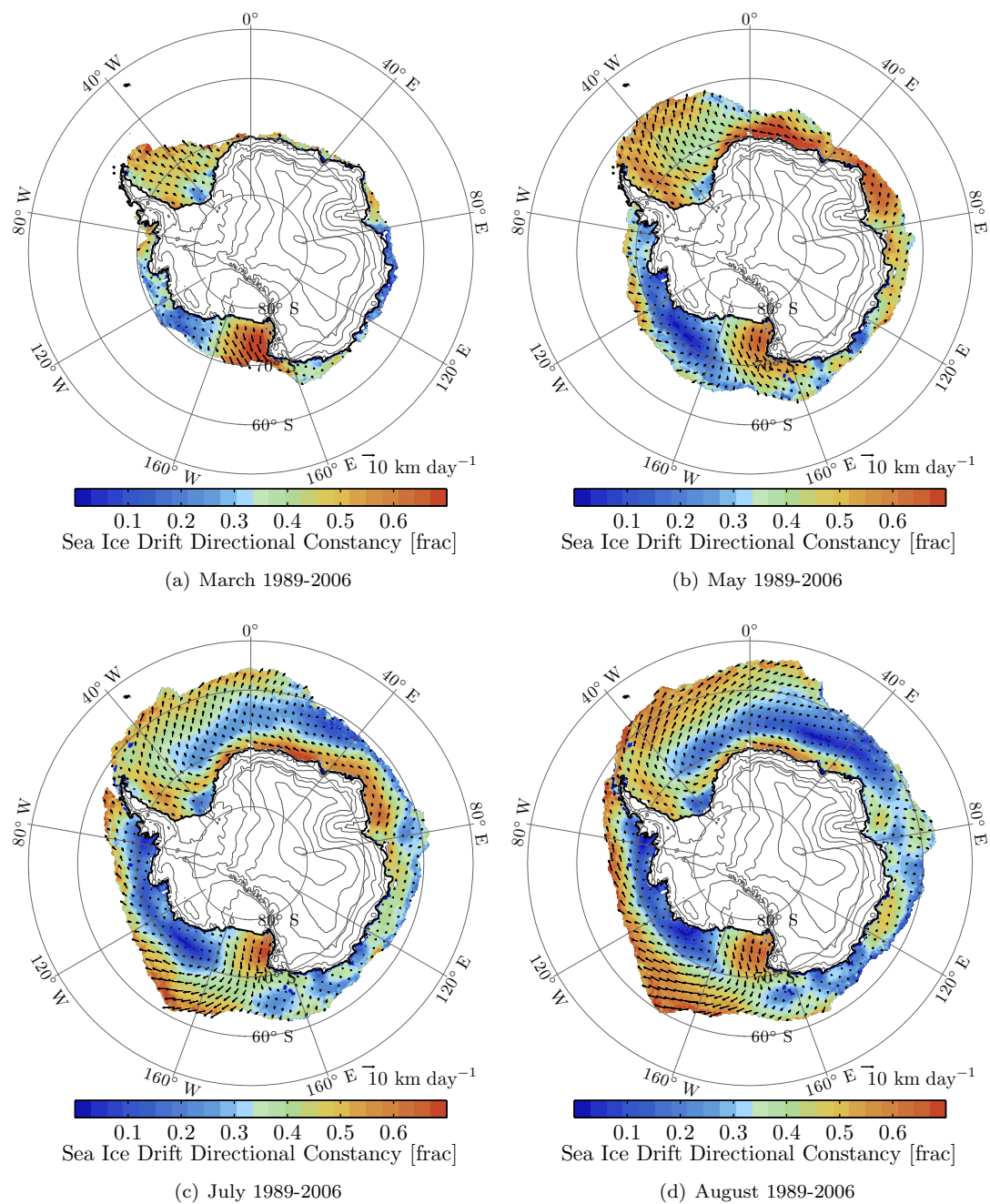
5.2 Sea Ice Transport

In this sub-chapter, I will discuss the variations and trends that occur in sea ice transport and, eventually, I will relate these changes to those revealed in the previous section (5.1). I will also point out regions where the mechanical redistribution of sea ice is of major importance and how these patterns can be associated with the wind field. Cavalieri and Parkinson (1981) report a strong interaction between the large-scale atmospheric circulation and the sea ice cover in the Ross and Weddell Seas for the year 1974. These results suggest that the transport in these areas plays a major role. At the time of their analysis, however, data availability was scarce and no information about the sea ice drift was available. Here, I will analyze the full sea ice motion record of the period 1989 to 2006.

Even though I will only analyze the relation to the wind field here, one should keep in mind that there are strong ocean currents present in the Southern Ocean that certainly have a strong effect on the sea ice motion. These currents include the two large cyclonic gyres in the Weddell and Ross Sea and the Antarctic Circumpolar Current. However, the ocean currents are to a large extent driven by the mean wind field and pressure distribution which, in turn, means that wind is the key driver of the motion and a comparison of the sea ice drift to the wind field should be valid in most cases.

In a similar fashion to the analysis in chapter 4.2, I will, here, describe the sea ice drift by using the directional constancy (defined in box 4.3). Sea ice drift vectors and directional constancy are mapped in figure 5.10. In March, when the ice pack forms, high values of directional constancy are present in the Ross and Weddell Seas and sea ice motion is dominated by a northward transport away from the Ross and Ronne Ice Shelves, respectively. This is in line with the southerly winds and high directional constancy illustrated in figure 4.10(a). Sea ice drift in the western Ross Sea has the highest directional constancy and is directed to the north-west where it drifts around Oates Land.

In May the sea ice cover has already advanced much further north. Except for the Bellingshausen and Amundsen Seas the drift has a rather high directional constancy everywhere and is directed to the north or north-west. North-westward drift occurs with a very high directional constancy along the East Antarctic coast in the Indian Ocean sector. This is clearly associated with strong and persistent easterly winds in winter that leave the continent and are deflected to the left by the Coriolis force in this region, as I have depicted and explained in chapters 4.2 and 4.3, and as can be seen in figure 4.10(b). In the Weddell Sea a large-scale, and rather constant northward drift of sea ice occurs. Even though the directional constancy of the wind field is rather low, the net geostrophic wind vectors are still southerly in this region which

**Figure 5.10:** (continued on page 88)

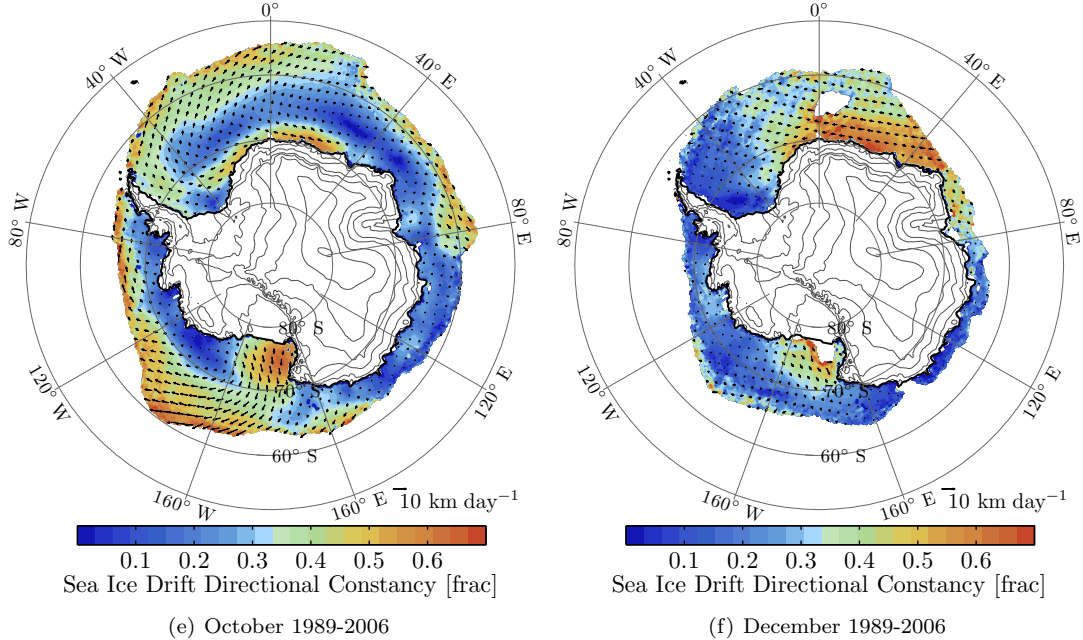


Figure 5.10: (continued) Observed sea ice motion vectors (only every sixth vector is plotted) and corresponding directional constancy.

is induced by a large-scale zonal pressure gradient in this area (cf. figure 4.9(b)). This indicates that the ice drift does not change its direction as fast as the atmospheric wind field and is more a result of the mean wind field which leads to a higher directional constancy. Due to the frequent penetration of cyclones into the Amundsen and Bellingshausen Seas directional constancy of the ice drift is very low in this region.

Until the month July the sea ice in the Ross and Weddell Seas extends as far as the west wind zone (cf. figure 5.10(c)). Here, the sea ice starts to turn into a eastward direction which becomes even more pronounced in August (cf. figure 5.10(d)) when the directional constancy along the ice edge becomes very high. Also the structure of the circumpolar pressure trough clearly stands out in August. In the Weddell Sea the expansion of the pressure trough towards the Antarctic Peninsula from July until October (cf. figures 4.9(c)) decreases the zonal pressure gradient and, as a result, the southerly geostrophic wind decreases. This is also visible in figures 5.10(c) through (e) where the directional constancy and the northward ice drift strongly decrease in the western Weddell Sea. In the western Ross Sea, however, this phenomenon does not occur. Despite the expansion of the pressure trough a slight zonal pressure gradient remains and northward ice drift persists with a high directional constancy throughout the year.

It seems that the sea ice extent only reaches as far as the west wind zone in late winter and early autumn if there is a region of southerly winds and an associated northward transport of sea ice as it is the case north to the Ross and Ronne Ice Shelves. Along the East Antarctic coast winds are easterly and confine the sea ice to the coast. An exception is the ice extent north to the Amery Ice Shelf. There, ice drift has a north-westward component and from late August to October it extends into the west wind zone (cf. figures 5.10(d) and (e)). Interestingly, also here a small northward bulge of the sea ice cover occurs as it was noticed already in section 5.1 for the north-eastern Weddell and Ross Seas. Apparently, these bulges are related to the extent of the sea ice cover into the zone of westerly winds and occur northeast to the region of northward sea ice drift.

In early summer when the ice pack disintegrates, ice drift and directional constancy generally decrease (cf. figure 5.10(f)). Exceptions are the south-western Ross Sea and a region of westward drift off the

coast of Enderby and Dronning Maud Lands. The latter is probably related to large-scale driven easterly winds in this region that persist throughout the summer.

The above relations between the wind field and the sea ice drift showed that the drift occurs approximately in the same direction as the wind direction. However, a more careful comparison would reveal that this is not always the case. In chapter 2.3, I have discussed the effect of the Ekman spiral on the sea ice. Accordingly, sea ice should drift at an angle of about 20° to 40° to the left of the wind direction. Subtracting the simulated wind direction from the observed sea ice drift direction, it yields in a distribution as illustrated in figure 5.11(a) for the average months of June through September in the period 1989 to 2006. A negative relative drifting angle implies a deflection to the left of the wind direction. The average angle (in blue) of about -29.5° is well within the expected range. However, the distribution reveals that only about half of all values have an average drifting angle between 0° and -45° . 90% of all values are between -95° and $+24^\circ$.

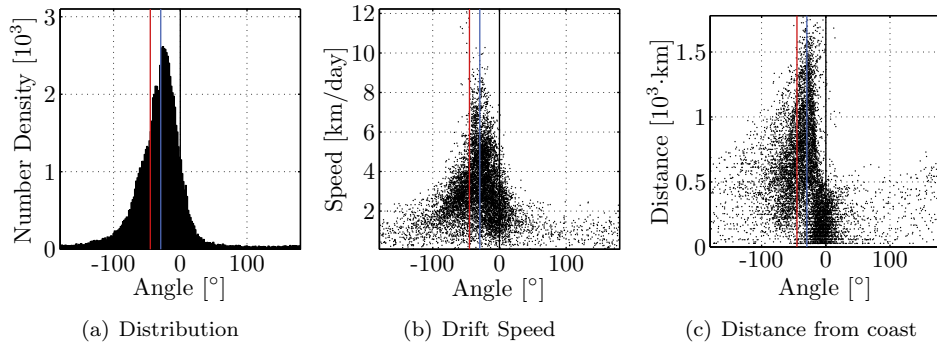


Figure 5.11: Difference between the direction of the sea ice drift and the wind direction over the sea ice covered ocean for the average months of June through September in the period 1989 to 2006. A negative angle translates to a turning to the left of the ice drift with respect to the wind. The red line denotes the theoretical surface drift of -45° and the blue line indicates the mean angle of about -29.5° : (a) a histogram of all angles separated in 200 bins of 1.8° ; (b) a scatterplot of all angles and the corresponding sea ice drift speed; and (c) a scatterplot of all angles and the corresponding distance from the coast.

Figure 5.11(b) illustrates that the relation between wind and drift directions is more pronounced for higher drift speeds which is essentially similar to the relation for higher wind speeds (not shown). A large scatter is present for values below 2 km/day. This implies that in regions where high sea ice drift velocities are found the drift direction obeys the wind direction. Moreover, an interesting relation between the relative drifting angle and the distance from the coast can be observed in figure 5.11(c) which implicitly shows the effect of lateral friction. Firstly, the scatter is much larger for the relative angle within the first 500 km from the coast. Secondly, within a distance of 300 to 400 km from the coast there is a larger amount of values with rather small angles. The average for all values within 300 km distance is about -13° and for all values within 100 km it is about -7° . These relations can be used to validate the dynamics of sea ice models. Here, however, it is important to notice that the drift direction might vary from the wind direction in order to understand the mechanical redistribution of the sea ice in either along-coast or off-shore direction.

Next, I will proceed with an analysis of the variabilities and trends of sea ice transport in meridional and zonal direction similar to the analysis performed in the previous section (5.1) for the sea ice cover. As sea ice concentration is highly variable in space and time, a volume or mass transport in each direction would be desirable. Due to the lack of ice thickness data, I will here use sea ice area flux which is defined in box 5.2.

Box 5.2: Sea Ice Area Flux

As sea ice thickness observations are still scarce and hard to obtain, Kwok (2005, 2009) defined sea ice area fluxes perpendicular to flux gates in the Arctic and Southern Oceans in order to estimate sea ice export fluxes of certain regions. Here, I will adopt this method in a slightly different form. Sea ice area flux is defined for each grid box by:

$$x\text{-direction : } F_x = u \cdot c \cdot dy, \quad (5.3a)$$

$$y\text{-direction : } F_y = v \cdot c \cdot dx, \quad (5.3b)$$

where dx and dy are the respective increment distances, and u and v the sea ice motion in each direction. The sea ice concentration is denoted by c . This method has the advantage that spatial variations of the area flux can be analyzed.

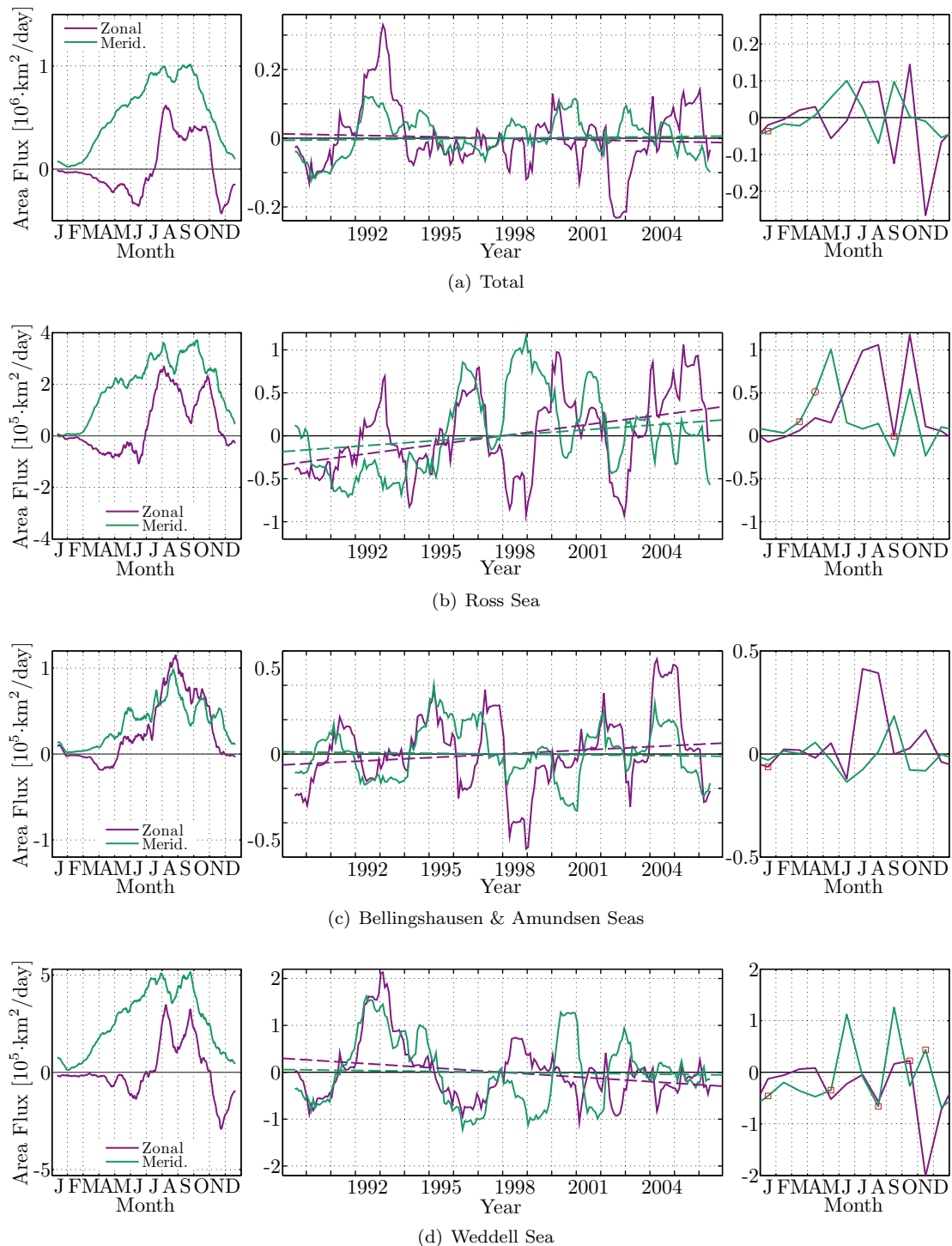
Figure 5.12(a) shows the mean seasonal cycle of meridional and zonal sea ice area flux for the total Southern Ocean in the left panel, the 12-month-running mean anomalies and trends in the middle panel, and the monthly trends in the right panel. A northward (positive) meridional transport persists throughout the whole year and increases in winter with an increasing sea ice area. The zonal transport is westward (negative) until June. Hereafter, it turns into an overall eastward (positive) transport when the ice extends into the west wind region. Interestingly, both the meridional and zonal transport show a decrease in late August and early September. This is associated with the semi-annual oscillation that I have described in chapter 4.2. At this time the circumpolar pressure trough is expanded and the westerlies are weaker along the ice edge. Consequently, the late winter decrease of transport is most pronounced in the seasonal cycles of the Ross and Weddell Seas (cf. figure 5.12(b) and (d)).

Anomalies of sea ice transport need to be interpreted with respect to the mean state so that a negative anomaly does not necessarily imply a weaker transport but rather a westward or southward component. This means that a negative zonal transport anomaly would translate to increased westward transport if the mean transport was already in that direction or a decreased transport if the background transport is directed to the east. The same consideration applies to positive or negative transport trends. The time series of the total sea ice transport in figure 5.12(a) does not show any clear trend and also the monthly trends vary throughout the year. Figure 5.14 clearly shows that this is caused by strong regional differences.

The Ross Sea experiences a strong increase of zonal ($0.38 \pm 0.35 \cdot 10^5$ km 2 /day per decade at a 95% confidence level, about 4.9% of the zonal Ross Sea area flux per decade) and meridional ($0.20 \pm 0.27 \cdot 10^5$ km 2 /day per decade at a 90% confidence level, about 3.5% of the meridional Ross Sea area flux per decade) transport as one can depict in figure 5.12(b). The monthly trends reveal a positive meridional trend in autumn and an even higher positive zonal trend in winter and spring. Map 5.14(a) illustrates that in the western Ross Sea the strongest annual northward transport trend can be found. In most regions it is significant at a 99% confidence level. If we compare this trend map to the sea ice concentration trend in map 5.7(a), we can identify that the increased sea ice extent in the north-western Ross Sea is related to an increased northward transport just south of this region. The ice extent increases in autumn, winter, and spring which is also the case for the northward transport. This finding is a, to my knowledge, yet unreported reason for an increasing sea ice extent in the north-western Ross Sea. The importance that the sea ice dynamics play in this region becomes apparent if we consider that, despite a warming of the atmospheric surface layer in winter and spring (cf. figure 4.7), sea ice extent and northward transport are increasing in the west of this sector.

In the eastern Ross Sea, however, the signatures are essentially different. Figure 5.7 shows that the zonal transport along the ice edge in the east is increasing, especially in winter (note the different scales in the figure). The meridional northward transport in the east, however, is strongly decreasing and compensates in the north-east for the increased zonal transport. This, together with strong positive temperature trends, might explain the decreasing sea ice cover in the north-eastern Ross Sea in spring.

The middle panel of figure 5.12(b) also shows that there is a large interannual variability of the sea ice

**Figure 5.12:** (continued on page 92)

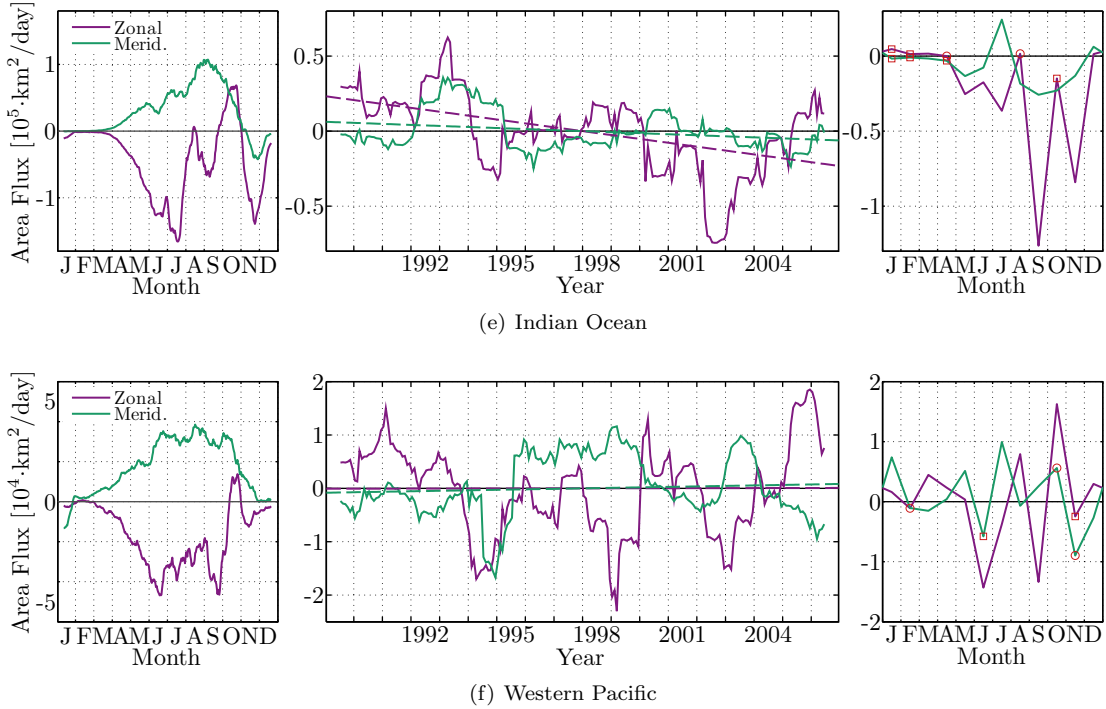
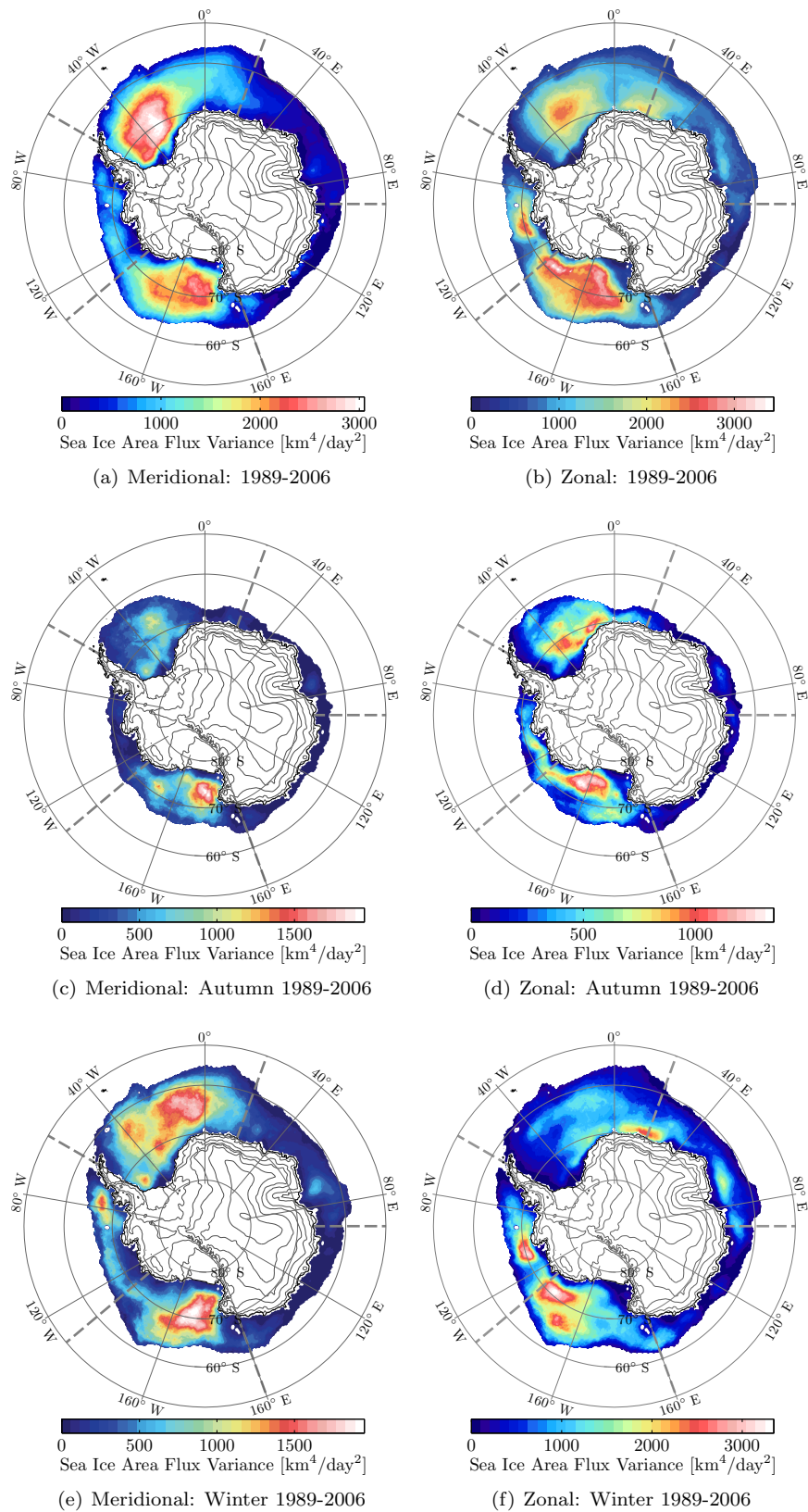


Figure 5.12: (continued) Left: Average seasonal cycle of meridional and zonal sea ice area flux. Middle: 12-month-running mean (solid) and trend (dashed) of meridional and zonal sea ice area flux anomalies. Right: Monthly trends of meridional and zonal sea ice area flux per decade. For the monthly trends circles indicate a 95% and squares a 90% confidence level.

transport, next to a high interannual variability of the sea ice extent in this region that I have already described in the previous section (5.1). By considering figure 5.13, that shows maps of the interannual variance of the transport anomalies (cf. box 4.1), we can notice that the Ross Sea is one of the two regions where highest variations of zonal and meridional transport are present. The variance of the meridional area flux is high in western Ross Sea in winter and in the eastern Ross Sea in spring. In the zonal direction, it varies most in the south-east in autumn and winter which implies that here transport can be either eastward or westward because the mean drift vectors and the directional constancy in figure 5.10 are very low in this region. During spring, zonal transport variations occur in the south-west which means that the transport in this area can be either north-westward or north-eastward. If we compare the strong interannual variance of the sea ice concentration in the north-eastern Ross Sea in figure 5.6 with the zonal and meridional area flux variations, we can observe that high sea ice concentration variance occurs just north-east of the area flux variations. This implies that these two variabilities are strongly coupled.

In order to further investigate the relation between the transport and the ice extent variations, figure 5.15 compares the 12-month-running mean values of the sea ice extent anomalies with those of the meridional area flux anomalies. Here, both relations that I previously discussed become apparent. Firstly, the strongly increasing meridional transport coincides with the increasing ice extent. Secondly, the interannual variability of the sea ice extent follows the meridional transport closely. This is also reflected in a very high correlation coefficient of 0.81 at a time lag of one month of the ice extent to the area flux which is significant at a 99% confidence level (cf. table 5.1). In other words, the meridional transport is responsible for most of the sea ice variability in the Ross Sea. The zonal transport, in contrast, shows a very weak and insignificant negative correlation of -0.17 which implies that it does not really play a role in terms of sea ice extent variations. How the variability and the transport relate to variations in the

**Figure 5.13:** (continued on page 94)

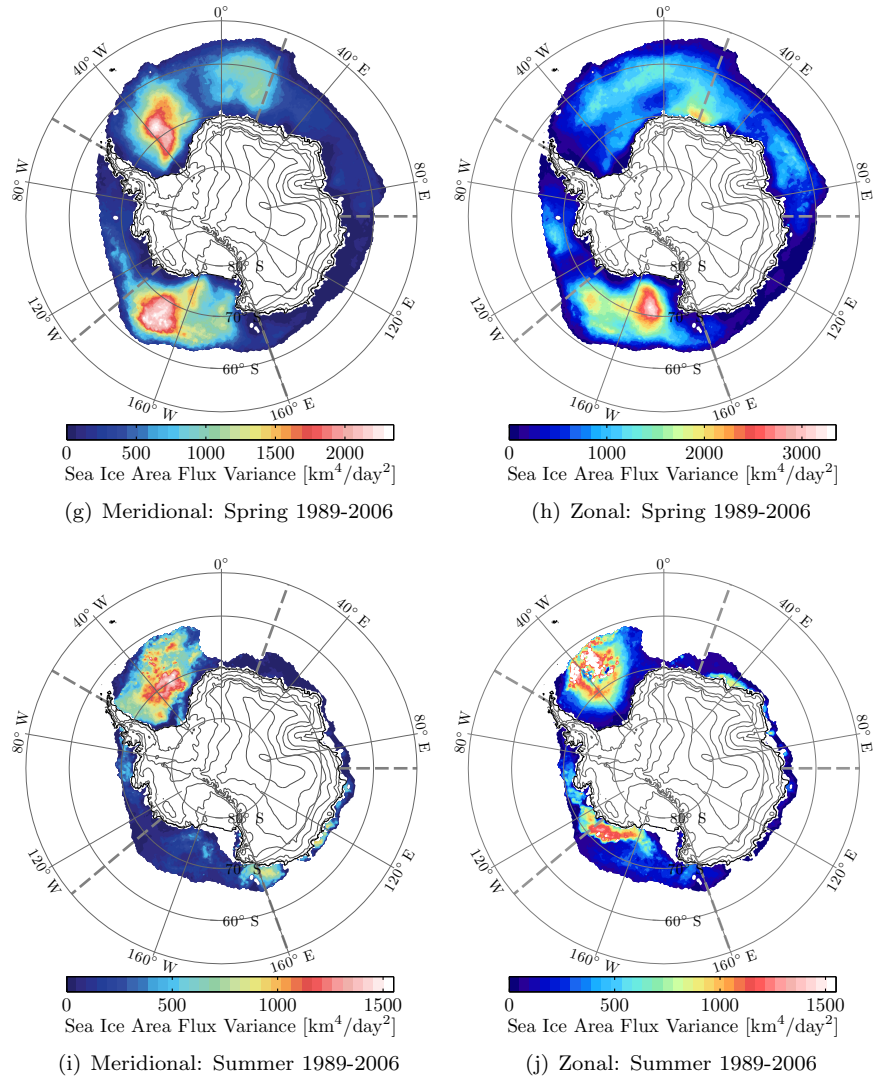


Figure 5.13: (continued) Variance of detrended meridional (left) and zonal (right) sea ice area flux anomalies. Dashed gray lines denote the five sectors.

atmospheric boundary layer in the Ross Sea region, will be discussed in chapter 6.1.

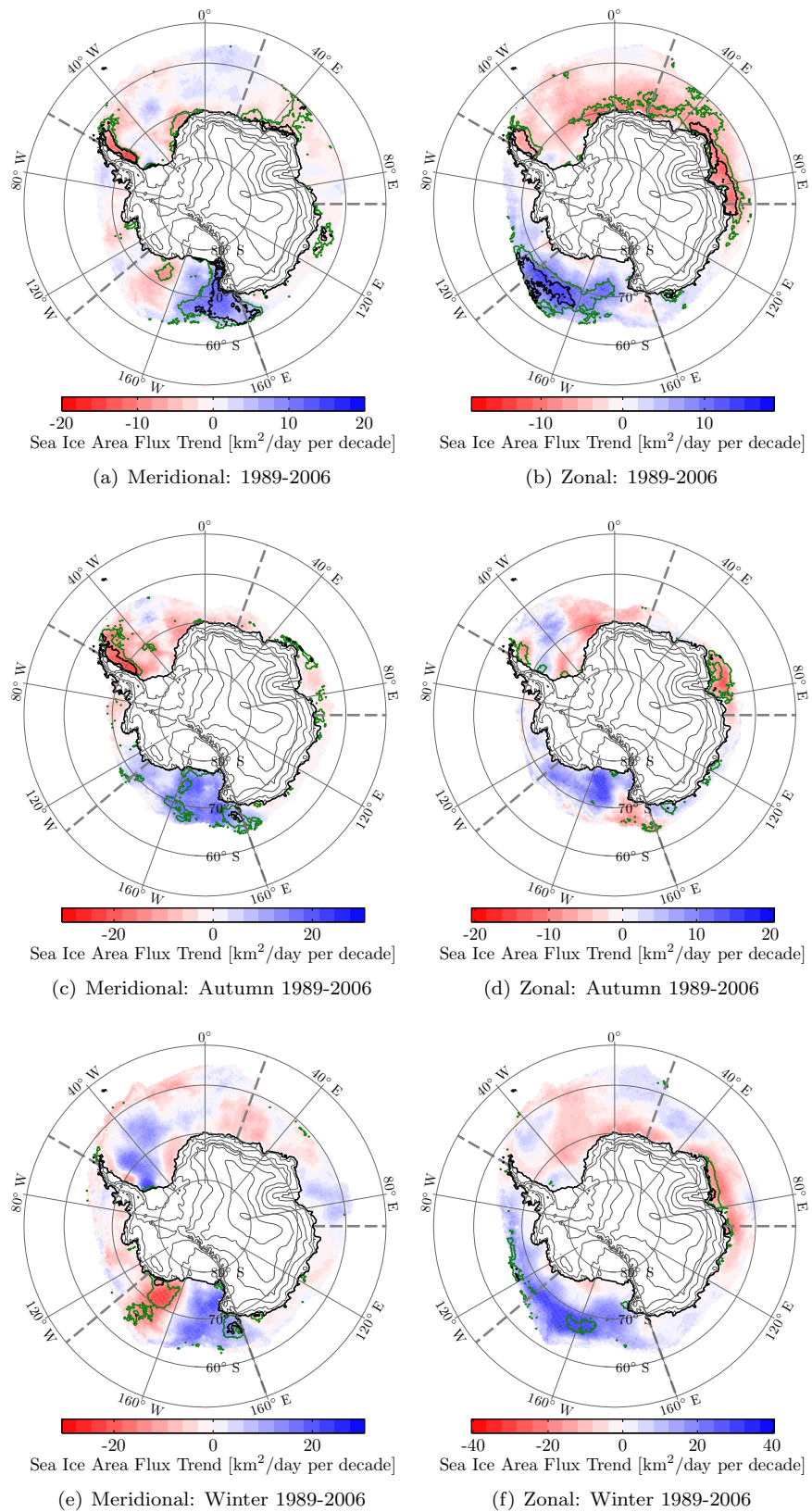
The Bellingshausen and Amundsen Seas sector is dominated by a northward transport in the early sea ice season and by an eastward transport from July to October which we can observe in the seasonal cycle in the left panel of figure 5.12(c). Another interesting feature is the strong peak of zonal transport in August. This explains characteristics observed in figure 5.4. Here, we could see a strong decrease of the daily change rate of sea ice area in the Ross Sea and an increase in the Bellingshausen and Amundsen Seas sector in August. Consequently, this is a result of a strong eastward transport from one sector to the other. It does not show any significant trend in one of the two transport directions. However, the zonal sea ice area flux seems to be slightly increasing mainly in July and August. This is due to an increase of eastward transport in the western Amundsen Sea coming from the Ross Sea which we can see in figure 5.14(f). Other than that, there are no significant changes of the transport which supports the hypothesis that the decreasing sea ice cover in this sector (cf. figure 5.7) is mainly related to an increasing warm air advection from lower latitudes in spring (cf. figure 4.7).

More interesting in terms of dynamical implications is the interannual variability of this sector. Figure 5.13 shows that there is considerable variance of the meridional transport in the Bellingshausen Sea in winter and high variance of zonal transport in the Amundsen Sea also in winter. This suggests that the interannual variations of the ice edge that are most pronounced in winter (cf. figure 5.6(c)) are related to transport variations. The Bellingshausen Sea extent variations are probably related to meridional and the Amundsen Sea to zonal area flux variabilities. Table 5.1 gives high and significant correlation coefficients to the sea ice extent for both transport directions which supports this hypothesis. The correlation to the zonal area flux anomalies is slightly higher. Figure 5.15(b) illustrates the relation between the sea ice extent and the zonal sea ice area flux anomalies. It also shows that the small trends are actually of opposite sign whereas the correlation is positive which means that the decreasing sea ice cover can probably not be explained by sea ice transport in this region. However, one might consider that an increased eastward area flux enhances the internal divergence of the ice pack as the Coriolis force acts northward and tears the ice pack apart. This could lead to more open water areas within the ice and a decreasing sea ice concentration.

The seasonal cycle in the Weddell Sea in the left panel of figure 5.12(d) reveals that there is a very strong northward transport throughout the sea ice season which is very similar to that of the Ross Sea. Figure 5.10 illustrated that the northward transport mostly takes place in the western Weddell Sea where the sea ice needs to turn north due to the Antarctic Peninsula as a topographic boundary. Zonal transport is westward (negative) from November until the end of June when easterly winds in the eastern part of the sector are dominant. During late winter and early spring when the sea ice extents as far as the westerlies the average zonal transport turns eastward (positive) with a strong dip in late August and September that is related to the semi-annual oscillation as I have described before.

The meridional transport trend in the Weddell Sea is only slightly negative. As figure 5.14 shows, this is due to a very regionally confined but strong decrease of the northward transport adjacent to the east coast of the Antarctic Peninsula which is significant in autumn and spring. In summer, it is rather strong as well but not significant. It is likely that this decrease causes the significant autumn decrease of the sea ice cover at the north-eastern end of the Antarctic Peninsula which is visible in figure 5.7(b). Additionally, the zonal transport trend in these regions is only slightly negative but significant which means that it probably turned from a north-eastward to a north-westward direction. From the Ronne Ice Shelf towards the north-east there is a strong but insignificant increase of northward transport in winter and spring. Associated with that is a stronger and also insignificant westward transport in both seasons in the eastern Weddell Sea. This means that more sea ice is transported along the coast to the west which, then, yields in a stronger northward transport. Finally, this increases the sea ice concentration in the north during winter and spring as it can be seen in figures 5.7(c) and (d). However, these meridional and zonal transport trends appear insignificant on the maps because they result mainly from a strong anomaly in the early 1990s as we can see in the time series of figure 5.12(d). The overall negative zonal trend of $-0.32 \pm 0.44 \cdot 10^5 \text{ km}^2/\text{day}$ per decade in the time series, however, is significant at a 90% confidence level (about -2.9% of the zonal Weddell Sea area flux per decade).

This turns the discussion to the interannual variability of the transport in the Weddell Sea which is dominated by the high anomalies in the 1990s and followed by much smaller amplitudes from the year 2000 onwards. Figure 5.13 shows that meridional area flux variance is high in the central Weddell Sea in winter and spring, and to some extent also in the remaining ice pack in summer. Zonal transport variations occur mostly close to the coast of Dronning Maud Land, and in the center of the summertime ice pack. It is remarkable that there seems to be no large variance of zonal transport in the west wind zone along the ice edge in winter. This implies that the interannual variation of the sea ice extent are not really affected by the zonal transport as variations only occur along the coast which is reflected in a rather low correlation coefficient in table 5.1. The meridional flux variability in the central Weddell Sea, in contrast, has a strong influence on how far north the ice extents (with a correlation coefficient of 0.61 at a time lag of one month that is significant at a 99% confidence level). Figure 5.15(c) illustrates this relation. It seems as the time lag changes in time. Sometimes the ice extent responds almost immediately to a change of the northward transport and at other times it takes much longer until there is a response

**Figure 5.14:** (continued on page 97)

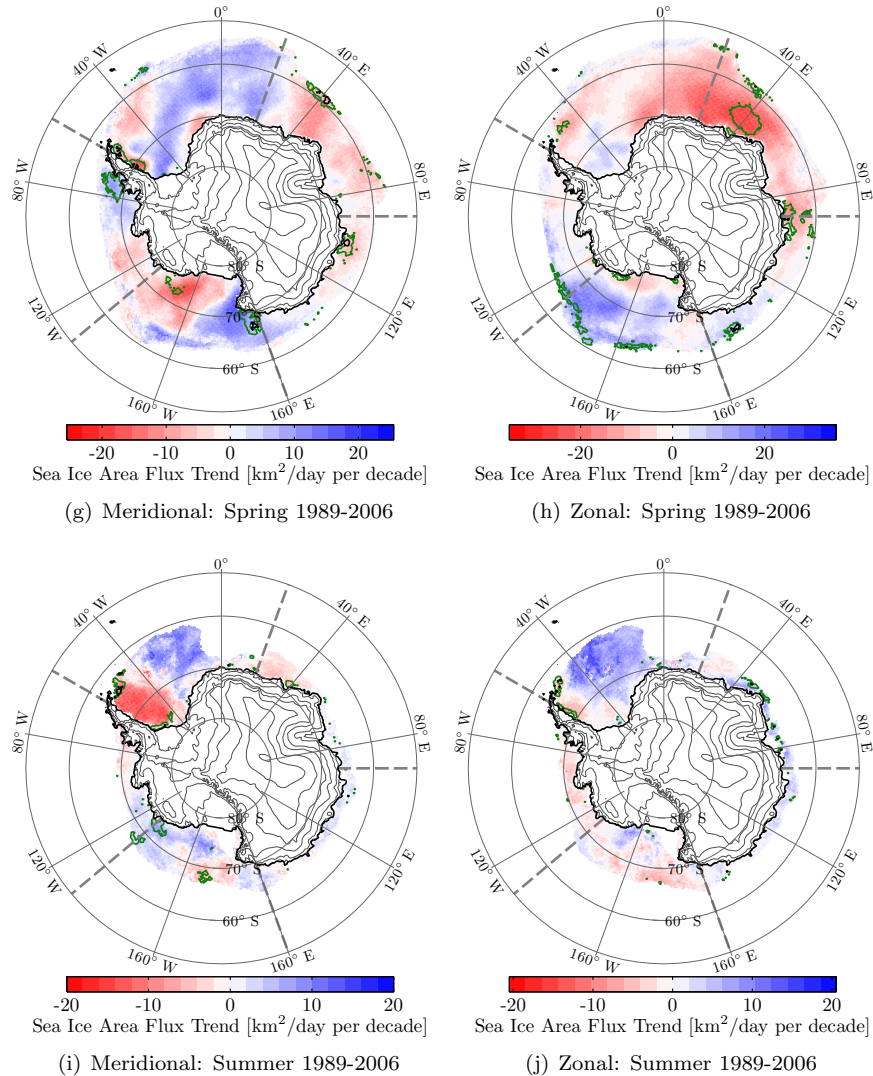


Figure 5.14: (continued) Decadal trend of meridional (left) and zonal (right) sea ice area flux anomalies. Dashed gray lines denote the five sectors, and the green and black contour lines indicate the 90% and 99% confidence level respectively.

of the ice edge.

The Indian Ocean sector is quite different from the other sectors in several respects as we can see in figure 5.12(e). It experiences strong variations of zonal transport throughout the year (cf. left panel). There is a strong westward transport by the dominant easterly winds in this region that I have described in chapter 4. Transport sets on in late March because the sea ice pack in this region builds up rather late. A strong westward and weaker northward transport is present until the end of July. In August, northward transport increases and the overall average westward transport decreases which is related to the fact that the sea ice edge reaches the westerlies in the east of the sector. The dip in September is probably again associated with the expansion of the circumpolar pressure trough and the northward movement of the westerlies. We can observe a strong eastward transport in October which is owing to the movement of the bulge in the north-eastern Weddell Sea into the Indian Ocean sector. This also explains the early spring peak of the annual cycle of the sea ice extent that we observed in the left panel

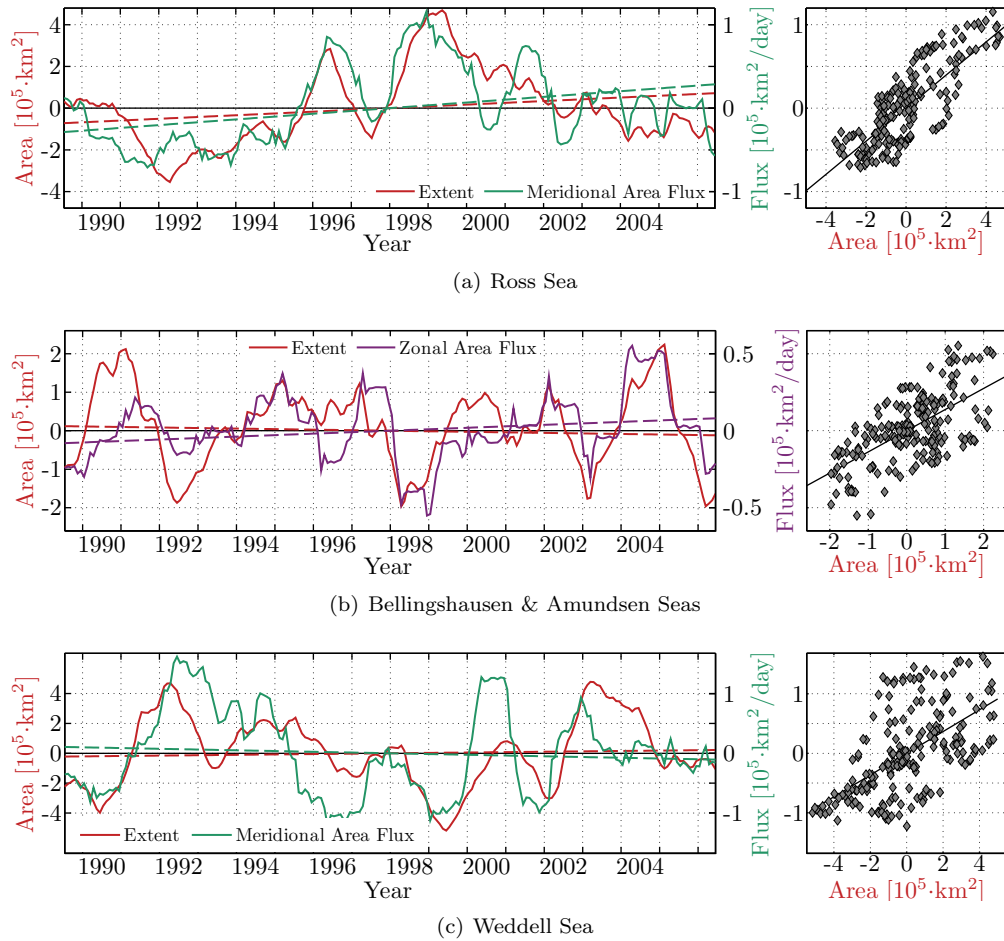


Figure 5.15: Time series of 12-month-running mean sea ice extent and mean area flux anomalies (left) with the long-term trend (dashed) and the corresponding scatterplot (right) for three sectors in which sea ice dynamics are very important.

Table 5.1: Correlation coefficients between the detrended 12-month-running mean of the sea ice extent anomalies and the meridional and zonal sea ice area flux anomalies for the total Southern Ocean and for each sector. All correlations are for a time lag of one month of the ice extent to the area flux. Significant values are highlighted with bold font and the subscript gives the corresponding confidence level in percent.

	Meridional Flux	Zonal Flux
Total	0.34	-0.14
Ross Sea	0.81₉₉	-0.17
Bellingshausen & Amundsen Seas	0.62₉₉	0.67₉₉
Weddell Sea	0.61₉₉	0.24
Indian Ocean	0.32	0.51₉₅
Western Pacific	0.39₉₀	-0.30

of figure 5.5(e).

There is a rather strong negative trend of the zonal transport of $-0.26 \pm 0.20 \cdot 10^5 \text{ km}^2/\text{day}$ per decade (about -4.9% of the zonal Indian Ocean sector area flux per decade) which is significant at a 95% confidence level (cf. middle panel of figure 5.12(e)). By considering the trend maps of figure 5.14, we can see that there is a significant increase of the westward area flux all along the coast which is most significant in the eastern part of the sector. Another feature that is apparent in spring is a strong negative trend in the central pack (cf. figure 5.14(h)). This results probably from the very strong negative anomaly in spring 2002 and is, hence, more related to interannual variations than to a long-term trend. In the meridional direction trends are very weak and mostly insignificant. The negative trends of the sea ice concentration anomalies in figure 5.7 along the coast of Enderby Land cannot be explained by changes of transport which supports the theory that these are related to the atmospheric warming in this region. The increasing ice concentration along the ice edge in the east of the sector, in contrast, might well be induced by the increased westward transport out of the region offshore of the Amery Ice Shelf. Moreover, a stronger westward transport induces internal convergence of the ice pack due to the Coriolis force that acts to the left of the transport direction. Consequently, the ice pack gets denser and the ice concentration increases. Figure 5.13 shows that there is considerable interannual variability of zonal transport in this region and also along the coast in the western part of the sector. Interannual meridional transport variations are, generally, very minor in the Indian Ocean sector.

At last, the Western Pacific sector is mainly dominated by a north-westward transport throughout the sea ice season which is also related to the overall low sea ice extent (cf. figure 5.5(f)). Trends in this sector are very small and insignificant. Further, neither the meridional nor the zonal transport show considerable interannual variations (cf. figure 5.13).

In conclusion, in this sub-chapter I have discussed the sea ice motion and the associated mechanical redistribution of the sea ice in detail and pointed out regional differences. This analysis resulted in new, unreported insights into the role that sea ice dynamics play in the Southern Ocean in terms of the sea ice extent. In the Ross Sea most of the interannual variability but also the long-term increasing sea ice extent in the west are explained by variations of the northward transport. Variations of the sea ice extent in the Weddell sea and the decreasing ice cover along the east coast of the Antarctic Peninsula are likewise associated with the meridional transport. In the Bellingshausen and Amundsen Seas both, meridional and zonal transport directions explain large parts of the interannual variability. The argumentation that transport and extent are strongly coupled is supported by the fact that trends and high variance values of the transport always occur downstream of the observed trends and increased variance of the ice concentration.

5.3 Open Water Formation and Sea Ice Production

In this last section of this chapter, I will briefly look at the open water areas within the ice pack and at the role that divergence and convergence play in terms of sea ice formation in open water. Open water

areas within the ice pack exist for two major reasons: Either the ice locally melts due to a heating from the atmosphere or the ocean, or the ice diverges and breaks due to wind or ocean current stress. In figure 5.3, one can observe that the open water within the wintertime ice pack in the Southern Ocean can generally be divided into open water that occurs close to the coast and open water that occurs close to the ice edge. The latter is mostly related to thermodynamic but also to dynamic reasons. In contrast, in the coastal region, open water areas must be related to an acceleration of the sea ice in offshore direction as, here, the atmosphere strongly cools the ocean surface in winter and open water would freeze almost immediately.

The total open water area of a region is defined in box 5.1. Its mean annual cycle is displayed in figures 5.16(a) to (h) for the total Southern Ocean and for the three denoted sectors. The minimum occurs in February which coincides with the minimum of total sea ice extent. However, the maximum is present in November whereas the ice extent maximum occurs in September. This is related to the fact that the ice edge starts to retreat in September but the open water formation processes within the ice pack due to the ice albedo feedback is much faster so that the open water area continues to increase.

Watkins and Simmonds (1999) discuss the annual cycle of the open water area in the Southern Ocean and report a strong surge of open water in late spring which is also visible in November in figure 5.16(a). They reason that in November the central axis of the circumpolar pressure trough crosses the ice edge while moving northward. This implies a change in the average direction of zonal transport. A resulting net westward transport of the ice leads to convergence in the central ice pack which we will see later. If the ice pack converges, ridging and rafting occurs which leads to a strong deformation and frequent cracks in the ice. These small open water areas, then, lead to an enhanced melt in the central ice pack due to the ice albedo feedback and enhanced heat conduction. This argumentation, however, is only valid if the dynamic and thermodynamic forcings act together. A convergence alone would not lead to a formation of large open water areas. Figure 5.12(a) confirms the switch from a net eastward to a net westward transport which supports the theory of Watkins and Simmonds (1999). Moreover, figures 5.16(b) to (d) show that the surge only occurs in the Ross and Weddell Seas which gives another reason to believe that the change of the net zonal transport direction amplifies the open water formation in late spring. As these are the only regions where the sea ice extends far north, they are under strong influence of the westerlies in late winter and early spring, and show a change of the mean zonal transport direction. This phenomenon points out that sea ice dynamics are also important on a seasonal timescale for the decay of the ice pack.

In order to assess the relative amount of open water with respect to the total sea ice extent, figures 5.16(e) to (h) show the average open water fraction which is scaled with the sea ice extent. We can observe that the relative open water fraction is highest in late summer and smallest at the end of July for the total Southern Ocean which means that it closely follows the thermodynamic forcing. In the Ross Sea, the open water fraction strongly decreases between mid February and the beginning of May and then stays constant at about 0.2 throughout the winter. Apparently, despite the atmospheric cooling the open water in this sector is retained throughout the winter. The open water fraction in the Bellingshausen and Amundsen Seas sector decreases more gradually and much later than in the Ross Sea. It does not increase as fast as in the Ross Sea in spring due to the absence of the open water surge. In the Weddell Sea, the open water fraction decreases until the end of July and follows the seasonal cycle more strictly. A strong increase is present in November. Further, the peak is reached already in December which does not coincide with the extent minimum. This is probably related to the very strong and pronounced surge in November and a very fast decay of the total ice pack hereafter.

The reason why the open water fraction is so persistent in winter in the Ross Sea is related to the existence of large coastal polynyas. Figure 5.17(a) shows the average September coastal open water for the period 1989 to 2006. It is defined as the inverse of the sea ice concentration that has a connection to the coast. A clear feature is a large open water area adjacent to the Ross Ice Shelf, the Ross Sea Polynya. Strong and persistent southerly off-shore winds (cf. figure 4.10) sustain this open water area during winter which explains the observed open water curve. Coastal polynyas are frequently present in winter all along the coast of the continent where strong and persistent katabatic winds leave the continent

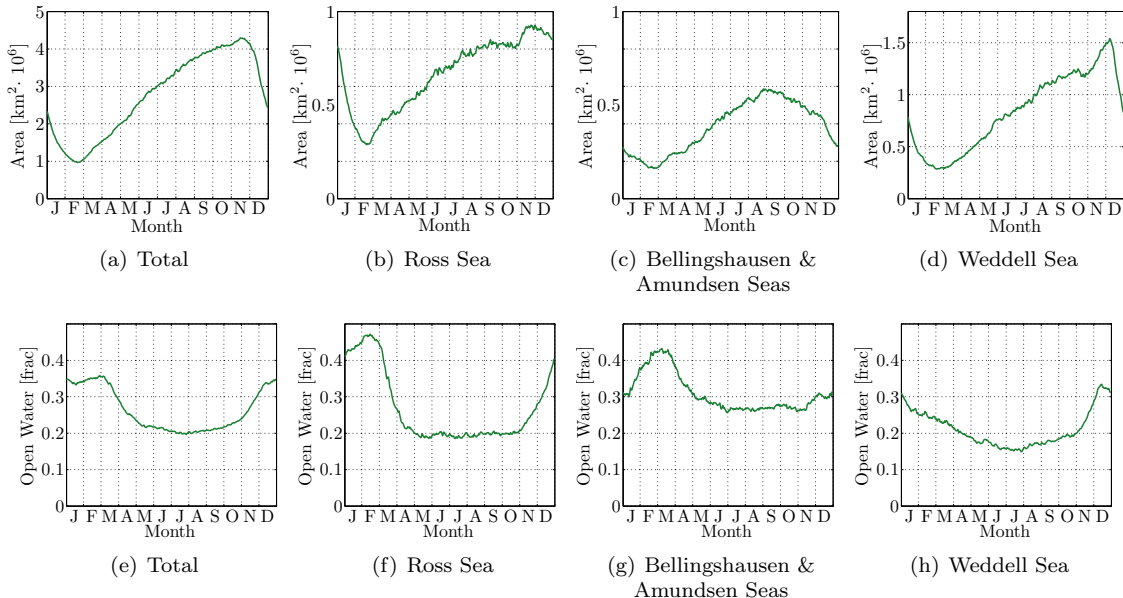


Figure 5.16: Average annual cycle of the daily open water area (a to d) and open water area scaled with sea ice extent (e to h) over the period 1989 to 2006 for the total Southern Ocean (a and e) and three sectors (b to d and f to h).

and induce off-shore motion. Adjacent to the Ronne Ice Shelf the Ronne Polynya is visible which is not as pronounced as the Ross Sea Polynya. At a short distance from the Ronne-Filchner Ice Shelf another polynya can be observed. However, this is not a real polynya but the stationary iceberg A23 which appears in this figure as a polynya due to the applied land-sea mask. In the eastern Weddell Sea at some distance off the coast an area of slightly higher open water fraction is present which is an artifact from the large Weddell Polynya that builds in winter far offshore due to upwelling warmer water (Barber and Massom, 2007). Sometimes the open water of this polynya is connected to the coast that is why it shows up in this figure.

Open water areas within the ice pack can be explained by considering the sea ice drift divergence. It is defined as:

$$\nabla \cdot \vec{U} = \frac{\partial u}{\partial x} + \frac{\partial v}{\partial y}. \quad (5.4)$$

Figure 5.17(b) illustrates this quantity for the average month of September in the considered period. Before interpreting the results, one needs to note several problems that arise. First of all, a grid structure is visible in the field which probably resembles the paths of the satellite. In this case the limit of the accuracy of the sea ice motion vectors is reached. Secondly, the issues in areas with strong interannual variability of the sea ice cover along the ice edge and in coastal regions, that I have discussed in chapter 3.3, clearly stand out. Even though vectors where the sea ice concentration was lower than 15% are not included, data is very noisy along the ice edge where fewer images contribute to the average vector. In the central ice pack, however, the divergence still gives valuable results for the long-term average. Vectors very close to the coast where the polynya occur would be very useful. Nevertheless, they were mostly removed due to inaccuracies.

In general, one would expect to find divergence in regions where sea ice gets accelerated by the wind field, for instance, in coastal areas with off-shore winds. If there is a lateral boundary in the direction of the ice drift or the wind and the sea ice decelerate, convergence (negative divergence) would be expected. Moreover, in terms of circulation, a cyclonic motion induces divergence and an anticyclonic motion convergence (on the southern hemisphere). Using these considerations, we can identify several

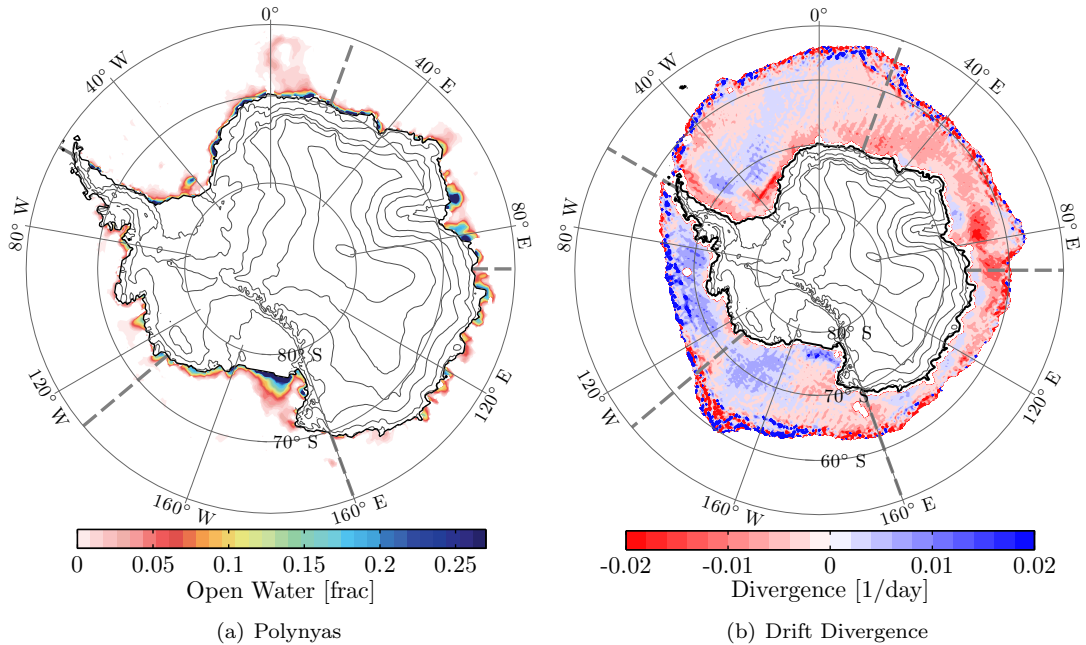


Figure 5.17: (a) Map of the average September polynyas in the period 1989 to 2006. (b) Map of the average September sea ice drift divergence in the period 1989 to 2006. Dashed contour lines denote the five sectors.

interesting features in figure 5.17(b). Adjacent to the Ross Ice Shelf where the Ross Sea Polynya is present, there is a region of strong divergence because the wind accelerates the sea ice off-shore. Just north of this region, we find an area of convergence. Here, the wind decelerates (cf. figure 4.10) and so does the sea ice. The cyclonic motion in the eastern Ross Sea (cf. figure 5.10) yields to a larger area of divergence. The same is valid for the Bellingshausen and Amundsen Seas.

North-west of the Amery Ice Shelf, close to the coast, off-shore transport results in divergence and a large polynya forms. Further north, strong convergence occurs where northward transported sea ice converges with sea ice transported from the east (cf. figure 5.10). Over the whole central pack of the western Indian Ocean sector and along the coast of the eastern Weddell Sea, we can observe a band of convergence. This is owing to the westward transport around the continent that has an overall anticyclonic direction of the drift. This convergence also explains why the sea ice is confined to the coast in regions of westward transport and in absence of any northward driving component.

In the western Weddell Sea, the westward transport continues despite of the absence of directionally constant easterly winds (cf. figure 4.10). Here, probably the Weddell Sea gyre is the key driver of this drift. Further to the west, the Antarctic Peninsula imposes a lateral boundary to the westward flow and convergence can be found all along the coast. The convergence leads, due to ridging and rafting, to much thicker sea ice in this area which explains the persistence of the ice pack even throughout the summer. Moreover, off-shore winds from the Ronne Ice Shelf (cf. figure 4.10) would imply a large coastal polynya such as in the Ross Sea. However, the formation of such a large polynya is suppressed by the strong convergence due to the general westward ice drift. Consequently, close to the coast a polynya forms, as it can be seen in figure 17(a), but it cannot extend far north because of dynamical reasons. In the more central western Weddell Sea, in contrast, the cyclonic motion of the ice drift induces ice divergence.

Not only can we use the divergence to describe where open water and thick ice areas occur but we can also use it to estimate locally the net transport out of, and into a grid box. If we, then, subtract this transport divergence from the total rate of change of the sea ice area (A) in one grid box from one day to the other, the residual should yield the amount of sea ice area that is produced or that melted in this

grid box. Consequently, sea ice area production P is defined as:

$$P = \frac{dA}{dt} - \left(\frac{dAu}{dx} + \frac{dAv}{dy} \right). \quad (5.5)$$

This quantity is, however, somewhat unrealistic as the ice thickness is not considered so that for example in an area of strong convergence ridging and rafting occurs and the sea ice area production gets negative even though no melting occurs. Also, the issues that I have discussed in relation to the divergence are introduced into this quantity. This implies that only long-term averages can be studied and uncertainties are very large. The accuracy decreases towards the ice edge and towards the coast. It is still worthwhile to briefly study the sea ice area production as it is illustrated in figure 5.18. A further argument that sea ice area production gives valuable results is that the basal freezing of ice that is omitted in this term only adds to the ice thickness but the freezing in open water areas, that is visible in this quantity, changes the total sea ice area.

The maps of figure 5.18 show the annual cycle of the sea ice area production. In March, when the ice pack starts to grow, large area production occurs in the open water region in the southern Ross Sea, adjacent to the Amery Ice Shelf, and along the coast of the western Weddell Sea. As the ice edge advances north from March to July a pulse of high area production along the ice edge becomes apparent that is rather induced by local freezing than by transport. We can, further, observe that area production remains positive throughout the winter in the southern Ross Sea but also adjacent to the Ronne Ice Shelf and in other coastal areas. Consequently, these regions where open water is present, are very important for sea ice formation. Here, sea ice forms fast as the strong cooling by the atmosphere rapidly freezes the open water. Hereafter, it is exported out of this region. Moreover, in May and July we can identify regions with negative values of area production in the western Weddell and Ross Sea at some distance north of the ice shelves. This implies that the sea ice is strongly thickening due to convergence. In October, the ice starts to melt from the ice edge and to some extent in the central pack. Nevertheless, the Ross Sea Polynya is still an area of ice formation. In December, the whole ice pack is subject to strong melting. Two features, the Weddell Sea Polynya and the Ross Sea Polynya, clearly stand out as completely ice free areas in this month.

The increasing northward transport in the Ross Sea and the decreasing northward transport in the Weddell Sea, that I have discussed in the previous section (5.2), suggest that also the sea ice production should have changed in the considered period. Despite the large uncertainties in the sea ice area production and the rather noisy dataset, I attempt to analyze the long-term changes in these two regions. Using yearly sea ice area production anomalies seems to give more robust results than the monthly values that I have used for other quantities. Figure 5.19(a) shows an increase of the area production in the Ross Sea of $1.26 \pm 1.75 \cdot 10^5 \text{ km}^2/\text{year}$ per decade which is statistically significant at a 90% confidence level (about 2.5% of the total production in the Ross Sea per decade). However, the given uncertainty is only of statistical origin and does not include uncertainties induced by the data retrieval. The Weddell Sea has a negative trend of $-2.92 \pm 3.70 \cdot 10^5 \text{ km}^2/\text{year}$ per decade which is statistically significant at a 90% confidence level (about -4.0% of the total production in the Weddell Sea per decade) and can be seen in figure 5.19(b). Even though uncertainties are large, the long-term changes coincide with what was expected according to the changes of the meridional transport.

These results are confirmed by a recently published study by Drucker et al. (2011) who compare the total sea ice production of the Ronne Polynya and the Ross Sea Polynya and find similar trends for the period 1992 to 2008. Their analysis is based on a procedure that was applied by Comiso et al. (2011) for the Ross Sea Polynya who also report a positive trend of this region. The procedure is confined to very local areas along the ice shelves and it makes use of high resolution satellite images. Further, they include estimates of ice thickness and report ice volume production rather than the here used ice area production. Drucker et al. (2011) further conclude that the production of the Ross Sea Polynya is three times as large as the production adjacent to the Ronne-Filchner Ice Shelf. This is, however, not comparable to the results in this thesis because production is expressed as the total sum in each sector. Another finding by Drucker et al. (2011) and previously by Kwok (2005) shows an increase in sea ice export across a

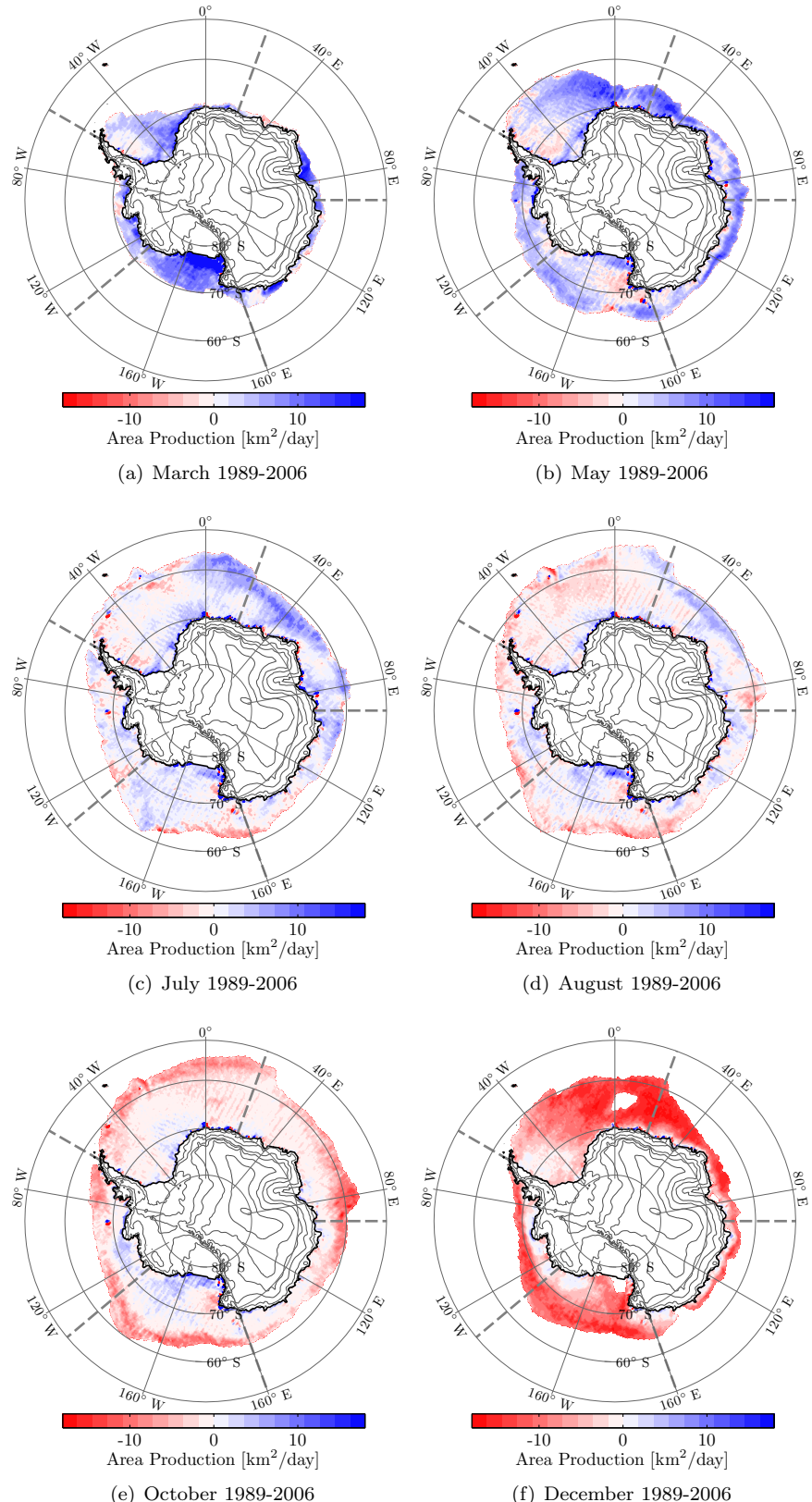


Figure 5.18: Sea ice area production retrieved with the daily rate of change of sea ice area and the sea ice divergence of each grid box. Dashed contour lines denote the five sectors.

flux-gate north of the Ross Ice Shelf. This is in line with the increasing meridional transport that I have described in section 5.2.

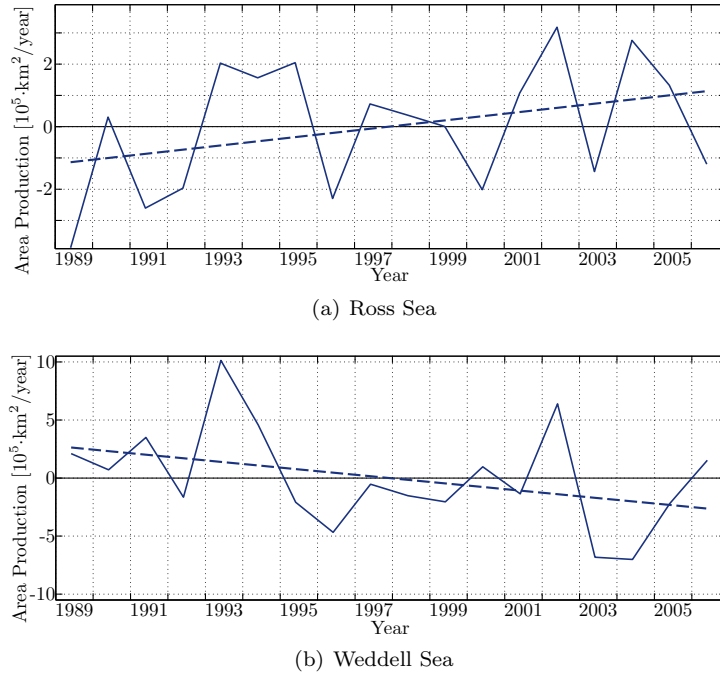


Figure 5.19: Time series of yearly sea ice area production anomalies and the corresponding trend (dashed) for the Ross Sea (a) and the Weddell Sea (b).

In conclusion, in this section, rather simple methods to analyze the open water area within the ice pack, the divergence of the ice, and the sea ice formation added to the overall understanding of the spatial distribution of the sea ice in the Southern Ocean. Further, I have related the change of sea transport to the sea ice formation processes in coastal open water areas. In the two sectors of high importance of the meridional sea ice transport to the sea ice extent, large areas with high sea ice area production exist along the coast north of the large ice shelves. The total sea ice area production in the Ross Sea sector is increasing and the one of the Weddell Sea is decreasing.

In the following chapter, I will analyze the relation of the northward transport of sea ice and the total sea ice extent in the Ross and Weddell Seas to the southerly wind field and the cold air pooling on the Ross and Ronne-Filchner Ice Shelves. This will combine findings of this chapter with those of the previous chapter and will reveal more insights into the atmosphere-ice interaction.

6 Regional Assessment of Cold Air Outflow over Sea Ice

In this part of my thesis I will use the findings of the last two chapters to further analyze the relation between variations in the atmospheric boundary layer and the sea ice. The previous chapter (5) showed that the mechanical redistribution of sea ice, especially in a meridional direction, plays a key role in the understanding of the variations of the sea ice cover in the Ross and Weddell Seas. I will assess the driving atmospheric forces behind these northward transport and extent variations. In chapter 4 I have described the cold air pooling over the large Ross and Ronne-Filchner Ice Shelves and the accumulation of cold and stable air on the sea ice covered ocean in front of these ice shelves in winter. A detailed analysis showed that the cold air pooling in front of the orographic barriers together with the large-scale pressure distribution set up a strong southerly wind system. These winds are responsible for an export of cold air over the sea ice. Now, I will further expand on this processes and explain the relation between sea ice formation and transport and the cold continental winds.

Chapters 4.3 and 4.4 showed that the topography and the cold air masses over the continent - over the large ice shelves in particular - are the factors that are responsible for the spatial patterns of the flow in coastal Antarctica. Southerly winds that we can find in the Ross and Weddell Seas, and that transport cold continental air over the sea ice exist only due to the presence of meridional orographic barriers, namely the Transantarctic Mountains and the Antarctic Peninsula. In other areas cold air is only transported along the coast in a westward direction due to the prevailing easterly winds.

The cold air is expected to have a profound effect on the sea ice. The southerly winds lead to a northward sea ice transport (cf. chapter 5.2) which, in turn, induces open water areas in coastal regions (cf. chapter 5.3). The open water, then, freezes very quickly because the air that is advected over the sea ice from the continent is extremely cold. In order to capture this process and compare the atmospheric variability to the sea ice, I have derived an index that I refer to as cold air outflow. Cold air export from the continent by the wind component that is perpendicular to the coast line is defined in box 6.1. The described process, eventually, leads to a higher northward sea ice transport if a higher outflow is present and at last causes a higher sea ice extent.

In order to test this hypothesis I will study the cold air outflow from the large Ross and Ronne-Filchner Ice Shelves in this chapter. Consequently, I will resume the regional analysis at the ice shelf edges that I have started in chapter 4.4. Further, I will relate the outflow to sea ice transport and extent in the Ross Sea in section 6.1 and in the Weddell Sea in section 6.2. As in chapter 4.4, I will do this for the winter month of July.

6.1 Ross Sea and Ice Shelf Area

In the Ross Sea southerly near-surface winds are much stronger than in the Weddell Sea and also more persistent throughout the year and from one year to the other. This is mainly related to the sheltering by the East Antarctic ice sheet and to the larger barrier that induces stronger temperature gradients across the ice shelf. Not only are those winds stronger, but also does their influence reach much further north than in the Weddell Sea. As we have seen in chapters 5.2 and 5.3, this directly influences the northward transport of the sea ice and the formation of coastal polynyas.

The high meridional transport yields in a high importance of the sea ice dynamics for the sea ice extent in this region as it is reflected in figure 5.15. If one now computes the correlation coefficient between the sea ice extent anomalies and the meridional transport anomalies (12-month-running mean) for each grid box in the Ross Sea as it is shown in figure 6.1, the spatial distribution of this relation shows a clear pattern. A band of high positive (between 0.5 and 0.8) and significant correlation is present from the ice shelf over the whole central Ross Sea towards the ice edge. This hints at an influence of the production in coastal areas on the sea ice extent as anomalies are transported from the coast towards the ice edge.

Box 6.1: Cold Air Outflow

Cold air that is exported from the Antarctic continent over the surrounding sea ice and ocean can be expressed as the product of the velocity of the wind component that is perpendicular to the coastline (V) with a positive value for winds leaving the continent and the potential temperature (θ) at a given location and height. Hence, it is a similar quantity to a heat flux and has the unit Kms^{-1} . However, to assess the cooling potential that the air has on the ocean surface (which is desired to relate it to sea ice processes), it needs to be referenced to the ocean surface temperature (θ_{ref}). A good approximation is given by the freezing temperature for sea water as a reference which is about $-1.8^\circ C$ (or $271.35 K$; cf. chapter 2.3). Cold air outflow F , then, is given by:

$$F_{i,x} = (\theta_{i,x} - \theta_{ref}) \cdot V_{i,x}, \quad (6.1)$$

where i and x denote the vertical level and the location along the coast, respectively. It should be mentioned further that the wind speed is set to zero if it is directed from the ocean towards the continent because this process is not of interest in this case. Consequently, cold air outflow is negative if it is strong (temperature deficit and positive wind speed) and positive if the air that leaves the continent is actually above the freezing temperature and induces melting of ice which is rather unlikely to occur.

The location of the evaluation of cold air outflow in the y -direction, perpendicular to the coastline, is crucial for the outcome. The temperature is influenced by a cooling or heating from the surface and the wind by the roughness of the terrain. In order to avoid the warming effect of the open water areas on the lower atmosphere in the outflow parameter, it should be assessed on the continental side of the coastline which will result in an undisturbed temperature deficit with respect to the ocean freezing temperature. The total cold air outflow along a segment of the coastline such as an ice shelf (between x_1 and x_2) in a discretized form is given for each atmospheric layer (i) by:

$$\hat{F}_i = \frac{\sum_{x=x_1}^{x_2} (\theta_{i,x} - \theta_{ref}) \cdot V_{i,x} \cdot dh_{i,x} \cdot dx_{i,x}}{\sum_{x=x_1}^{x_2} dh_{i,x} \cdot \sum_{x=x_1}^{x_2} dx_{i,x}}, \quad (6.2)$$

where dh and dx are the increments in the vertical and horizontal direction for each grid box, respectively.

Since the flow patterns of the wind field and the sea ice drift agree very well, it is reasonable that the northward transport variability that is responsible for most of the variations of the sea ice extent is driven by the atmospheric forcing. In order to assess the influence of the wind on the sea ice transport, I have selected years with low sea ice extent (1991 to 1995, 1997, 2002, and 2004 to 2006) and years of high sea ice extent (1996, 1998, and 1999 to 2001) in the Ross Sea from figure 5.5. Afterwards, I subtracted the average fields of the years of low sea ice extent from the average fields of high sea ice extent for each month. The resulting pressure and wind field differences between the two cases for the average month of July are illustrated in figure 6.2(a).

For the selected years a large difference of the sea ice extent in July occurs in the north-eastern Ross Sea and is illustrated by the green and brown contour lines. The distribution of the pressure difference shows that there is an amplification of the zonal pressure gradient in the years of higher sea ice extent with an associated stronger southerly flow. This is confirmed by findings of Kwok (2005) and Drucker et al. (2011). In figure 6.2(b) the related difference of the meridional flux is shown which reveals a strong increase of the northward transport throughout almost the whole Ross Sea. It is strongest close to the Ross Ice Shelf and looks almost identical to the pattern of figure 6.1. This supports the theory that a change of the southerly wind field during the time when the ocean is sea ice covered affects the northward transport of sea ice considerably. An analysis of the pressure difference for each month (not shown) revealed that the pattern is very variable throughout the year and not always as clear as in July

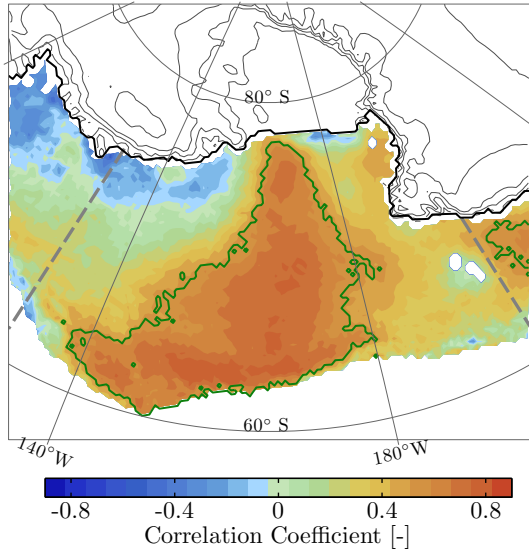


Figure 6.1: Correlation coefficient between the 12-month-running mean of the Ross Sea sea ice extent anomalies and the meridional sea ice area flux of each grid box with a time lag of the extent of one month. The green contour line denotes the 95% confidence level. The gray dashed lines indicate the Ross Sea sector.

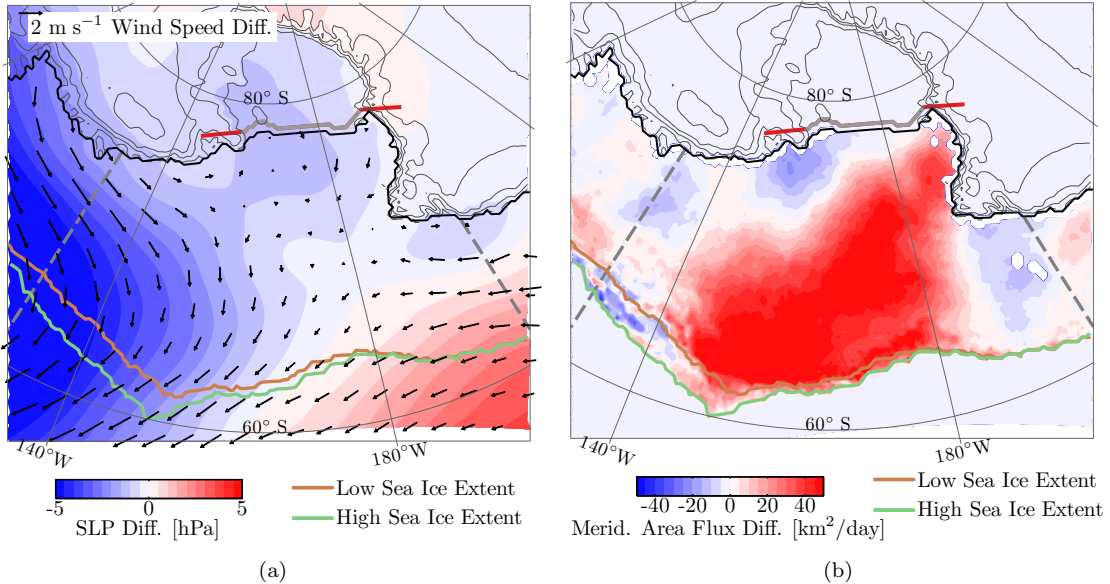


Figure 6.2: Average July difference between years of low and high sea ice extent (cf. text) in the Ross Sea sector for surface pressure and the associated surface layer wind vectors (a), and for the meridional sea ice area flux (b). The red and gray line denotes the transect that is used for the profile shown in figure 4.20(a). The gray line is the part of the transect situated on the ice shelf.

which is, probably, related to the few years that were compared. Nevertheless, a clear tendency of an increased pressure gradient is visible.

It is rather likely that the increased synoptic-scale zonal pressure gradient also effects the amount of cold air that is exported from the Ross Ice Shelf. The pressure distribution as shown in figure 6.2(a) implies that in years of high sea ice extent the cyclonic activity in the south-eastern Ross Sea is higher.

Accordingly, the piling up of cold air against the Transantarctic Mountains should be increased and a stronger cold air export should take place. In order to study this relation, cold air outflow along the Ross Ice Shelf edge (cf. transect indicated in figure 6.2) is calculated as described in box 6.1 by equation 6.1.

The vertical cross-section of the cold air outflow from the Ross Ice Shelf for the average month July is shown in figure 6.3. Despite the lower near-surface wind speeds observed in figure 4.20(a), the outflow is strongest close to the surface where the air has the strongest cooling potential on the ocean's surface and, then, rapidly decreases with height with increasing temperatures. In the horizontal it is strongest towards the western side of the ice shelf because of the strong jet. This confirms the hypothesis stated previously that the surface deficit on the ice shelf is lower towards the west due to a higher cold air export. The jet also causes an outflow that reaches higher up on the western side. The overall strongest outflow with about -200 K m s^{-1} occurs close to the surface at a distance of about 200 km away from the Transantarctic Mountains.

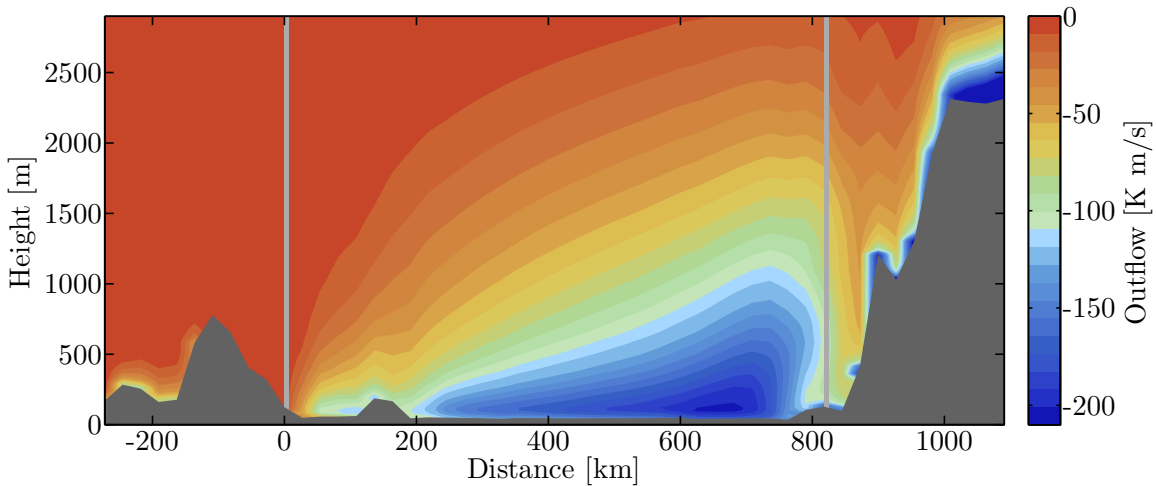


Figure 6.3: Cross-section along the transect across the Ross Ice Shelf edge that is outlined in figure 6.2 with the Transantarctic Mountains to the west (right in the figure). Average July (1989 to 2006) cold air outflow is shown in color. The viewing angle is from the ocean onto the ice shelf. The two light gray vertical lines indicate the ice shelf.

The next question that arises and needs to be addressed is how the outflow varies in time. Studying daily profiles for a certain period of time (not shown), we can see that variations of cold air that leaves the ice shelf are very strong and vary on a synoptic timescale or shorter. The horizontal maximum of the outflow seems to be variable along the ice shelf edge and its position and strength changes with the amount of cold air pooling on the ice shelf and the large-scale forcing. This variability on a synoptic scale and also the conclusion that the described barrier wind system is the dominant wind system in this region agrees with the findings of O'Connor et al. (1994), Parish et al. (2006), Seefeldt and Cassano (2008), and Steinhoff et al. (2009).

For an analysis of the variability on a longer, interannual timescale that is likely to affect the sea ice, the total cold air outflow from the Ross Ice Shelf between the two vertical gray bars in figure 6.3 was determined according to equation 6.2 in box 6.1. We can see a time series of the 12-month-running mean of the anomalies of this quantity in the left panel of figure 6.4 in green and the Ross Sea sea ice extent in red. The apparent negative correlation between the two time series is confirmed by the scatter plot and the regression line in the right panel of figure 6.4. The correlation coefficient is -0.52 at a 95% confidence level for a time lag of one month of the sea ice extent anomalies to the outflow anomalies. This relation implies that in years of high cold air outflow from the Ross Ice Shelf the sea ice extent in the Ross Sea is high. It is also not surprising that there is a significant (at a 95% confidence level) and even higher negative instantaneous correlation between the outflow and the meridional sea ice transport

with a coefficient of -0.56.

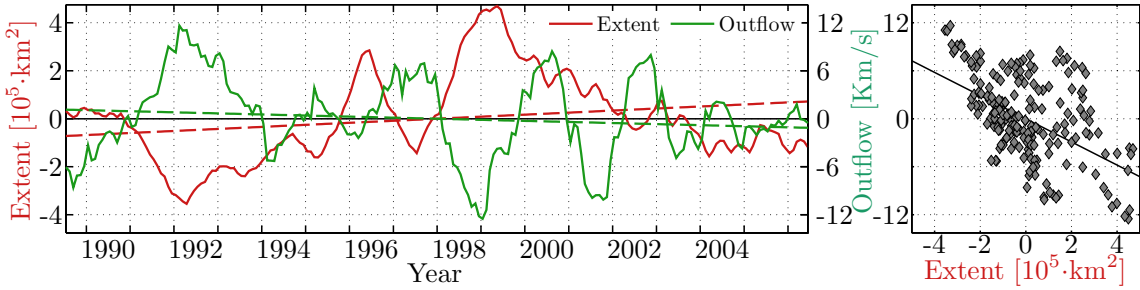


Figure 6.4: Left panel: Time series of the 12-month-running mean Ross Sea sea ice extent anomalies (red) and Ross Ice Shelf cold air outflow anomalies (green). The dashed lines show the respective long-term trends. Right panel: Scatter plot of the two variables on the left with linear fit. The corresponding correlation coefficient is -0.52 at a 95% confidence level for a time lag of one month.

Retrieving such high correlation coefficients from the averaged quantities, it is interesting to see where the relation is strongest in a spatial sense. Therefore, I correlated the 12-month-running mean outflow anomalies from the Ross Ice Shelf with the 12-month-running mean meridional sea ice area flux and sea ice concentration anomalies which are shown in figures 6.5(a) and (b), respectively. One can observe a band of high and significantly negative correlations between the outflow and the meridional transport in the central Ross Sea extending from the Ross Ice Shelf. Interestingly, the correlation is only high on the eastern side in front of the ice shelf. In the west, where the southerly winds are strongest, where they have the highest directional constancy, and where most of the outflow takes place, the correlation is rather weak. However, the correlation with the sea ice concentration in figure 6.5(b) shows a zonal band of a significantly high negative correlation extending from the east to the west of the Ross Sea.

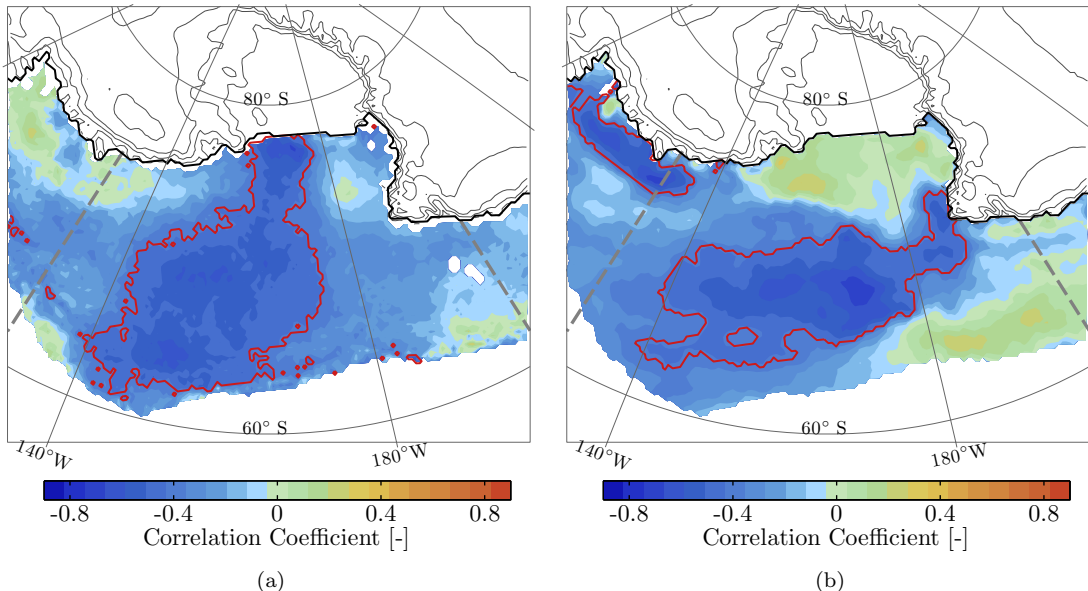


Figure 6.5: Instantaneous correlation coefficients between the 12-month-running mean of the Ross Ice Shelf cold air outflow anomalies and the meridional sea ice area flux anomalies (a) as well as the sea ice concentration anomalies (b) for each grid box. The red contour line denotes the 95% confidence level. The gray dashed lines indicate the Ross Sea sector.

Two considerations should be made when studying figure 6.5(b). Firstly, the correlation seems not to be significant at the sea ice edge which is surprising because we have derived a significant correlation with the sea ice extent. Nevertheless, the sea ice edge varies throughout the year and all months have been correlated so that at the outer ice pack the sea ice cover is only present in late winter and early autumn which lowers the correlation coefficient. Secondly, the correlation is most negative in the region where sea ice convergence occurs which directly links the sea ice concentration to the meridional transport. Even though the correlation is not significant we can notice a tendency towards a positive correlation coefficient in the southern Ross Sea which implies more open water areas in months of high outflow. The northward transport is enhanced and accelerated, and, subsequently, in the convergence region where the drift usually decelerates more ice accumulates. Moreover, we can notice another region of high negative correlation in the southern Amundsen Sea. This is probably caused by the enhanced large-scale cyclonic circulation in this region in years of high outflow that pushes the sea ice against the coast and causes a high concentration.

At last, figure 6.4 shows an overall increasing outflow trend (negative) of $-1.33 \pm 1.40 \text{ K m s}^{-1}$ per decade (about -1.6% of the average total outflow) which, however, is only significant at a 85% confidence level. Still, a higher outflow would be expected according to the positive trend of the sea ice extent and agrees with an increasing area production and transport. The very strong meridional sea ice transport increase and the positive temperature trends provide a hint that the trend of temperature and wind speed at the ice shelf edge might be of opposite sign. As the outflow is a product of the two variables the trend might be weakened. Figure 6.6 shows the time series for each season. Whereas austral spring outflow slightly decreases, autumn and winter outflow increases. Although none of these trends is significant, they seem resonable in terms of sea ice concentration and meridional transport trends that show an increase in the western Ross Sea mainly in autumn and winter.

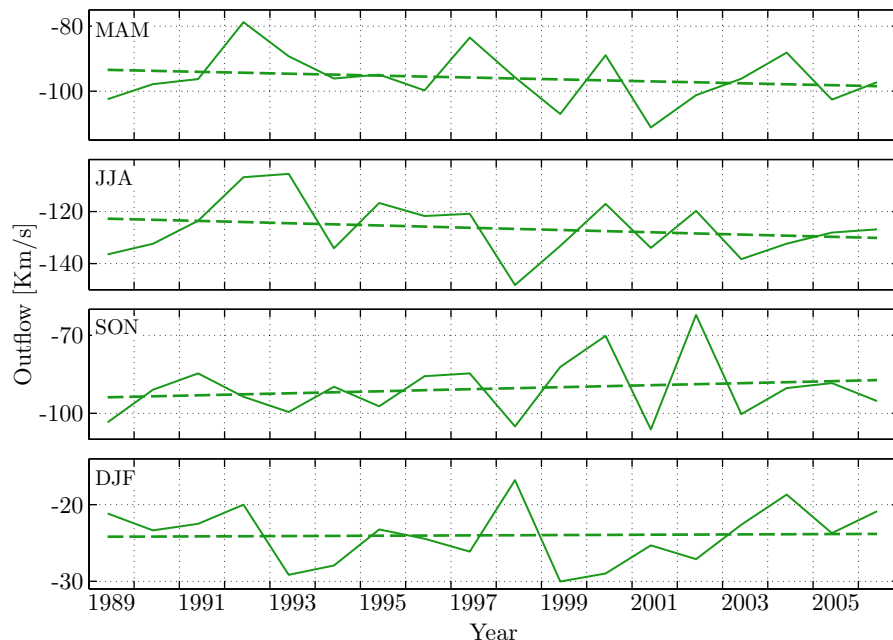


Figure 6.6: Total outflow from the Ross Ice Shelf for each (austral) season. The dashed lines indicate the trends. None of the trends is significant.

Overall, the cold air outflow that is forced by the large-scale pressure distribution and the cold air pooling on the ice shelf is responsible for a large part of the sea ice transport and extent variability in the Ross Sea. It is quite likely that the increased sea ice production in the southern Ross Sea and the increased northward transport and sea ice concentration in the western Ross Sea are caused by an

increasing cold air outflow close to the Transantarctic Mountains. For a more robust statement further analysis on the outflow trends would be necessary.

6.2 Weddell Sea and Ronne-Filchner Ice Shelves

The barrier wind effect over the Ronne-Filchner Ice Shelves and the Weddell Sea that I have studied in chapter 4.4 is not as clear as over the Ross Sea and Ice Shelf but there is an amplified large-scale southerly forcing close to the mountain range that exports large amounts of cold air from the ice shelves. Furthermore, the southerly winds are weaker and the temperature deficit close to the surface is stronger. This suggests that the outflow of cold air is more dominated by the temperature contribution than by the wind. It also implies that the dynamical forcing of the atmosphere on the sea ice in the southern Weddell Sea is, probably, weaker but sea ice grows thicker due to the lower temperatures. In order to analyze the effects of cold air outflow from the Ronne-Filchner Ice Shelves on the sea ice, I will proceed as in the previous section (6.1).

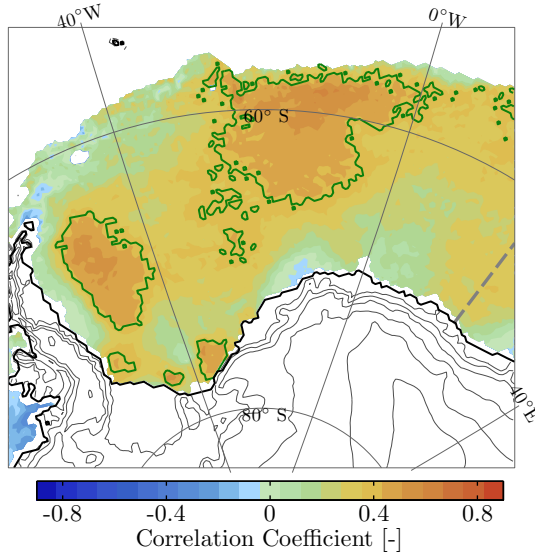


Figure 6.7: Correlation coefficient between the 12-month-running mean of the Weddell Sea sea ice extent anomalies and the meridional sea ice area flux anomalies of each grid box with a time lag of the extent of one month. The green contour line denotes the 95% confidence level. The gray dashed lines indicate the Weddell Sea sector.

The relation between the Weddell Sea meridional sea ice transport and the sea ice extent that I have revealed in chapter 5.2 showed that there the sea ice dynamics play an important role but are not as determining for the sea ice extent as it is the case in the Ross Sea. A lower overall correlation does not necessarily mean that the meridional transport is not of high importance locally. Therefore, figure 6.7 shows a map of the correlation coefficient between the sea ice extent anomalies and the meridional transport anomalies. There are two major areas of significantly positive correlation: one parallel to the Antarctic Peninsula and the other in the central north. This suggests that there are different regimes that influence the sea ice extent. Hypothetically, a higher northward transport in one of the regions could cause a higher extent just north of the increased transport. Moreover, we can identify significantly positive correlations close to the ice shelves that are, probably, strongly influenced by off-shore winds. In terms of cold air outflow from the ice shelves, these regions and the region close to the Antarctic Peninsula are of interest.

As in section 6.1, I have selected years of low (1989, 1990, 1993, 1996, 1999, 2000, 2002) and high (1991, 1992, 1994, 1995, 2003, 2004) sea ice extent in the Weddell Sea in consideration of figure 5.5

and computed the differences between the average months. This should highlight the influence of the atmospheric circulation on the sea ice. Figures 6.8(a) and (b) show the average July difference of the surface pressure with the associated surface layer wind vectors (a) and of the meridional sea ice area flux (b), respectively. The years of high sea ice extent for this month show an increased sea ice cover especially in the north-west (cf. brown and green contour lines). We can further notice that there is a higher cyclonic activity north of the ice edge. Related to this pressure difference are strengthened southerly winds in the western and weakened southerly or even northerly winds in the central Weddell Sea. The meridional area flux difference shows, as expected, a similar pattern as the wind forcing (cf. figure 6.8(b)).

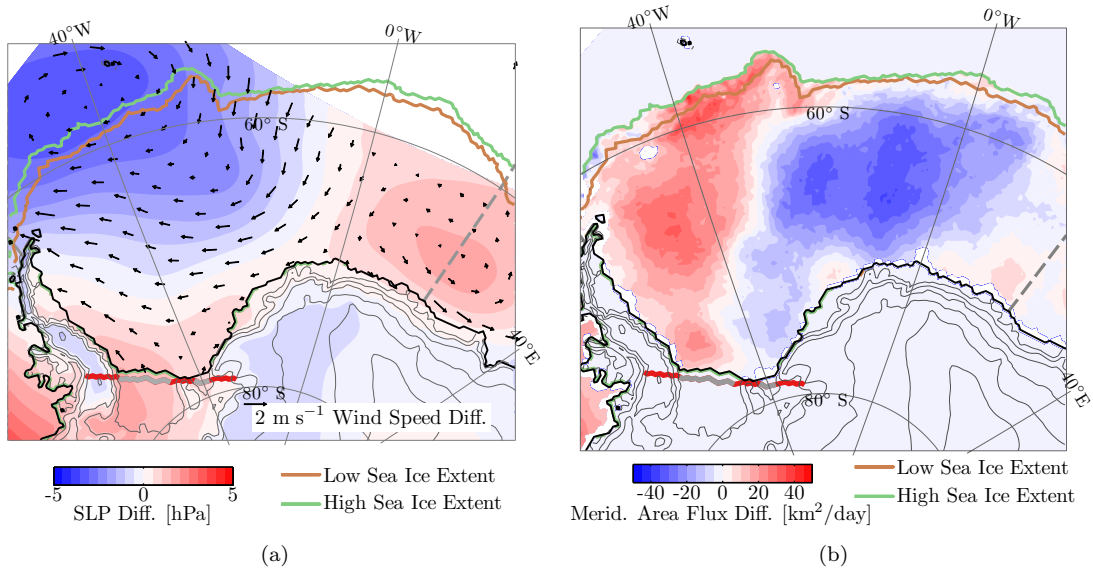


Figure 6.8: Average July difference between years of low and high sea ice extent in the Weddell Sea sector (cf. text) for surface pressure and the associated surface layer wind vectors (a), and for the meridional sea ice area flux (b). The red and gray lines denote the transect that is used for the profile shown in figure 4.20(b). The gray line is the part of the transect situated on the ice shelf.

According to the negative meridional transport anomaly for the average month of July in the central Weddell Sea, we would also expect a negative correlation between the meridional transport and the sea ice extent in this area. However, figure 6.7, surprisingly, shows a positive correlation coefficient. Again, by considering all months of the difference between the low and high sea ice extent cases (not shown), I can conclude that the patterns of the pressure difference are extremely variable throughout the year, so that no clear tendency is visible. Nevertheless, the sea ice transport always changes accordingly. This also leads to the effect that the difference of the sea ice extent is not clearly larger in one single region throughout the year but varies in different regions. I infer that this is caused by the very large sector for which the sea ice extent is determined and a high sea ice extent in the west might be caused by different processes than a high sea ice extent in the east. So in order to distinguish different signals, a definition of smaller sectors would be necessary.

We would expect - judging from the results that were gained in the Ross Sea - that the meridional sea ice transport and the sea ice concentration in the western Weddell Sea are strongly linked to the cold air outflow from the Ronne-Filchner Ice Shelves and that the eastern parts are forced by other processes. Along the cross-section of the ice shelves that I have used in figure 4.20(b), I calculated the cold air outflow which is illustrated in figure 6.9. Similar to the cold air outflow over the Ross Ice Shelf, the outflow over the Ronne and Filchner Ice Shelves increases in height and strength towards the mountain barrier. It is always the strongest close to the surface where the highest cooling potential is present. In

general, the values across both ice shelf edges are lower than across the Ross Ice Shelf edge because wind speeds are much lower in this case. Further, we can see that Berkner Island is an important orographic feature to enhance cold air outflow on the Filchner Ice Shelf.

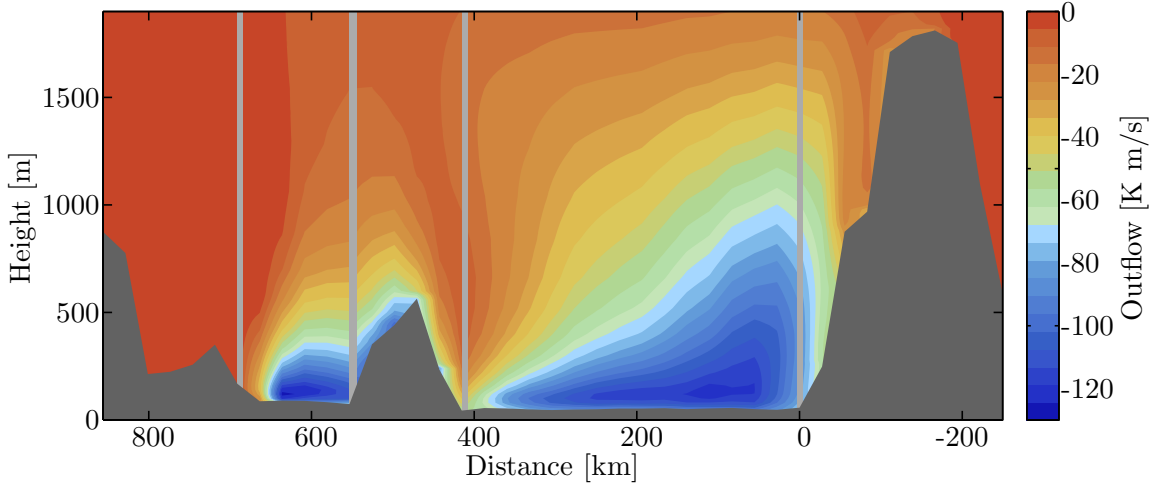


Figure 6.9: Cross-section along the transect across the Ronne-Filchner Ice Shelf edges that is outlined in figure 6.8 with the Antarctic Peninsula to the west (right in the figure). Average July (1989 to 2006) cold air outflow is shown in color. The viewing angle is from the ocean onto the ice shelves. The light gray vertical lines indicate the ice shelves.

According to equation 6.2 in box 6.1, I have calculated the total cold air outflow for both ice shelves (between the gray lines in figure 6.9) separately and as total. Not surprisingly the two time series correlate very well with a correlation coefficient of 0.60 at a 99% confidence level. The discrepancies rather arise from a difference in cold air pooling than in the large-scale forcing.

Figure 6.10 (left panel) illustrates the time series of the 12-month-running mean cold air outflow anomalies from the Ronne and Filchner Ice Shelves together (in green). The red curve denotes the 12-month-running mean of the Weddell Sea sea ice extent anomalies. There is no significant correlation between the two time series. However, if one only uses the first seven years of the dataset (until the blue line), the scatter plot (right panel) shows a significant negative correlation of -0.74 at a 90% confidence level. The northward sea ice area flux anomalies also correlate well during this period with a coefficient of -0.66 at a 90% confidence level. So, if the cold air outflow is a determining factor in parts of the Weddell Sea, there is a strong variability of the sea ice extent in these parts in the first years of the time series. In the other years sea ice extent variations are, probably, related to other processes. In the period 1996 to 2000 the outflow is rather strong but there is still an overall negative sea ice extent anomaly in the Weddell Sea. Towards the end of the time series the variability of the outflow is rather low and sea ice extent anomalies are not correlated. This decreasing variability towards the end of the time series is also visible in figure 6.4. Interestingly, the outflow from the Ross Ice Shelf and the outflow from the Ronne-Filchner Ice Shelves are negatively correlated with a coefficient of -0.35 at a 90% confidence level. This is caused by the large-scale forcing that triggers the cold air outflow and is also a reason for the Antarctic dipole that I have described in chapter 5.1.

In a next step, it is of interest to see how outflow relates spatially to the sea ice transport and extent and if it is possible to determine the regions where it is dominant to confirm the speculations made before. Figure 6.11(a) shows the correlation coefficients between the outflow and the meridional area flux anomalies and figure 6.11(b) those between the outflow and the sea ice concentration anomalies. As in the Ross Sea, we can also see a large area of significantly negative correlation extending from the ice shelves to the sea ice edge for the meridional transport in the western Weddell Sea. The chain of reasoning of the impact of the outflow on sea ice also holds for the sea ice concentration that is negatively correlated to the

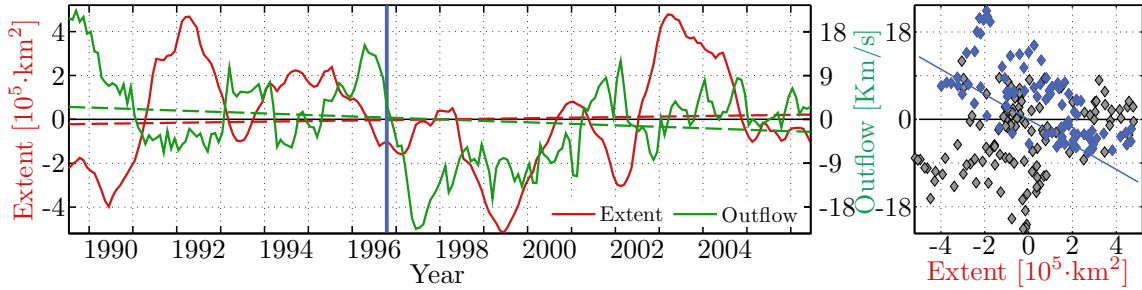


Figure 6.10: Left panel: Time series of the 12-month-running mean Weddell Sea sea ice extent anomalies (red) and Ronne-Filchner Ice Shelves cold air outflow anomalies (green). The dashed lines show the respective long-term trends. Right panel: Scatter plot of the two variables on the left with linear fit. No correlation between the two datasets is visible for the total time series. The correlation coefficient of all data until the year 1996 (in blue) is -0.74 at a 90% confidence level for a time lag of one month.

outflow north of the transport dependence where the sea ice accumulates and that is positively correlated at the coast where it is exported. Consequently, a higher cold air outflow from the Ronne-Filchner Ice Shelves induces an increased northward transport of sea ice and an increasing concentration at the ice edge.

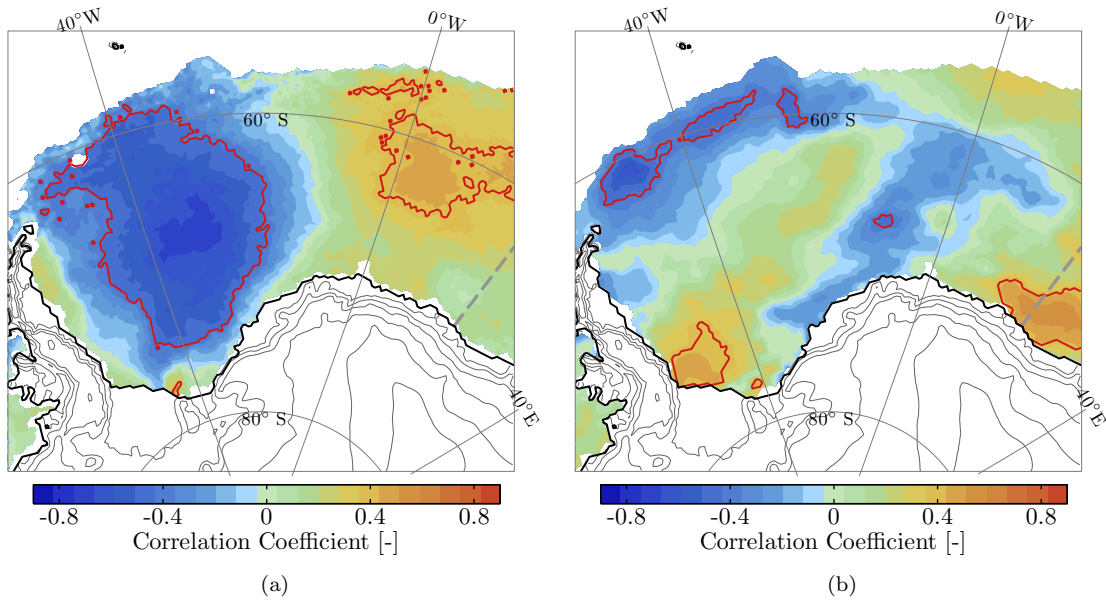


Figure 6.11: Instantaneous correlation coefficients between the 12-month-running mean of the Ronne-Filchner Ice Shelves cold air outflow anomalies and the meridional sea ice area flux anomalies (a) as well as the sea ice concentration anomalies (b) for each grid box. The red contour line denotes the 95% confidence level. The gray dashed lines indicate the Weddell Sea sector.

Further, in the eastern Weddell Sea the sea ice extent is, apparently, not correlated with the outflow which confirms the expected zonal differences of the determining factors. There is some significant positive correlation to the meridional area flux which is decreased if there is a cyclonic large-scale forcing that supports the outflow as it is the case in figure 6.8. Quite likely there is also a link to the westward transport of the sea ice along the coast of Dronning Maud Land, as there the sea ice concentration decreases in the east and increases in the west in years of high outflow. Consequently, the westward sea

ice area flux must be enhanced by stronger easterly winds.

At last, the question arises whether the observed trends of the Weddell Sea sea ice retrieved in chapter 5 can be explained by long-term changes of the outflow. The dashed green line in the left panel of figure 6.10 shows an overall increase of the cold air outflow from the Ronne-Filchner Ice Shelves with a trend of $-3.04 \pm 2.32 \text{ K m s}^{-1}$ per decade (about -5.3% of the average outflow) at a 90% confidence level (note that a negative trend implies an increasing outflow due to the definition). This trend is rather surprising as there is an overall decreasing sea ice area production in the Weddell Sea that one could see in chapter 5.3. Now, we could argue that the overall Weddell Sea sea ice area production is not comparable to the outflow as the outflow is only of importance in the western Weddell Sea. However, Drucker et al. (2011) report a decreasing sea ice production in the southern Weddell Sea adjacent of the Ronne Ice Shelf for the period 1992 to 2008 which we would, indeed, expect to be related to the cold air outflow. If we only consider the period 1992 to 2006 of the outflow time series, the trend actually becomes positive which translates to a decreasing cold air outflow even though this trend is insignificant. Consequently, the increasing outflow that is found for the total time series mainly arises from the first two years where a strong positive anomaly is present.

On a seasonal timescale different signs of the cold air outflow are visible in figure 6.12. There is a significant cold air outflow increase in austral winter with a trend of $-14.2 \pm 17.5 \text{ K m s}^{-1}$ per decade at a 90% confidence level (about 16.0% of the total). This agrees with the strong increase of the meridional area flux in winter (and also in spring) in figure 5.14. However, this increase is, to a large extent, related to a very low winter outflow in the first years of the time series which is the reason why the trends in figure 5.14 are not significant at this time of the year.

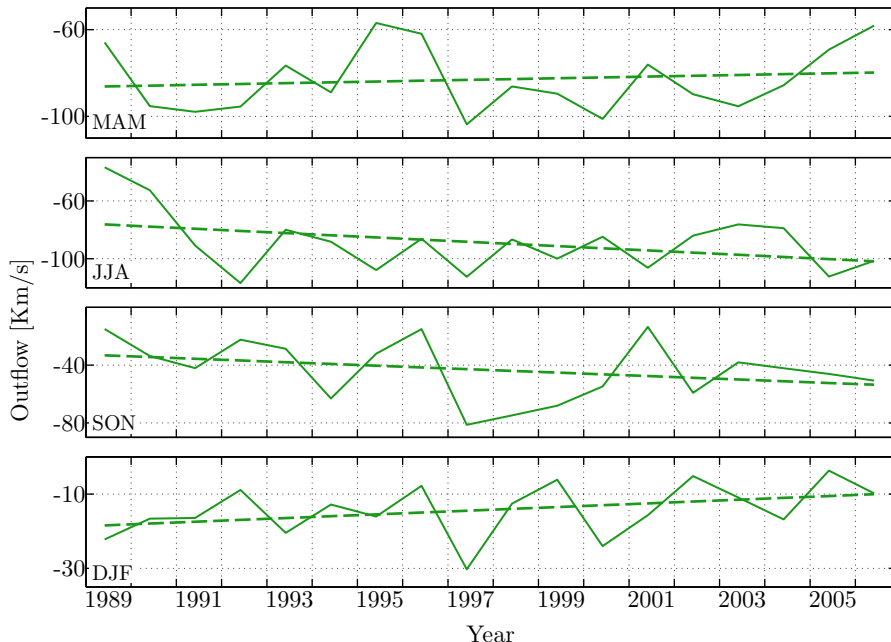


Figure 6.12: Total outflow from the Ronne-Filchner Ice Shelves for each (austral) season. The dashed lines indicate the trends. Spring and autumn trends are not significant. Wintertime outflow is increasing with a trend of $-14.2 \pm 17.5 \text{ K m s}^{-1}$ per decade at a 90% confidence level (about 16.0% of the total) and summertime outflow is decreasing with a trend of $4.66 \pm 5.99 \text{ K m s}^{-1}$ per decade at a 95% confidence level (about 32.7% of the total).

An important finding can be retrieved from the cold air outflow in summer (and to a lesser extent also in autumn) that is significantly decreasing with a trend of $4.66 \pm 5.99 \text{ K m s}^{-1}$ per decade at a 95% confidence level (about 32.7% of the total). The decrease implies that the summertime cold air outflow, that is low anyway, almost vanishes towards the end of the time series. As temperatures are around the

melting point over the sea ice during this season, a reduced cold air outflow from the ice shelves has a strong impact on the sea ice along the east-coast of the Antarctic Peninsula where usually an ice pack remains during the summer. It is not only a change of the temperature that plays a role but also the decreasing southerly winds that cause the decreasing northward transport in summer and autumn which is visible in figure 5.14. More ice melt in summer, then, leads to a stronger absorption of solar radiation by the ocean and a warmer ocean also implies a later freezing of the sea ice in autumn what we identify by the negative trends in figure 5.7. The decreasing cold air outflow and sea ice in summer and autumn also have strong impacts on the ice shelves along the Antarctic Peninsula because less sea ice and a higher absorption of solar radiation by the ocean can have a strong destabilizing effect on the ice shelves. This suggests that further research on the circulation changes along the Antarctic Peninsula and the related changes of cold air outflow is necessary.

In sum, throughout this chapter we could see that the cold air outflow from the large ice shelves captures most of the sea ice variability in the western Weddell and Ross Seas where the dynamical impacts of the atmosphere on the sea ice are very important. The correlation maps between the cold air outflow and the transport also agree with the maps of the variance of the meridional transport in chapter 5.2 and with those of the atmospheric forcing in chapter 4. The anomalies of the climate system are amplified in these regions due to the meridional mountain ranges that provide a barrier for the circulation and the transport of cold air masses.

7 Conclusions & Discussion

In this final chapter of my thesis I will summarize and contextualize all findings of my research. Moreover, I will review several critical aspects that arose throughout the thesis and point out where further research is necessary. By combining the key aspects of the results of each of the last three chapters, I will highlight regional factors that control the Antarctic sea ice.

The motivation to write this thesis arose from the lack of understanding of the direct atmospheric processes that determine the Antarctic sea ice variability and long-term changes. It is well known that the large-scale circulation variations through the Southern Annular Mode (SAM) and El Niño/Southern Oscillation (ENSO) provide an external forcing mechanism that is related to the sea ice variability in the Southern Ocean, especially in the Ross, Bellingshausen, and Amundsen Seas (cf. chapter 1). However, the physical processes that are associated with these relations or, in other words, the dominant factors of sea ice formation and decay for each region in the Southern Ocean are not yet determined. Moreover, the spatial distributions of the variability and the trends are also still not understood. I have described, analyzed, and interpreted several important impacts that the atmospheric boundary layer dynamics and the cold air masses from the Antarctic continent have on the evolution of the sea ice on a regional scale.

The analysis is based on an 18-year period from 1989 to 2006 which is limited by the data availability of the atmospheric and sea ice data that I have used. Even though this is a rather short period to analyze long-term trends in the climate system, it is possible to detect major relations and processes. The effect of using such a short time period in a climate system with a high variability becomes obvious in the low significance of some of the derived trends.

I have used data produced by a regional atmospheric climate model that was adapted for simulating the climate of polar regions (RACMO2.1/ANT) to describe the atmospheric boundary layer over the coastal Antarctic continent, the ice shelves and the sea ice covered ocean. The strong longwave radiative cooling over Antarctica sets up a very stable layer of cold air close to the surface. The cold air that is constantly produced over the slopes of the ice sheet is transported on to the ice shelves by strong and persistent katabatic winds in winter. Here, it accumulates and builds up a thick cold air layer which extends also over the sea ice in winter, especially in the Ross and Weddell Seas, adjacent to the large Ross and Ronne-Filchner Ice Shelves. An analysis of the surface layer potential temperature showed that this cold air is subject to strong interannual variations.

The northward transport of the cold continental air is associated with strong southerly winds that we can find in the western Ross and Weddell Seas. A climatological large-scale zonal pressure gradient along the coast exists throughout most of the year with higher pressure in the west due to the cooling effect of the mountain ranges and lower pressure in the east due to the frequent passage of cyclones. The southerly winds are amplified towards the mountain barrier which can be explained with horizontal thermal gradients. The cold air is pushed against the mountain barrier and leads to tilted isentropic surfaces. Very close to the surface on the ice shelves this thermal gradient is reversed because larger amounts of cold air are exported from the ice shelf on the western side. This results in the formation of a boundary layer jet over the Ross Ice Shelf. Over the Ronne-Filchner Ice Shelves and the Weddell Sea the effect is less pronounced which is related to a smaller topographic barrier that alters the flow.

An analysis of the long-term trends of the near-surface temperature and pressure fields showed a very high regional complexity and large statistical uncertainties which is caused by the strong interannual variability and regionally varying strength of the meridional exchange of cold continental air with warmer air from the north. Temperature trends are, to some extent, consistent in their spatial distribution with those that I have mentioned in the introduction of this thesis. There are two regions of major significant warming: one over the Bellingshausen, Amundsen, and eastern Ross Sea, and the other along the coast of Dronning Maud and Enderby Lands. Trends depend on the season and might even be reversed at a different time of the year. Strongest trends can be observed in winter. In terms of near-surface temperature trends and their relation to the sea ice changes, it is very important to notice that the temperature is not an independent variable and is rather influenced by the changing sea ice cover. Both

regions with positive temperature trends are influenced by an increased advection of warmer air masses from the north. Trends of the near-surface pressure and wind fields over the Southern Ocean in the considered time period are even more complex and less significant than those of the temperature. Again, they vary strongly with the season.

I have attempted to derive the single terms of the momentum budget in order to associate the variability and changes in the Antarctic atmospheric boundary layer with the single forcing terms of the wind field. This would be of high interest as we could distinguish the forcing that is imposed on the boundary layer by the large-scale circulation and the forcing that is caused by variations that happen very close to the surface. The latter are for example the regional accumulation of cold air and associated thermal gradients. However, several difficulties arose while explicitly solving the terms of the momentum budget. These are caused by the extrapolation procedure of the background temperature profile to the surface. The changing depth of the cold air layer and the local vertical structure of the temperature profile do not allow to use a fixed set of atmospheric layers to linearly extrapolate the upper atmosphere temperature lapse rate to the surface. Further efforts to accurately derive these terms are necessary and very important in order to detect the sources of the variability. Even though the terms were not accurately derived, they showed that the cold air outflow from the large ice shelves onto the sea ice and the southerly near-surface winds in the Ross and Weddell Seas are the result of a combined effect of large-scale forcing and thermal gradients in the atmospheric boundary layer due to cold air pooling. I have emphasized that the meridional topographic barriers, the Transantarctic Mountains and the Antarctic Peninsula, are responsible for the observed patterns and the enhanced meridional transport of cold air masses.

A comparison of the variability and trends of the sea ice concentration and the meridional sea ice transport revealed a very high regional importance of the sea ice dynamics for the distribution of the sea ice. Not surprisingly, these regions are the Ross and Weddell Seas. The patterns of the wind field mostly coincide with patterns of the sea ice drift. Strongest and most constant northward ice drift occurs in the western Ross Sea where most persistent southerly winds are observed. Along the coast of East Antarctica the easterly winds confine the sea ice to a rather narrow band along the coast that is dominated by a zonal westward drift. Another region of northward transport occurs in the western Weddell Sea, even though the effect is not as pronounced as in the Ross Sea. In the regions where we can observe a northward transport the sea ice extents as far as the west-wind zone in winter where the overall drifting direction turns eastward.

In the Ross Sea, I have identified the meridional transport as determining factor of the sea ice extent which reflects a high importance of the sea ice dynamics and the driving wind stress. Just north of the area where strongest increasing sea ice cover can be observed in the western Ross Sea, the northward sea ice transport has strongly increased. In the Bellingshausen and Amundsen Seas both, the zonal and meridional transport are important for the sea ice extent. However, there are no significant trends of the transport that might explain the decreasing sea ice cover in this sector. This also indicates that, probably, the increasing warm air advection from the north in late winter and spring is responsible for the observed long-term changes in this region. The same holds for the decreasing sea ice concentration observed along the coast of Dronning Maud and Enderby Lands in summer and early autumn. In this part of the Southern Ocean (Indian Ocean sector) the zonal sea ice transport is somewhat important to the sea ice cover variations. In the Western Pacific Sector no significant trends were found and sea ice dynamics seem to play only a minor role for the variability. At last, in the Weddell Sea there is also a strong relation between the northward transport of sea ice and the sea ice extent. The decreasing sea ice cover in the north-west might be related to a decreasing northward sea ice transport along the Antarctic Peninsula.

The source regions of the large amounts of sea ice that are transported northward in winter in the Ross and Weddell Sea are the large coastal polynyas adjacent to the ice shelves. They form due to the persistent southerly winds from the continent. If the sea ice is exported out of these regions the open water surface refreezes almost immediately due to the very cold air. Using the divergence of the sea ice area flux together with the rate of change of the sea ice concentration, I have derived a term that I refer to as 'sea ice area production'. Sea ice area production in the Ross Sea shows an increasing

trend, consistent with the meridional transport and sea ice cover trends. The same relation holds for the Weddell Sea where sea ice production has been decreasing.

The cold air outflow from the Ross and Ronne-Filchner Ice Shelves has been defined as the product of the wind speed perpendicular to the ice shelf edges and the temperature deficit of the air with respect to the freezing temperature of the ocean. This quantity confirms that large parts of the variability of the Ross Sea and western Weddell Sea sea ice cover and transport are associated with the cold air outflow from the ice shelves. In the Ross Sea the positive transport and concentration trends might even be explained with a slightly increasing cold air outflow. The cold air outflow from the Ronne-Filchner Ice Shelves shows an overall increase which is mainly due to a large low outflow anomaly at the beginning of the time series. By considering seasonal outflow trends, I have shown that the Ross Ice Shelf outflow increase takes place in autumn and winter and that the Ronne-Filchner Ice Shelves outflow is decreasing in summer and increasing in winter and spring. In order to confirm this relation more research with a longer time series is required.

A combination of all these results leads to the following chain of reasoning. The variability of the large-scale circulation and the accumulation of cold air on the large ice shelves forces variations of cold air outflow from the continent over the sea ice along the mountain barriers. The strong off-shore winds induce a northward transport of sea ice which is causing the formation of large open water areas in coastal regions where sea ice is produced. If the winds are stronger, more sea ice is exported and if the temperature of the cold air is lower, sea ice forms more quickly on the open water. The variability of the northward transport, then, is associated with variations of the sea ice concentration north of the region of meridional transport where it accumulates. This, eventually, results in anomalies of the sea ice extent.

The findings do not only imply that the variability of the sea ice can, to a large extent, be explained by variations in the atmospheric boundary layer, but they do also confirm that the regional atmospheric climate model that was used for this study is able to reproduce the climate variability on a very regional scale what further enables one to study the processes that take place over coastal Antarctica. The described relation between the sea ice and the lower atmosphere might even be stronger in reality than the one that I have retrieved. It is expected that the horizontal resolution of the model (even though it is really high) leads to a slight underestimation of the wind speed and the formation of cold air over the continent because the slopes might be slightly underestimated. Further, the model is forced with sea ice cover data from the ERA-Interim database. As I have shown in this thesis this implies several inaccuracies and inconsistencies. The usage of the original satellite data might also alter the coastal wind and temperature fields, especially in coastal areas and along the ice edge where discrepancies are the largest.

By using the cold air outflow parameter, I have stressed that the combined wind and temperature signal is important to capture the sea ice variations. Temperature or wind variations and trends alone (cf. chapter 4) did not show this relation. This stresses that it is not possible to solely explain the sea ice variability around Antarctica by only considering the surface temperature or the thermodynamic forcing of the sea ice. It is crucial to include the sea ice dynamics that lead to a mechanical redistribution of the sea ice and induce the formation of open water areas within the ice pack where large amounts of sea ice can be produced throughout the winter. Further, the results imply that there is a significant influence of the continent on the sea ice variability even at the sea ice edge because the cold air outflow has been assessed at the ice shelf edges before the atmosphere is directly influenced by the sea ice or the ocean.

I have shown that the cold air outflow is a combined effect resulting from the large-scale forcing and the boundary layer processes. The redistribution of the cold air in the boundary layer along the mountain barriers would not be possible without the large-scale forcing. This relates the findings of this thesis to the observed relation between the SAM and ENSO, and the sea ice cover. The mountain barriers are responsible for an amplification of the large-scale circulation anomalies which is also a reason why the observed interannual variability of temperature, wind and sea ice in the western Ross and Weddell Seas is the largest.

Table 7.1 summarizes different correlation coefficients between detrended 12-month-running mean

anomalies of several parameters for the Ross Sea. These are the sea ice extent, the meridional sea ice transport, the cold air outflow from the Ross Ice Shelf, the SAM/AAO, and the Southern Oscillation Index (SOI) (both datasets from the National Oceanic and Atmospheric Administration, Climate Prediction Center, www.cpc.ncep.noaa.gov/data/indices and www.cpc.ncep.noaa.gov/products/precip/CWlink). The important role of the sea ice dynamics in the Ross Sea is again pointed out as the correlation coefficient between the meridional sea ice area flux anomalies and the sea ice extent anomalies is the largest. Surprisingly, the ENSO signal shows the second largest correlation coefficient to the sea ice extent for the selected period, even though several authors have found a stronger relation to the SAM variability in the Ross Sea than to ENSO (cf. chapter 1). In general, the SAM index has the lowest coefficients. The cold air outflow also significantly correlates with both the SAM index and the SOI. This means that the outflow is high during a positive phase of the SAM or SOI.

Table 7.1: Correlation coefficients between the detrended 12-month-running mean of the Ross Sea sea ice extent anomalies, Ross Sea meridional area flux anomalies, Ross Ice Shelf cold air outflow anomalies, SAM/AAO index, and SOI (both datasets from the National Oceanic and Atmospheric Administration, Climate Prediction Center, www.cpc.ncep.noaa.gov/data/indices and www.cpc.ncep.noaa.gov/products/precip/CWlink). All correlations with the sea ice extent have a time lag of one month of the sea ice extent. All correlations are significant and the subscript gives the corresponding confidence level in percent.

	Merid. Flux	Outflow	SAM/AAO	SOI
Extent	0.81 ₉₉	-0.52 ₉₅	0.47 ₉₅	0.78 ₉₉
Merid. Flux		-0.56 ₉₅	0.46 ₉₅	0.59 ₉₉
Outflow			-0.59 ₉₅	-0.41 ₉₀
SAM/AAO				0.34 ₉₀

The very high value of the relation of the SOI to the sea ice extent implies that there are other mechanisms that must cause a dependence of the ice cover at the ice edge on ENSO. Possible impacts that need further research are imposed by the cyclonic activity along the sea ice margin, or changes in the ocean heat flux and circulation. These processes are very likely to influence the sea ice edge that extends in winter as far as the westerlies where the influence by the continent on the spatial distribution vanishes.

Moreover, in the introduction (chapter 1) I have also mentioned that the long-term increasing sea ice cover could not be related to long-term changes of the SAM or ENSO. The hypothesis of the ozone depletion as a cause of a stronger large-scale circulation and an increasing sea ice extent that was suggested by Turner et al. (2009) is not rejected by the findings of my thesis. The slightly increasing outflow might, indeed, be related to an increasing cyclonic activity in the Ross Sea. In order to proof this, more analysis is necessary.

One might also raise the question of how the warming global climate effects the sea ice because it seems as there is no expected response of the total sea ice cover in Southern Ocean. However, there are several regions of significant warming where air from the lower latitudes is advected over the sea ice. The decreasing trends in the Bellingshausen and Amundsen Seas and, probably also to some extent, the decrease in the western Weddell Sea might, indeed, be related to a long-term warming climate. Most of the temperature trends, however, do not considerably influence the winter sea ice around Antarctica, yet. This is due to the very low prevailing temperatures where a small increase is not really effective. A warming only becomes of concern in summer when the temperatures reach the melting point and the summer decay might be amplified. The fact that the temperatures over the Antarctic continent do not rise as fast as they do in other regions might also lead to an enhanced meridional exchange of heat with the lower latitudes which, in turn, implies a stronger cold air outflow and increasing sea ice cover. One should also consider the stability of the atmospheric boundary layer over the continent. Turner et al. (2006) report a strong warming of the middle troposphere in the last decades. As there is no such strong warming at the surface, this implies an increasing stability of the boundary layer and a stronger surface temperature deficit which might lead to an increase of the cold air drainage into coastal areas

which, again, would cause an increasing sea ice cover. Consequently, it is rather difficult to make a clear statement on the impacts of warming or cooling on the Antarctic sea ice.

In order to further study the implications of long-term changes in the climate system on the Antarctic sea ice, more complex sea ice models are necessary that should be able to capture the regional importance of the sea ice dynamics realistically. A better representation of the sea ice dynamics in models does not only promise to simulate the Antarctic sea ice cover more realistically but it does also allow to find relations between the large-scale circulation and the sea ice. Long-term projections of the behavior of the Antarctic sea ice are also very interesting in terms of the response of the West Antarctic Ice Sheet on the warming climate because less sea ice would have an additional destabilizing effect on the ice sheet.

In conclusion, the findings of my thesis have shown that the sea ice dynamics are the key to understand most of the interannual Antarctic sea ice variability. Further, I have pointed out that the near-surface atmospheric forcing is the main driver of these variations. The cold air outflow from the continent captures large parts of the variability, and even provides possible explanations for the long-term increasing sea ice cover.

Bibliography

- Allison, I. (1989). The East Antarctic sea ice zone: Ice characteristics and drift. *GeoJournal*, 18: 103–115. doi:10.1007/BF00722394
- Andreas, E.L. (1987). A theory for the scalar roughness and the scalar transfer coefficients over snow and sea ice. *Boundary-Layer Meteorology*, 38(1): 159–184
- Andreas, E.L. (2002). Parameterizing Scalar Transfer over Snow and Ice: A Review. *Journal of Hydrometeorology*, 3(4): 417–432. doi:10.1175/1525-7541(2002)003<0417:PSTOSA>2.0.CO;2
- Andreas, E.L. and Ackley, S.F. (1982). On the Differences in Ablation Seasons of Arctic and Antarctic Sea Ice. *Journal of Atmospheric Sciences*, 39(2): 440–447. doi:10.1175/1520-0469(1982)039<0440:OTDIAS>2.0.CO;2
- van Angelen, J.H., van den Broeke, M.R., and van de Berg, W.J. (2011a). Momentum budget of the atmospheric boundary layer over the Greenland ice sheet and its surrounding seas. *Journal of Geophysical Research*, 116(D10): D10101. doi:10.1029/2010JD015485
- van Angelen, J.H., van den Broeke, M.R., and Kwok, R. (2011b). The Greenland Sea Jet: A mechanism for wind-driven sea ice export through Fram Strait. *Geophysical Research Letters*, 38(12): L12805. doi:10.1029/2011GL047837
- Ball, F.K. (1956). The theory of strong katabatic winds. *Australian journal of physics*, 9: 373–386
- Ball, F.K. (1957). The Katabatic Winds of Adélie Land and King George V Land. *Tellus*, 9(2): 201–208. doi:10.1111/j.2153-3490.1957.tb01874.x
- Ball, F.K. (1960). Winds on the ice slopes of Antarctica. In *Antarctic Meteorology: Proceedings of the symposium held in Melbourne, February 1959*, pages 9–16. Oxford, London, New York, Paris: Pergamon Press
- Bamber, J.L., Gomez-Dans, J.L., and Griggs, J.A. (2009). *Antarctic 1 km Digital Elevation Model (DEM) from Combined ERS-1 Radar and ICESat Laser Satellite Altimetry*. Boulder, Colorado USA: National Snow and Ice Data Center, digital media edition
- Barber, C.B., Dobkin, D.P., and Huhdanpaa, H. (1996). The quickhull algorithm for convex hulls. *ACM Trans. Math. Softw.*, 22: 469–483. doi:10.1145/235815.235821
- Barber, D.G. and Massom, R.A. (2007). The Role of Sea Ice in Arctic and Antarctic Polynyas. In W.O. Smith and D.G. Barber, eds., *Polynyas: Windows to the World*, number 74 in Elsevier Oceanography Series, pages 1–54. Amsterdam, Oxford
- van de Berg, W., van den Broeke, M., Reijmer, C., and van Meijgaard, E. (2005). Characteristics of the Antarctic surface mass balance, 1958–2002, using a regional atmospheric climate model. *Annals of Glaciology*, 41(1): 97–104. doi:10.3189/172756405781813302. 28th Symposium of the Scientific-Committee on Antarctic Research, Bremen, GERMANY, JUL 28-29, 2004
- van de Berg, W., van den Broeke, M., Reijmer, C., and van Meijgaard, E. (2006). Reassessment of the Antarctic surface mass balance using calibrated output of a regional atmospheric climate model. *Journal of Geophysical Research*, 111(D11104): 1–15. doi:10.1029/2005JD006495
- van de Berg, W.J., van den Broeke, M.R., and van Meijgaard, E. (2007). Heat budget of the East Antarctic lower atmosphere derived from a regional atmospheric climate model. *Journal of Geophysical Research*, 112(D23101): 1–14. doi:10.1029/2007JD008613
- van de Berg, W.v., van den Broeke, M., and van Meijgaard, E. (2008). Spatial structures in the heat budget of the Antarctic atmospheric boundary layer. *The Cryosphere*, 2(1): 1–12. doi:10.5194/tc-2-1-2008
- Bouillon, S., Maqueda, M.A.M., Legat, V., and Fichefet, T. (2009). An elastic-viscous-plastic sea ice model formulated on Arakawa B and C grids. *Ocean Modelling*, 27(3-4): 174–184. doi:10.1016/j.ocemod.2009.01.004
- Brandt, R.E., Warren, S.G., Worby, A.P., and Grenfell, T.C. (2005). Surface Albedo of the Antarctic Sea Ice Zone. *Journal of Climate*, 18(17): 3606–3622. doi:10.1175/JCLI3489.1
- van den Broeke, M. and Bintanja, R. (1995). The interaction of katabatic winds and the formation of blue-ice areas in East Antarctica. *Journal of Glaciology*, 41(138): 395–407
- van den Broeke, M. and van Lipzig, N. (2003a). Factors controlling the near-surface wind field in Antarctica. *Monthly Weather Review*, 131(4): 733–743
- van den Broeke, M., van Lipzig, N., and van Meijgaard, E. (2002). Momentum budget of the East Antarctic atmospheric boundary layer: Results of a Regional Climate Model. *Journal of the Atmospheric Sciences*, 59(21): 3117–3129
- van den Broeke, M.R. (1998). The semi-annual oscillation and Antarctic climate. Part 1: Influence on near surface temperatures (1957–79). *Antarctic Science*, 10(2): 175–183. doi:10.1017/S0954102098000248
- van den Broeke, M.R. (2000a). On the interpretation of Antarctic temperature trends. *Journal of Climate*, 13(21): 3885–3889. doi:10.1175/1520-0442(2000)013<3885:3AOTIOAT>2.0.CO%3B2
- van den Broeke, M.R. (2000b). The semi-annual oscillation and Antarctic climate. Part 4: A note on sea ice cover in the Amundsen and Bellingshausen Seas. *International Journal of Climatology*, 20(4): 455–462. doi:

- 10.1002/(SICI)1097-0088(20000330)20:4<455::AID-JOC482>3.0.CO;2-M
- van den Broeke, M.R. (2009a). Reynolds averaged conservation equations. In *Lecture Notes in Boundary-Layer Meteorology*, 2. Utrecht: Utrecht University
- van den Broeke, M.R. (2009b). The stable ABL. In *Lecture Notes in Boundary-Layer Meteorology*, 7. Utrecht: Utrecht University
- van den Broeke, M.R., van As, D., Reijmer, C.H., and van de Wal, R.S.W. (2004). Surface radiation balance in Antarctica as measured with automatic weather stations. *Journal of Geophysical Research*, 109: D09103. doi:10.1029/2003JD004394
- van den Broeke, M.R., Fettweis, X., and Mölg, T. (2011). Surface Energy Balance. In V.P. Singh, P. Singh, and U.K. Haritashya, eds., *Encyclopedia of Snow, Ice and Glaciers*, Encyclopedia of Earth Sciences Series, pages 1112–1123. Dordrecht: Springer. doi:10.1007/978-90-481-2642-2_132
- van den Broeke, M.R. and van Lipzig, N.P.M. (2002). Impact of polar vortex variability on the wintertime low-level climate of East Antarctica: results of a regional climate model. *Tellus A*, 54(5): 485–496. doi:10.1034/j.1600-0870.2002.201383.x. Climate Conference 2001, Utrecht, Netherlands, Aug, 2001
- van den Broeke, M.R. and van Lipzig, N.P.M. (2003b). *Response of wintertime Antarctic temperatures to the antarctic oscillation: Results of a regional climate model*, volume 79 of *Antarctic Research Series*. Washington, D.C.: American Geophysical Union. ISBN 0-87590-973-6. International Workshop on Antarctic Peninsula Climate Variability, Clinton, NY, 2002
- van den Broeke, M.R., Reijmer, C., van As, D., van de Wal, R., and Oerlemans, J. (2005). Seasonal cycles of Antarctic surface energy balance from automatic weather stations. *Annals of Glaciology*, 41(1): 131–139. doi:10.3189/172756405781813168
- Carleton, A.M. (2003). Atmospheric teleconnections involving the Southern Ocean. *Journal of Geophysical Research*, 108(C4): 8080. doi:10.1029/2000JC000379
- Cavalieri, D., Gloersen, P., Parkinson, C., Comiso, J., and Zwally, H. (1997). Observed hemispheric asymmetry in global sea ice changes. *Science*, 278(5340): 1104–1106. doi:10.1126/science.278.5340.1104
- Cavalieri, D. and Parkinson, C. (2008). Antarctic sea ice variability and trends, 1979–2006. *Journal of Geophysical Research*, 113(C07004): 1–19. doi:10.1029/2007JC004564
- Cavalieri, D., Parkinson, C., Gloersen, P., and Zwally, H.J. (updated 2008, 1996). *Sea Ice Concentrations from Nimbus-7 SMMR and DMSP SSM/I Passive Microwave Data, 1989–2007*. Boulder, Colorado USA: National Snow and Ice Data Center, digital media edition
- Cavalieri, D., Parkinson, C., and Vinnikov, K. (2003). 30-Year satellite record reveals contrasting Arctic and Antarctic decadal sea ice variability. *Geophysical Research Letters*, 30(18): 1–4. doi:10.1029/2003GL018031
- Cavalieri, D., Thorsten, M., and Comiso, J. (updated daily, 2004). *AMSR-E/Aqua Daily L3 25 km Brightness Temperature and Sea Ice Concentration Polar Grids V002, 2003–2010*. Boulder, Colorado USA: National Snow and Ice Data Center, digital media edition
- Cavalieri, D.J. and Parkinson, C.L. (1981). Large-Scale Variations in Observed Antarctic Sea Ice Extent and Associated Atmospheric Circulation. *Monthly Weather Review*, 109(11): 2323–2336. doi:10.1175/1520-0493(1981)109<2323:LSVIOA>2.0.CO;2
- Cavalieri, D.J., Parkinson, C.L., Gloersen, P., Comiso, J.C., and Zwally, H.J. (1999). Deriving long-term time series of sea ice cover from satellite passive-microwave multisensor data sets. *Journal of Geophysical Research*, 104(C7): 15803–15814. doi:10.1029/1999JC900081
- Comiso, J. (2009). *Polar Oceans from Space*, volume 41 of *Atmospheric and Oceanographic Science Library*. New York, Dordrecht, Heidelberg, London: Springer
- Comiso, J.C., Kwok, R., Martin, S., and Gordon, A.L. (2011). Variability and trends in sea ice extent and ice production in the Ross Sea. *Journal of Geophysical Research*, 116(C4): C04021. doi:10.1029/2010JC006391
- Comiso, J.C. and Nishio, F. (2008). Trends in the sea ice cover using enhanced and compatible AMSR-E, SSM/I, and SMMR data. *Journal of Geophysical Research*, 113(C2): C02S07. doi:10.1029/2007JC004257
- Comiso, J.C., Parkinson, C.L., Gersten, R., and Stock, L. (2008). Accelerated decline in the Arctic sea ice cover. *Geophysical Research Letters*, 35(1): L01703. doi:10.1029/2007GL031972
- Coon, M.D. (1980). A Review of AIDJEX Modeling. In R.S. Pritchard, ed., *Sea Ice Processes and Models: Proceedings of the Arctic Ice Dynamics Joint Experiment International Commission on Snow and Ice Symposium*, pages 12–27. Seattle and London: University of Washington Press
- Coon, M.D., Maykut, G.A., Pritchard, R.S., Rothrock, D.A., and Thorndike, A.S. (1974). Modeling the Pack Ice as an Elastic-Plastic Material. In *AIDJEX Bulletin*, 24, pages 1–105. Seattle: University of Washington
- Curry, J.A., Schramm, J.L., and Ebert, E.E. (1995). Sea Ice-Albedo Climate Feedback Mechanism. *Journal of Climate*, 8(2): 240–247. doi:10.1175/1520-0442(1995)008<0240:SIACFM>2.0.CO;2
- Cushman-Roisin, B. and Beckers, J.M. (2011). *Introduction to Geophysical Fluid Dynamics: Physical and Numerical Methods*. New York: Academic Press

- ical Aspects*, volume 101 of *International Geophysics Series*. Burlington, San Diego, London: Elsevier Academic Press, 2 edition
- Dee, D.P., Uppala, S.M., Simmons, A.J., Berrisford, P., Poli, P., Kobayashi, S., Andrae, U., Balmaseda, M.A., Balsamo, G., Bauer, P., Bechtold, P., Beljaars, A.C.M., van de Berg, L., Bidlot, J., Bormann, N., Delsol, C., Dragani, R., Fuentes, M., Geer, A.J., Haimberger, L., Healy, S.B., Hersbach, H., Hólm, E.V., Isaksen, L., Kållberg, P., Köhler, M., Matricardi, M., McNally, A.P., Monge-Sanz, B.M., Morcrette, J.J., Park, B.K., Peubey, C., de Rosnay, P., Tavolato, C., Thépaut, J.N., and Vitart, F. (2011). The ERA-Interim reanalysis: configuration and performance of the data assimilation system. *Quarterly Journal of the Royal Meteorological Society*, 137(656): 553–597. doi:10.1002/qj.828
- Deser, C., Walsh, J.E., and Timlin, M.S. (2000). Arctic Sea Ice Variability in the Context of Recent Atmospheric Circulation Trends. *Journal of Climate*, 13(3): 617–633. doi:10.1175/1520-0442(2000)013<0617:ASIVIT>2.0.CO;2
- Doran, P.T., Priscu, J.C., Lyons, W.B., Walsh, J.E., Fountain, A.G., McKnight, D.M., Moorhead, D.L., Virginia, R.A., Wall, D.H., Clow, G.D., Fritsen, C.H., McKay, C.P., and Parsons, A.N. (2002). Antarctic climate cooling and terrestrial ecosystem response. *Nature*, 415(6871): 517–520. doi:10.1038/nature710
- Drucker, R., Martin, S., and Kwok, R. (2011). Sea ice production and export from coastal polynyas in the Weddell and Ross Seas. *Geophysical Research Letters*, 38(17): L17502. doi:10.1029/2011GL048668
- Eicken, H. (2003). From the Microscopic, to the Macroscopic, to the Regional Scale: Growth, Microstructure and Properties of Sea Ice. In D.N. Thomas and G.S. Dieckmann, eds., *Sea Ice: An Introduction to its Physics, Chemistry, Biology and Geology*, chapter 2, pages 22–81. Oxford, UK: Blackwell Science Ltd. doi:10.1002/9780470757161.ch2
- Ekman, V.W. (1905). On the influence of the Earth's rotation on ocean currents. *Archive for Mathematics, Astronomy and Physics*, 2(11): 1–52
- Emery, W., Fowler, C., and Maslanik, J. (1995). *Satellite Remote Sensing of Ice Motion*. Oceanographic Applications of Remote Sensing. Boca Raton: CRC Press
- Ettema, J., van den Broeke, M., van Meijgaard, E., van de Berg, W., Box, J., and Steffen, K. (2010). Climate of the Greenland ice sheet using a high-resolution climate model, Part 1: Evaluation. *The Cryosphere*, 4: 511–527. doi:10.5194/tc-4-511-2010
- Ettema, J., van den Broeke, M.R., van Meijgaard, E., van de Berg, W.J., Bamber, J.L., Box, J.E., and Bales, R.C. (2009). Higher surface mass balance of the Greenland ice sheet revealed by high-resolution climate modeling. *Geophysical Research Letters*, 36(12): L12501. doi:10.1029/2009GL038110
- Feltham, D.L. (2008). Sea ice rheology. *Annual Review of Fluid Mechanics*, 40: 91–112. doi:10.1146/annurev.fluid.40.111406.102151
- Feltham, D.L., Untersteiner, N., Wettlaufer, J.S., and Worster, M.G. (2006). Sea ice is a mushy layer. *Geophysical Research Letters*, 33(14): L14501. doi:10.1029/2006GL026290
- Fowler, C. (updated 2008, 2003). *Polar Pathfinder Daily 25 km EASE-Grid Sea Ice Motion Vectors, 1989-2006*. Boulder, Colorado USA: National Snow and Ice Data Center, digital media edition
- Garratt, J. (1994). *The atmospheric boundary layer*. Cambridge atmospheric and space science series. Cambridge: Cambridge University Press. ISBN 9780521467452
- Gloersen, P., Campbell, W.J., Cavalieri, D., Comiso, J.C., Parkinson, C.L., and Zwally, H.J. (1992). *Arctic and Antarctic Sea Ice, 1978-1987: Satellite Passive-Microwave Observations and Analysis*. Number 511 in NASA Special Publication. Washington, D.C.: Scientific and Technical Information Program, NASA
- Goosse, H., Lefebvre, W., de Montety, A., Crespin, E., and Orsi, A. (2009). Consistent past half-century trends in the atmosphere, the sea ice and the ocean at high southern latitudes. *Climate Dynamics*, 33(7): 999–1016. doi:10.1007/s00382-008-0500-9
- Haas, C. (2003). Dynamics versus Thermodynamics: The Sea Ice Thickness Distribution. In D.N. Thomas and G.S. Dieckmann, eds., *Sea Ice: An Introduction to its Physics, Chemistry, Biology and Geology*, chapter 3, pages 82–111. Oxford, UK: Blackwell Science Ltd. ISBN 9780470757161. doi:10.1002/9780470757161.ch3
- Hansen, J., Ruedy, R., Sato, M., and Lo, K. (2010). Global Surface Temperature Change. *Reviews of Geophysics*, 48(4): RG4004. doi:10.1029/2010RG000345
- Heil, P., Hutchings, J.K., Worby, A.P., Johansson, M., Launiainen, J., Haas, C., and D. Hibler III, W. (2008). Tidal forcing on sea-ice drift and deformation in the western Weddell Sea in early austral summer, 2004. *Deep Sea Research Part II: Topical Studies in Oceanography*, 55(8-9): 943–962. doi:10.1016/j.dsr2.2007.12.026. Ice Station POLarstern (ISPOL): Results of interdisciplinary studies on a drifting ice floe in the western Weddell Sea
- Hibler III, W.D. (1979). A Dynamic Thermodynamic Sea Ice Model. *Journal of Physical Oceanography*, 9(4): 815–846. doi:10.1175/1520-0485(1979)009<0815:ADTSIM>2.0.CO;2

- Holton, J. (2004). *An introduction to dynamic meteorology*, volume 88 of *International Geophysics Series*. Burlington, San Diego, London: Elsevier Academic Press, 4 edition
- Hunke, E.C. and Dukowicz, J.K. (1997). An Elastic-Viscous-Plastic Model for Sea Ice Dynamics. *Journal of Physical Oceanography*, 27(9): 1849–1867. doi:10.1175/1520-0485(1997)027<1849:AEVPMF>2.0.CO;2
- Hunke, E.C., Notz, D., Turner, A.K., and Vancoppenolle, M. (2011). The multiphase physics of sea ice: a review. *The Cryosphere Discussions*, 5(4): 1949–1993. doi:10.5194/tcd-5-1949-2011
- Hunkins, K. (1966). Ekman drift currents in the Arctic Ocean. *Deep Sea Research and Oceanographic Abstracts*, 13(4): 607–620
- IPCC (2007). *Climate Change 2007: The Physical Science Basis. Contribution of Working Group I to the Fourth Assessment Report of the Intergovernmental Panel on Climate Change*. Cambridge, United Kingdom and New York, NY, USA: Cambridge University Press
- Jacobs, S.S., Giulivi, C.F., and Mele, P.A. (2002). Freshening of the Ross Sea During the Late 20th Century. *Science*, 297(5580): 386–389. doi:10.1126/science.1069574
- Jeffries, M.O., Worby, A.P., Morris, K., and Weeks, W.F. (1997). Seasonal variations in the properties and structural composition of sea ice and snow cover in the Bellingshausen and Amundsen Sea, Antarctica. *Journal of Glaciology*, 43(143): 138–151
- Jourdain, N. and Gallée, H. (2011). Influence of the orographic roughness of glacier valleys across the Transantarctic Mountains in an atmospheric regional model. *Climate Dynamics*, 36(5): 1067–1081. doi:10.1007/s00382-010-0757-7
- King, J.C. and Turner, J. (1997). *Antarctic Meteorology and Climatology*. Cambridge atmospheric and space science series. Cambridge: Cambridge University Press
- Kottmeier, C., Olf, J., Frieden, W., and Roth, R. (1992). Wind Forcing and Ice Motion in the Weddell Sea Region. *Journal of Geophysical Research*, 97(D18): 20373–20383. doi:10.1029/92JD02171
- Kuipers Munneke, P. (2009). *Snow, ice and solar radiation*. Ph.D. thesis, University of Utrecht
- Kuipers Munneke, P., van den Broeke, M.R., Lenaerts, J.T.M., Flanner, M.G., Gardner, A.S., and van de Berg, W.J. (2011). A new albedo parameterization for use in climate models over the Antarctic ice sheet. *Journal of Geophysical Research*, 116(D5): D05114. doi:10.1029/2010JD015113
- Kwok, R. (2005). Ross Sea Ice Motion, Area Flux, and Deformation. *Journal of Climate*, 18(18): 3759–3776. doi:10.1175/JCLI3507.1
- Kwok, R. (2009). Outflow of Arctic Ocean Sea Ice into the Greenland and Barents Seas: 1979–2007. *Journal of Climate*, 22(9): 2438–2457. doi:10.1175/2008JCLI2819.1
- Kwok, R. and Comiso, J.C. (2002a). Southern Ocean Climate and Sea Ice Anomalies Associated with the Southern Oscillation. *Journal of Climate*, 15(5): 487–501. doi:10.1175/1520-0442(2002)015<0487:SOCASI>2.0.CO;2
- Kwok, R. and Comiso, J.C. (2002b). Spatial patterns of variability in Antarctic surface temperature: Connections to the Southern Hemisphere Annular Mode and the Southern Oscillation. *Geophysical Research Letters*, 29(14): 1705. doi:10.1029/2002GL015415
- Kwok, R., Cunningham, G.F., Wensnahan, M., Rigor, I., Zwally, H.J., and Yi, D. (2009). Thinning and volume loss of the Arctic Ocean sea ice cover: 2003–2008. *Journal of Geophysical Research*, 114(C7): C07005. doi:10.1029/2009JC005312
- Lachlan-Cope, T.A., Connolley, W.M., and Turner, J. (2001). The Role of the Non-Axisymmetric Antarctic Orography in forcing the Observed Pattern of Variability of the Antarctic Climate. *Geophysical Research Letters*, 28(21): 4111–4114. doi:10.1029/2001GL013465
- Lefebvre, W., Goosse, H., Timmermann, R., and Fichefet, T. (2004). Influence of the Southern Annular Mode on the sea ice-ocean system. *Journal of Geophysical Research*, 109(C9): C09005. doi:10.1029/2004JC002403
- Lenaerts, J. and van den Broeke, M. (2011). Modeling of snowdrift in Antarctica with a regional climate model, Part II: Results. *Submitted to Journal of Geophysical Research*
- Lenaerts, J., van den Broeke, M., Déry, S., van Meijgaard, E., van de Berg, W., Palm, S., and Sanz Rodrigo, J. (2011). Modeling snowdrift in Antarctica with a regional climate model, Part I: Methods and model evaluation. *Submitted to Journal of Geophysical Research*
- Lenaerts, J.T.M., van den Broeke, M.R., Dery, S.J., König-Langlo, G., Ettema, J., and Munneke, P.K. (2010). Modelling snowdrift sublimation on an Antarctic ice shelf. *The Cryosphere*, 4(2): 179–190. doi:10.5194/tc-4-179-2010
- van Lipzig, N.P.M., van Meijgaard, E., and Oerlemans, J. (2002). The spatial and temporal variability of the surface mass balance in Antarctica: results from a regional atmospheric climate model. *International Journal of Climatology*, 22(10): 1197–1217. doi:10.1002/joc.798
- Liu, H., Jezek, K., Li, B., and Zhao, Z. (2001). *Radarsat Antarctic Mapping Project digital elevation model version 2*. Boulder, Colorado USA: National Snow and Ice Data Center, digital media edition

- Liu, J., Curry, J.A., and Martinson, D.G. (2004). Interpretation of recent Antarctic sea ice variability. *Geophysical Research Letters*, 31(2): L02205. doi:10.1029/2003GL018732
- van Loon, H., Taljaard, J.J., Sasamori, T., London, J., Hoyt, D.V., Labitzke, K., and Newton, C.W. (1972). *Meteorology of the southern hemisphere*, volume 13 of *Meteorological Monographs*. Boston: American Meteorological Society
- Mahrt, L. (1982). Momentum Balance of Gravity Flows. *Journal of the Atmospheric Sciences*, 39(12): 2701–2711
- Mahrt, L. (1999). Stratified Atmospheric Boundary Layers. *Boundary-Layer Meteorology*, 90: 375–396. doi: 10.1023/A:1001765727956
- Maslanik, J., Fowler, C., Key, J., Scambos, T., Hutchinson, T., and Emery, W. (1997). AVHRR-based Polar Pathfinder Products for Modeling Applications. *Annals of Glaciology*, 25: 388–392
- MATLAB® (2009). *MATLAB 7.8.0 (R2009a) - The Language Of Technical Computing*. The MathWorks, Inc.
- Mayewski, P.A., Meredith, M.P., Summerhayes, C.P., Turner, J., Worby, A., Barrett, P.J., Casassa, G., Bertler, N.A.N., Bracegirdle, T., Naveira Garabato, A.C., Bromwich, D., Campbell, H., Hamilton, G.S., Lyons, W.B., Maasch, K.A., Aoki, S., Xiao, C., and van Ommen, T. (2009). State of the Antarctic and Southern Ocean climate system. *Reviews of Geophysics*, 47(1): RG1003. doi:10.1029/2007RG000231
- Maykut, G.A. and Untersteiner, N. (1971). Some Results from a Time-Dependent Thermodynamic Model of Sea Ice. *Journal of Geophysical Research*, 76(6): 1550–1575. doi:10.1029/JC076i006p01550
- McPhee, M. (2008). *Air-Ice-Ocean Interaction: Turbulent Ocean Boundary Layer Exchange Processes*. New York, Dordrecht, Heidelberg, London: Springer. doi:10.1007/978-0-387-78335-2
- McPhee, M.G. (1975). Ice-Ocean Momentum Transfer for the AIDJEX Ice Model. In *AIDJEX Bulletin*, 29, pages 93–111. Seattle: University of Washington
- McPhee, M.G. (1992). Turbulent Heat Flux in the Upper Ocean Under Sea Ice. *Journal of Geophysical Research*, 97(C4): 5365–5379. doi:10.1029/92JC00239
- van Meijgaard, E., van Ulft, L., van de Berg, W., Bosveld, F., van den Hurk, B., Lenderink, G., and Siebesma, A. (2008). The KNMI regional atmospheric climate model RACMO version 2.1. Technical Report 302, Royal Netherlands Meteorological Institute
- Minnett, P.J. and Key, E.L. (2007). Meteorology and Atmosphere-Surface Coupling in and around Polynyas. In W.O. Smith and D.G. Barber, eds., *Polynyas: Windows to the World*, number 74 in Elsevier Oceanography Series, pages 127–161. Amsterdam, Oxford: Elsevier
- Monaghan, A.J., Bromwich, D.H., Chapman, W., and Comiso, J.C. (2008). Recent variability and trends of Antarctic near-surface temperature. *Journal of Geophysical Research*, 113(D4): D04105. doi:10.1029/2007JD009094
- Notz, D. (2009). The future of ice sheets and sea ice: Between reversible retreat and unstoppable loss. *Proceedings of the National Academy of Sciences*, 106(49): 20590–20595. doi:10.1073/pnas.0902356106
- Notz, D. and Worster, M.G. (2006). A one-dimensional enthalpy model of sea ice. *Annals of Glaciology*, 44(1): 123–128. doi:10.3189/172756406781811196
- Notz, D. and Worster, M.G. (2009). Desalination processes of sea ice revisited. *Journal of Geophysical Research*, 114(C5): C05006. doi:10.1029/2008JC004885
- Oberhuber, J.M. (1993). Simulation of the Atlantic Circulation with a Coupled Sea Ice-Mixed Layer-Isopycnal General Circulation Model. Part I: Model Description. *Journal of Physical Oceanography*, 23(5): 808–829. doi:10.1175/1520-0485(1993)023<0808:SOTACW>2.0.CO;2
- O'Connor, W.P., Bromwich, D.H., and Carrasco, J.F. (1994). Cyclonically Forced Barrier Winds along the Transantarctic Mountains near Ross Island. *Monthly Weather Review*, 122(1): 137–150
- Overland, J.E. (1984). Scale Analysis of Marine Winds in Straits and along Mountainous Coasts. *Monthly Weather Review*, 112(12): 2530–2534. doi:10.1175/1520-0493(1984)112<2530:SAOMWI>2.0.CO;2
- Overland, J.E. and Davidson, K.L. (1992). Geostrophic drag coefficients over sea ice. *Tellus A*, 44(1): 54–66. doi:10.1034/j.1600-0870.1992.t01-5-00006.x
- Overland, J.E., Reynolds, R.M., and Pease, C.H. (1983). A Model of the Atmospheric Boundary Layer Over the Marginal Ice Zone. *Journal of Geophysical Research*, 88(C5): 2836–2840. doi:10.1029/JC088iC05p02836
- Parish, T. (1984). A Numerical Study of Strong Katabatic Winds over Antarctica. *Monthly Weather Review*, 112(3): 545–554
- Parish, T. and Cassano, J. (2001). Forcing of the wintertime antarctic boundary layer winds from the NCEP-NCAR global reanalysis. *Journal of Applied Meteorology*, 40(4): 810–821. doi:10.1175/1520-0450(2001)040<0810:FOTWAB>2.0.CO;2
- Parish, T. and Cassano, J. (2003). The role of katabatic winds on the Antarctic surface wind regime. *Monthly Weather Review*, 131(2): 317–333
- Parish, T. and Waight, K. (1987). The Forcing of Antarctic Katabatic Winds. *Monthly Weather Review*, 115(10):

- Parish, T.R. (1981). The katabatic winds of Cape Denison and Port Martin. *Polar Record*, 20: 525–532. doi: 10.1017/S0032247400003934
- Parish, T.R. (1983). The Influence of the Antarctic Peninsula on the Wind Field Over the Western Weddell Sea. *Journal of Geophysical Research*, 88(C4): 2684–2692
- Parish, T.R. and Bromwich, D.H. (1987). The surface windfield over the Antarctic ice sheets. *Nature*, 328(6125): 51–54. doi:10.1038/328051a0
- Parish, T.R., Cassano, J.J., and Seefeldt, M.W. (2006). Characteristics of the Ross Ice Shelf air stream as depicted in Antarctic Mesoscale Prediction System simulations. *Journal of Geophysical Research*, 111(D12): D12109. doi:10.1029/2005JD006185
- Parkinson, C.L. and Cavalieri, D.J. (2008). Arctic sea ice variability and trends, 1979–2006. *Journal of Geophysical Research*, 113(C7): C07003. doi:10.1029/2007JC004558
- Parkinson, C.L., Cavalieri, D.J., Gloersen, P., Zwally, H.J., and Comiso, J.C. (1999). Arctic sea ice extents, areas, and trends, 1978–1996. *Journal of Geophysical Research*, 104(C9): 20837–20856. doi:10.1029/1999JC900082
- Parkinson, C.L. and Comiso, J.C. (2008). Antarctic sea ice parameters from AMSR-E data using two techniques and comparisons with sea ice from SSM/I. *Journal of Geophysical Research*, 113(C2): C02S06. doi:10.1029/2007JC004253
- Parkinson, C.L. and Washington, W.M. (1979). A Large-Scale Numerical Model of Sea Ice. *Journal of Geophysical Research*, 84(C1): 311–337. doi:10.1029/JC084iC01p00311
- Perovich, D.K. (1996). The Optical Properties of Sea Ice. *CRREL Monograph*, 96-1: 25
- Prandtl, L. (1942). *Führer durch die Strömungslehre*. Braunschweig: Verlag F. Vieweg & Sohn, 3 edition
- Reijmer, C.H., van Meijgaard, E., and van den Broeke, M.R. (2005). Evaluation of temperature and wind over Antarctica in a Regional Atmospheric Climate Model using 1 year of automatic weather station data and upper air observations. *Journal of Geophysical Research*, 110(D04103): 1–12. doi:10.1029/2004JD005234
- Reijmer, C.H., Van Meijgaard, E., and Van Den Broeke, M.R. (2004). Numerical studies with a regional atmospheric climate model based on changes in the roughness length for momentum and heat over Antarctica. *Boundary-Layer Meteorology*, 111(2): 313–337. doi:10.1023/B:BOUN.0000016470.23403.ca
- Rothrock, D. (1975a). The Energetics of the Plastic Deformation of Pack Ice by Ridging. *Journal of Geophysical Research*, 80(33): 4514–4519
- Rothrock, D.A. (1975b). The Steady Drift of an Incompressible Arctic Ice Cover. *Journal of Geophysical Research*, 80(3): 387–397. doi:10.1029/JC080i003p00387
- Santer, B.D., Wigley, T.M.L., Boyle, J.S., Gaffen, D.J., Hnilo, J.J., Nychka, D., Parker, D.E., and Taylor, K.E. (2000). Statistical significance of trends and trend differences in layer-average atmospheric temperature time series. *Journal of Geophysical Research*, 105(D6): 7337–7356. doi:10.1029/1999JD901105
- Schwerdtfeger, W. (1975). The Effect of the Antarctic Peninsula on the Temperature Regime of the Weddell Sea. *Monthly Weather Review*, 103(1): 45–51. doi:10.1175/1520-0493(1975)103(0045:TEOTAP)2.0.CO;2
- Schwerdtfeger, W. (1979). Meteorological Aspects of the Drift of Ice From the Weddell Sea Toward the Mid-Latitude Westerlies. *Journal of Geophysical Research*, 84(C10): 6321–6328. doi:10.1029/JC084iC10p06321
- Schwerdtfeger, W. (1984). *Weather and climate of the Antarctic*. Number 15 in Developments in Atmospheric Science. Amsterdam: Elsevier
- Screen, J.A. (2011). Sudden increase in Antarctic sea ice: Fact or artifact? *Geophysical Research Letters*, 38(13): L13702. doi:10.1029/2011GL047553
- Seefeldt, M.W. and Cassano, J.J. (2008). An Analysis of Low-Level Jets in the Greater Ross Ice Shelf Region Based on Numerical Simulations. *Monthly Weather Review*, 136(11): 4188–4205. doi:10.1175/2008MWR2455.1
- Seefeldt, M.W., Cassano, J.J., and Parish, T.R. (2007). Dominant regimes of the Ross Ice Shelf surface wind field during austral autumn 2005. *Journal of Applied Meteorology and Climatology*, 46(11): 1933–1955. doi: 10.1175/2007JAMC1442.1
- Semtner, A.J. (1976). A Model for the Thermodynamic Growth of Sea Ice in Numerical Investigations of Climate. *Journal of Physical Oceanography*, 6(3): 379–389. doi:10.1175/1520-0485(1976)006<379:AMFTTG>2.0.CO;2
- Semtner, A.J. (1984). On modelling the seasonal thermodynamic cycle of sea ice in studies of climatic change. *Climatic Change*, 6: 27–37. doi:10.1007/BF00141666
- Shu, Q., Qiao, F., Song, Z., and Wang, C. (2011). Sea ice trends in the Antarctic and their relationship to surface air temperature during 1979–2009. *Climate Dynamics*, pages 1–9. doi:10.1007/s00382-011-1143-9
- Sigmond, M. and Fyfe, J.C. (2010). Has the ozone hole contributed to increased Antarctic sea ice extent? *Geophysical Research Letters*, 37(18): L18502. doi:10.1029/2010GL044301
- Simmons, A., Uppala, S., Dee, D., and Kobayashi, S. (2007). ERA-Interim: New ECMWF reanalysis products from 1989 onwards. *ECMWF Newsletter*, 110: 25–35

- Stammerjohn, S., Martinson, D., Smith, R., Yuan, X., and Rind, D. (2008). Trends in Antarctic annual sea ice retreat and advance and their relation to El Nino-Southern Oscillation and Southern Annular Mode variability. *Journal of Geophysical Research*, 113(C03S90): 1–20. doi:10.1029/2007JC004269
- Steinhoff, D.F., Chaudhuri, S., and Bromwich, D.H. (2009). A Case Study of a Ross Ice Shelf Airstream Event: A New Perspective. *Monthly Weather Review*, 137(11): 4030–4046. doi:10.1175/2009MWR2880.1
- Stroeve, J., Holland, M.M., Meier, W., Scambos, T., and Serreze, M. (2007). Arctic sea ice decline: Faster than forecast. *Geophys. Res. Lett.*, 34(9): L09501. doi:10.1029/2007GL029703
- Stroeve, J. and Meier, W. (updated 2011, 1999). *Sea Ice Trends and Climatologies from SMMR and SSM/I, 1989–2007*. Boulder, Colorado USA: National Snow and Ice Data Center, digital media edition
- Stull, R. (1988). *An Introduction to Boundary Layer Meteorology*. Atmospheric Sciences Library. Dordrecht, Boston, London: Kluwer Academic Publishers. ISBN 9789027727695
- Stull, R. and Ahrens, C. (2000). *Meteorology for scientists and engineers*. Earth Science Series. Brooks/Cole. ISBN 9780534372149
- Thompson, D.W.J. and Solomon, S. (2002). Interpretation of Recent Southern Hemisphere Climate Change. *Science*, 296(5569): 895–899. doi:10.1126/science.1069270
- Thorndike, A. and Colony, R. (1982). Sea Ice Motion in Response to Geostrophic Winds. *Journal of Geophysical Research*, 87(C8): 5845–5852
- Thorndike, A., Rothrock, D., Maykut, G., and Colony, R. (1975). The Thickness Distribution of Sea Ice. *Journal of Geophysical Research*, 80(33): 4501–4513
- Trauth, M. and Sillmann, E. (2010). *MATLAB Recipes for Earth Sciences*. Springer. ISBN 9783642127618
- Turner, J., Colwell, S.R., Marshall, G.J., Lachlan-Cope, T.A., Carleton, A.M., Jones, P.D., Lagun, V., Reid, P.A., and Iagovkina, S. (2005). Antarctic climate change during the last 50 years. *International Journal of Climatology*, 25(3): 279–294
- Turner, J., Comiso, J.C., Marshall, G.J., Lachlan-Cope, T.A., Bracegirdle, T., Maksym, T., Meredith, M.P., Wang, Z., and Orr, A. (2009). Non-annual atmospheric circulation change induced by stratospheric ozone depletion and its role in the recent increase of Antarctic sea ice extent. *Geophysical Research Letters*, 36(L08502): 1–5. doi:10.1029/2009GL037524
- Turner, J., King, J.C., Lachlan-Cope, T.A., and Jones, P.D. (2002). Climate change (Communication arising): Recent temperature trends in the Antarctic. *Nature*, 418(6895): 291–292. doi:10.1038/418291b
- Turner, J., Lachlan-Cope, T.A., Colwell, S., Marshall, G.J., and Connolley, W.M. (2006). Significant Warming of the Antarctic Winter Troposphere. *Science*, 311(5769): 1914–1917. doi:10.1126/science.1121652
- Vancoppenolle, M., Fichefet, T., Goosse, H., Bouillon, S., Madec, G., and Maqueda, M.A.M. (2009). Simulating the mass balance and salinity of Arctic and Antarctic sea ice. 1. Model description and validation. *Ocean Modelling*, 27(1-2): 33–53. doi:10.1016/j.ocemod.2008.10.005
- Wang, Z. and Meredith, M.P. (2008). Density-driven Southern Hemisphere subpolar gyres in coupled climate models. *Geophysical Research Letters*, 35(14): L14608. doi:10.1029/2008GL034344
- Warner, R.M. (1998). *Spectral analysis of time-series data*. Methodology in the social sciences. New York: Guilford Press. ISBN 9781572303386
- Watkins, A.B. and Simmonds, I. (1999). A late spring surge in the open water of the Antarctic sea ice pack. *Geophysical Research Letters*, 26(10): 1481–1484. doi:10.1029/1999GL900292
- Watson, D.F. (1992). *Contouring: A guide to the analysis and display of spatial data*. Oxford: Pergamon Press
- Weller, G. (1980). Spatial and Temporal Variations in the South Polar Surface Energy Balance. *Monthly Weather Review*, 108(12): 2006–2014. doi:10.1175/1520-0493(1980)108<2006:SATVIT>2.0.CO;2
- White, P.W. (2003). IFS Documentation Cycle CY23r4, Part IV: Physical Processes (CY23r4). Technical report, ECMWF Research Department
- Wilks, D.S. (1995). *Statistical Methods in the Atmospheric Sciences*, volume 59 of *International Geophysics Series*. Burlington, San Diego, London: Elsevier Academic Press
- Williams, W.J., Carmack, E.C., and Ingram, R.G. (2007). Physical Oceanography of Polynyas. In W.O. Smith and D.G. Barber, eds., *Polynyas: Windows to the World*, number 74 in Elsevier Oceanography Series, pages 55–85. Amsterdam, Oxford
- Wiscombe, W.J. and Warren, S.G. (1980). A Model for the Spectral Albedo of Snow. I: Pure Snow. *Journal of Atmospheric Sciences*, 37(12): 2712–2733. doi:10.1175/1520-0469(1980)037<2712:AMFTSA>2.0.CO;2
- Wolfe, J., Renfrow, S., Pharris, K., Barton, K., and Meier, W. (2011). All About Sea Ice. Digital media
- Worby, A.P., Massom, R.A., Allison, I., I., L.V., and Heil, P. (1998). East Antarctic sea ice: a review of its structure, properties and drift. In M.O. Jeffries, ed., *Antarctic sea ice: physical processes, interactions and variability*, volume 74 of *Antarctic Research Series*, pages 41–67. Washington, D.C.: American Geophysical Union

- Yuan, X. (2004). ENSO-related impacts on Antarctic sea ice: a synthesis of phenomenon and mechanisms. *Antarctic Science*, 16: 415–425. doi:10.1017/S0954102004002238
- Yuan, X. and Martinson, D. (2000). Antarctic sea ice extent variability and its global connectivity. *Journal of Climate*, 13(10): 1697–1717. doi:10.1175/1520-0442(2000)013<1697:3AASIEVA>2.0.CO%3B2
- Yuan, X. and Martinson, D.G. (2001). The Antarctic dipole and its predictability. *Geophysical Research Letters*, 28(18): 3609–3612. doi:10.1029/2001GL012969
- Zhang, J. (2007). Increasing Antarctic sea ice under warming atmospheric and oceanic conditions. *Journal of Climate*, 20(11): 2515–2529. doi:10.1175/JCLI4136.1
- Zwally, H., Comiso, J., Parkinson, C., Cavalieri, D., and Gloersen, P. (2002). Variability of Antarctic sea ice 1979–1998. *Journal of Geophysical Research*, 107(C5): 1–19. doi:10.1029/2000JC000733
- Zwally, H.J., Comiso, J.C., Parkinson, C.L., Campbell, W.J., and Carsey, F.D. (1983). *Antarctic Sea Ice, 1973–1976: Satellite Passive-Microwave Observations*. Number 459 in NASA Special Publication. Washington, D.C.: Scientific and Technical Information Program, NASA

Acknowledgment

I would like to thank Michiel van den Broeke for his extremely supportive supervision throughout the research for my thesis from a theoretical, organizational, and, above all, motivational perspective. Not only do the ideas of this thesis result from many extensive discussions with him, but he did also give me the opportunity to get involved with scientific research. He helped me with situating my research interests and shaping my future plans. I am very thankful to Jan van Angelen and Jan Lenaerts for their advice and support whenever I needed it. Their suggestions for improvements and explanations of fundamental knowledge have an enormous contribution to my thesis. Further, thanks to Willem Jan van de Berg's advice, I could solve several problems in relation to the model data.

I really appreciate the support from all other people at the IMAU who are responsible for the large amounts of knowledge that I could gain throughout the past two years of my studies which also helped me in writing this thesis. I would like to especially mention the support of Thomas Röckmann who gave me the opportunity to broaden my knowledge in a different field than the polar climate, to gain experience in applied research, and to financially realize my studies.

I am very thankful to Heike for her great suggestions for improvements and, more importantly, for her endless mental support and motivation. I thank my family, Carmen, Simon and Fabian, for always supporting me even from a large distance. I would like to thank all fellow students from the student room, especially Fabien, Mattia, Mirena, Niels, Roos, and Wim for their very inspiring and helpful discussions, and for their great company during uncountable lunch and coffee breaks. Moreover, I thank Mirena and Stamatis for letting me feel at home in a foreign country and supporting me in any situation.

Finally, I would like to express that I really appreciate the provision of the sea ice concentration and motion data that is the fundamental basis to my thesis by the National Snow and Ice Data Center. In particular, I would like to acknowledge the data provided by Cavalieri et al. (1996, updated 2008), Cavalieri et al. (2004, updated daily), and Fowler (2003, updated 2008).